



HAL
open science

Observabilité de surface et mélange vertical liés à la (sous)mésoéchelle en milieu côtier : application au golfe de Gascogne

Adam Ayouche

► To cite this version:

Adam Ayouche. Observabilité de surface et mélange vertical liés à la (sous)mésoéchelle en milieu côtier : application au golfe de Gascogne. Oceanography. Université de Bretagne occidentale - Brest, 2021. English. NNT : 2021BRES0056 . tel-03651446

HAL Id: tel-03651446

<https://theses.hal.science/tel-03651446>

Submitted on 25 Apr 2022

HAL is a multi-disciplinary open access archive for the deposit and dissemination of scientific research documents, whether they are published or not. The documents may come from teaching and research institutions in France or abroad, or from public or private research centers.

L'archive ouverte pluridisciplinaire **HAL**, est destinée au dépôt et à la diffusion de documents scientifiques de niveau recherche, publiés ou non, émanant des établissements d'enseignement et de recherche français ou étrangers, des laboratoires publics ou privés.

THESE DE DOCTORAT DE

L'UNIVERSITE
DE BRETAGNE OCCIDENTALE

ECOLE DOCTORALE N° 598
Sciences de la Mer et du littoral
Spécialité : *Océanographie physique et environnement*

Par

Adam AYOUCHE

**Surface observability and vertical mixing linked with (sub)mesoscale in
a coastal region: Bay of Biscay application**

Thèse présentée et soutenue à **Plouzané**, le **08 Juillet 2021**
Unité de recherche : **Laboratoire d'Océanographie Physique et Spatiale (LOPS)**

Rapporteurs avant soutenance :

Robert HETLAND Senior scientist,PNLL, Richland, WA 99352, USA
Xavier CAPET Directeur de Recherche CNRS LOCEAN, Paris

Composition du Jury :

Président du Jury :
Yves MOREL Directeur de Recherche CNRS LEGOS, Toulouse

Examineurs :
Robert HETLAND Senior scientist,PNLL, Richland, WA 99352, USA
Xavier CAPET Directeur de Recherche CNRS LOCEAN, Paris
Villy KOURAFALOU Professor, RSMAS/U. Miami, Miami, FL 33149, USA
Guillaume ROULLET Professeur UBO, LOPS, Brest

Directeur de thèse :
Xavier CARTON Professeur UBO, LOPS Brest

Invité(s)

Nadia AYOUB Chargée de Recherche CNRS LEGOS, Toulouse
Guillaume CHARRIA Chercheur IFREMER LOPS, Brest ; Co-Directeur de thèse
Amandine NICOLLE Maître de Conférences ENSTA Bretagne, Brest

Dedicated to my family.

Acknowledgments

Let me thank to all my supporters who were indispensable for the achievement of this Ph.D. research.

First of all, I would like to express my appreciation to Dr. Guillaume Charria, who encouraged me to follow this research and guided me towards the understanding of the art of numerical modelling. I truly believe that working in the LOPS research laboratory stimulates scientific thinking and innovation. Dr. Charria's guidance, patience, helpful discussions, planning management, administrative tasks management, availability and rigorousness are considerably appreciated.

I would like to acknowledge the valuable discussions and input of Pr. Xavier Carton. His contributions to scientific discussions helped me to shape my Ph.D. research. Pr. Carton's valuable time, careful readings, involvement in sharing scientific ideas and help in resolving modellings issues were undoubtedly and greatly esteemed. I will always be thankful to Pr. Xavier Carton for being a good mentor and for guiding me on the right scientific path.

I would also like to express my gratitude and sincere consideration for Dr. Nadia Ayoub. Dr. Ayoub's scientific questionings, discussions and ideas were greatly appreciated and esteemed.

I also acknowledge the suggestions, scientific questions and discussions from my committee members: Dr. Yves Morel, Dr. Bernard Le Cann and Dr. Andrea Doglioli.

This work would not materialize without the technical support of Mr. Sébastien Theetten. His commitment, patience and help were highly necessary and appreciated.

These acknowledgements would not be complete without mentioning the LOPS team, Ifremer administration team (Carole Despinoy, Nathalie Dridi-Moreul) and the Ph.D. school members (Isabelle Bondu, Gaelle Le Faou and Elodie Benon). It was my pleasure working with them and I warmly appreciate their ideas, support and good humour. Special thanks goes to Dr. Guillaume Roulet for sharing Fluid2d numerical code, and to Dr. Sabine Schmidt for sharing valuable data.

My deepest appreciation belongs to my family for their patience and understanding.

Contents

1	Introduction	9
1.1	Context	9
1.2	River plume structure and dynamics	10
1.3	Instabilities in river plumes	15
1.4	Vertical mixing in river plumes	20
1.5	River plumes in the Bay of Biscay	25
1.6	Thesis outline	27
2	Methodology	29
2.1	Primitive Equations	29
2.1.1	Turbulent closure schemes	31
2.2	The Bay of Biscay Realistic Configuration	33
2.2.1	The CROCO model numerics	34
2.2.2	Grid and initial conditions of the realistic simulation	35
2.2.3	Vertical and Lateral boundaries	37
2.2.4	Computational workflow	37
2.3	Non-Hydrostatic approximation	38
2.3.1	Fluid2D Model	38
2.3.2	Linear stability analysis	39
3	River plumes in homogeneous and steady ocean	41
3.1	Introduction	41
3.2	Article	42
3.3	Conclusions et Perspectives	84
3.4	Notes on chapter 3	86
4	Vertical shear processes in river plumes	87
4.1	Introduction	87
4.2	Article	88
4.3	Conclusions et Perspectives	147
4.4	Notes on chapter 4	148
5	River plumes in turbulent ocean	149
5.1	Introduction	149
5.2	Article	150
5.3	Conclusions et Perspectives	175
5.4	Notes on Chapter 5	176

6	Conclusions and Perspectives	178
6.1	the PhD objectives and Workflow	178
6.2	Summary of Chapter 3	179
6.3	Summary of Chapter 4	181
6.4	Summary of Chapter 5	183
6.5	General Conclusions	185
6.6	Perspectives	188
	Bibliography	191
	Abstract	214

List of Figures

1-1	River plume regions (Vertical structure). Source: Hetland [2005] . . .	14
1-2	River plume regions (Horizontal structure). Source: Horner-Devine et al. [2015]	14
1-3	River plume regions, conditions of their existence and mixing processes specific to each region. Source : Horner-Devine et al. [2015] . .	22
1-4	Circulation in the Bay of Biscay. Source: Koutsikopoulos et al. [1998]	25
2-1	Bathymetry of the Bay of Biscay configuration.	36
6-1	Summary of the main results of this thesis.	188

List of Tables

1.1	Links between dimensionless numbers and instabilities.	19
2.1	Constants p , m and n in GLS turbulent closure schemes.	33

Chapter 1

Introduction

1.1 Context

The coastal environment is subject to multiple physical processes (e.g. tides, density currents, fronts) and is facing a wide range of economical and societal challenges. The physical processes rely on the wide range of spatial and temporal scales for oceanic motions: the large scale, the mesoscale and the submesoscale. Submesoscale processes (< 10 km) have been widely explored in the deep ocean (e.g. eddies and western boundary currents such as the Gulf Stream and the Oman Coastal Current) [Gula et al., 2016, McWilliams, 2016, Morvan and Carton, 2020]. These processes are more challenging in the coastal ocean where the Rossby radius of deformation is on the order of few kilometers.

Submesoscales in the coastal ocean are prominent in features such as filaments and fronts¹. For example, in the Bay of Biscay fronts can result from the contribution of tides (Ushuant front) and from the evolution of river plumes (e.g. Loire and Gironde rivers) [Yelekçi et al., 2017]. River plumes are areas rich in organic and inorganic matters. They are also subject to climate change and anthropogenic pressures, e.g. microplastics can be trapped in these plumes and cause dramatic damage to marine life. The biological productivity in these coastal environments relies on nutrient concentration. Fine scale physical processes will disturb the nutrient distribution and then potentially limit or enhance the associated biological

¹regions where the Rossby Radius of deformation can be small (few kms)

production. In order to characterize the impact of fine scale physical processes on nutrient cycle, scales of few kilometers in fronts need to be considered. The latter emphasizes the need of high resolution modelling and observations to characterize the biological production in such regions. For example, recent high resolution (< 1 km) in-situ observations in the Changjiang river plume front addressed the contribution of mass trapping and enhanced light penetration in large algal biomass [Zhang et al., 2020].

Due to the importance of river plumes in regulating the coastal marine ecosystem, the present study aims at investigating the submesoscale processes (dynamics, instabilities and vertical mixing) in river plumes in the Bay of Biscay constrained by bathymetric features and external forcings (tides, winds).

1.2 River plume structure and dynamics

The interaction between freshwater from an estuary and the open ocean results in a river plume. River plumes are complex coastal features where the interaction between Earth rotation, bottom friction, atmospheric forcing, tides, and river discharge (stratification and sheared flows) is important.

The freshwater intrusion is accompanied by inorganic, organic and polluted material transport to the open ocean. The river discharge acts as a source of buoyancy and momentum near the river mouth. The latter impact is enhanced when interacting with tides which tend to enhance mixing in these regions. The freshwater is mixed in most cases in the estuary with offshore water coming from the open ocean.

River plumes can be classified by a variety of spatial scales. This classification leads to identify different river plume structures and dynamics. A classification of river plumes based on the Kelvin number K , the ratio between the plume width and the Rossby radius of deformation, has been introduced by Garvine [1995]. The Kelvin number classification introduces three different river plumes and their relative dynamics:

- Small scale river plumes (low K) where inertial motions near the river mouth overcomes Earth rotation. The dynamics in these river plumes is non linear and the Coriolis effect is not important.
- Intermediate scale river plumes ($K \sim 1$) where inertial motions and Earth rotation are both important.
- Large scale river plumes (large K) where Earth rotation is important, which results in the freshwater turning to the right in the Northern Hemisphere (Coriolis effect) once it exits the estuary.

In large scale river plumes, the freshwater acts as a coastal current dominated by its own baroclinic dynamics. In particular, this is the case for the Gaspé current where the wind tends to enhance the alongshore freshwater transport to the open ocean [Sheng, 2001]. This can be explained as winds tend to tighten fluid stream lines and therefore to accelerate the freshwater flow.

The Garvine [1995] classification allows us to understand the horizontal structure of a river plume, since it originated from vertically averaged primitive equations. But the river plume extent or structure is also important in the vertical direction and its vertical shape might be disturbed by external forcing or by the river discharge itself. In the vertical direction, river plumes can be classified as [Yankovsky and Chapman, 1997]:

- **Surface trapped river plumes** where the buoyant plume remains concentrated on the surface forming a shallow layer where stratification is important (e.g. Columbia river plume). In other words, the river plume base does not interact with the bottom.
- **Bottom trapped river plumes** When the river plumes base interacts with the bottom and/or when freshwater spans the water column entirely. The bottom-attached river plumes may also result from interactions between downwelling winds and a surface trapped river plume. Indeed, downwelling winds tend to push the water against the coast and favors an incropping of the river plume base and its interaction with the bottom. The Ekman transport (of

downwelling winds) is cumulated over time; this may cause the river plume to become bottom attached during a short or a long period of time.

River plumes are classified in different regions summarized in [Figure 1-1](#) and [Figure 1-2](#). These regions are submitted to different physical forcings (atmospheric forcings, tides and river discharge) which define their resulting dynamics. These regions and their relative dynamics are introduced in [Horner-Devine et al. \[2015\]](#) and are described below:

- **The Estuary** is the channel connecting the freshwater from a river source to the open salty ocean. In this channel, freshwater from the river source and salty water mix forming an open exchange of inorganic and organic matters. The exchange between freshwater and salty water is largely due to tides. Tides (low tides) bring the fresh water from the estuary to the open ocean and favor the mixing between fresh and salty waters. At high tides, tidal currents favor a high sediment concentration. At low tides, tidal currents bring nutrients or sedimentation to the open ocean. Winds also impact the estuarine dynamics. Downwelling favorable winds push the freshwater against the outflow direction; this increases the salinity gradient and reduces the circulation. Upwelling favorable winds allow the freshwater to be more surface trapped and the salinity gradients are weak below. Estuaries are also subject to overheating or to overcooling which may happen in summer or winter, respectively. The heat exchange is enhanced in estuaries due to their limited vertical and horizontal extents.
- **The Near field** is the region located near the river mouth and governed by sheared flows and advection processes. In this region, the buoyancy structure is similar to the estuarine buoyant structure and their dynamics are linked. At the mouth of the estuary, the freshwater outflow encounters bathymetric features or a transition over the bottom slope. The latter defines the lift-off point, where the river plume detaches from the bottom. Tides are also prominent in the near field region; they enhance the kinetic energy and its conversion to potential energy. In this region, lateral spreading is important;

this impacts the momentum and buoyancy exchanges between the ambient coastal waters and the river freshwater. The interaction between the near field and tidal oscillations can increase or decrease the buoyancy anomaly and momentum which drive the dynamics in this region. Tides may form numerous fronts in this region (tidal fronts) which can be important in low wind cases; then a tidal plume forms near the river mouth.

- **The Mid field** is the connection between the near field and the far field in a river plume. A critical distinction between the near and mid fields is the lift-off point or where the river plume becomes subcritical (Froude number greater than 1). In this region, winds are important and the initial input of discharge momentum is diminished. At low winds and for small scale river plume, the midfield is named as a **bulge** or an anticyclonic gyre as sketched in figure 1-2. The **bulge** is an anticyclonic eddy near the river mouth and grows offshore with a ballooning effect² In the bulge, a competition between cyclonic and anticyclonic motions take place. This competition results from the lateral shear and Coriolis effect. In a real ocean, a bulge may not form in seasons where the wind is important and may be disrupted by baroclinic instability. The bulge growth is reduced by tidal currents.
- **The Far field or Coastal current** is the region where a fraction of the freshwater is transported in the downstream direction. The structure and dynamics of this region is related to the presence of external forcings (winds or ambient current) which if directed as the coastal current, would lead to an increase in the freshwater transport with values near the mid-field freshwater transport. For example, downwelling winds would lead to a thin river plume and therefore the coastal current and the mid-field width's are equivalent. Even with the interaction with different ageostrophic motions (e.g. wind induced Ekman current) the coastal current remains in geostrophic balance. As we get far from the river mouth, the discharge in the coastal current diminishes.

The interaction of river plumes with different atmospheric (winds, heat, evap-

²The bulge keeps growing in the absence of external forcing (such as wind or an ambient current).

oration and precipitation), gravitational (tides) and mechanical (river discharge) forcing defines its shape, structure and dynamics. The dynamics and structure of river plumes are then disturbed from an equilibrium state and act as a reservoir of kinetic energy. These disturbances lead to different instabilities that will be discussed in the next section.

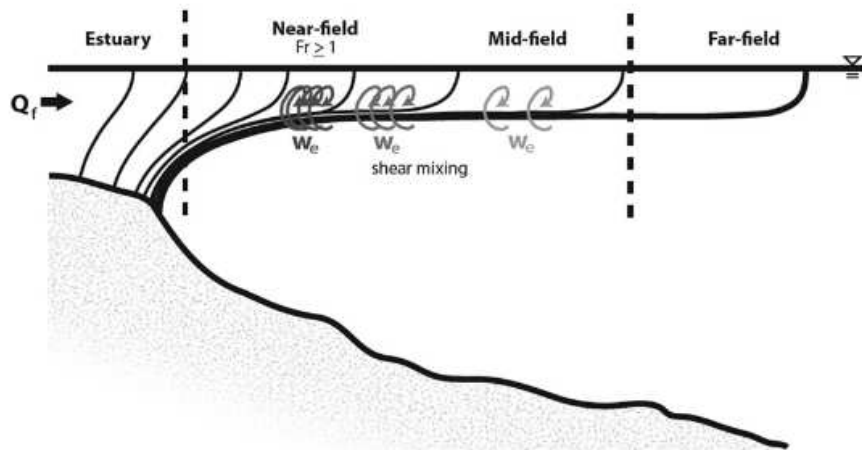


Figure 1-1: River plume regions (Vertical structure). Source: [Hetland \[2005\]](#)

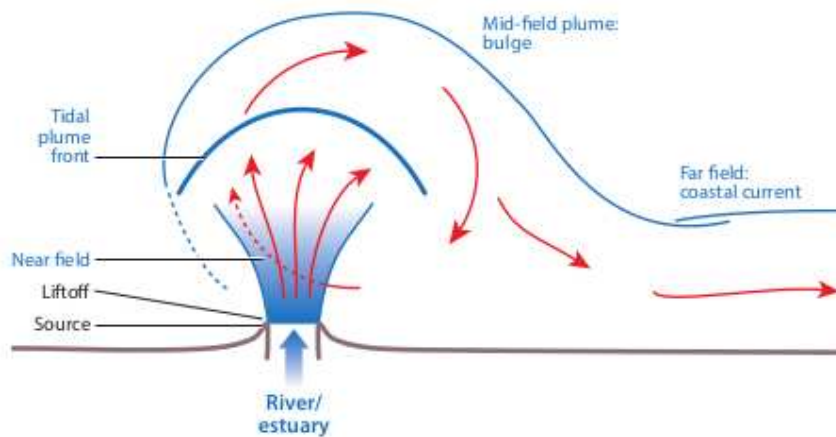


Figure 1-2: River plume regions (Horizontal structure). Source: [Horner-Devine et al. \[2015\]](#)

Summary of Section 1.2 River plume structure and dynamics

- The Garvine classification helps to identify the governing dynamics in a river plume: (i) - small scale river plumes where the Coriolis effect is not important, (ii) - intermediate scale river plume where the Earth rotation and inertial motions are both equivalent and (iii) - large scale river plumes where the Coriolis effect is important.
- In the vertical dimension, two different plumes exist: (i) - surface trapped plumes where the freshwater remains at the surface and the stratification is important and (ii) - bottom trapped plumes where the freshwater spans the entire water column. The bottom trapped river plumes may result also from the interaction between downwelling winds and surface trapped plumes.
- River plumes are distinguished by their complex geometry with different regions: (i) - the estuary, a channel between the river source and the open ocean, (ii) - the near-field, the region near the river mouth where sheared flows and advection processes are prominent, (iii) - the mid-field, the region where an anticyclonic gyre is formed in low wind cases and (iv) - the far-field, the region where a fraction of the freshwater is transported in the downstream direction.

1.3 Instabilities in river plumes

River plumes are oceanic features subject to different instabilities. The nature of these instabilities might be geostrophic or ageostrophic. The geostrophic instabilities are baroclinic or barotropic with a small Rossby number³ dynamics, their growth is longer in time and their scales are larger (mesoscale or large scale). Ageostrophic instabilities are different in their dynamics as they trigger smaller scale (submesoscale) motions with fast growth (of the order of a day or a week).

Instabilities scales are also closely related to the Rossby radius of deformation which depends on stratification and depth. Stratification is enhanced in river plumes, and depths are shallower which bring the Rossby radius of deformation to a range of scales between 1 and 10 km⁴.

³ $R_o \sim \frac{U}{fL}$, where f is the Coriolis parameter, U and L are characteristic velocity and length, respectively

⁴ N^2 is between 10^{-4} and 10^{-2} s^{-2} , H the water depth is of the order of 10 m and $f \sim 10^{-4} \text{ s}^{-1}$ which gives a Rossby radius of deformation $R_d = \frac{NH}{f} \sim [1-10] \text{ km}$

These instabilities may exist in different regions of the river plume. In estuaries, shear flows may induce vertical shear instabilities. These instabilities are located at the sheared interface between two layers with different densities. When two fluids of different densities are (highly) sheared, billows may start to form at the interface, a result of Kelvin-Helmholtz (KH) instability. Kelvin Helmholtz instabilities are the link between internal waves which are generated by a combination of wind and tidal forcing and turbulent mixing [Held et al., 2019]. Shi et al. [2019a] observe that in the Yangtze river estuary, Kelvin Helmholtz instabilities develop. They used a high resolution non-hydrostatic numerical model (NHWAVE) to find that these vertical shear instabilities exist at the density interface and their intensity are related to tides. They note that these instabilities grows fast (6 min) and their horizontal (60 m) and vertical length scales (6 to 7 m) are small but their contribution to turbulent mixing is important once billows start appearing. In the Frazer estuary, Kelvin-Helmholtz instabilities are observed using an echo sounder and a linear analysis is evaluated using the linear analysis stability (Taylor-Goldstein equation). These instabilities are concentrated above or below the density interface. The KH instability forms on one side of the density interface and mixing is dominant along the interface pycnocline [Tedford et al., 2009]. When there is a sharp density difference between two layers (a jump), Holmboe instability may exist. Ortiz et al. [2002] note that these counter-propagating instabilities (propagation in the opposite direction of the sheared flow) occur for large Richardson numbers⁵. Using the Taylor-Goldstein equation, they find that these instabilities develop in the slower layer at a much larger growth rate than in the faster layer. Using numerical simulations, Smyth and Winters [2003] find that sharp density interfaces can be formed in high Prandtl number⁶ flows which induce Holmboe instabilities. Holmboe instabilities lead the shear flow to a turbulent state where irreversible mixing may happen. Holmboe waves grows slower than Kelvin-Helmholtz waves. Despite small growth rates, the latter are important for ocean mixing. Indeed, the slower growth rate allows Holmboe instabilities to

⁵ $R_i \sim \frac{N^2}{S^2}$ where $S^2 \sim (\partial_z u)^2 + (\partial_z v)^2$ is the vertical shear and N^2 is the Brunt Vaisala frequency.

⁶ $P_r \sim \frac{\nu}{\kappa}$, where ν is the vertical viscosity and κ is the vertical diffusivity

enhance the amount of mixing in the ocean.

River plume is subject to small scales instabilities in a front of a tidal plume [Pritchard and Huntley, 2002]. A ship-borne instrument with a high horizontal resolution (less than 25 cm) at the top of the water column (4 m) has been used in their study. Their focus is mainly on frontal features at the plume interface where multiple internal hydraulic jumps are dominant. A classification of instabilities has been provided in these regions and described as two different categories: (i) - Super-critical regime (Froude number⁷ larger than one) where the instability is dominant at the front interface and (ii) - Sub-critical regime (Froude number lower than one) where the instability is at the rear of a gravity head current. The latter instability explains the presence of internal hydraulic jumps as suggested in Garvine [1984].

In river plumes, baroclinic instabilities are suppressed in some cases despite strong lateral density gradients in some regions such as a front [Hetland, 2017]. A combination of realistic numerical simulations of the Mississippi-Atchafalaya river plume and idealized simulations of a buoyancy driven flow over a sloping bottom have been used in their study. They introduce a new parameter called the Slope Burger number⁸ which is a function of the bottom slope and related to the buoyancy lateral gradients. This parameter indicates that baroclinic instability does not form except for cases where a transition between symmetric and baroclinic instabilities happens. Forcings such as winds or tides may induce more mixing in cases of slower growth rates and therefore suppress instabilities. In river plumes, a key parameter limiting the existence of baroclinic instabilities is the Rossby radius of deformation which may reach the range of values for which smaller scales and faster instabilities can develop.

These small scale structures and their influence on a tidal river plume structure have been studied by Iwanaka and Isobe [2018]. They used field surveys near a river

⁷ $F_r \sim \frac{U}{NH}$ where U is a characteristic velocity, N is the square root of the Brunt Vaisala frequency and H is the water depth.

⁸ $S \sim \frac{N\alpha}{f}$ where N is the square root of the Brunt Vaisala frequency, α is the bottom slope and f is the Coriolis parameter

mouth, balloon photography and CTD measurements to determine the horizontal and vertical structures of the Hiji river plume. In conjunction with these field measurements, they used a nonhydrostatic numerical model to determine the origin of these fine scale structures near the river mouth. In their study, the tidal plume front results in a meander with a wavelength of the order of 10 m. Vertical tidal oscillations induce small eddies with a horizontal wavelength smaller than 100 m. Their numerical non hydrostatic model was able to reproduce these small scale features due to frictionless processes. The disturbances in the horizontal and vertical plans result from Kelvin-Helmholtz and inertial instabilities. Although these instabilities exist, their description is limited by the horizontal and vertical resolutions used in their numerical model.

Tidal plumes and fronts dynamics in the Columbia river plume are important due to their important non-linear processes [Akan et al., 2017]. They show, using numerical simulations (ROMS model) that tidal fronts exhibit strong fluid acceleration and salinity gradients on scales smaller than 100 m and with ageostrophic motions (the local dynamical Rossby number reaches values up to 50). During ebb-tides, short time scales (limited by edd-tide period) instabilities (centrifugal and horizontal shear instabilities) happen in a tidal front. Although these instabilities exist, sharp front disturbances lead to large local Rossby numbers with negative relative vorticity and simulated motions are limited by the grid size of their numerical model.

Winds impact the structure and shape of river plumes. Downwelling favorable winds alter the shape and structure of a river plume frontal region and enhance the freshwater transport [Lv et al., 2020]. These authors used a series of numerical idealized simulations (submesoscale permitting) with 1 km horizontal resolution (ROMS model). They show that the response of a river plume to downwelling-favorable winds undergoes different stages: (i) destratification, (ii) restratification and (iii) homogenization. Ekman transport resulting from a downwelling favorable wind drives the river plume against the coast and leads to a steepening of the isopycnals (isohalines). The latter results in a destratification and as the wind blows

continuously, instabilities are triggered. The suppression of the bulge and the establishment of symmetric instability enhance the freshwater transport. The latter provides a source of negative Ertel potential vorticity. After a moderate to high wind, a transition from symmetric instability to baroclinic instability takes place. The authors show that even during weak winds stages, instabilities still develop and stratify the river plume front.

In river plumes, numerous instabilities can exist, triggered by different forcings (river discharge, winds, tides) in different regions (estuary, near and far fields). These instabilities disturb the vertical structure of a river plume. Some of these instabilities are linked to dimensionless numbers that I summarize in Table 1.1. Although the analysis of instabilities helps to understand non-linear processes governing a river plume dynamics. Characterizing the vertical mixing processes is needed to understand the dynamics of the plume and the associated water and matter transport. The next chapter is dedicated to the vertical mixing processes in different regions of a river plume.

Dimensionless number	Instabilities
1. Rossby number <ul style="list-style-type: none"> • $R_o < 1$ • $R_o \sim O(1)$ 	Geostrophic (baroclinic and/or barotropic) Ageostrophic (baroclinic and/or symmetric)
2. Richardson number <ul style="list-style-type: none"> • $R_i < 0.25$ 	Vertical shear (Kelvin-Helmholtz)
3. Prandtl number <ul style="list-style-type: none"> • $P_r \sim O(1)$ 	Holmboe
4. Froude number <ul style="list-style-type: none"> • $F_r > 1$ • $F_r < 1$ 	Small scale (fronts) Small scale (the rear of a gravity head current)
5. Slope Burger number <ul style="list-style-type: none"> • $S \geq 0.3$ 	Weak instabilities

Table 1.1: Links between dimensionless numbers and instabilities.

Summary of Section 1.3 Instabilities in river plumes

- Vertical shear instabilities (Kelvin-Helmholtz and Holmboe) have been observed in estuaries and develop at the density interface between two fluid layers. Kelvin-Helmholtz instabilities result in billows, small-scale vortices with sizes about few meters. Holmboe instabilities form at sharp density interfaces in highly turbulent flows (high Prandtl number).
- Frontal regions are subject to ageostrophic instabilities characterized by smaller wavelengths and faster growth rates/periods. This ageostrophic instability generation is limited by the grid size in numerical models.
- Baroclinic instabilities are suppressed in most cases despite strong lateral density gradients, except when a transition between baroclinic instability and symmetric instability occurs.
- The interaction between downwelling winds and river plumes triggers frontal symmetric instabilities. This interaction also favors the suppression of the bulge and an enhanced freshwater transport.

1.4 Vertical mixing in river plumes

The relation between vertical mixing and river plume vertical structure is important to understand the freshwater life cycle. In river plumes, different mechanisms are responsible for the radial spread of freshwater over salty ambient water. These mechanisms also impact the deflection of this freshwater due to the Coriolis effect, and the friction with the bottom boundary layer; this keeps a river plume in contact with the bottom (in estuary) and increases the freshwater transport offshore [Yankovsky and Chapman, 1997]. Their study does not include forcings such as winds and tides. Therefore the vertical mixing is related only to river discharge and interaction with the bottom, if the river plume is bottom attached.

Freshwater mass properties in the near-field region have been examined using a 1.5 layer reduced gravity model and numerical simulations [Hetland, 2005]. He showed that in this region, a competition between lateral spreading and vertical mixing is a key parameter to understand the fate of the buoyant plume. One key parameter in his study is the Froude number which determines the nature of the

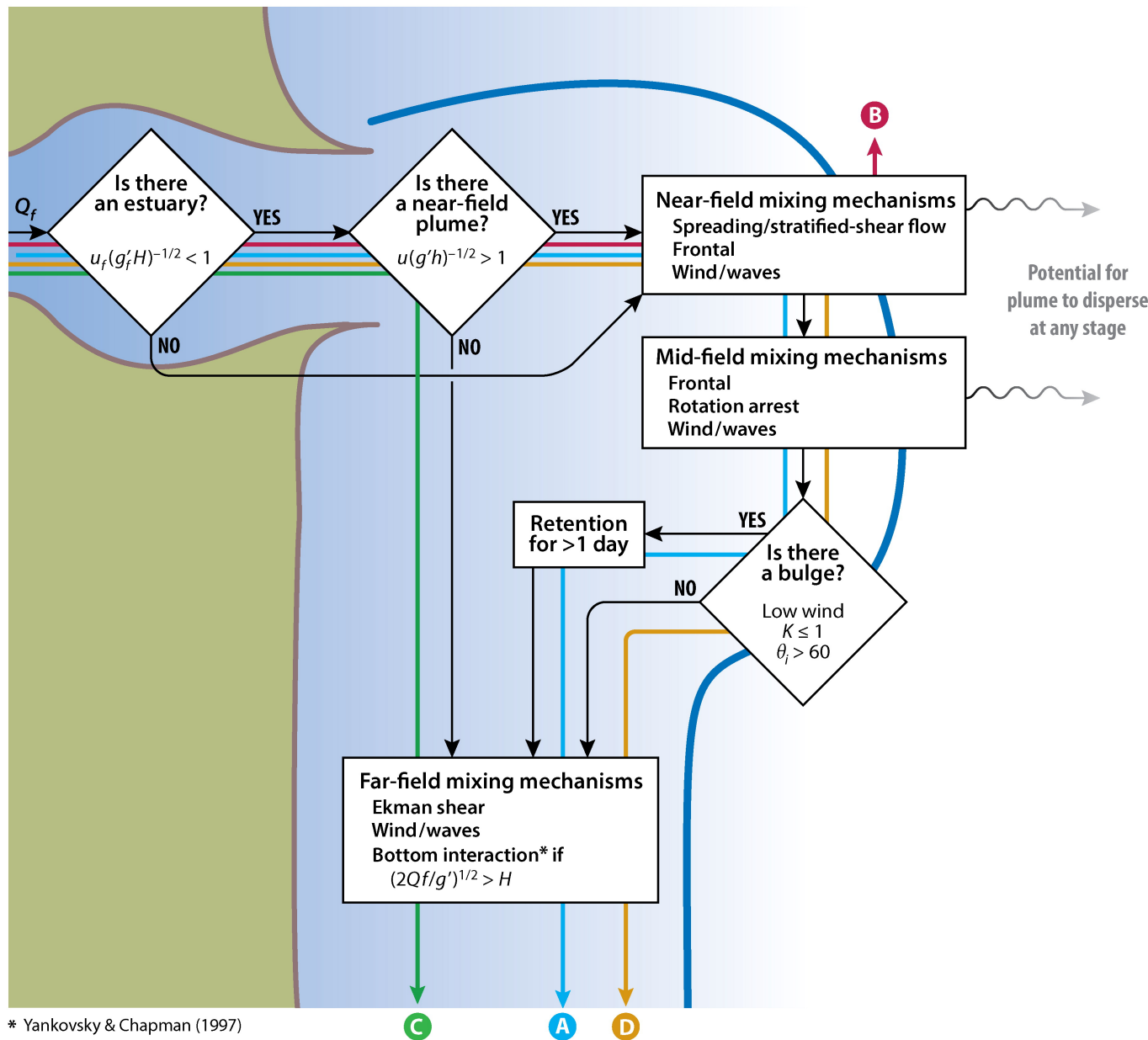
outflow. Once the freshwater buoyant plume is established, the net dilution is related to local mixing rates. The competition between lateral spreading and net mixing in a river plume near-field region results in: (i) local mixing being stronger than lateral spreading which leads to a deceleration of the flow or (ii) local mixing being weaker which leads to an acceleration of the plume.

A river plume carries materials and freshwater from a river source to the open ocean. Along this path, different processes such as mixing and coastal transport take place [Horner-Devine et al., 2015]. A definition of mixing in river plume as sources of momentum and buoyancy across isopycnal surfaces is given in their study. Mixing processes in river plumes are different within the bulge, near-field and far-field regions as sketched in Figure 1-3.

They summarize different mixing process in these regions as:

- **Near-field mixing:** Intense turbulence and mixing can be observed in this region where dissipation rates reaching $\epsilon \sim 10^{-4}$ to $10^{-3} \text{ m}^2.\text{s}^{-3}$. In this region, a shoaling of the buoyant structure is observed which results in an acceleration of the upper layer; therefore, intense mixing and turbulence are observed seaward of the liftoff point. The interaction between ambient salty water and freshwater leads to a decrease in mixing which results in river plume deceleration. River plume lateral spreading in this region leads to high mixing associated with stratified-sheared flows. Vertical shear ($S^2 \sim \partial_z^2 u$) can be high in some river plumes (Mississippi, Congo rivers) reaching values up to $0.5\text{-}1 \text{ s}^{-2}$ at the plume base. Density differences observed in this region lie between 15 and 20 kg.m^{-3} bringing the Richardson number lower below the critical value of 0.25 . This results in Kelvin-Helmholtz instability and therefore into more intense mixing. Kelvin-Helmholtz billows appear and their amplitude is proportional to the Ozmidov length scale⁹.
- **Far-field mixing:** In this region, wind stress generates lower turbulence with observed values of dissipation rates $\epsilon \sim 2*10^{-6}$ to $10^{-5} \text{ m}^2.\text{s}^{-3}$. These values are one to two order of magnitudes lower than what is observed in the near-field

⁹defined as the square root of the ratio between the dissipation rate of turbulent kinetic energy and the third power of the Brunt-Väisälä frequency



AR Horner-Devine AR, et al. 2015.
Annu. Rev. Fluid Mech. 47:569–94

Figure 1-3: River plume regions, conditions of their existence and mixing processes specific to each region. Source : Horner-Devine et al. [2015]

and frontal regions. Wind stress is not only important in this region but acts over the entire river plume; therefore its impact enhances turbulence. Vertical mixing induced by wind stress is observed in the surface Ekman layer where vertical shear and flow speed are large. The Ekman transport plays a major role in the surface mixing and in the interior vertical shear mixing. Wind di-

rection influences the thickness of the river plume: (i) - downwelling-favorable winds thicken the river plume and (ii) - upwelling-favorable winds thin the river plume which impact vertical mixing. Winds supply river plumes with kinetic energy sufficient to increase turbulent mixing, but Coriolis effect limits the net mixing and prevents the river plume from accelerating continuously. At the ocean surface, wave-breaking results in enhanced turbulence, with dissipation rates ϵ reaching values from 10^{-3} to $10^{-1} \text{ m}^2.\text{s}^{-3}$; their influence is substantial in regions where the wave height is close to river plume thickness (e.g. in the surf zone).

- **Frontal mixing:** Intense turbulence is observed in tidal plume fronts with dissipation rates similar in magnitudes to near-field region ($\epsilon \sim 10^{-4}$ - $10^{-3} \text{ m}^2.\text{s}^{-3}$). The contribution of river plume fronts to the total mixing budget is still an active subject of research. River plume front is considered as a high turbulence region with an exponential decay behind it. In these narrow bands (wavelengths lower than 100 m), the mixing is maintained when the frontal region area increases (e.g. large tidal plume). When the river plume front speed drops below the ambient internal wave speed, internal waves solitons are released which increases the 3D turbulence.

River discharge and Earth rotation have an important effect on the net mixing in a river plume as shown in [Cole and Hetland, 2016]. With idealized numerical simulations (ROMS model), they studied a small width river plume (width lower than the Rossby deformation radius) in rotating and non-rotating frameworks. They showed the importance of Earth rotation in the evolution of the near-field region. Indeed, the Coriolis effect limits the net river plume mixing even when the discharge is high [Cole and Hetland, 2016]. This evolution differs in a non-rotating river plume as mixing is increased when the discharge is increased. At the river mouth, two important parameters define the regime of a river plume: (i) - strong coastal freshwater transport increased the mixing near the source and (ii) - strong buoyancy favors lateral spreading and shear mixing. Although these parameters are important, Earth rotation limits the net mixing and lateral spreading via a downstream flow;

this leads to a more stratified far-field especially when the river discharge is high.

Internal waves (IWs) are important processes in some river plumes; they are responsible for enhanced turbulence and mixing. In small river plumes (width smaller than the Rossby deformation radius), high frequency internal waves are generated and propagated offshore [Osadchiev, 2018]. He used field surveys (CTD and ADCP) and high resolution ocean color imagery (10 m and 30 m) in the Mzymta river plume located in the northeastern part of the Black Sea. In the absence of any apparent tide-topography interactions, internal waves solitons are released from the frontal region of the plume whenever the front speed drops below the water wave speed ahead of it [Nash and Moum, 2005]. River plume kinetic energy is transformed to 3D turbulence in the bottom and frontal zones of a river plume. This energy conversion is due to the generation, propagation and dissipation of internal waves. These IWs favor mixing and reduction in the freshwater volume.

Summary of Section 1.4 Vertical mixing in river plumes

- In the near-field region of the plume, intense mixing, associated with stratified-sheared flows, is observed when the plume lateral spreading increases.
- In the far-field region of the plume, mixing is mainly associated with winds. The mixing in this region is concentrated at the surface Ekman layer.
- In the frontal region of the plume, the mixing is maintained when the frontal region area increases. Internal waves solitons are also released when the river plume front speed drops below the ambient internal wave speed.

1.5 River plumes in the Bay of Biscay

The Bay of Biscay is a semi-enclosed basin located in the northeastern Atlantic ocean. The ocean dynamics in this basin are influenced by large scale, mesoscale and submesoscale processes. Indeed, the Bay of Biscay is known for strong wind and tides variability, mesoscale eddies, density fronts and currents as sketched in Figure 1-4.

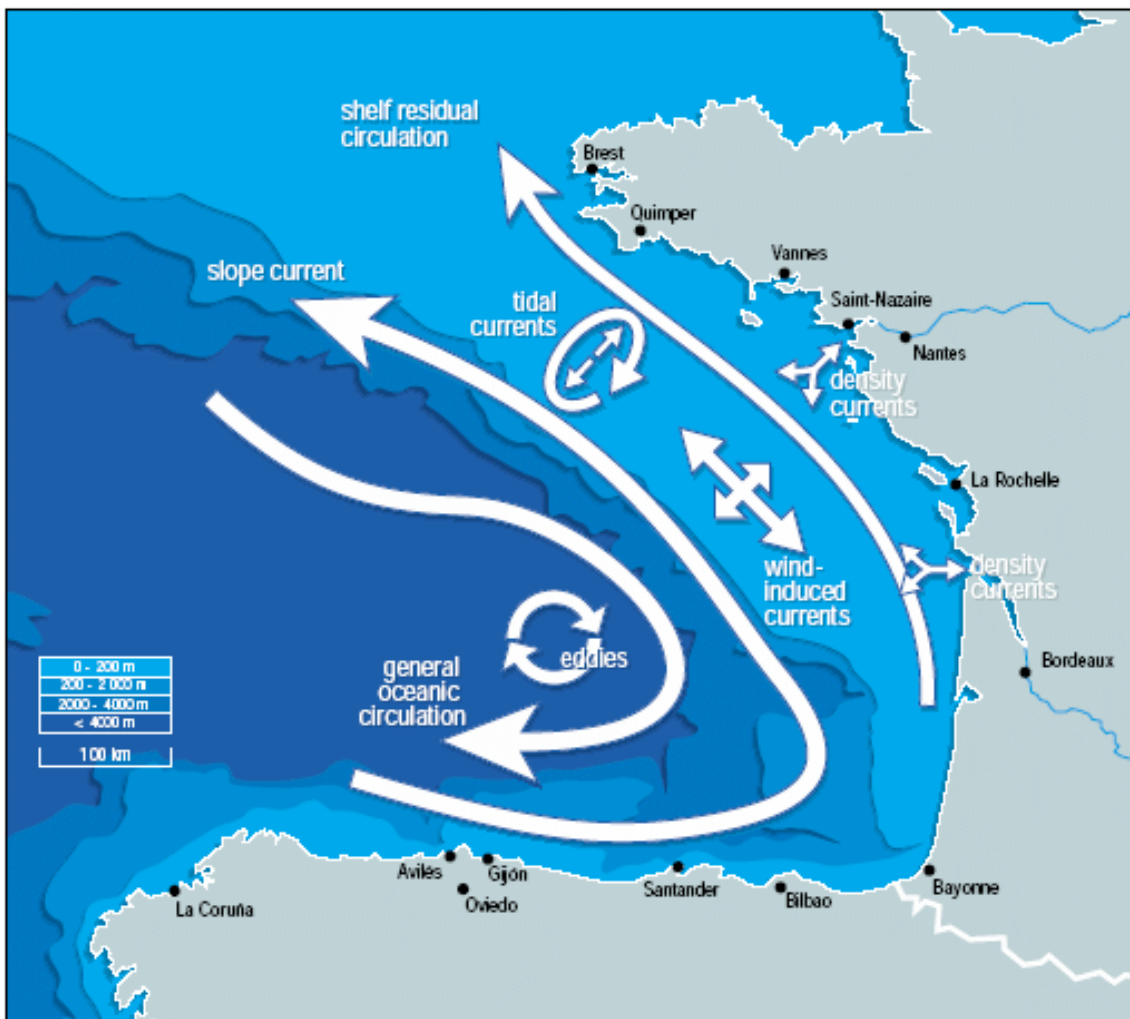


Figure 1-4: Circulation in the Bay of Biscay. Source: [Koutsikopoulos et al. \[1998\]](#)

The density fronts are sources of submesoscale activity and biological productivity. In the Bay of Biscay, density fronts are delimiting the region of freshwater influence (ROFI) [[Yelekçi et al., 2017](#)]. The former authors used singularity exponents¹⁰ on MODIS datasets and on MARS3D numerical simulations to identify the

¹⁰A tool used in identifying discontinuities in image processing

occurrence of such fronts. Their analysis revealed that this frontal activity is prominent in winter and is largely due to the contribution of the Loire and Gironde river plumes. The Loire, Gironde and Adour rivers are an important source of freshwater in the Bay of Biscay [Lazure et al., 2009, Costoya et al., 2017]. They represent $> 75\%$ of the total river runoff in the bay, with an annual river discharge of $900 \text{ m}^3 \text{ s}^{-1}$; their plumes reach a noticeable extension during downwelling favorable wind periods.

The Loire and Gironde river plumes extension results in northward currents along the coast [Puillat et al., 2004]. They reach a maximum extent in winter with a peak in January ($3 * 10^4 \text{ km}^2$), and a minimum extension in summer during July ($4 * 10^3 \text{ km}^2$) [Lazure and Jegou, 1998]. Their maximal extent in winter is related to higher river discharges ($> 1000 \text{ m}^3 \text{ s}^{-1}$). In summer, river discharges barely exceed $200 \text{ m}^3 \text{ s}^{-1}$.

Summary of Section 1.5 River plumes in the Bay of Biscay

- The frontal activity induced by density currents is prominent in winter.
- The main sources of freshwater in the Bay of Biscay are the Adour, Gironde and Loire rivers.
- The Loire and Gironde river plumes form northward currents that reach their maximal extent during winter.

1.6 Thesis outline

The main objectives of this PhD study are to understand:

- The evolution of the vertical and horizontal **structures** of river plumes and the nature of their **dynamics**.
- The nature, intensity and location of different **instabilities** (geostrophic and ageostrophic) in river plumes.
- The budget of different processes carrying out the **vertical mixing** within different regions in river plumes.

The different issues are addressed in the context of the Gironde river plume. These questions have been investigated using idealized and realistic simulations. Idealized simulations allow us to analyze the Gironde river plume fate (dynamics, instabilities and mixing) in a homogenous ocean at rest, to quantify different physical processes. In addition, the realistic simulations allow us to understand how the Gironde river plume¹¹ will be influenced, in a turbulent ocean, by atmospheric forcings, tides and ambient stratification.

Thus, to analyze these different issues, the PhD manuscript is organized as follows:

- **Chapter 2:** Numerical modelling is a key tool in understanding the dynamics of the Gironde river plume. Therefore, this chapter will be dedicated to the description of the numerical models¹² used in this manuscript.
- **Chapter 3:** In this chapter, a submesoscale-resolving idealized (or simplified) numerical study is performed on a Gironde-like river plume. The importance of the different drivers is detailed. The analysed drivers are the river discharge, wind and semi-diurnal tides. This study of high-frequency processes over a short period of time allows us to understand how these external forcings interact with a river plume and the ambient ocean (at rest here). This

¹¹dynamics, instabilities and mixing

¹²in hydrostatic and non-hydrostatic approximations

interaction leads to different instabilities which are located in different regions of the river plume, depending on the forcing. Vertical mixing processes are also examined using a mean stratification budget to understand the dominant process in this budget for each case.

- **Chapter 4:** In this chapter, a 2D Boussinesq, non-hydrostatic idealized numerical study is performed in river plume estuary and near-field regions with different physical conditions¹³. These parameters are the plane river plume base thickness, the vertical shear intensity and the bottom slope. This high resolution and short term study with high frequency outputs permits to understand the development of short scale eddies (billows) at the interface between two layers. Different ageostrophic instabilities are examined and the analysis of the most unstable modes allows us to understand the decay or the growth of these instabilities. Turbulent mixing of mass and momentum is also studied using the buoyancy fluxes and vertical shear production terms of the eddy kinetic energy budget. The sensitivity to different experiments provides informations on the dependance of these non-linear processes (instabilities and turbulent mixing) to different physical settings.
- **Chapter 5:** In this chapter, a submesoscale-permitting high-frequency realistic numerical study is performed in the Bay of Biscay. Two different months have been studied which correspond to a contrast between small and average river discharges corresponding to different seasons (winter and summer). The intensity, nature and localisation of different instabilities have been examined. The vertical mixing processes have been quantified at the ocean surface (and bottom) to distinguish the different processes which remove or inject energy near this boundary. A bulk budget of stratification is evaluated in the ocean interior. This budget is related to the turbulent closure scheme used in the numerical model.
- **Chapter 6:** In this chapter, general conclusions are drawn and perspectives are provided.

¹³Hydrology, dynamics and bathymetry

Chapter 2

Methodology

2.1 Primitive Equations

In the ocean different scales exist from the large scale (atmospheric forcing) to microscale turbulence. In our case, mesoscale (eddies) and submesoscale (filaments, fronts) motions are really important and can be characterized by the radius of deformation. These motions are characterized by the Navier-Stokes (dynamics) and mass conservation equations (thermodynamic) [Vallis, 2006]. In these equations, several approximations are made:

- The Coriolis co-parameter¹ forcing can be considered neglected except at the Equator or for strong vertical motions (such as convection).
- The hydrostatic approximation represents the balance between gravity and pressure vertical gradient. This approximation is limited to regions where flow curvature is limited and when we do not consider acoustic wave dynamics.
- The Boussinesq approximation in which we consider the variations of temperature not significant and therefore this impact the density which is related to buoyant motions.
- The incompressibility approximation where acoustic waves are filtered out and fluid parcels conserve their volume while being in motion.

¹ $f^* = 2\Omega \cos(\phi)$ where ϕ is the latitude and Ω is the Earth rotation rate

Thus, one can write these equations as :

$$\partial_t u + u\partial_x u + v\partial_y u - fv = \frac{-1}{\rho_0} \partial_x P + \nu(\partial_{xx} u + \partial_{yy} u) + \partial_z(K_v \partial_z u) \quad (2.1)$$

$$\partial_t v + u\partial_x v + v\partial_y v + fu = \frac{-1}{\rho_0} \partial_y P + \nu(\partial_{xx} v + \partial_{yy} v) + \partial_z(K_v \partial_z v) \quad (2.2)$$

$$\partial_t C + u\partial_x C + v\partial_y C + w\partial_z C = \partial_z(K_c \partial_z C) + \kappa(\partial_{xx} C + \partial_{yy} C) \quad (2.3)$$

$$\partial_z P = -\rho g \quad (2.4)$$

$$\partial_x u + \partial_y v + \partial_z w = 0 \quad (2.5)$$

u , v and w are the velocities in three different directions (x, y, z). f is the Coriolis parameter and can be expressed (Taylor decomposition) as $f = f_0 + \beta y$ at the first order (zeroth order is for f-plane approximation and $f = f_0$). g is the gravity acceleration and ρ the potential density. C can be any passive tracer and here will represent the salinity or temperature. $\nu = \frac{\mu}{\rho}$ (μ is the dynamic viscosity) is the kinematic viscosity. In general κ the diffusivity is an order of magnitude lower than ν . Body forces (Ekman, bottom stresses, heat influx) are parameterized in the vertical mixing of momentum and tracers at the ocean vertical boundaries (surface and bottom) and we write:

At the sea surface $z = \eta(x, y, t)$ where η represents the sea surface height

$$K_m \partial_z u = \tau_x^s(x, y, t) \quad (2.6)$$

$$K_m \partial_z v = \tau_y^s(x, y, t) \quad (2.7)$$

$$K_C \partial_z C = \frac{Q_C}{\rho_0 C_p} \quad (2.8)$$

Where τ_x^s and τ_y^s represent surface wind stress in the x and y directions. Q_C

represents the surface concentration flux which is the net heat flux (Q_{net}) and the Evaporation minus Precipitation rates ($E - P$). Q_{net} can be written as:

$$Q_{\text{net}} = \text{SW} - \text{LW} - \text{LT} - \text{ST} - \text{BT} \quad (2.9)$$

where SW is short wave radiation (solar radiations), LW is the net heat loss due to long wave radiation, LT is latent heat flux, ST is sensible heat flux and BT is a geothermal heat flux from the bottom (negligible).

On the other hand, interior ocean mixing is parameterized by turbulent closure schemes. Considering that ocean mixing is anisotropic², we distinguish two main turbulent closure schemes : K-profile (KPP, [Large et al. \[1994\]](#)) and Generic Length Scale (GLS, [Umlauf and Burchard \[2005\]](#)). These closure schemes will be described hereafter.

2.1.1 Turbulent closure schemes

KPP Parameterization

The interior mixing in K-Profile turbulent closure scheme is considered as shear and convective mixing processes. We write the tracer and momentum mixing coefficient (K) as :

$$K = K^{\text{sh}}(z) + K^{\text{iw}}(z) + K^{\text{dd}}(z) \quad (2.10)$$

Where :

$$K^{\text{sh}}(z) = \begin{cases} K_{0,c} & \text{if } R_i < 0 \\ K_0 \left[1 - \left(\frac{R_i}{R_{i0}} \right)^3 \right] & \text{if } 0 < R_i < R_{i0} \\ 0 & \text{if } R_i > R_{i0} \end{cases}$$

Here $R_i = \frac{N^2}{S^2} = \frac{-\frac{g}{\rho_0} \partial_z \rho}{\partial_z u^2 + \partial_z v^2}$ is the Richardson Number (N^2 is the Brunt Vaisala frequency and S^2 is the vertical shear, ρ is the potential density and ρ_0 is a mean density). $K_{0,c}$ is a constant suited for convective or static instability (negative Brunt

²This is not true for microscale turbulence where horizontal and vertical scales are equivalent and small (Large Eddy Simulations models).

Vaisala frequency). $R_{i0} = 0.7$ is a critical Richardson Number which limits the interior mixing. $K_0 = 5 * 10^{-3} \text{m}^2 \text{s}^{-1}$ which limits interior mixing in case of shear mixing. $K^{iw}(z)$ is a background constant for internal waves mixing. $K^{dd}(z)$ is a constant for double diffusive processes which can be applied for cases such as salt fingering (not considered here). This turbulent closure is completed with surface and bottom parameterizations. At the surface, KPP is well suited for Ekman problems and a non-local counter flux gradient is applied whenever the surface forcing is unstable. At the bottom, KPP mixes from the bottom to a critical Richardson number ($R_{icr} = 0.3$).

GLS Parameterization

The starting point in the generic two equations model is the turbulent kinetic energy (TKE) budget written as:

$$\partial_t \text{TKE} + u_i \partial_{x_i} \text{TKE} = D_{\text{TKE}} + P + G - \epsilon \quad (2.11)$$

Where u_i and u'_i represent the mean and perturbations of the velocity in the direction of the cartesian coordinate X_i . D_{TKE} represent the viscous and turbulent terms, P and G are the production of turbulent kinetic energy by mean horizontal and vertical shears and buoyancy. ϵ is the turbulent kinetic energy dissipation rate and its knowledge is required to solve the TKE budget.

A statistical field variable ψ is introduced and related to turbulent kinetic energy and dissipation rate

$$\Psi = \psi(\text{TKE}, \epsilon) \quad (2.12)$$

Where ψ is an invertible function and ϵ can be deduced from TKE and Ψ following relations below. We introduce an integral length scale

$$l = (c_\mu^0)^3 \frac{\text{TKE}^{\frac{3}{2}}}{\epsilon} \quad (2.13)$$

and the statistical field

$$\Psi = (c_\mu^0)^p * \text{TKE}^m l^n \quad (2.14)$$

where c_μ^0 is a constant of the model. From these equations, we write the Ψ transport equation as

$$\partial_t \Psi + u_i \partial_{x_i} \Psi = D_\Psi + \frac{\Psi}{\text{TKE}} (c_{\Psi_1} P + c_{\Psi_3} G - c_{\Psi_2} \epsilon) \quad (2.15)$$

From the following, we can deduce the dissipation rate as

$$\epsilon = (c_\mu^0)^{3+(\frac{p}{n})} \text{TKE}^{(\frac{3}{2})+(\frac{m}{n})} \Psi^{-\frac{1}{n}} \quad (2.16)$$

Where p , m and n are real constants which define the GLS turbulent closure scheme shown in the table 2.1 below

Turbulent closure scheme	p	m	n
$k-\omega$ [Wilcox, 1988]	-1	$\frac{1}{2}$	-1
$k-\epsilon$ [Rodi, 1987]	3	$\frac{3}{2}$	-1
$k-kl$ [Mellor and Yamada, 1982]	0	1	1

Table 2.1: Constants p , m and n in GLS turbulent closure schemes.

These turbulent closure schemes are in general defined with stability (wall) functions which limit the mixing to a critical Richardson number. Two general stability functions are used in numerical modelling: (i) - Canuto A. [Canuto et al., 2001] which limits the mixing to Richardson number of 1 and (ii) - Kantha and Clayson [1994] which limits the mixing to a Richardson number of 0.25. The latter is used in estuaries or river plume idealized numerical models.

2.2 The Bay of Biscay Realistic Configuration

In this section, we introduce different major characteristics of the Coastal and Regional Ocean COmmunity Model (CROCO based on ROMS) as well as the numerical properties of the Bay of Biscay configuration. The CROCO numerical model is fully described in different studies [Shchepetkin and McWilliams, 2005, Debreu et al.,

2012]. Further technical informations about this numerical model can be found in the CROCO website³. The strategy adopted in this modelling framework is based on: (i) - atmospheric forcing provided from ERA-Interim datasets and implemented using bulk definitions, (ii) - open boundary conditions are extracted from regional simulations with the MARS3D model and (iii) - tides constituents are set from the global atlas FES2014. We will focus on describing how this strategy is adapted for the Bay of Biscay region.

2.2.1 The CROCO model numerics

The CROCO model primitive equations are discretized horizontally on the Arakawa C-grid [Arakawa and Lamb, 1977]. This grid is well suited to solve (sub)mesoscale motions. The primitive equations are represented as fluxes which allow to conserve the momentum and tracers. The numerical model solves barotropic equations using a smaller time step than the 3D equations. The split-explicit temporal discretization used in this model is characterized by a leap-frog predictor and a 3rd order Adams-Moulton corrector [Shchepetkin and McWilliams, 2005].

The numerical model uses a Total Variation Diminishing Scheme (TVD) for the momentum, both vertically and horizontally, which preserves the monotonicity of the outflow [Harten, 1983]. The tracers (salinity and temperature) vertical and horizontal schemes are the Zico extension fifth order WENO (a weighted ENO with improvements of the weights formula) [Rathan and Naga Raju, 2018]. These momentum and tracers schemes have the advantage of being less dispersive. They are also useful for sharp gradients, that may occur in some outflows such as river plumes, by preventing spurious oscillations or wiggles.

In order to prevent/limit numerical diapycnal mixing in our simulations, the salinity and temperature are rotated along isopycnals [Lemarié et al., 2012]. Explicit viscosity and diffusivity are implemented using the Smagorinsky parametrization (molecular viscosities and diffusivities). This parametrization ensures that the flow remains turbulent (Reynolds number $Re \sim 10^6$) while preventing numerical diffusion of the advection schemes [Gröbelbauer et al., 1993, Lowe et al., 2005]. A vertical

³<https://www.croco-ocean.org/>

subgrid-scale mixing scheme is parametrized using the turbulent closure scheme KPP (K-Profile Parametrization scheme, Large et al. [1994]). This scheme is applied at the surface and the bottom boundaries and complemented with an interior mixing scheme. Full details about this turbulent closure scheme are given in section 2.1.1.

Open boundaries conditions are characterized using the Chapman and Flather scheme for 2D components (sea surface height and barotropic velocities) [Chapman, 1985, Marchesiello et al., 2001]. An Orlandi scheme is used for the 3D momentum and tracers [Orlandi, 1976]. These boundaries are forced using large scale barotropic and 3D velocities, and tracers. In addition and to prevent internal signals reflexions, a sponge layer (cosine profile) is used with an enhanced explicit viscosity.

In order to build the Bay of Biscay configuration and to run the numerical simulation, a grid is required with initial conditions, lateral and vertical boundaries. These fields are described in the next sections and have been preprocessed using tools mainly developed by Sébastien Theetten.

2.2.2 Grid and initial conditions of the realistic simulation

The simulations grid covers a zonal range between 0 and 7 °W, and a meridional range between 43 and 49 °N (figure 2-1). It includes the Bay of Biscay (North-East Atlantic Ocean) and a small part of the English Channel. The grid size is 1261×1557 ρ -points and 40 σ in the vertical direction. The mean horizontal resolution is 400 m and the vertical resolution is 16 cm at the surface and 440 m above the deepest depth 4900 m. The σ levels are stretched at the surface ($\theta_s = 5$) and at the bottom ($\theta_b = 0.4$) with the critical depth $h_c = 30$ m.

The bathymetry is a combination of HOMONIM bathymetry from the Shom⁴ (100 m horizontal resolution) and of EMODNET bathymetry⁵ for regions E3 and E4 (115 m horizontal resolution). In order to limit high pressure gradient errors [Beckmann and Haidvogel, 1993] linked to regions with steep bathymetric gradients, the bathymetry is smoothed using the criteria $\frac{\Delta h}{h} < 0.2$. Since the bathymetry resolution is under the model resolution, smoothing is required here.

⁴<https://data.shom.fr>

⁵<https://portal.emodnet-bathymetry.eu>

The model is initialized using MARS3D daily average BACH1000 simulations (March and August 2008) with 1 km horizontal resolution and 100 σ layers [Charria et al., 2017, Akpınar et al., 2020]. These fields have been interpolated on our grid. The strategy of this study is considered as an initial value problem. The initial value problem considers the interaction of rivers and a turbulent ocean and does not require a long term spin-up. Two rivers are considered here, the Gironde and Loire. They are initialized over one grid point at the most end of the Gironde and Loire estuaries. In CROCO, these rivers are considered as sources of momentum. In order to characterize these rivers, freshwater temperature and salinity are prescribed as monthly averages from MAGEST⁶ datasets and the BOBYCLIM climatology [Vandermeirsch et al., 2010]. They are also forced with river discharges, uniformly distributed over the σ layers. The latter are provided by Banque Hydro France⁷ for Dordogne, Garonne (Gironde as a combination of both Dordogne and Garonne rivers) and Loire rivers. More detailed description about the initialization of these rivers is given in chapter 5.

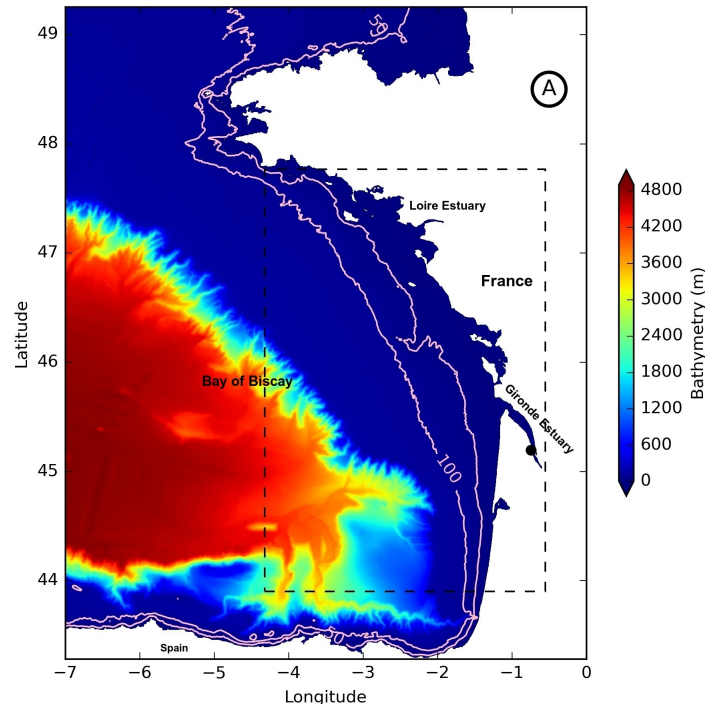


Figure 2-1: Bathymetry of the Bay of Biscay configuration.

⁶MAGEST in-situ observing network part of the DIAGIR project, we thank Sabine Schmidt for providing these data

⁷<https://www.hydro.eaufrance.fr>

2.2.3 Vertical and Lateral boundaries

The lateral open boundaries in the north and the west sides of the domain are forced using MARS3D daily averages. The model boundaries are forced by the sea surface height, the barotropic and 3D velocities, and the tracers (salinity and temperature). In addition, 15 tide constituents extracted from FES2014 tidal model are added through these lateral boundaries for the barotropic velocities and the sea surface height.

The vertical boundaries are prescribed at the surface using Fairall bulk definitions [Fairall et al., 1996] and at the bottom using bottom stress. At the surface, bulk definitions are based on air-sea interactions. The air-sea interactions are computed using the wind stress, heat and freshwater fluxes. The wind stress is computed from the C_d drag coefficient, model SST and wind velocities at 10 m. The net heat flux is based on different fields described in section 2.1. The freshwater flux is computed as the Evaporation minus Precipitation. These fields (wind stress, heat and freshwater fluxes) are extracted from 3 hourly ERA-Interim data [Dee et al., 2011] and are interpolated online to the model grid. The bottom stress is computed using a logarithmic formulation (the quadratic Von-Karman law) with a bottom roughness $z_0 = 5$ mm; this formulation is written as:

$$\tau_{bx} = \frac{\kappa^2}{\ln^2\left(\frac{z}{z_0}\right)} \sqrt{u^2 + v^2} u \quad (2.17)$$

$$\tau_{by} = \frac{\kappa^2}{\ln^2\left(\frac{z}{z_0}\right)} \sqrt{u^2 + v^2} v \quad (2.18)$$

where $\kappa = 0.41$ is the Von-Karman constant and z is the elevation above the bottom (vertical mid-elevation point of the bottom cell).

2.2.4 Computational workflow

The model runs for two months March and August 2008. The time step of the model is 15 seconds with hourly outputs. The numerical model is parallelized for distributed memory and message-passing interface (MPI) architectures. The grid

is partitioned in subdomains (40×42 in xi and eta directions) using 1680 processors. Other processors have been attributed to the output writing. Each simulation takes 7 hours on the wall clock time. Model simulations were carried out with GENCI (French National High-Performance Computing Organization) computational resources administered at the CINES (National Computing Center for Higher Education).

2.3 Non-Hydrostatic approximation

In this section, we will present the non-hydrostatic approximation used in a 2D numerical model, and in the linear stability analysis based on primitive equations. This approximation is used in chapter 4 to explore different non-linear processes that can exist in river estuaries and/or the near field region of a river plume.

2.3.1 Fluid2D Model

Fluid2d is a versatile 2D Python-Fortran Computational Fluid Dynamics model⁸. This numerical model is discretized on a C-Arakawa grid, where buoyancy and vorticity are defined at model cell centers; and velocity and stream functions are defined at cell edges and cell corners respectively. The time discretization is a Runge-Kutta third order scheme. The time step of the model is $dt = 0.01$ seconds. The advection scheme is a fifth order upwind which does not require an explicit viscosity or diffusivity. The model extent is 10 m vertically and 40 m horizontally. The grid size is 2048*512 in the (x-z) plane. The model uses 2D Boussinesq equations with a non-hydrostatic approximation that we summarize below:

$$\partial_t \omega + J(\psi, \omega) = \partial_x b \quad (2.19)$$

$$\partial_t b + J(\psi, b) = -N^2 \partial_x \psi \quad (2.20)$$

⁸<https://mespages.univ-brest.fr/roullet/fluid2d/index.html>

$$\partial_{xx}^2 \psi + \partial_{yy}^2 \psi = \omega \quad (2.21)$$

where ω is the vorticity, b is the buoyancy field, J the jacobian operator, N^2 is the Brunt Vaisala frequency and ψ the streamfunction. The model runs for 4 minutes with 0.25 seconds outputs.

Full details about the initial conditions of the numerical simulations performed using this model are given in chapter 4.

2.3.2 Linear stability analysis

The linear stability analysis is performed using the non-hydrostatic (NH) approximation. We consider an incompressible and stratified fluid with no Coriolis effect. No viscosity, nor diffusivity are considered for this analysis. The NH primitive equations are written as:

$$\partial_x u + \partial_z w = 0 \quad (2.22)$$

$$\frac{D\mathbf{u}}{Dt} = -\nabla p + b\mathbf{k} \quad (2.23)$$

$$\frac{Db}{Dt} = 0 \quad (2.24)$$

where $\mathbf{u} = u\mathbf{i} + w\mathbf{k}$ (\mathbf{i} and \mathbf{k} are the horizontal and vertical unit vectors, respectively) is the velocity vector, p is the pressure scaled by a mean density ρ_0 , b is the buoyancy and $\frac{D}{Dt} = \partial_t + \mathbf{u} \cdot \nabla$ is the material derivative.

We linearize these fields around a background state and we write:

$$b(x, z, t) = B(z) + b'(x, z, t) \quad (2.25)$$

$$u(x, z, t) = U(z) + u'(x, z, t) \quad (2.26)$$

$$w(x, z, t) = W(z) + w'(x, z, t) \quad (2.27)$$

$$p(x, z, t) = P(z) + p'(x, z, t) \quad (2.28)$$

where $(B(z), U(z), P(z))$ are the background fields assumed steady and in hydrostatic balance. The prime fields denote perturbations around the background flow.

The prime fields are written as:

$$(b', u', w', p') = (\hat{b}(z), \hat{u}(z), \hat{w}(z), \hat{p}(z)) \exp(\sigma t + ikx) \quad (2.29)$$

where the real part of σ is the growth rate, $-\frac{\text{Im}(\sigma)}{k}$ is the phase speed and k is the horizontal wavenumber. The hat fields are eigenfunctions.

We inject these fields in the linearized NH primitive equations combined into pair of equations for the vertical velocity and the buoyancy field and represented in matrix form as:

$$\sigma \begin{pmatrix} \frac{d^2}{dz^2} - k^2 & 0 \\ 0 & I \end{pmatrix} \begin{pmatrix} \hat{w} \\ \hat{b} \end{pmatrix} = \begin{pmatrix} -ikU(\frac{d^2}{dz^2} - k^2) + ikU_{zz} & -k^2 \cos(\alpha) + ik \sin(\alpha) \frac{d}{dz} \\ -B_z & -ikU \end{pmatrix} \begin{pmatrix} \hat{w} \\ \hat{b} \end{pmatrix} \quad (2.30)$$

The subscript z indicates a vertical derivative and α characterizes the bottom slope angle.

Vertical boundaries conditions are $\hat{w} = \hat{b} = 0$

The Howard's semicircle theorem [Kochar and Jain, 1979] is used to get only physical solutions bounded by the mean flow velocity extreme values:

$$(c_r - 0.5(U_{\min} + U_{\max}))^2 + c_i^2 \leq 0.5(U_{\max} - U_{\min}) \quad (2.31)$$

where $c_r = -\frac{\text{Im}(\sigma)}{k}$ is the phase velocity and $c_i = \frac{\text{Re}(\sigma)}{k}$.

This linear analysis is used in complement to fluid2d numerical model in chapter 4 to understand unstable processes and turbulent mixing in stratified sheared flows such as buoyant plumes.

Chapter 3

River plumes in homogeneous and steady ocean

In this chapter, an idealized study of the Gironde river plume is presented. In this study, the dynamics, instabilities and mixing is analyzed in this plume in regards of different physical processes (river discharge, winds, tides). The main results have been published in Geophysical and Astrophysical Fluid Dynamics (GAFD) journal.

3.1 Introduction

Dans ce chapitre, j'aborderai les instabilités (géostrophiques et non-géostrophiques) et les processus de mélange vertical menant à la restratification ou à la déstabilisation du panache fluvial en surface. En raison de l'interaction entre de nombreux degrés de liberté physiques et géométriques, je limiterai cette étude à l'influence des eaux fluviales (température, salinité, débit des rivières), des forçages atmosphériques (vent) et la marée.

Cette étude est basée sur une expérience de référence où un panache de rivière n'est forcé que par un débit fluvial modéré. Des expériences de sensibilité sont effectuées à partir de cette référence, où chaque processus (vent, marée, intensité des débits fluviaux et température de l'eau douce) est étudié indépendamment.

La stratégie ici est de définir un cadre qui est bien adapté pour des instabilités de sous-mésoéchelle et une analyse du mélange. Le modèle numérique à haute résolu-

tion (équations primitives) permet la résolution de ces petites échelles ¹. Ce modèle résolvant explicitement les processus à sous-mésoéchelle permet de capturer les mouvements ageostrophiques et géostrophiques dans le bulge (gyre anticyclonique) et le courant côtier dans un panache de rivière.

Malgré les simplifications de cette étude, les instabilités symétriques, baroclines et barotropes, et de cisaillement verticale ² sont bien représentées. L'emplacement, la nature et l'intensité de ces instabilités dans le bulge (gyre anticyclonique) et le courant côtier (champ lointain) pour chaque expérience sont analysés.

L'existence d'instabilités et leur mécanisme de génération ont été explorés à l'aide de critères isopycnaux reposant sur la vorticit   potentielle d'Ertel (Hoskins et Charney-Stern) et un bilan d'  nergie cin  tique turbulente (uniquement les termes de production et de flux de flottabilit  ). Ces diagnostics sont bien adapt  s aux processus de sous-m  so  chelle ou de m  so  chelle (diff  rents de la th  orie quasi-g  ostrophique qui est utilis  e dans les r  gions frontales par exemple).

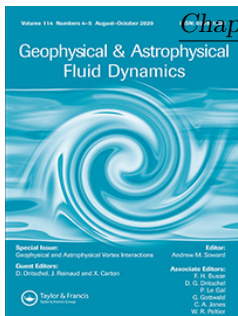
Les processus de m  lange vertical sont d  finis    l'aide d'un bilan de stratification dans le bulge et dans le courant côtier. Le bilan de stratification est param  tr   par les processus de m  lange de la vorticit   potentielle d'Ertel et de la frontog  n  se/frontolyse. Les processus de m  lange sont   troitement li  s au sch  ma de fermeture turbulente dans un mod  le num  rique.

Ces r  sultats ont   t   publi  s dans un journal scientifique GAFD (Geophysical and Astrophysical Fluid Dynamics) et le contenu de cet article est pr  sent   dans la section suivante.

3.2 Article: Instabilities and vertical mixing in river plumes

¹Sauf dans les r  gions frontales o   les longueurs d'onde peuvent   tre trop petites (l'  paisseur du front est \sim le rayon de d  formation de Rossby).

²sont d  finies ici comme Kelvin-Helmholtz, mais ces processus non lin  aires sont plus pr  cis et repr  sent  s dans une approximation non hydrostatique.



Geophysical & Astrophysical Fluid Dynamics

ISSN: (Print) (Online) Journal homepage: <https://www.tandfonline.com/loi/ggaf20>

Instabilities and vertical mixing in river plumes: application to the Bay of Biscay

Adam Ayouche , Xavier Carton , Guillaume Charria , Sebastien Theetens & Nadia Ayoub

To cite this article: Adam Ayouche , Xavier Carton , Guillaume Charria , Sebastien Theetens & Nadia Ayoub (2020) Instabilities and vertical mixing in river plumes: application to the Bay of Biscay, *Geophysical & Astrophysical Fluid Dynamics*, 114:4-5, 650-689, DOI: [10.1080/03091929.2020.1814275](https://doi.org/10.1080/03091929.2020.1814275)

To link to this article: <https://doi.org/10.1080/03091929.2020.1814275>



© 2020 The Author(s). Published by Informa UK Limited, trading as Taylor & Francis Group



Published online: 16 Sep 2020.



Submit your article to this journal 



Article views: 530



View related articles 



View Crossmark data 

GEOPHYSICAL & ASTROPHYSICAL FLUID DYNAMICS
2020, VOL. 114, NO. 4–5, 650–689
<https://doi.org/10.1080/03091929.2020.1814275>



OPEN ACCESS Check for updates

Instabilities and vertical mixing in river plumes: application to the Bay of Biscay

Adam Ayouche^a, Xavier Carton^a, Guillaume Charria ^a, Sebastien Theettens^a and Nadia Ayoub^b

^aLaboratory for Ocean Physics and Satellite remote sensing (LOPS), UMR6523, Ifremer, Univ. Brest, CNRS, IRD, Brest, France; ^bCNRS, CNES, IRD, Laboratoire d'Etudes en Géophysique et Océanographie Spatiales (LEGOS UMR5566), Université de Toulouse, Toulouse, France

ABSTRACT

In the Bay of Biscay (north-east Atlantic), long-living eddies and the frontal activity that they induce substantially contribute to mesoscale and submesoscale dynamics. Tides and river plumes also contribute to frontal activity. Biological productivity is sensitive to river plume fronts and to external forcings (tides and wind). Considering the importance of river plumes, we study here the structure, stability and vertical mixing processes in such river plumes (similar to those generated by the Gironde river). Restratification budget is considered here for evaluating stirring (frontogenetic/frontolytic) or vertical mixing (parametrised here from Ertel potential vorticity mixing) processes. Using high-resolution idealised numerical simulations, we analyse the evolution of the bulge and of the coastal part of this plume and we conduct sensitivity experiments to the river discharge, to southwesterly winds and to M2 tides. The bulge and the coastal current are stable (unstable) in case of moderate (high) river discharge, due to mixed barotropic/baroclinic instabilities. In the unstable case, near surface symmetric and vertical shear instabilities develop in the coastal current and in the core of the bulge where the Rossby number is large. When southwesterly winds blow, the river plume is squeezed near the coast by Ekman transport. The river plume is then subject to frontal symmetric, baroclinic, barotropic and vertical shear instabilities in the coastal part, north of the estuary (its far field). Conversely, in the presence of M2 tides, the river plume is barotropically, baroclinically and symmetrically unstable in its near field. Interior vertical mixing is induced by advective (stirring) and frontogenetic processes. Frontogenesis is dominant in the far-field (in the presence of southwesterlies) or in the near-field (when M2 tide is active). Frontogenesis is important in the far-field region in unforced river plumes (both with moderate and high river discharges). Potential vorticity is eroded in the far-field when southwesterlies blow. This is primarily due to the frictional processes which are dominant at the surface. This study has identified the instabilities which affect a river plume in different cases, and the local turbulent processes which alter the stratification.

ARTICLE HISTORY

Received 31 January 2020
Accepted 20 August 2020

KEYWORDS

River plumes; Gironde river;
(sub)mesoscale instabilities;
vertical mixing; stratification

CONTACT Adam Ayouche adam.ayouche@ifremer.fr, aayouche@ifremer.fr

© 2020 The Author(s). Published by Informa UK Limited, trading as Taylor & Francis Group
This is an Open Access article distributed under the terms of the Creative Commons Attribution-NonCommercial-NoDerivatives License (<http://creativecommons.org/licenses/by-nc-nd/4.0/>), which permits non-commercial re-use, distribution, and reproduction in any medium, provided the original work is properly cited, and is not altered, transformed, or built upon in any way.

1. Introduction

Over the last decades, there has been a growing interest in the Bay of Biscay for economic and scientific reasons. This semi-enclosed region is recognised for multiple oceanographic features: as part of the north-east Atlantic Ocean, it is influenced by a general anticyclonic circulation in the open ocean and by a poleward flow over the shelf break, the Iberian poleward slope current (IPC) (Pingree and Le Cann 1990, Charria *et al.* 2013, Teles-Machado *et al.* 2015). The circulation in the Bay of Biscay is also forced by northwesterly and southwesterly winds, moderate tides, or seasonal river discharges. These forcings drive coastal currents, upwellings and downwellings and vertical mixing of the water masses.

Over the shelf-break and in the deep ocean, mesoscale activity is manifested in long living quasi-stationary anticyclonic eddies in northern Spain, and in the central basin, respectively, called 4°W eddy and slope water oceanic eddies (SWODDIES) (Pingree and Sinha 2001, Caballero *et al.* 2014). The IPC perturbations mainly result in the generation of these strong eddies. When they are not trapped by topography, the 4°W eddy and SWODDIES are, respectively, driven by density forcing and they are advected to the west. The slope water oceanic eddies have typical migration speeds of 2 cm s^{-1} comparable with long Rossby waves phase speed (βR_d^2 with $R_d = 25 - 30 \text{ km}$ the Rossby radius of deformation in the abyssal plain and $\beta = 1.5 \times 10^{-11} \text{ m}^{-1} \text{ s}^{-1}$) (Pingree and Sinha 2001, Caballero *et al.* 2014). A warm anticyclone, generated over the shelf-break after wind relaxation and drifting northwards after several weeks, has been observed using high-frequency radar data (Rubio *et al.* 2018). The eddies mentioned above have similar characteristics: a radius of 25–50 km, a vertical extent ranging from 100 m to 2 km and a rotation period between 7 h and 3.5 days. The 4°W eddy and SWODDIES have lifetimes, respectively, of about seven months and one year (Pingree and Sinha 2001, Caballero *et al.* 2014).

In the shallower region over the continental shelf, the Bay of Biscay is characterised by two main riverine inputs (the Loire and the Gironde rivers). These two rivers provide a noticeable runoff in the bay, with an annual average discharge of $900 \text{ m}^3 \text{ s}^{-1}$ each (Lazure *et al.* 2009). Obviously, this discharge is small compared to those of the Columbia or of the Mississippi rivers ($10,000 \text{ m}^3 \text{ s}^{-1}$ and $30,000 \text{ m}^3 \text{ s}^{-1}$). The Columbia and Mississippi river plumes are subject to tide and wind-driven dynamics, respectively, comparable to Gironde river plume. Indeed, the Columbia river plume is subject to tide stirring and mixing in its near field where many fronts are formed (Kilcher and Nash 2010). On the other hand, the Mississippi river plume is subject to Eastward wind-driven currents which alter its far-field and exhibit a large freshwater transport toward the shelf break and the DeSoto Canyon (Schiller *et al.* 2011). Therefore, the Gironde river can be considered as a river system where both effects (wind and tides) can be analysed in a single region. When the river flow enters the coastal ocean, the expansion of the plume in the near field is linked to the river discharge: the momentum of the plume layer dominates its buoyancy (Horner-Devine *et al.* 2015). Conversely, the Coriolis force brings the plume back along the coast (to the right of the plume in the Northern Hemisphere). At the river mouth, and for weak wind forcing, this plume curvature can create an anticyclonic bulge; the bulge radius can grow up to a few internal Rossby radii (Garvine 1999). The plume characteristics depend on the relative influences of the stratification created by the freshwater discharge and its mixing with the ambient, saline waters. Near the estuary (in the near field of the plume), this mixing is governed by the flow acceleration, by variable advection and by turbulent processes

(Horner-Devine *et al.* 2015). In the far-field region of the plume, the wind influence dominates the mixing processes (Fong and Geyer 2001). Tides can also affect river plumes. Flood-ebb tidal straining generates periodic fluctuations of the density stratification (Simpson *et al.* 1990, Isobe 2005, Iwanaka and Isobe 2018); conversely, this stratification alters the tidal currents (Visser *et al.* 1994, Li and Rong 2012).

Based on O'Donnell definition, in the absence of wind an along-shore coastal current forms. The vertical structure of this coastal current is delimited by a plume front (offshore extent of buoyant water). The plume front encounters the bottom at a location called “the inshore edge of the frontal zone.” From this specific location, inshore and offshore regions are formed as sketched in figure 8.10(c) in (O'Donnell 2010) and as defined in Lentz and Largier (2006). The ratio of the areas of those two regions (inshore area over offshore area) is controlled by topography. This ratio is small in the case of steep bottom slope and important in the case of gentle bottom slope (Garvine 1999, Avicola and Huq 2002, Lentz and Helfrich 2002).

In the Bay of Biscay, the shape and extent of each river plume depends on the river discharge and on the wind patterns (Lazure and Jegou 1998); the Loire river plume can reach 50.7°N (Kelly-Gerreyn *et al.* 2006) (figure 1).

During the MODYCOT 99-3 experiment (Puillat *et al.* 2004), the Gironde river plume reached the offshore area of the Loire estuary and a lens of 100–150 km diameter is formed. The Loire and Gironde river plumes form northward currents parallel to the coast which have been observed using surface drifting buoy trajectories (Castaing 1984, Puillat *et al.* 2004). The Loire and Gironde river plumes extension is maximal in winter with a peak in January ($3 \times 10^4 \text{ km}^2$) and it is minimal in summer with a low extension in July ($4 \times 10^3 \text{ km}^2$) (figure 1) (Lazure and Jegou 1998). The inflow speed is $u_e = Q/(hL)$, where h is the maximum estuarine depth, Q the river discharge and L the width at the estuary mouth. The maximum and minimum inflow speeds occur respectively in winter and summer, with a maximum in January of about 2 cm s^{-1} for the Gironde (a mouth width of $\sim 10 \text{ km}$ and depth of $\sim 10 \text{ m}$) and $\sim 1 \text{ cm s}^{-1}$ for the Loire river (a depth of $\sim 10 \text{ m}$ and a mouth width of $\sim 20 \text{ km}$) and a minimum in August of $\sim 0.5 \text{ cm s}^{-1}$ for the Gironde river and $\sim 0.25 \text{ cm s}^{-1}$ in Loire river (Costoya *et al.* 2017). We note that the inflow speed is the residual (tides filtered) inflow from the estuary to the open ocean. Phytoplankton and zooplankton seasonal cycles are also sensitive to the river plume dynamics, which is subject to mixing and stratification modifying the photosynthetic available radiations (Botas *et al.* 1990, Lavín *et al.* 2006).

River plumes can be affected by various, geostrophic or ageostrophic, instabilities, due to the velocity and density anomalies that they create in the coastal ocean. Ambient stratification or bottom topography can also influence these instabilities. In the bulge and frontal regions, the main instabilities are baroclinic, barotropic and Kelvin–Helmholtz instabilities.

Baroclinic instabilities can occur for wide plumes (Hetland 2017). Baroclinic instabilities of the Gaspe current (the freshwater current originating from the St Lawrence estuary) have been observed in SST images and have been modelled numerically at 2–3 km resolution (Sheng 2001), but few observations of barotropic instabilities are available. For tidally forced plumes, Kelvin–Helmholtz billows can result from vertical shear instability of horizontal currents at the bottom of the plume, in the near-field region. This

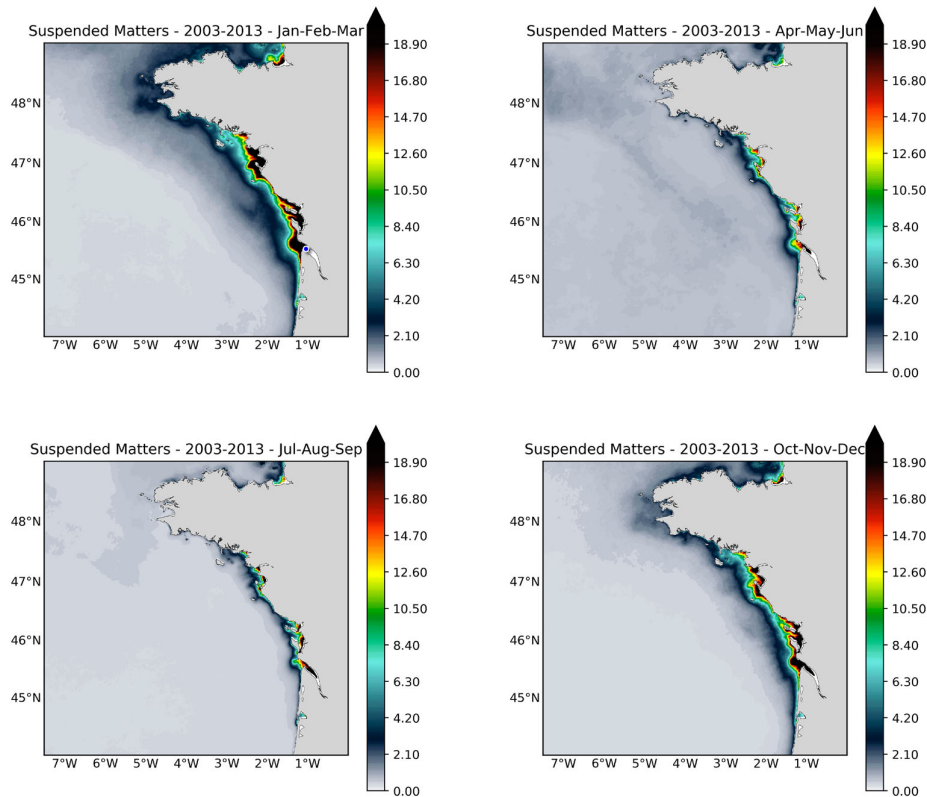


Figure 1. Suspended matters for top row: (left) Winter, (right) Spring and bottom row: (left) Summer and (right) Fall. The quarterly climatology is based on MERIS/ESA and MODIS/NASA data from 2003 to 2013, following the approach developed in Gohin (2011) and processed in the MARC project (<http://marc.ifremer.fr/>). Location of Le Verdon MAGEST *in situ* observing network station in the Gironde estuary (blue point – top left).

instability also increases the mixing of freshwater with ambient saline water (MacDonald and Geyer 2004, Kilcher and Nash 2010).

The instabilities affecting narrow river plumes (with estuary width limited to a few kilometers) under external forcing have not yet been studied with a very high-resolution model. With a two-layer model, de Kok (1997) shows that northeasterly and easterly winds favour the stratification onset, and baroclinic instability in a Rhine river plume settings. This instability creates salinity front meanders which considerably reduce the trapped coastal water. Winds or tides tend to inhibit instabilities through mixing. Instabilities are strongest in summer and mixing overcomes instabilities in other seasons (Hetland 2017).

In the present work, a submesoscale resolving model is used to perform idealised numerical simulations of a river plume (the Gironde). In particular, we will address the following questions:

- what is the 3D structure of this plume, considering the bulge and the coastal current?
- what is the effect of different forcings (wind, tidal, mean flow . . .) on this structure?

654  A. AYOUCHE ET AL.

- which types of instabilities, both geostrophic and ageostrophic can affect this plume and under which conditions?
- what are the consequences of the instabilities on the 3D mesoscale structure of the plume, in particular via the vertical mixing induced by the submesoscale features, and via the energy transfer that they achieve?

The paper will thus be organised as follows: the model configuration, simulations and methods will be described in section 2, the 3D structure of the plume in section 3.1, the instabilities affecting it in section 3.2 and the impact of submesoscale effects on the plume structure in section 3.3. The main results will be discussed in section 4 and conclusions will be provided.

2. Materials and methods

2.1. Model configuration

The simulations are performed using the Coastal and Regional COmmunity CROCO. CROCO and CROCO TOOLS are provided by <https://www.croco-ocean.org> (Shchepetkin and McWilliams 2005, Debreu *et al.* 2012). CROCO (based on ROMS) is a split-explicit, free-surface, hydrostatic, primitive equation ocean model. The model uses sigma coordinates in the vertical; orthogonal curvilinear coordinates are used in the horizontal; the variables are discretised on an Arakawa C-Grid. The horizontal resolution is 200 m; 128 σ -layers discretise the flow vertically; these layers are stretched at the surface and at the bottom with $\theta_s = 5$, $\theta_b = 0.4$ and $h_{\min} = 10$ m. The model time step is 30 s with model outputs every 2 h.

The horizontal advection of momentum and tracers is performed with the Zico extension fifth order WENO scheme (a weighted ENO with improvements of the weights formula) (Rathan and Raju 2016). It has the advantage of being little dissipative and of not imposing a CFL (Courant-Friedrichs-Lewy) constraint. The vertical advection is a parabolic conservative scheme for both momentum and tracers. The model implicit vertical mixing is configured using the $k - \omega$ turbulent closure scheme with a Kantha Clayson stability function (Kantha and Clayson 1994, Umlauf and Burchard 2005, Warner *et al.* 2005). The background vertical diffusivities (for both momentum and tracers) are $Kv_b = 5 \times 10^{-6} \text{ m}^2 \text{ s}^{-1}$ and $Kt_b = 5 \times 10^{-6} \text{ m}^2 \text{ s}^{-1}$. A Smagorinsky-like viscosity have been used for lock-exchange problem which takes place when two reservoirs of different densities interact with each other in a horizontal closed domain (Gröbelbauer *et al.* 1993, Lowe *et al.* 2005). The quadratic Von-Karman law (logarithmic law) is used for bottom friction with a bottom roughness $z_0 = 5$ mm.

The domain extent is [142 km, 445 km, 100 m] in the x , y , z directions respectively with a bathymetry varying zonally (no meridional variations) (figure 2).

The estuary is located in the middle of the domain with a 20 km length, 6 km width and a uniform depth of 10 m. The freshwater discharge is prescribed in the eastern, most, part of the estuary; it is distributed over 31 grid points and ramped over 2 days with a hyperbolic tangent tendency. The freshwater sources temperature and salinity are 13°C and 20 psu, respectively. The freshwater source salinity is chosen as an average from the MAGEST *in situ* observing network time series (at 1 m depth) during the January–February 2019 period

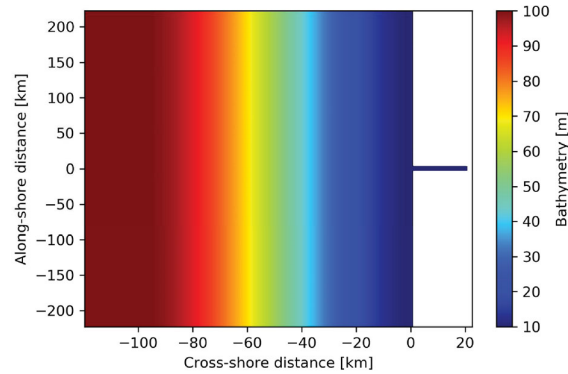


Figure 2. Bathymetry of the idealised numerical model configuration. (Colour online)

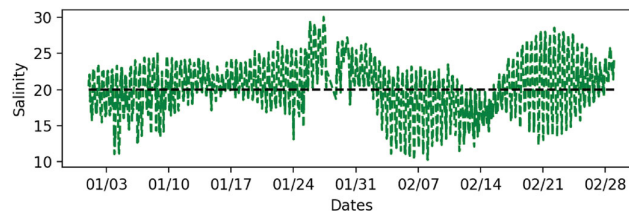


Figure 3. Le Verdon MAGEST station time series of salinity at ~ 1 m depth during January and February 2019. The black dashed line shows the 20 psu salinity value used for idealised simulations. (Colour online)

as shown in figure 3. The Le Verdon station was considered here; its location is shown in figure 1.

The initial conditions are rest (no current) with a homogeneous ocean ($T_0 = 13^\circ\text{C}$ and $S_0 = 35$ psu). The background temperature and salinity values are based on BOBYCLIM, an *in situ* climatology in the Bay of Biscay (Vandermeirsch *et al.* 2010). Following previous studies (Vic *et al.* 2014, Palma and Matano 2017), we choose similar values for background and freshwater temperatures. A simulation using a different freshwater temperature (9°C instead of 13°C) has been compared to the reference configuration. We show that the change in temperature has a small effect on the circulation and the buoyancy in the river plume without changing its global shape or structure. For example, after 12 simulated days, we obtain small differences in sea surface height (~ 0.7 cm), in the vertically averaged u and v momentum (~ 4 cm s^{-1}) and in the vertically averaged density (~ 0.6 kg m^{-3}). Therefore, we decide to consider the 13°C freshwater temperature similar to the background values. In the case of non-tidal simulation, the Orlanski-type (Orlanski 1976) open boundaries conditions for both momentum (2D and 3D) and tracers is used at the western, southern and northern part of the domain; a sponge layer of 30 km is added with a cosine profile viscosity (values ranging from 0 (inner boundary) to 13 m 2 s $^{-1}$ (outer boundary)) to avoid reflections and to dissipate any noise generated at the boundaries. In the tidal case, we used Chapman open boundary conditions for the surface elevation (Chapman 1985), and Flather open boundary conditions for the barotropic velocity components combination (Marchesiello *et al.* 2001). For the 3D tracers and momentum, an Orlanski open boundary

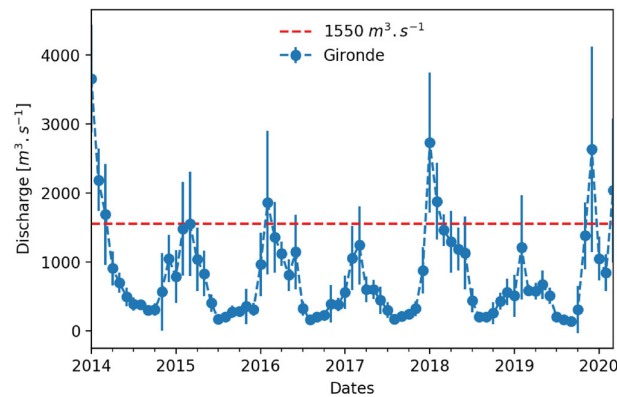
656  A. AYOUCHE ET AL.

Figure 4. The Gironde estuary is fed by the Garonne and Dordogne rivers. The discharges for these two rivers are obtained from hydrological stations and retrieved through the French national service “Banque Hydro” (<https://www.hydro.eaufrance.fr>). They are added together to estimate the Gironde discharge. Blue dots show the monthly discharge mean. For each month, the standard deviation of the river discharge is represented by a vertical bar. The red dashed line shows the $1550 \text{ m}^3 \text{ s}^{-1}$ discharge value used in idealised simulations. (Colour online)

condition is used. A sponge layer was also used. This idealised configuration is based on the Gironde river plume dynamics for different parameters (i.e. salinity gradients, estuary width, river discharge, bathymetry slope) but we decided not to consider supplementary constraints such as the coastal shape (including existing small islands) or other existing rivers (as the Loire river plume further North in the Bay of Biscay) to avoid complex interactions. This choice was dedicated to optimise numerical framework to understand instability and mixing dynamics in the river plume.

2.2. Model experiments

In this part, a description of the sensitivity experiments simulated in this study is provided. The duration of all the numerical simulations presented in this study is 16 days. The simulation length is based on two criteria: first, it has been defined as the typical time range necessary, in idealised condition, to reach a balanced regime in the river plume and to have at least one week for analyses; the second is related to the observed high river discharge in winter. As shown in figure 4, the simulated river discharge is close to winter monthly averages values.

The reference experiment has a river discharge of $1550 \text{ m}^3 \text{ s}^{-1}$ and no external forcing. The discharge value defined here is based on monthly-averaged observations from hydrological stations, provided by the French national service “Banque Hydro” (<https://www.hydro.eaufrance.fr>). These discharge values correspond to estuarine flood periods. Sensitivity to a high discharge value of $10,000 \text{ m}^3 \text{ s}^{-1}$ has been studied without external forcings to evaluate the model response to extreme flux conditions. Such a high discharge is not reached in the Bay of Biscay but has been studied here to explore the Gironde river plume in the case of an extreme (unrealistic) flood. This extreme river discharge helps to understand the dynamics for plumes comparable to the Congo or the

Table 1. List of simulations and their specific forcings.

Experiments	River forcing	External forcings
Reference	Discharge ($1550 \text{ m}^3 \text{ s}^{-1}$)	–
High Discharge	Discharge ($10,000 \text{ m}^3 \text{ s}^{-1}$)	–
Tide	Discharge ($1550 \text{ m}^3 \text{ s}^{-1}$)	M2 Tide (1.5 m amplitude)
Wind	Discharge ($1550 \text{ m}^3 \text{ s}^{-1}$)	SW Wind ($\tau_{\max} = 0.02 \text{ N m}^{-2}$)

Mississippi river (Vic *et al.* 2014, Hetland 2017). Sensitivity to tides has been analysed using the reference discharge and M2 tide component with an amplitude of 1.5 m. Model outputs (M2 tide configuration) have been detided using a Fast Fourier Transform (FFT) as in Walters and Heston (1982). To investigate the impact of the southwesterly wind regime, no wind is applied during the first 8 simulation days then the wind stress is ramped over 4 days (with a tanh tendency) up to $\tau_{\max} = 0.02 \text{ N m}^{-2}$. Table 1 summarises the configurations used in the present study.

2.3. Methods

2.3.1. Diagnostics for river plume instabilities

The instability of river plumes leading to the generation of eddy kinetic energy is analysed using the transfer of kinetic and potential energy from the mean to the submesoscale turbulent flows. A scale decomposition is performed on the velocity and buoyancy fields. In this decomposition, the mean flow represents the large scales and perturbations represent the meso-scales and submeso-scales. The decomposition on the velocity and buoyancy fields is expressed as $\mathbf{u} = \bar{\mathbf{u}} + \mathbf{u}'$ and $b = \bar{b} + b'$. Overbar and prime denote temporal mean over one day as follows $\bar{\bullet} = (1/T) \int_{t-T/2}^{t+T/2} \bullet dt$ (mean flow) and deviations relative to this mean (perturbations), respectively. The horizontal (HRS) and vertical (VRS) shear stresses and the vertical buoyancy flux (VBF) (instantaneous values) are expressed as in Gula *et al.* (2016) and Capuano *et al.* (2018) as

$$\text{HRS} = -u'^2 \partial_x \bar{u} - u' v' [\partial_y \bar{u} + \partial_x \bar{v}] - v'^2 \partial_y \bar{v}, \quad (1)$$

$$\text{VRS} = -u' w' \partial_z \bar{u} - v' \partial_z \bar{v}, \quad (2)$$

$$\text{VBF} = w' b'. \quad (3)$$

Barotropic instability is characterised by a positive HRS (transfer from MKE (mean kinetic energy) to EKE (eddy kinetic energy)). Baroclinic instability is related to a positive vertical buoyancy flux (VBF). Mixed barotropic and baroclinic instabilities occur when VBF and HRS are positive at the same location. Kelvin–Helmholtz instability is represented as a positive VRS. Negative values of VBF, VRS, HRS represent a contribution to the mean flow (Kang 2015, Evans Contreras *et al.* 2019).

Submesoscale processes and their contribution to instabilities can be related to changes in the Ertel potential vorticity (Q) (Ertel 1942, Schubert *et al.* 2004) and in stratification due to external forcings (winds, tides, eddies). The Ertel potential vorticity can be expressed in isopycnal coordinates as (Morel and McWilliams 2001)

$$Q = \frac{f + \zeta_\rho}{h_\rho}, \quad (4)$$

658  A. AYOUCHE ET AL.

where $\zeta_\rho = (\partial_x v - \partial_y u)_\rho$ is the relative vorticity computed in isopycnal coordinates, h_ρ is the isopycnal thickness and f is the Coriolis parameter.

The rotation, stratification and vertical shear are important to understand the river plume dynamics (Nash *et al.* 2009, Pan and Jay 2009). Therefore to understand the nature of the regime (geostrophic or ageostrophic) and to understand the importance of shear mixing in river plumes, we will analyse the Richardson Number and the local Rossby Number expressed as

$$R_o = \frac{\partial_x v - \partial_y u}{f}, \quad R_i = \frac{N^2}{S^2}, \quad (5)$$

where $N^2 = -(g/\rho_0)\partial_z \rho$ is the Brunt-Vaisala frequency and $S^2 = (\partial_z u)^2 + (\partial_z v)^2$ is the vertical shear in which u and v are the instantaneous along-shore and cross-shore velocities, respectively.

When R_i and R_o are $O(1)$ submesoscale processes prevail (Thomas *et al.* 2008, McWilliams 2016). According to the criteria of Hoskins (1974), negative fQ and $R_i < 1$ indicate the existence of symmetric instabilities (see also Morel and McWilliams 2001, Thomas *et al.* 2013). We calculate the cross-shore gradient $\partial_x Q$. We identify where its sign changes across and along isopycnals. This indicates baroclinic and barotropic instabilities (Charney–Stern criterion).

2.3.2. Diagnostics for river plume vertical mixing

The last diagnostics for this paper is to analyse changes in stratification in a given volume driven by two main mechanisms: frontogenesis and changes in potential vorticity (Marshall and Nurser 1992, Marshall *et al.* 2001, Lapeyre *et al.* 2006, Thomas and Ferrari 2008). In our case, we consider the volume, variable in time, delimited by the outcropping at the surface to the river plume base (isopycnals 1024 kg m^{-3} for Reference, Tide and SW wind simulations and 1022 kg m^{-3} for High discharge simulation). We write the mean stratification over the considered volume

$$f \Delta \overline{N^2} = \text{FRONT} + \Delta q. \quad (6)$$

Here we express the frontogenesis term (FRONT) as the temporal cumulative sum of $\int_{V(t)} \partial_t(\zeta b) dV$ over previous time steps (here 2 h) where ζ is the relative vorticity and $b = -g\rho/\rho_0$ is the buoyancy. Where ρ_0 is the mean density in the domain. The potential vorticity is expressed as

$$q = \int_V \boldsymbol{\omega}_a \cdot \nabla b dV, \quad (7)$$

where $\boldsymbol{\omega}_a = f\mathbf{k} + \nabla \times \mathbf{u}$.

Following Marshall and Nurser (1992), we write the equation of conservation of Ertel potential vorticity as

$$\partial_t q + \nabla \cdot \mathbf{J} = 0 \quad (8)$$

which leads to

$$\partial_t q = -\mathbf{u} \cdot \nabla q + (\nabla \times \mathbf{F}) \cdot \nabla b + (f\mathbf{k} + \nabla \times \mathbf{u}) \cdot \nabla D. \quad (9)$$

The terms on the right-hand side of this equation represent advection (first term), torque or friction (second term) and buoyancy fluxes (third term). The second and third terms

are related to vertical mixing of mass or momentum that we can write as

$$F = \nabla \cdot (K_m \partial_z \mathbf{u}_h) = F_v, \quad (10)$$

where the subscript h denotes the horizontal components. In addition, F is the body force in Navier-Stokes, which can be related to vertical mixing of momentum (F_v) (we neglect here lateral mixing (F_l), it is implicit in the advection scheme of our model). In the CROCO model, surface and bottom forcings in vertical mixing of momentum are parametrised by wind stress and bottom stress. The third term is related to vertical mixing of tracers (remember that ocean and river temperatures are the same). We write

$$D = \partial_z (K_b \partial_z b), \quad (11)$$

where D is the source term in the mass conservation equation (no explicit horizontal diffusivity is considered here), which here is represented by the vertical mixing of buoyancy. At the surface, vertical mixing of mass can be associated to river input, heat exchange, and evaporation and precipitation. Thus, one can express the fluctuations in potential vorticity as resulting from friction, diabatic and advection processes

$$\frac{\partial q}{\partial t} = \text{ADV} + \text{FRIC} + \text{DIAB} + \text{Pres}. \quad (12)$$

The last term (Pres) represents the curl of pressure gradient (zero by definition). The last equation is analysed in a volume that varies in time

$$\partial_t \int_{V(t)} q \, dV = \int_{V(t)} (\text{ADV} + \text{FRIC} + \text{DIAB}) \, dV + \text{BVP}. \quad (13)$$

The last term represents the PV advection along the bounding isopycnals here the surface and the river plume base. The ADV (advective mixing), FRIC (frictionless mixing), DIAB (diabatic mixing), Pres (Pressure) and BVP (boundary value problem) are detailed in [Appendix](#) and are discussed in [Callendar *et al.* \(2011\)](#).

3. Results

3.1. River plume 3D structure and dynamics

In this part, the interaction of the river freshwater with the open ocean and its sensitivity to different forcing are analysed by means of 3D hydrological and dynamical structures.

3.1.1. Reference configuration

The river plume is divided into two regions: the anticyclonic gyre (bulge) and the coastal current (figure 5). The river plume evolves in three steps as shown in figure 5.

During the first stage, the bulge expands, trapping water exiting from the estuary. In this case, the salinity value increases from 20 to 30 psu, from the river to the bulge. This indicates mixing of the freshwater with the seawater (which has salinity of 35 psu); note also that some seawater enters the estuary, on its southern side, during this stage. This shows that the outflow at the river estuary undergoes some adjustment and is not yet steady. The second stage lasts from days 3 to 10 approximately. Then, the riverine freshwater feeds the

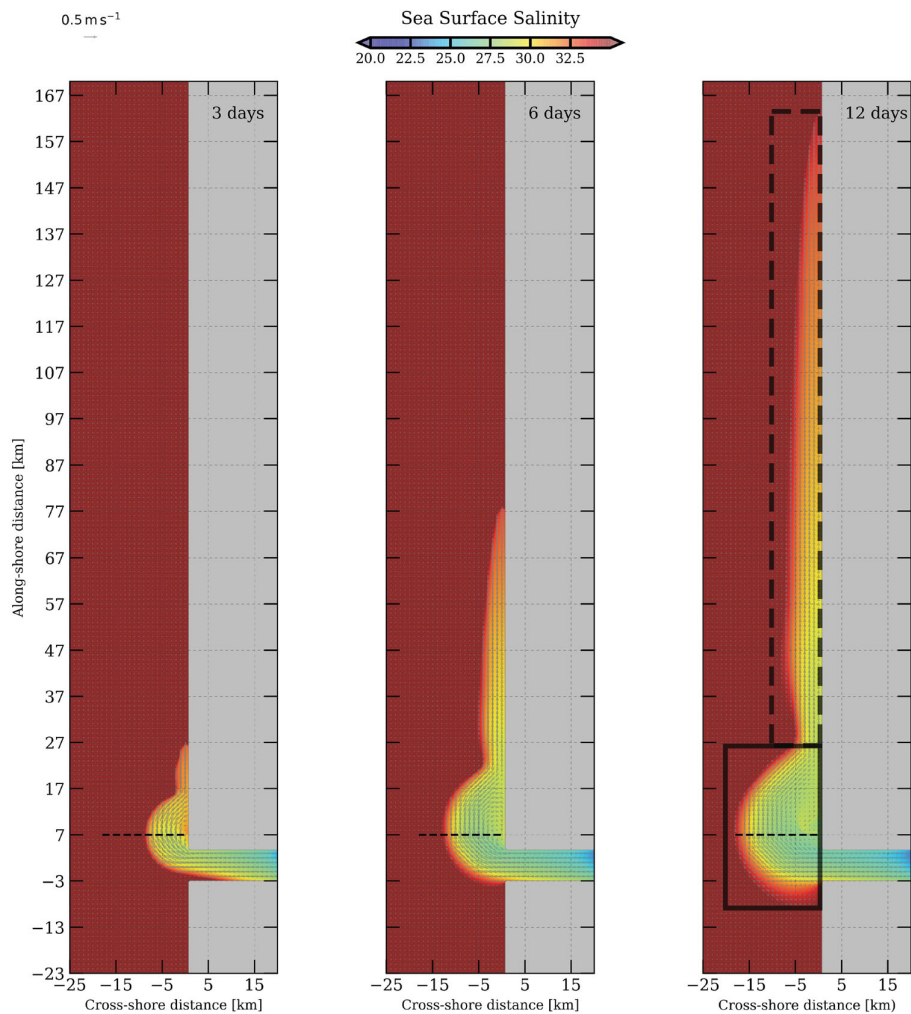
660  A. AYOUCHE ET AL.

Figure 5. Sea Surface Salinity at three different time steps – Reference Configuration. The black dashed line represents zonal vertical sections shown hereafter. The bold black rectangle represents the bulge region. The bold dashed rectangle defines the coastal current. (Colour online)

bulge, where the salinity decreases from 30 to 25 psu. Thus the mixed water concentrates at the edge of the bulge, forming a salinity front. In this case, seawater is not detected into the estuary. The bulge itself starts to feed the coastal current which progresses northward along the coast as a coastal surface current of freshwater. In the third stage (after day 10), the coastal current is well established for more than 100 km northward (though its nose continues to head northward) and instabilities can develop along it. The coastal current width reaches half of the bulge. The surface salinity map shows a complex pattern in the bulge with strong gradients near the coast. This is due to the recirculation of the riverine water at this location. This pattern will appear even more clearly in the surface relative

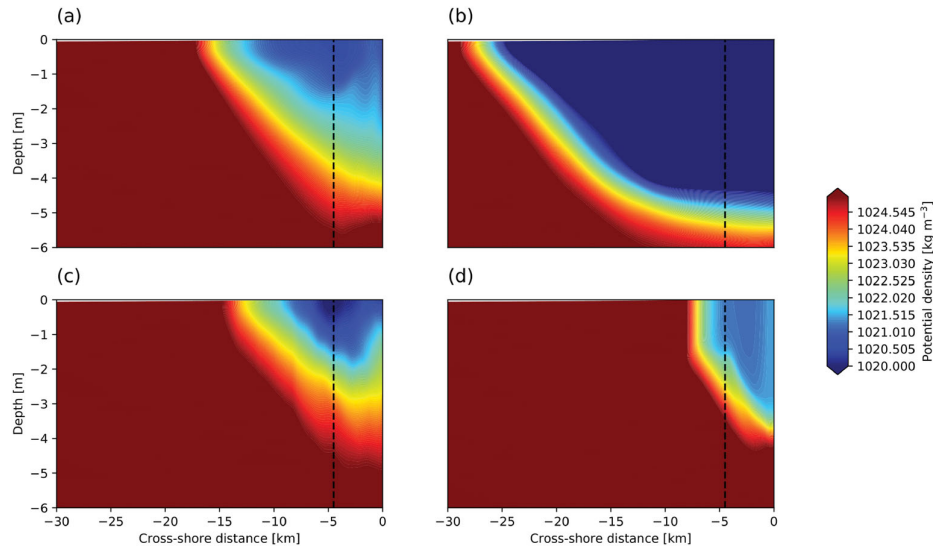


Figure 6. Vertical sections of Potential density (day 12): (a) Reference, (b) High Discharge, (c) Tide, (d) SW wind. The black dashed line represents the vertical profiles (density and N^2) shown hereafter. (Colour online)

vorticity map. For the study of the plume structure, we will consider that the flow state at day 12 is a quasi-final situation with both a bulge and an established coastal current.

At this time, the bulge width and depth reach 20 km and 5 m (see the vertical section of density at alongshore distance 7 km on figure 6(a)).

The river plume base is located at ~ 4 m depth (with a density gradient between 3 and 5 m depth) or near the isopycnal 1024 kg m^{-3} . A measure of the freshwater thickness in the bulge or the coastal current is defined by Hetland (2005) as

$$h_f = \int_{-H}^0 \left(1 - \frac{S}{S_0}\right) dz, \quad (14)$$

i.e. via an integral from the local bottom to the surface of the ocean; S_0 is the background salinity (here 35 psu) and S is the local plume salinity. The value thus obtained for the freshwater thickness (2 m) is well correlated with the potential density profile which shows a maximal gradient between 3 and 5 m depths (figure 7).

The buoyancy vertical gradient (Brunt-Vaisala frequency) has a peak at 3.5 m depth which is equivalent to the river plume base depth (~ 4 m). A secondary peak of the buoyancy vertical gradient at 1.5 m depth is related to the surface recirculation of the freshwater in the bulge.

Figure 8(a) is a horizontal map of the relative vorticity at day 12 for the end state of the plume.

The circulation in the bulge is anticyclonic except at two locations: (a) in its core where a small filament of positive vorticity can be seen due to freshwater recirculation, and (b) in the frontal region, where a narrow strip of positive vorticity lies between the ambient and the fresh water masses. In the coastal current, positive relative vorticity is also found

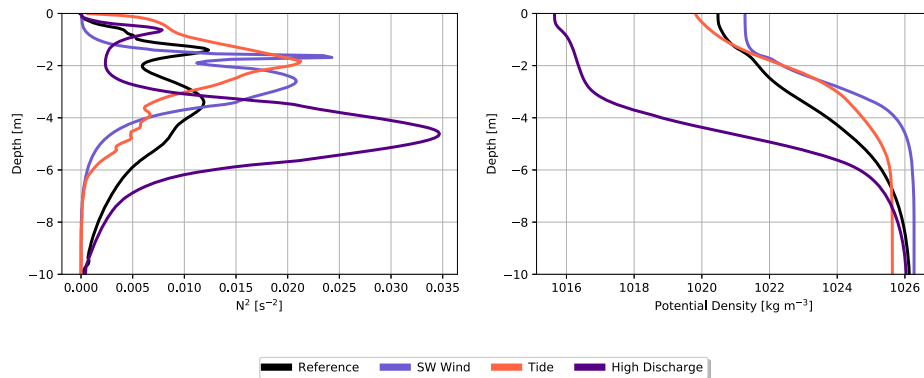
662  A. AYOUCHE ET AL.

Figure 7. Brunt–Vaisala (left) and potential density (right) vertical profiles (12 day). (Colour online)

in the frontal region, while strong negative vorticity ($\zeta/f < -1$) is located near the coast due to the frictional effect there (thus forming a strong shear layer). The flow is clearly ageostrophic ($R_o \sim O(1)$) at fronts and where strong curvature occurs, i.e. around the bulge, between the bulge and the coastal current, and at the northern nose of the coastal current. Vertically, the relative vorticity distribution (at alongshore position 7 km) is as follows. Near the surface (top 2 m) and near the estuary mouth (5 km from the coast), the local Rossby Number $R_o \sim O(1)$ (figure 9(a)).

High Rossby numbers ($R_o \sim O(1)$) are also found in the frontal region, in a thin layer of 1 m depth and roughly 1 km width. In the other parts of the bulge, $R_o < 1$. This shows coexistence of geostrophic and ageostrophic motions in the bulge. The latter is in good agreement with the total kinetic energy spectrum as it is characterised by a k^{-2} slope at the river plume base and by a slope between k^{-3} and k^{-4} at the surface (figure 10).

Thus, the dynamics is essentially driven by balanced processes near the surface, while frontal and ageostrophic processes dominate the evolution of the plume base.

3.1.2. Sensitivity experiments

External forcings have a noticeable impact on the horizontal and vertical shape and structure of the river plume. In the case of high discharge, the bulge develops quickly (figure 11): after 2 days, its width already reaches 15 km (the final size of the bulge in the reference configuration) and it grows to 30 km after 12 days.

Under these conditions seawater is not able to penetrate into the estuary because the strong outward flux prevents it. The coastal current then extends to more than 160 km northward after 12 days. Its width represents half of that of the bulge. Salinity values are now significantly higher than 20 psu only in the coastal current, which faces the open sea, and at the centre of the bulge which contains the riverine water that has outflowed first, and has slightly mixed with seawater. The strong outflow velocities constrain water mixing to occur in a thin frontal region, highly sheared. In the final stage (day 12), the vertical section of density (figure 6(b)) also shows a high gradient concentrated both on the side and below the bulge. Correspondingly, a higher density stratification is now observed at a depth of 5 m or near the 1022 kg m^{-3} isopycnal, with a freshwater thickness of 3 m (figure 7).

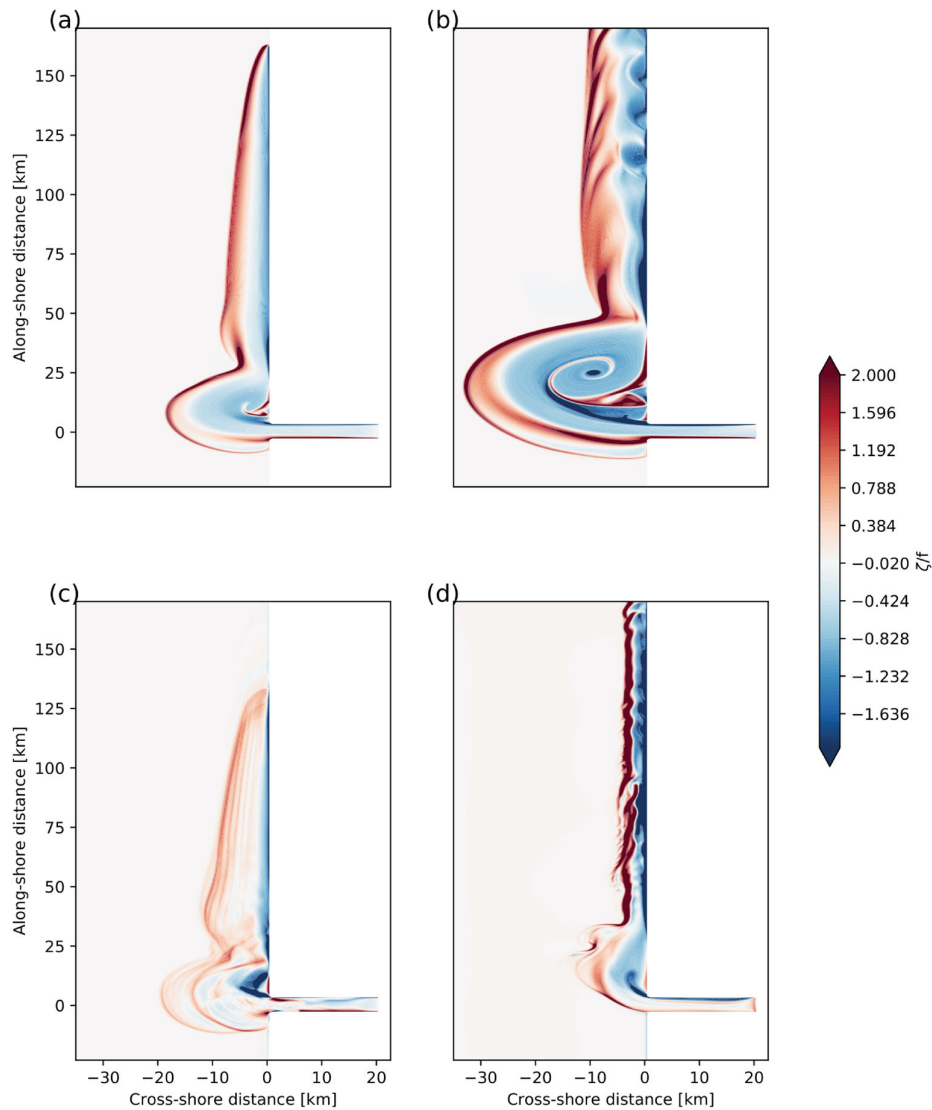


Figure 8. Surface scaled relative vorticity (day 12): (a) Reference, (b) High Discharge, (c) Tide, (d) SW wind. (Colour online)

Again, a near surface peak in vertical buoyancy gradient is related to the surface freshwater recirculation (in the upper meter).

In terms of relative vorticity, intense circulation occurs in the bulge with spiral strips of positive vorticity. This strip detaches from the frictional layer at the coast and wraps into the growing bulge. A thin layer of positive vorticity can again be seen at the edge of the bulge and of the coastal current (in the frontal region with the open sea, see figure 8(b)). Ageostrophic motions ($R_o \sim O(1)$) are present at the edges and within the core of the bulge in the top 5 m. The more intense circulation here leads to larger horizontal and vertical

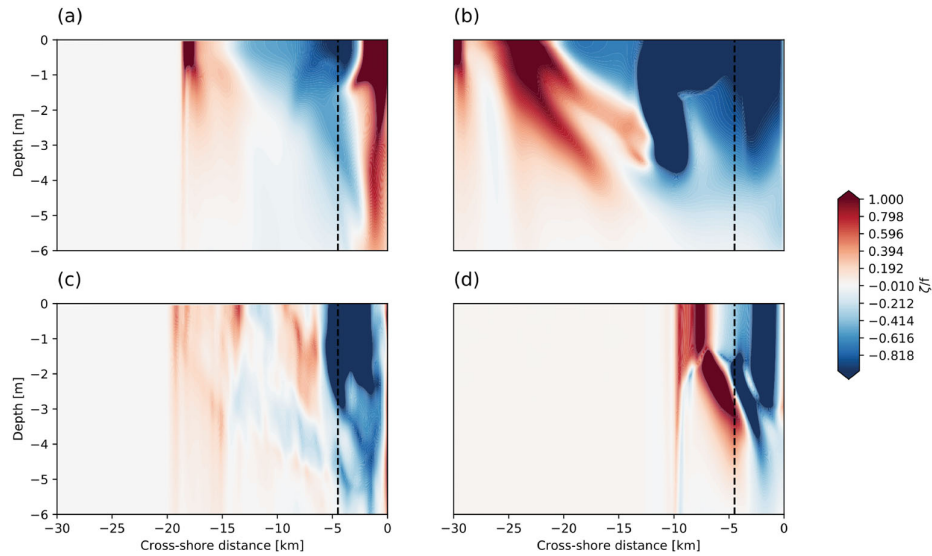
664  A. AYOUCHE ET AL.

Figure 9. Vertical sections of scaled relative vorticity (day 12): (a) Reference, (b) High Discharge, (c) Tide, (d) SW wind. (Colour online)

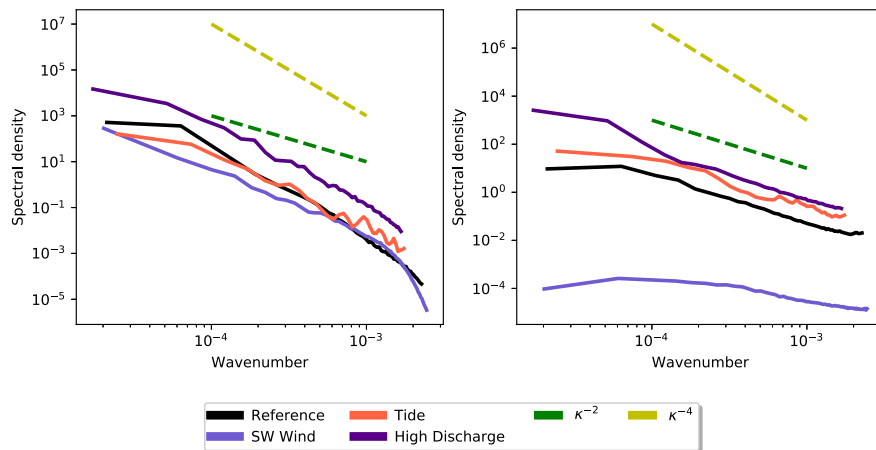


Figure 10. KE density spectrum at the surface (left) and at the river plume base (right). (Colour online)

velocity shears; filamentary instability of the coastal current front and shear instability at the coast, forming a row of small vortices, result from these velocity shears (figure 8(b)).

When forced by SW winds, the river plume grows slowly and weakly with regards to the bulge extension (figure 12).

Indeed, the offshore edge of the bulge reaches barely 5 km by the end of the simulation when the wind intensity is at its highest. The maximum wind intensity reached in our study is $\tau_{\max} = 0.02 \text{ N m}^{-2}$. The wind direction chosen here corresponds to a winter situation (where the ocean is homogeneous) as shown in Le Boyer *et al.* (2013)

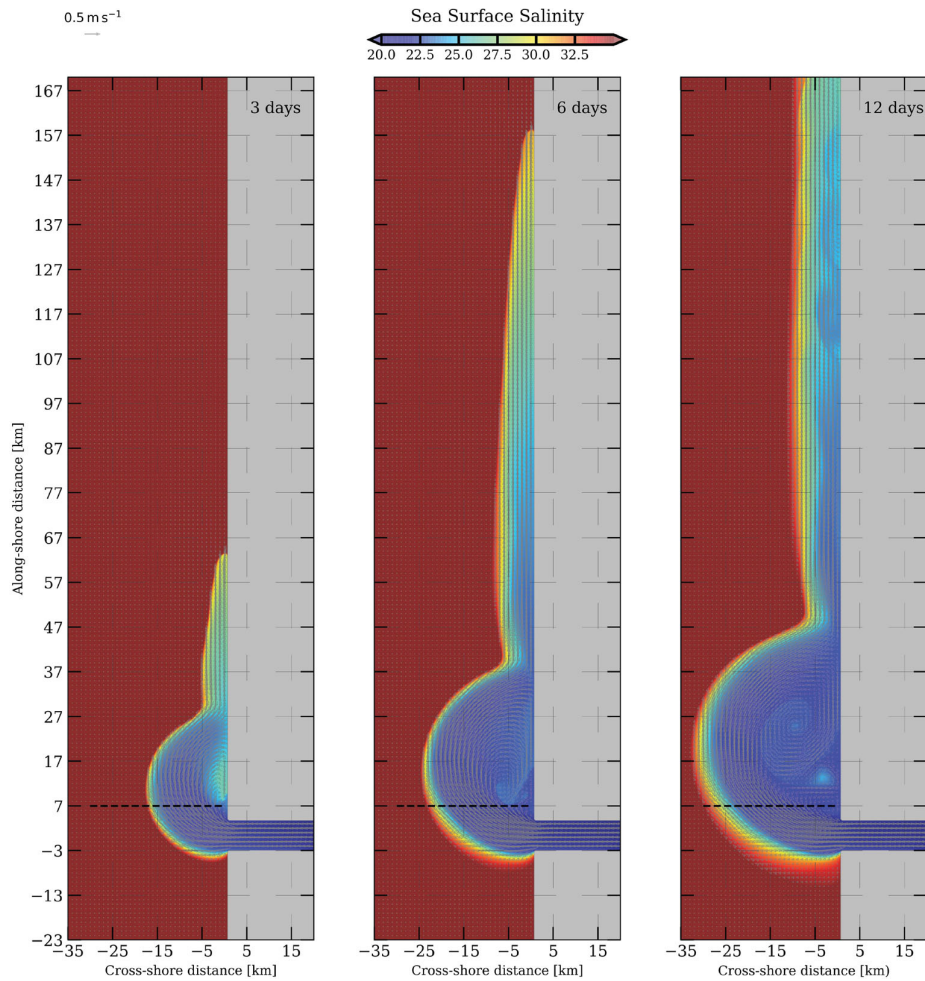


Figure 11. Sea surface salinity at three different time steps – high discharge configuration. The black dashed line represents zonal vertical sections shown hereafter. (Colour online)

(their figure 5). The bulge slowly grows during 8 days before the onset of the wind. After this period, the southeastward Ekman transport promoted by SW winds (winds blowing toward the coast, not alongshore, when Ekman transport is intensified) prevents the bulge from growing more, acting against the river outflow, and pressing the bulge close to the coast. Therefore, this wind direction (SW winds) favours a more intense plume development toward the north and lower salinity values resulting from the plume confinement toward the coast. The coastal current is very thin (less than 3 km wide), patchy and its water is strongly diluted with seawater (salinity values reach 32 psu at kilometre 150 in alongshore distance). In the vertical section of density (at kilometre 7 in alongshore distance), an outcropping can be seen near the coast, as freshwater is pushed to the coast by Ekman transport (figure 6(d)). In terms of relative vorticity, the external frontal region is

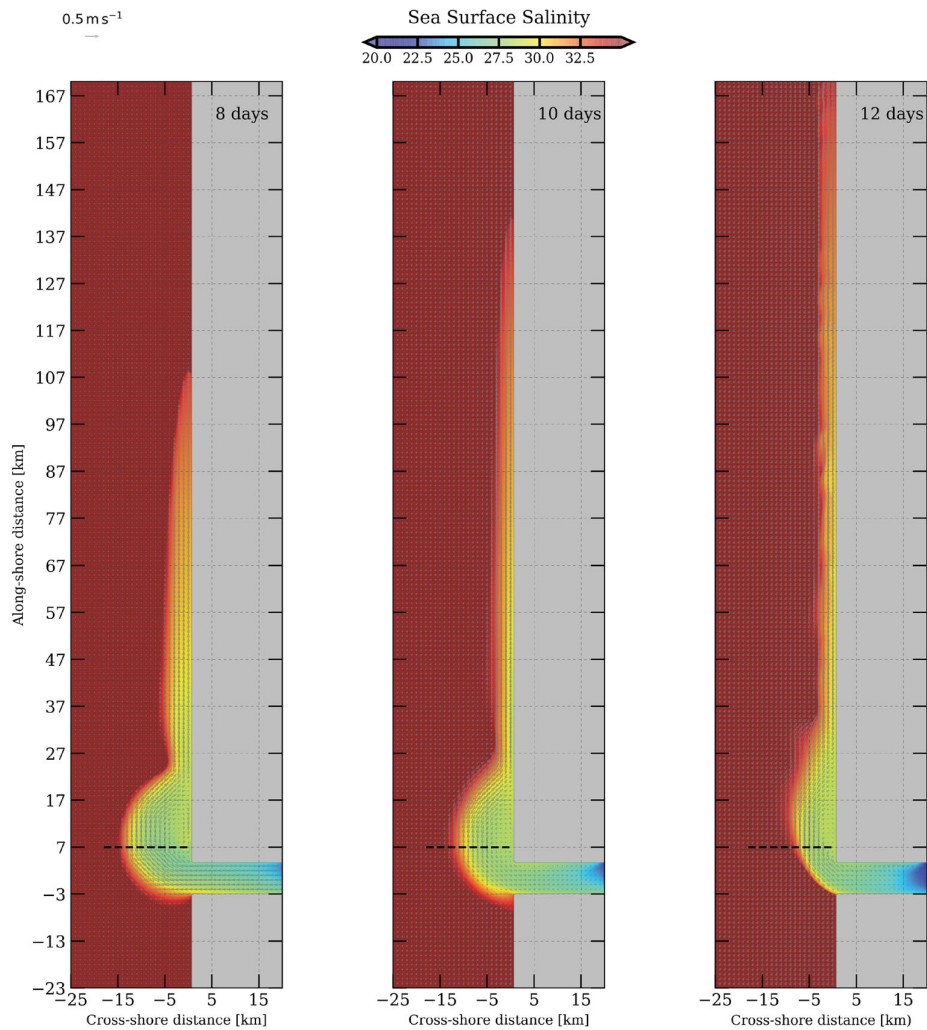
666  A. AYOUCHE ET AL.

Figure 12. Sea surface salinity at three different time steps – SW Wind Configuration. The black dashed line represents zonal vertical sections shown hereafter. (Colour online)

perturbed by short waves (figure 8(d)) so that relative vorticity (or Rossby number) significantly varies around the bulge rim. The coastal current has a jet-like shape (being narrow, it is strongly sheared on both sides), and the features of instability (filaments and meanders) generate local curvature and ageostrophic motions ($R_o \sim O(1)$). Frontal activity (strong ageostrophic motions) can be observed through the river plume vertical structure corresponding to strong local Rossby number on both sides of the jet. Here the front is ~ 1 km wide and frontal activity is constrained by the effective resolution of the model.

When tide acts on the plume, the bulge and coastal current grow through the 12 days of simulation and the bulge finally reaches a width of 15 km. Nevertheless, their spatial

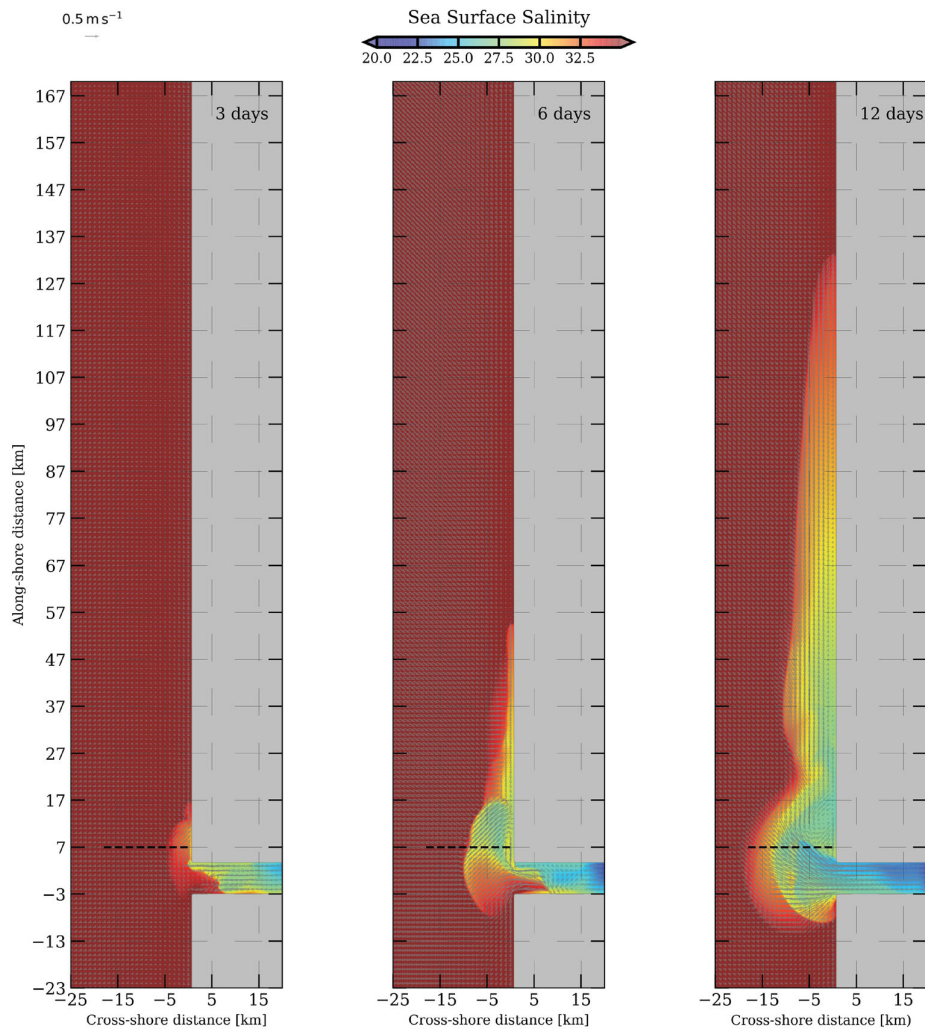


Figure 13. Sea surface salinity at three different time steps – Tide Configuration. The black dashed line represents zonal vertical sections shown hereafter. (Colour online)

structure is complex. Firstly, seawater penetrates into the estuary (see days 3 and 6 in figure 13) when shoreward motion is favoured by the tidal flow.

Secondly, several salinity fronts exist both in the bulge and in the coastal current. They are due to the local concentration of salt by the tidal oscillation (see figure 13). Furthermore, the current oscillation also results in local concentrations of velocity shear, hence of mixing. This results in a succession of increasingly mixed areas seaward, in the whole plume. The vertical density structure of the river plume also shows these oscillations (figure 6(c)). Saltier water is located between the core of the bulge and the coast, again due to the fact that the bulge is fed by bursts of freshwater. In the river plume, the vertical density gradient lies between 2 and 4 m depth and the freshwater thickness is 2 m

(figure 7). Figure 8(c) confirms that several fronts exist in both the bulge and the coastal current; these are locations of strong positive relative vorticity ($R_o \sim O(1)$). These positive vorticity strips are linked to previous tidal pulsations. Highly negative relative vorticity is found at the coast (again due to the velocity shear there) and in the bulge, north of the estuary, close to the coast (again where the current is strongly sheared). The vertical structure of the Rossby number shows different strong scaled vorticity ($R_o \sim O(1)$) in the near field (5 km from the coast and top 3 m) and weak scaled vorticity ($R_o < 1$) in the far field, except along vertical strips, corresponding to the fronts previously mentioned (figure 9(c)).

3.2. River plume instability analysis

3.2.1. Reference configuration

The isopycnic Charney-Stern criterion (CSC) was calculated with the cross-shore Ertel potential vorticity gradient ($\partial_x Q$) at the base of the river plume (remember that the Rossby number is large at the edge of the plume). This gradient changes sign both in the bulge and in the coastal current (figure 14(a)); in the bulge, sign reversals are found both at the external front and near the coast, north of the estuary.

Again, this corresponds to the strong velocity shears previously mentioned. In the coastal current, the sign reversal occurs twice (between the frictional layer at the coast and the jet axis, and between the jet axis and the external front).

Figure 15(a) shows a vertical section of CSC along the zonal section north of the estuary. In the bulge, $\partial_x Q$ changes sign both along and across isopycnals.

In the near field (5 km from the coast), $\partial_x Q$ values are large and change sign mostly along isopycnals. At the bulge periphery, the distribution of $\partial_x Q$ is more filamentary and is weaker with positive and negative values. These elements suggest that barotropic instability is more likely to develop, in particular near the coast. Baroclinic instability is not ruled out but may be weaker.

To investigate the possibility of non-geostrophic instability (symmetric instability or Kelvin-Helmholtz instability), we also examine the distributions of fQ and of the Richardson number R_i (figures 16(a) and 17(a)).

At the river plume base fQ is positive almost everywhere in the river plume except in a narrow region in the coastal current where weak negative values can be observed. At the river plume base, the Richardson number values are $R_i \sim O(1)$ almost everywhere except at the northern edge of the bulge and at the junction between the bulge and the coastal current (R_i higher than 0.25 and lower than 1) (figure 17(a)). This suggests that symmetric instability and vertical shear instabilities are not strong in this case.

Now, we present vertically integrated values from the plume base to the surface of the energy transfers HRS, VRS and VBF when the plume is developed (day 10). We will show that these values are weaker in the reference configuration than in the sensitivity experiments. This is due to the fact that the plume gains energy when forcing is added. The energy of this mean flow can then feed the perturbations.

In this reference configuration, weak positive values for the vertically integrated HRS, VBF and VRS are found in the river plume (figure 18).

Higher HRS and VRS values can be observed in the bulge at the transition near the coast and the estuary. This is due to high and baroclinic fluid acceleration and the bulge recirculation. Positive HRS values can be observed at the southern and northern edges of

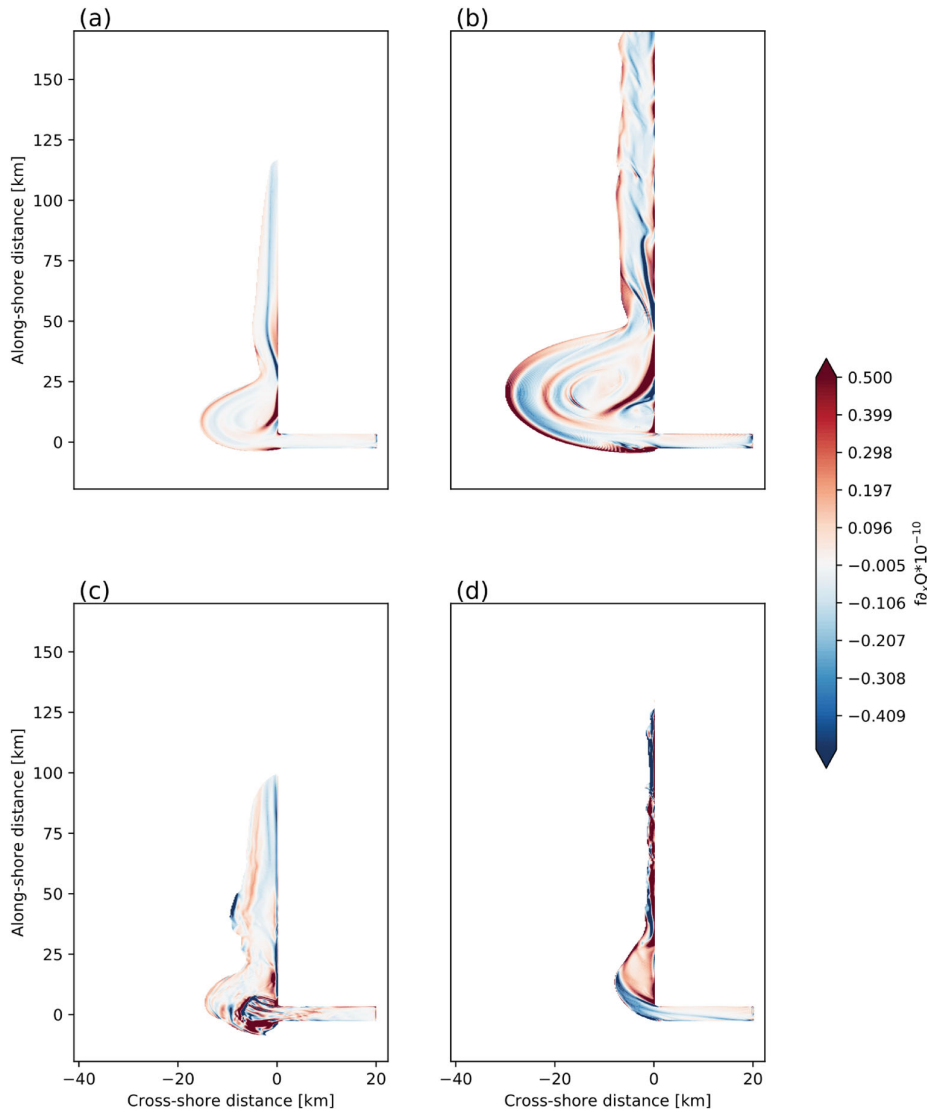


Figure 14. $f_{\partial_x} Q$ at the river plume base (day 12) for (a) Reference, (b) High Discharge, (c) Tide, (d) SW wind. (Colour online)

the bulge, in the recirculation region of this latter and in the coastal current. Both positive and negative values of HRS are concentrated at the edges of freshwater recirculation in the bulge. VBF is concentrated in the periphery of the bulge and in the coastal current. VRS is very small. These results are in agreement with the stability criteria previously examined, showing that barotropic instability is dominant (in particular at the estuary), and baroclinic instability may occur rather at the rim of the bulge but they (instabilities) do not seem to grow significantly.

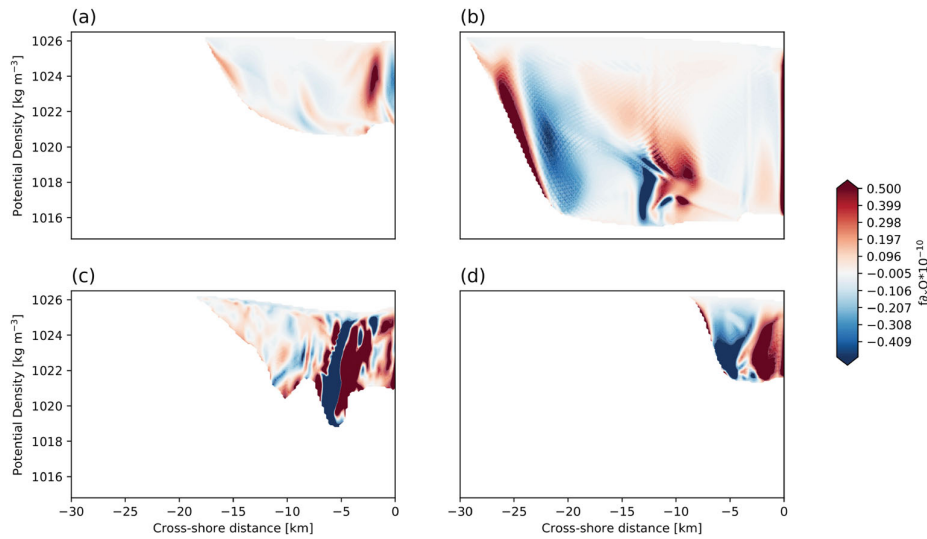
670  A. AYOUCHE ET AL.

Figure 15. Vertical section $f\partial_x Q$ (day 12) for (a) Reference, (b) High Discharge, (c) Tide, (d) SW wind. (Colour online)

3.2.2. Sensitivity experiments

Firstly, we examine the case of a high rate of discharge. At the river plume base, narrow and intense filaments of negative and positive $\partial_x Q$ (cross-shore gradient of isopycnic Ertel potential vorticity) are found all across the bulge and the coastal current (figure 14(b)). The vertical section of this quantity shows that this gradient changes sign both across and along isopycnals inside the bulge and at its edges (figure 15(b)).

At the river plume base, fQ is negative in the coastal current near the coast (figure 16(b)), indicating symmetric instability there. At the western edge of the coastal current, and near its junction with the bulge, the Richardson number ranges from 0.25 to 1, likely related to Kelvin–Helmholtz instability (figure 17(b)). At the rim of the bulge, values of the Richardson number also range in $0.25 < R_i < 1$. The vertical section north of the estuary shows negative values of fQ near the surface of the bulge (figure 19(b)), well correlated with patches of $R_i < 0.25$; patches of low R_i are also found at the base of the bulge (at 3 m depth; see figure 20(b)).

For a high rate of discharge, strong positive HRS, VBF and VRS values are found in the core of the bulge, at its western and/or southwestern edges and in the coastal current (figure 21).

In this latter, HRS is strong near the coast, while VBF and VRS are intense in the northern and external region. In the northern part of the bulge, near the coastal current, negative HRS, VBF and VRS values can be observed. Therefore, barotropic, baroclinic and Kelvin–Helmholtz instabilities develop in the bulge and in the coastal current. This is confirmed in particular by the map of scaled relative vorticity at day 12 showing filaments southwest of the bulge and at the edge of the coastal current and small vortices along the coast, in the coastal current. In this case, vertical shear, horizontal shear (barotropic), symmetric and baroclinic instabilities exist in different regions of the river plume.

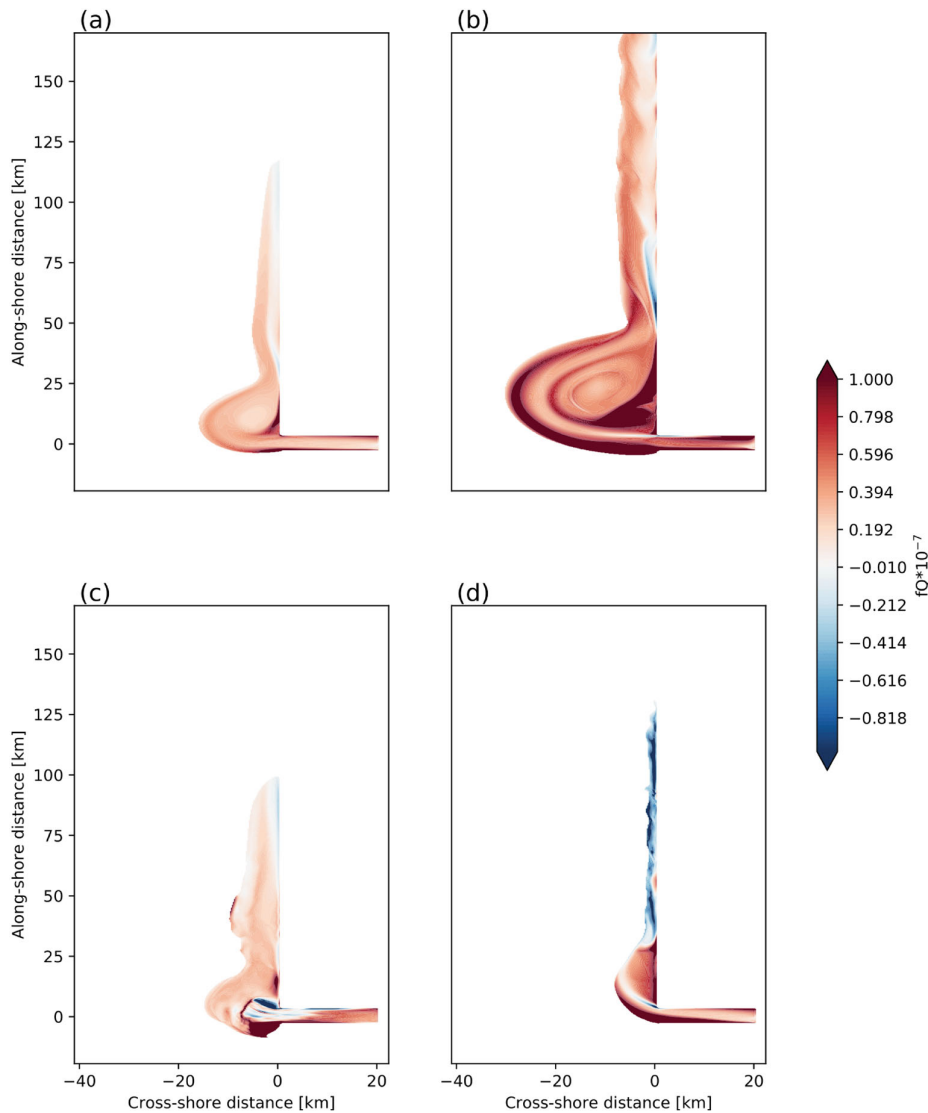


Figure 16. fQ at the river plume base (day 12) for (a) Reference, (b) High discharge, (c) Tide, (d) SW wind. (Colour online)

Under the action of SW winds, the cross-shore potential vorticity gradient changes sign along the river plume base and across isopycnals with intense values near the surface and in the coastal current (figures 14(d) and 15(d)). At the river plume base, fQ is positive in the bulge core while negative values can be observed in the coastal current (figure 16(d)). The Richardson number values range from 0.25 to 1 at the river plume base, especially in the coastal current, at the same locations as negative fQ values (figure 17(d)). The vertical distribution of Richardson Number shows weak values, $R_i < 0.25$, in the upper 2 or 3 m

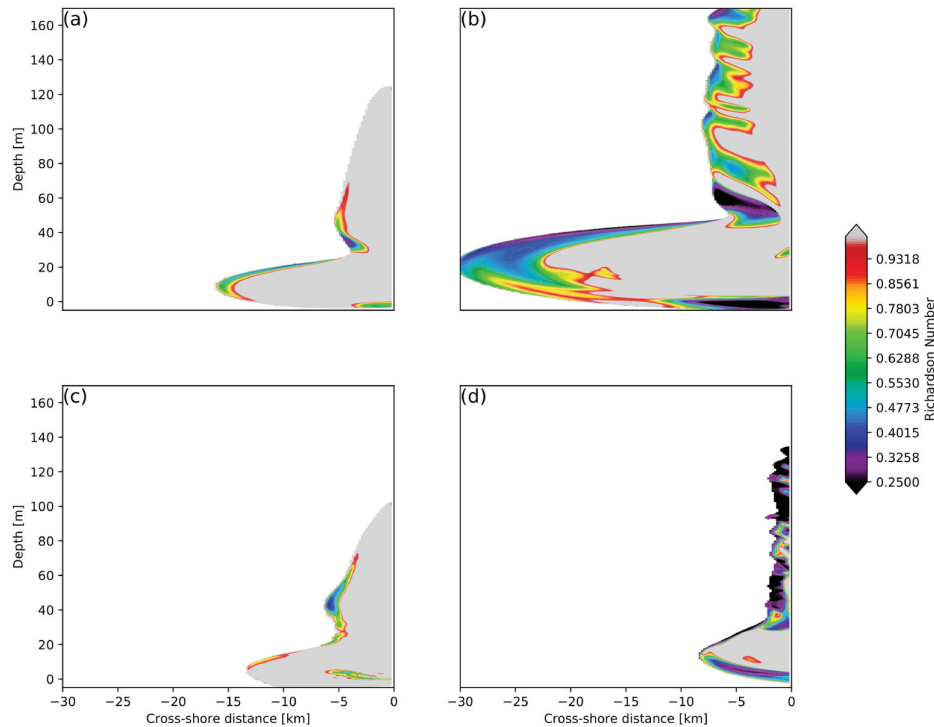
672  A. AYOUCHE ET AL.

Figure 17. Richardson number at the river plume base (day 12) for (a) Reference, (b) High discharge, (c) Tide, (d) SW wind. (Colour online)

of the river plume (figure 20(d)). At the base of the river plume, strong positive values of HRS, VRS and VBF co-exist in the external half of the bulge. In the coastal current, the positive patterns of HRS and of VRS contain small-scale structures (figure 22).

Indeed, the wind induces strong vertical and horizontal velocity shear. Thus, horizontal and vertical shear, baroclinic and symmetric instabilities exist in the river plume far field. They are manifested by short waves, filaments and cusps in the scaled relative vorticity.

When an M2 tidal residual current acts on the plume, the cross-shore potential vorticity gradient changes sign in both regions (bulge and coastal current) but with different intensities at the river plume base (figure 14(c)). Strong values can be observed in the near field and weaker values in the far field. Vertically, it can be seen that the cross-shore potential vorticity gradient in the bulge changes sign across isopycnals, with more intensity in the near field (8 km from the coast; see figure 15(c)). Concerning ageostrophic instabilities, fQ is negative and $0.25 < R_i < 1$, in the near field and along the river plume base (figures 16(c) and 17(c)). The Richardson number is also small at the edge of the plume. Vertically, strong negative fQ values can be observed in the near field, extending through the water column (figure 19(c)). The vertical distribution of the Richardson number in the bulge shows values ranging from 0.25 to 1 in the upper 2 m (figure 20(c)). Therefore, barotropic and baroclinic instabilities may take place in the plume, while Kelvin–Helmholtz is again likely to occur at the plume periphery. In terms of energy transfers, weak positive HRS and strong positive

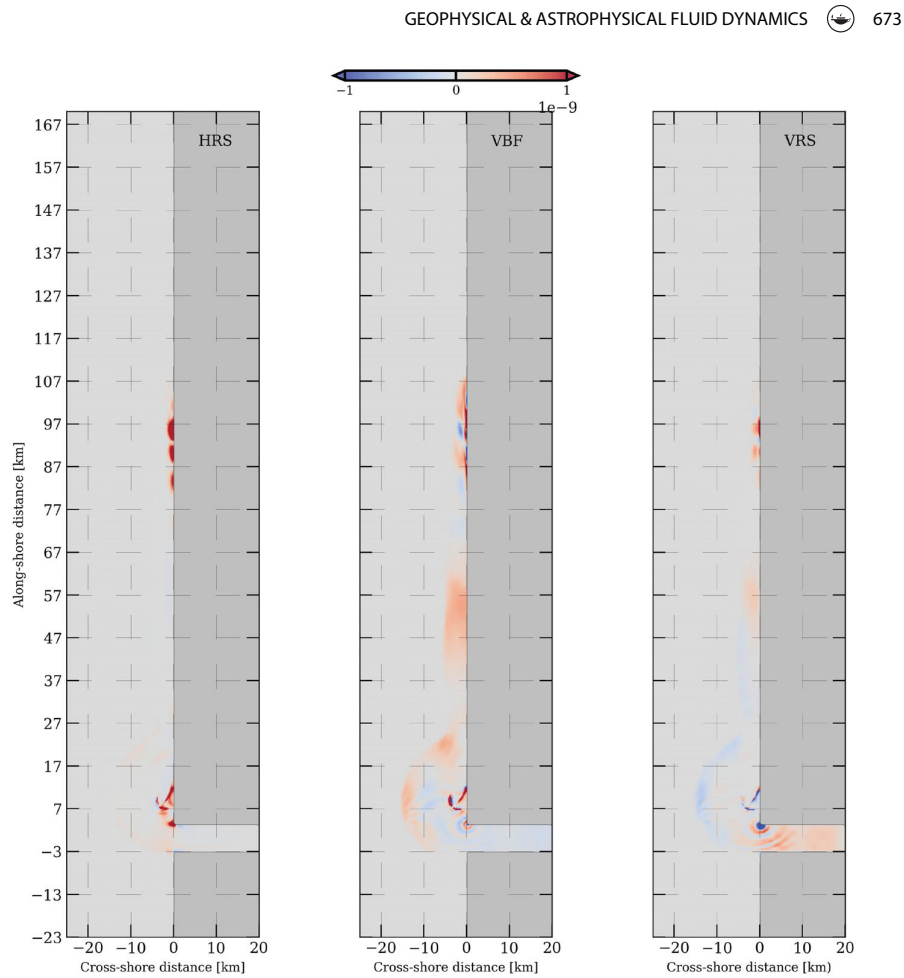


Figure 18. Integrated (from river plume base to surface – day 10) HRS (left), VBF (middle) and VRS (right) for the reference configuration. (Colour online)

VRS and VBF values coexist in the bulge or the near field. Altered positive and negative VRS and VBF values can be seen in the near field because of squeezing and stretching motions due to tidal oscillations (figure 23).

In the coastal current, positive values occur at different locations. Positive HRS values can be observed in the northern edge of the coastal current. The vertical integrated VBF is dominant at the seaward side of the plume in the coastal current region.

3.3. Vertical mixing

In this part, we analyse the processes altering the stratification in the river plume (Ekman transport, frontogenesis, restratification) and their relations with Ertel Potential vorticity (anomaly). Vertical mixing processes (mass and momentum) are estimated from the equation of conservation of Ertel potential vorticity as explained in the Methods section.

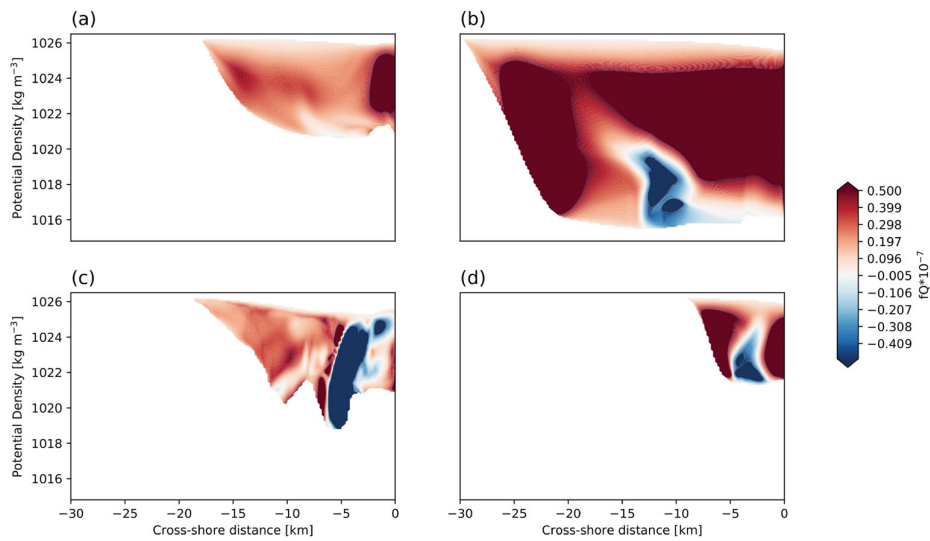
674  A. AYOUCHE ET AL.

Figure 19. Vertical sections (isopycnal) fQ (day 12) for (a) Reference, (b) High Discharge, (c) Tide, (d) SW wind. (Colour online)

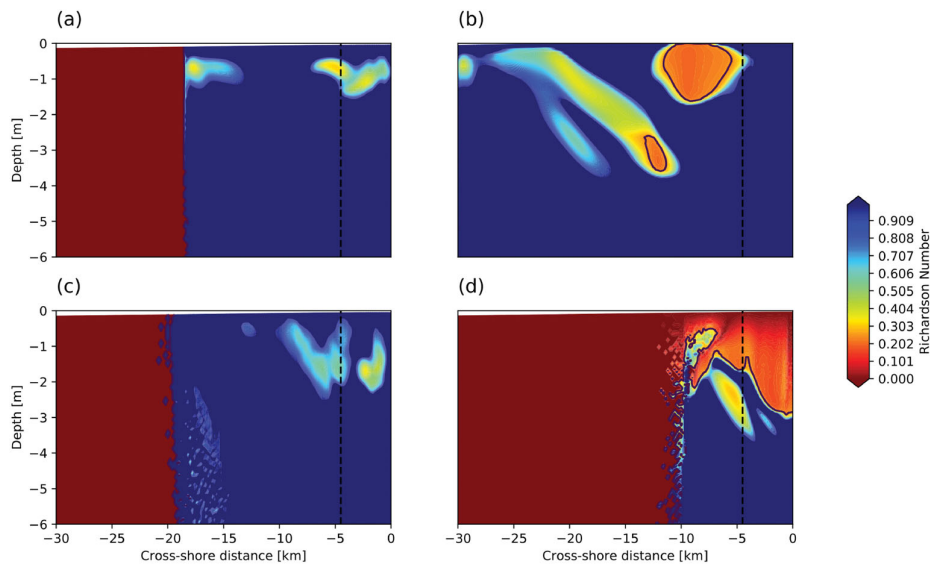


Figure 20. Vertical section Richardson Number (day 12) for (a) Reference, (b) High Discharge, (c) Tide, (d) SW wind. The black solid contour indicates the critical Richardson number $Ri_c = 0.25$. (Colour online)

Ocean mixing is anisotropic and is considered important in the vertical direction. Turbulent mixing can be inherited from vertical mixing in our study but related to a scale decomposition (large scale, mesoscale, submesoscale), which thus differs from the 3D micro-scale turbulence (related to Reynolds decomposition). This turbulent mixing (resulting from

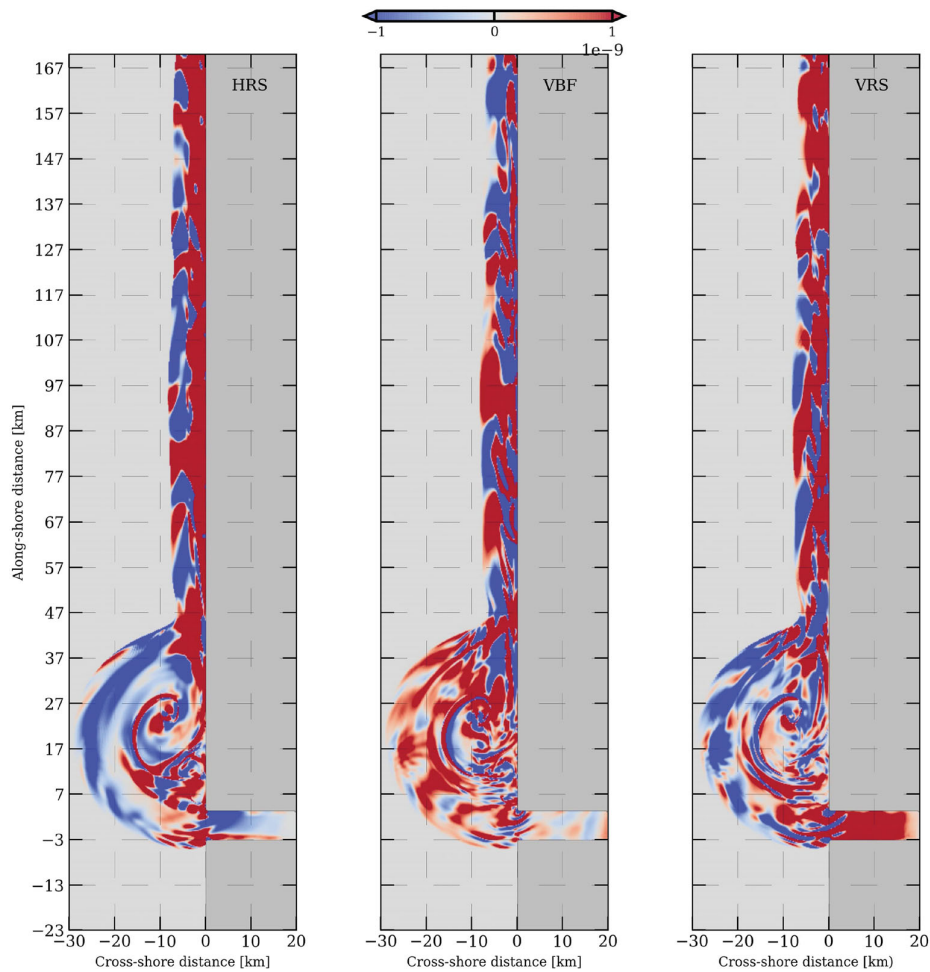


Figure 21. Integrated (from river plume base to surface – day 10) HRS (left), VBF (middle) and VRS (right) for the high discharge configuration. (Colour online)

Reynolds decomposition) is not the subject of this paper and will not be discussed any further as our model does not permit to solve such small-scale processes.

3.3.1. Reference configuration

The variation in river plume stratification, from the base to the surface, is driven by a combination of frontogenesis, and of conservative and non-conservative effects leading to variations of potential vorticity. The contribution of these processes to density variations is different in the various regions of the plume. In the reference case, both effects increase with time at different rates to alter the river plume. During the first 10 days, frontogenesis is the leading process as the river plume settles in the open ocean, and as freshwater first recirculates in the bulge and then forms the coastal current. During this period, frontogenesis dominates over effects altering the potential vorticity distribution (figure 24(a)).

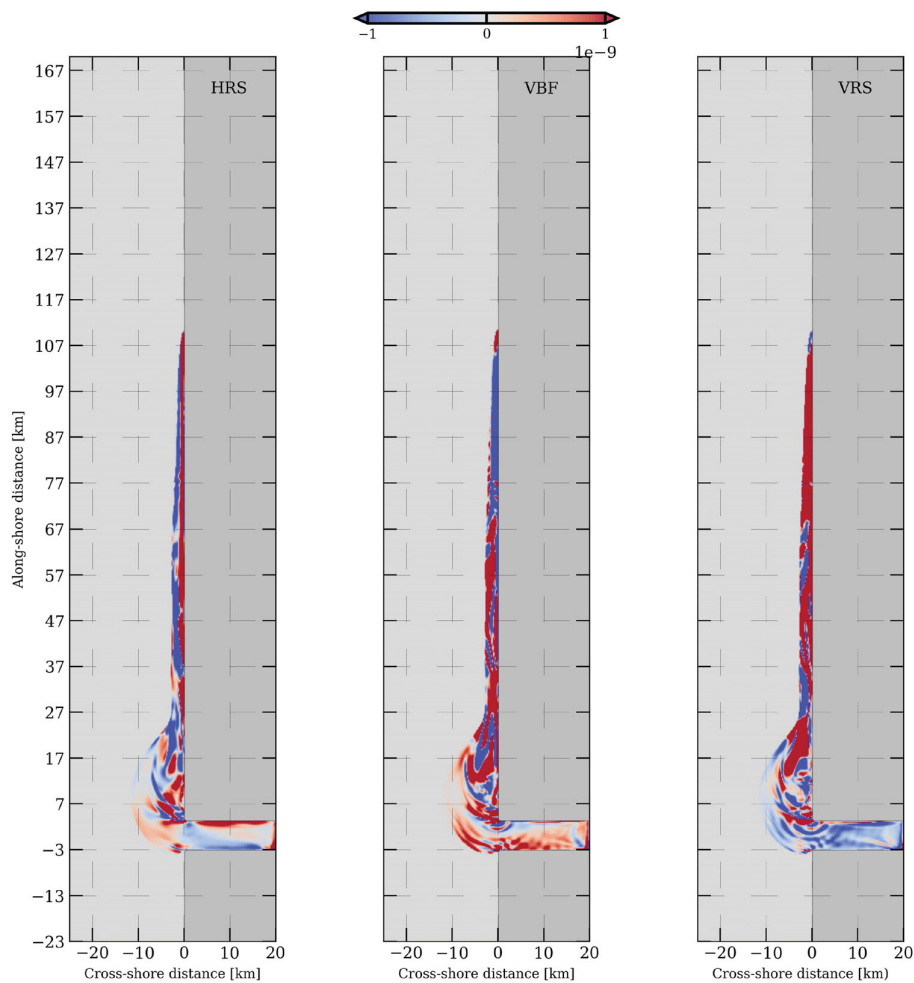


Figure 22. Integrated (from river plume base to surface – day 10) HRS (left), VBF (middle) and VRS (right) for the SW wind configuration. (Colour online)

After this period, the potential vorticity variations overcome the effect of frontogenesis in altering the bulge stratification. This can be related to the complex recirculation of freshwater in the bulge which creates spirals of relative vorticity. The situation is different in the coastal current, where, over the duration of the simulation, frontogenesis remains the leading process (figure 24(e)).

The internal processes altering potential vorticity in the bulge and in the coastal current are evaluated in terms of potential vorticity budget. The contributions of advection, non-conservative processes (frictional and diabatic) and of boundary effects, to the temporal variation of potential vorticity, are examined here in both regions of the river plume (figure 25(a,e)).

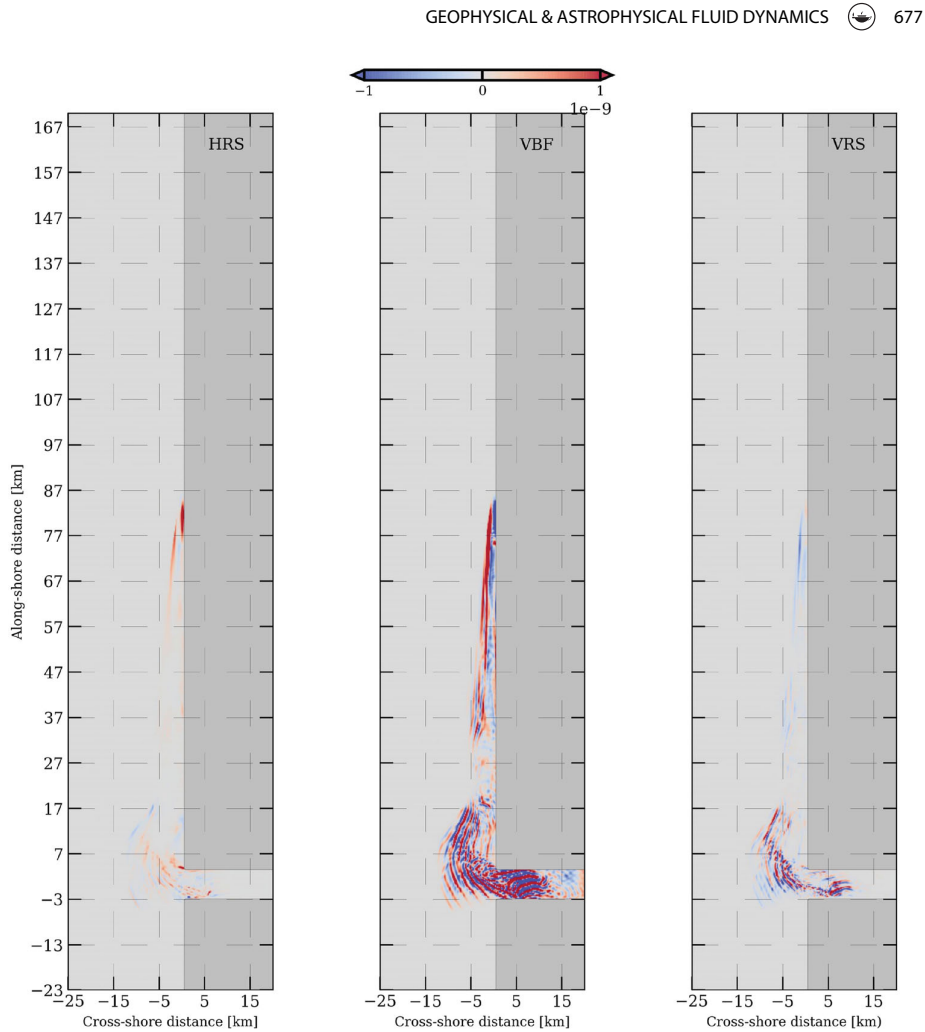


Figure 23. Integrated (from river plume base to surface – day 10) HRS (left), VBF (middle) and VRS (right) for the Tide configuration. (Colour online)

In a general case, frictional processes would be due to the surface wind stress, to unsteady and non-uniform forcings and to geostrophic current shears. In the absence of wind and of tide, the frictional flux of potential vorticity is essentially due to the velocity shear.

In the reference case, non-conservative processes (friction and diabatic mixing) contribute to reduce potential vorticity in the bulge. The frictional flux of potential vorticity is negative and is primarily due to the flow separation observed at early stages of the river plume evolution and to high velocity gradients in frontal region. Another non-conservative process is diabatic mixing which alters the strength of stratification. Here, we observe a buoyancy gain: stratification increases. The boundary value problem (BVP) term closes the budget as the volume of integration is time dependent. The BVP term indicates the advection of potential vorticity in the plume, along the bounding isopycnals.

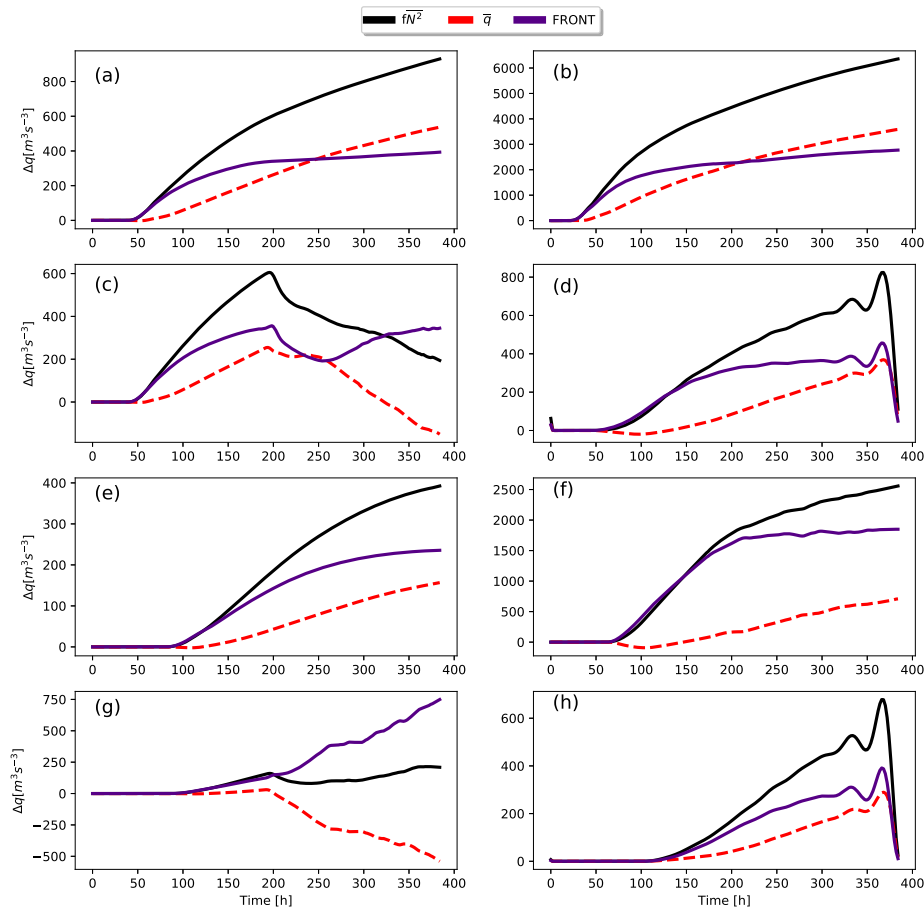


Figure 24. Stratification, frontogenesis and PV anomaly for (a) the Reference, (b) High discharge, (c) SW wind, (d) M2 Tide configurations in the bulge and (e–h) same configurations in the coastal current. (Colour online)

In the reference case, the BVP term balances the non-conservative processes. In the bulge, it dominates the potential vorticity budget. By contrast, in the coastal current, non-conservative processes (among which, friction is chief) tend to reduce/destroy potential vorticity; but friction is balanced by the BVP term.

3.3.2. Sensitivity experiments

In the case of high discharge, the bulge stratification is primarily driven by frontogenesis during the first 8 days of the simulation, then by potential vorticity variations during the last 8 days (figure 24(b),(f)). In the coastal current, frontogenesis is the chief mechanism altering stratification. The order of magnitude of such processes is 10 times higher than in the reference case (moderate discharge). The kinetic energy density spectrum shows a k^{-2} slope at the river plume base, corresponding to frontogenesis processes, and a k^{-3} slope at the surface corresponding to quasi geostrophy (figure 10). The internal processes

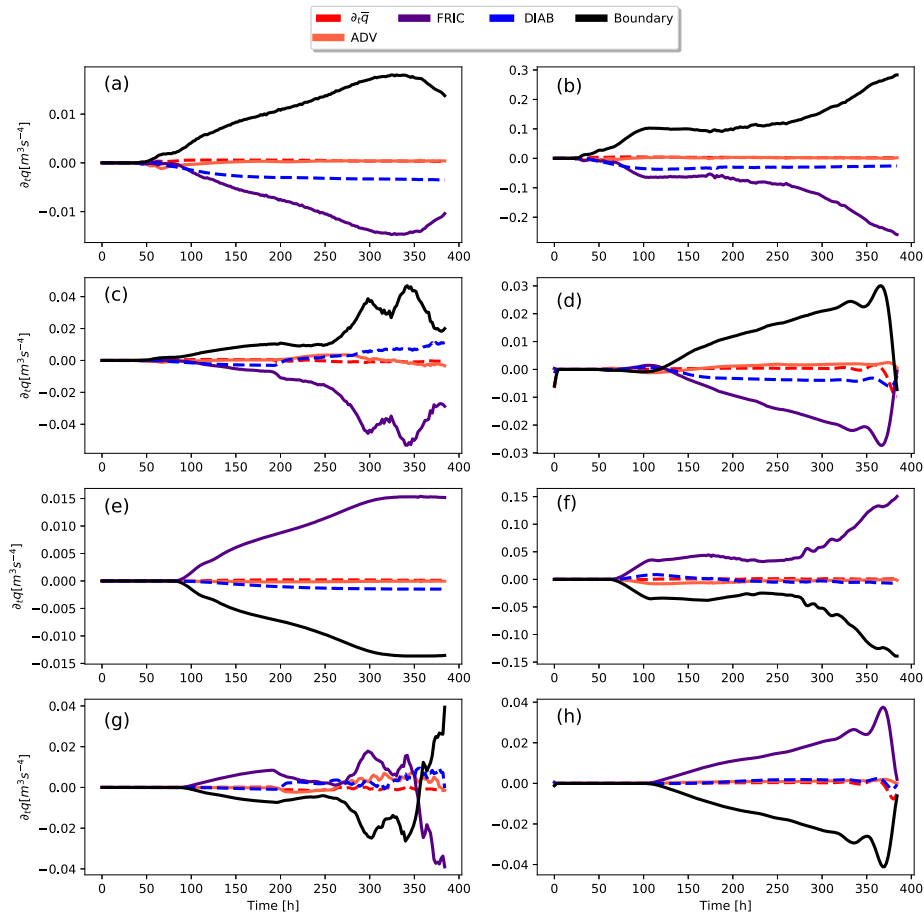


Figure 25. Pv flux terms for (a) the Reference, (b) High discharge, (c) SW wind, (d) M2 Tide configurations in the bulge and for (e–h) same configurations in the coastal current. (Colour online)

modifying potential vorticity in both the bulge and the coastal current, are also dominated by advection and mixing. Results comparable to those in the reference case are observed but with higher magnitude (figure 25(b,f)).

In the case of SW winds, stratification decreases after 8 days as does potential vorticity in the near field region while frontogenesis increases due to the mixing induced by winds (figure 24(c,g)). Meanwhile, in the coastal current, even with the presence of strong stratification, potential vorticity decreases while frontogenetic processes dominate over the integration time. A k^{-2} slope characterises the kinetic energy spectrum at the surface and the river plume base which indicates the importance of frontogenesis in this case (figure 10).

Different processes can be distinguished for potential vorticity removal from or injection into the ocean interior (figure 25(c,g)). In the bulge, discharge and SW winds interact resulting in a negative diabatic potential vorticity flux, and a positive frictional flux. The

negative diabatic flux indicates a surface buoyancy loss especially at the surface. Non-conservative processes are balanced by the BVP term. Interior potential vorticity variations are related to advection and the related shear. In the coastal current, a similar result is obtained as interior potential vorticity variations are governed by advective and shear processes. At the surface, friction plays an important role in potential vorticity removal in the coastal current.

When tides are taken into account, the variations in stratification are dominated by frontogenetic processes in both the bulge and the coastal current, over the entire simulation period (figure 24(d,h)). This latter diagnostic agrees with the k^{-2} kinetic energy spectrum slope at the surface and at the river plume base (figure 10). In both river plume regions, the dominant process in the potential vorticity budget is advection and shear (figure 25(d,h)). In particular, stretching or squeezing of the water column and shear flows are generated by tidal oscillations. At the surface, friction plays an important role in the bulge, where vertical mixing of momentum is more intense.

4. Discussion

4.1. River plume hydrology and dynamics

In this paper, we studied the 3D structure and stability of a river plume. We addressed the impact of different forcings (discharge, wind and tide) on the plume (geostrophic or ageostrophic) dynamics.

Firstly, we observe the formation of an anticyclonic recirculating gyre (the bulge) once the freshwater enters the salty open ocean. In the absence of external forcings, the bulge grows in time, extending offshore. The bulge growth was considered by Nof and Pichevin (2001) or by Isobe (2005) as a ballooning effect due to the inertial recirculation. In the case of high discharge, its width and thickness increase significantly, due in part to the higher inflow velocities leading to instability at the edge of the bulge. In this frontal region, a layer with Rossby number $O(1)$ indicates the presence of ageostrophic motions (McWilliams 1984, Voropayev and Filippov 1985). Spiraling filaments, with $O(1)$ Rossby number and ageostrophic motions, then grow in the bulge core. Both the frontal region and the filaments grow when increasing the discharge. These filaments are due to the inner recirculation of bulge waters with different densities (different salinities). Indeed some of these waters have started mixing with seawater, while others are original estuarine waters. The dynamical adjustment of the bulge is associated with intensifying relative vorticity due to the continuous discharge (Spall and Price 1998). The simulated and idealised Gironde river plume in our study is similar to previous realistic studies in the Bay of Biscay regarding its radius (bulge radius) and freshwater thickness (Costoya *et al.* 2017).

A spatially uniform SW wind generates an Ekman transport which constrains the bulge to the coast; also the freshwater deepens near the coast, increasing the stratification (Fong and Geyer 2001, Lentz and Largier 2006). In the small bulge interior, strong ageostrophic motions are due to intense kinetic energy input; vertical vorticity and surface buoyancy fluxes are induced by the down front wind (Oort *et al.* 1994).

In the presence of a residual circulation of a M2 tide, the offshore growth of the bulge reaches an equilibrium between the influence of the tidal oscillations, and of the river discharge. The result is similar to that of Isobe (2005), who discussed the ballooning of the

bulge and its stabilisation by tidal currents. Strong ageostrophic motions, near the estuary mouth, are due to periodic deformation (by flow and ebb) and to fluid column stretching and squeezing. This has been discussed in Maccready *et al.* (2002) using a conceptual model, and in Halverson and Pawlowicz (2008) using satellite imagery and *in situ* observations. They showed that turbulence remains close to the estuary mouth, for a river plume subject to tides during winter (well-mixed conditions).

Secondly, after few inertial periods a coastal current develops. In the absence of external forcings, the coastal current progresses to the north; it usually has half of the bulge width. This current grows with the unstable bulge as discussed in Horner-Devine (2009). The plume dynamics is geostrophic except at its external front (and sometimes along the coast) where strong ageostrophic motions can be observed (Yankovsky and Chapman 1997). In the case of downwelling favourable wind, the coastal current width is similar to the bulge width; this corresponds to an increase of northward freshwater transport (Chao 1987, 1988). As such a wind blows, the streamlines gets closer, due to Ekman transport, and the fluid is accelerated as a jet-like flow. This gives rise to strong ageostrophic circulation ($R_o \sim O(1)$) in the frontal region (as explained in Thomas and Lee 2005; and in Choi and Wilkin 2007). When a tidal current is present, the coastal current is similar in shape and width to that in the reference case (case of moderate discharge). The coastal current is then in geostrophic balance (see also the studies by Guo and Valle-Levinson 2007, Hunter *et al.* 2010, Lai *et al.* 2016).

When we vary the parameters and physical effects acting on the plume, its modelled structure and dynamics evolves from that of the Gironde, to those of the Hudson and Columbia rivers (Hickey *et al.* 1998, Chant *et al.* 2008, Horner-Devine 2009).

4.2. River plume instabilities

To analyse the possible existence of plume instabilities (barotropic, baroclinic, Kelvin–Helmholtz, symmetric instabilities), we computed the energy transfer terms (HRS, VRS, VBF) from the eddy kinetic budget and the Rayleigh–Kuo, Charney–Stern and Hoskins criteria based on Ertel potential vorticity in isopycnic coordinates; we also evaluated the Richardson number. The use of isopycnic Ertel potential vorticity in this study is motivated by the need to adequately describe submesoscale and ageostrophic motions. Ertel potential vorticity differs from the quasi-geostrophic potential vorticity which is used for mesoscale dynamics studies (Rhines and Schopp 1991, Marshall and Adcroft 2010). Indeed the quasi-geostrophic approximation fails in frontal regions (regions of strong salinity/density gradients) and for intense motions (when R_o is $O(1)$).

We have shown the existence of different instabilities in the river plume. In the reference case (moderate discharge), instabilities are slowly growing. Increasing the river discharge intensifies instabilities. Using the Hoskins and Richardson number criteria, we have shown that symmetric instabilities develop near the surface in the bulge and in the coastal current. These instabilities coexist with baroclinic instability near the front, in particular in the bulge and with barotropic instability near the coast. At the northern edge of the coastal current, vertical shear and baroclinic instabilities coexist, as in the Mississippi river plume during periods of weak forcing (Hetland 2017). Symmetric instability will be replaced by baroclinic or barotropic ones when the Richardson number R_i is $O(1)$. Kelvin–Helmholtz

instability can play a stabilising role to symmetric instabilities, as shown via linear analysis in the Stone model (Stone 1966, Stamper and Taylor 2016).

In the case of SW winds (down-front winds), the wind induced shear and the flow shear give rise to all instabilities (barotropic, baroclinic, symmetric and Kelvin–Helmholtz) in the coastal current and in the small bulge. Winds aligned with the frontal velocity lead to frontal symmetric instability as suggested by D’Asaro *et al.* (2011). In this case, downfront winds catalyse energy release from the front to the surrounding turbulence. Baroclinic instability in the presence of downfront winds was previously shown by de Kok (1997), using a two-layer model. Baroclinically unstable conditions occur as the result of vertical velocity shear; this instability gives rise to frontal meanders with wavelengths between 18 and 30 km.

Finally, M2 Tides contribute to the rise of symmetric, barotropic and baroclinic instabilities in the near field region subject to intense turbulence. These instabilities can be due to the symmetrically unstable tidal front; this front becomes baroclinically and barotropically unstable near the estuary mouth. This result agrees with the results of the studies by Brink (2012, 2013). They show, using idealised simulations, that the existence of symmetric instabilities in tidal front is due to the sharpness of this latter and a well-mixed bottom boundary layer under the front. The growth of baroclinic instability in tidal fronts depends on bottom friction and topography slope.

Thus, during a typical winter, the Gironde river plume may undergo different instabilities but external forcings then play an important role. Yelekci (2017) showed, using realistic simulations, that baroclinic instabilities are dominant in the Gironde river plume, in winter. She attributed this instability to surface cooling which releases available potential energy leading to the deepening of the mixed layer depth.

4.3. River plume vertical mixing

Then the weakening or strengthening of the river plume have been investigated. Diapycnal or vertical mixing have been analysed via potential vorticity budget.

Firstly, we showed that frontogenesis and potential vorticity variations are important in altering the stratification. In the reference case (moderate discharge), the frontogenetic processes are important in the coastal current; they are induced by high strain at the edges of this latter. In the bulge, both frontogenetic and shear processes are important; potential vorticity variations are the strongest near the end of the simulation (about 10 days). A similar analysis (though with an order of magnitude stronger) was obtained for the high discharge case, except in the bulge, where potential vorticity variations overcome frontogenesis after 8 days. In the absence of wind stress and of tides, the frontogenesis contribution comes from the frontal region where high salinity gradients and ageostrophic motions are observed. In the absence of external forcings, the energy distribution is similar to that of quasi-geostrophic turbulence, in the bulge core at the surface, while ageostrophic effects dominate at the river plume base.

In the presence of down-front winds, the wind shear stress triggers frontogenetic process near the surface. In the small bulge, a submesoscale regime prevails. The downfront wind erodes potential vorticity while the frontogenetic processes induced by wind are important in both regions and particularly in the coastal current. In the presence of a residual tidal circulation, frontogenetic processes drive the changes in stratification in the whole river

plume. This agrees with the k^{-2} slope in energy spectrum, both at the bulge surface and base, in relation with submesoscale motions.

Secondly, we showed that the interior potential vorticity variations are controlled by differential advection. The Haynes and McIntyre impermeability theorem states that a balance is reached between non-conservative fluxes and the boundary value term (at bounding isopycnals). At the surface, velocity shear due to flow separation at the edges of the estuary, and friction related to vertical mixing of momentum in frontal regions are dominant. This explains the decay of potential vorticity in the coastal current in the presence of downwelling favourable winds. Indeed, stratification is altered by mixing associated with baroclinic instability and frontogenetic processes. Many atmospheric studies (Hoskins and Pedder 1980, Branscome *et al.* 1989, Barry *et al.* 2000) and oceanic studies (Lapeyre *et al.* 2006, Thomas and Ferrari 2008), in settings similar to ours, have shown similar results. Potential vorticity destruction by down-front winds has been analysed in Thomas (2005); they show that potential vorticity erosion is due to frictionless mixing. Frontogenetic processes are important at the edges of the plume, where strong cyclonic vorticity dominates. Therefore, we associate the cyclonic submesoscale ageostrophic circulation developed in the frontal region to frontogenetic processes induced by wind stirring or to shear and strained flow in general.

When tidal currents are present, ageostrophic motions dominate in the near field of the river plume subject to frontogenetic processes. These processes are key for restratification especially in tidal fronts. When strong tides act near the mouth of the Columbia River, sharp density and velocity fronts appear at the edges of the freshwater plume and perpendicularly to the coast; they result from frontogenetic processes during ebb tide cycles (Akan *et al.* 2017).

Frontogenesis in our study may also be compared to atmospheric straining at different levels of the atmosphere (Haynes and Shuckburgh 2000, Laïné *et al.* 2011).

5. Summary

The short time evolution of a Gironde-like river plume has been investigated. Idealised 3D numerical simulations have highlighted the dynamics of the river plume, and its instabilities. The bulge (the recirculating anticyclonic gyre) keeps growing in time in the absence of external forcings. This growth is limited by M2 tides and it is suppressed by downfront winds (southwesterly winds). After a few inertial periods, the coastal current is advected to the north with half of the bulge's width in the reference, high discharge and tidal forcing cases. In a system driven by downfront winds, the coastal current is the dominant feature with a jet-like outflow structure. The river plume dynamics is mainly geostrophically balanced except at the edges of the bulge and the coastal current (regions of strong salinity gradients) where ageostrophic motions are dominant.

The existence of numerous instabilities in different configurations has been highlighted. The (co)existence of baroclinic, barotropic, vertical shear instabilities and symmetric instabilities, with different combinations, is observed in the cases of high discharge and of downwelling favourable winds. Symmetric, baroclinic and barotropic instabilities co-exist in the near field region (close to the estuary mouth), in M2 tide case. The nature of these instabilities can be different in the frontal region where ageostrophic motions are important.

684  A. AYOUCHE ET AL.

The stratification variations are due to potential vorticity advective mixing and frontogenetic processes. Frontogenetic processes can be dominant in cases of wind forcing or of tides but in different regions (far-field (wind forcing), near field (tidal forcing)). In the case of moderate or high discharge without any external forcings, both processes are important in the bulge, but in the far-field region, frontogenesis dominates largely.

Other effects can impact the geostrophic and ageostrophic dynamics and the mixing in a river plume. For example, turbulence in the ocean outside the plume, or the morphology of the estuary (as shown in Pimenta *et al.* 2011) or bottom friction (which can damp the development of instabilities – Brink 2013, Hetland 2017), can contribute to the river plume dynamics. They will be considered in a sequel of this study, with realistic numerical simulations.

Investigating the river plume dynamics at fine scales (with 200 m horizontal resolution) has shown the development of different instabilities, in various parts of the plume, and their sensitivity to external forcings. The vertical mixing in the river plume appears as resulting from a complex combination of frontogenesis and of non-conservative effects leading to variations of potential vorticity. These findings will be used in our next study to validate a realistic numerical simulation of the Gironde river plume in the Bay of Biscay, and to understand its instabilities and the vertical mixing affecting it.

Acknowledgments

This study is part of the COCTO project (SWOT science team program) funded by the CNES. The PhD Thesis of A. Ayouche is funded by Brittany region and Ifremer. Model simulations were carried out with GENCI (French National High-Performance Computing Organization) computational resources administered at the CINES (National Computing Center for Higher Education). The authors thank Bernard Le Cann and Robert Hetland for their fruitful advices and discussions. The authors thank Sabine Schmidt for providing the MAGEST *in situ* observations. MAGEST Verdon station was part of the DIAGIR project. The authors thank the two anonymous referees for their insightful and thoughtful comments.

Disclosure statement

No potential conflict of interest was reported by the author(s).

Funding

This study is part of the COCTO project (SWOT science team program) funded by the CNES. The PhD Thesis of A. Ayouche is funded by Brittany region and Ifremer.

ORCID

Guillaume Charria  <http://orcid.org/0000-0001-5204-1654>

References

- Akan, C., Moghimi, S., Ozkan-Haller, H.T., Osborne, J. and Kurapov, A., On the dynamics of the mouth of the Columbia river: Results from a three-dimensional fully coupled wave-current interaction model. *J. Geophys. Res. Oceans* 2017, **122**, 5218–5236.
- Avicola, G. and Huq, P., Scaling analysis for the interaction between a buoyant coastal current and the continental shelf: Experiments and observations. *J. Phys. Oceanogr.* 2002, **32**, 3233–3248.

- Barry, L., Craig, G. and Thuburn, J., A GCM investigation into the nature of baroclinic adjustment. *J. Atmos. Sci.* **2000**, *57*, 1141–1155.
- Botas, J., Fernández, E., Bode, A. and Anadón, R., A persistent upwelling off the Central Cantabrian Coast (Bay of Biscay). *Estuar. Coast. Shelf Sci.* **1990**, *30*, 185–199.
- Branscome, L., Gutowski, W. and Stewart, D., Effect of surface fluxes on the nonlinear development of baroclinic waves. *J. Atmos. Sci.* **1989**, *46*, 460–475.
- Brink, K., Baroclinic instability of an idealized tidal mixing front. *J. Marine Res.* **2012**, *70*, 661–688.
- Brink, K., Instability of a tidal mixing front in the presence of realistic tides and mixing. *J. Marine Res.* **2013**, *71*, 227–252.
- Caballero, A., Ferrer, L., Rubio, A., Charria, G., Taylor, B.H. and Grima, N., Monitoring of a quasi-stationary eddy in the Bay of Biscay by means of satellite, in situ and model results. *Deep-Sea Res. Pt. II-Top. Stud. Oceanogr.* **2014**, *106*, 23–37. Oceanography of the Bay of Biscay.
- Callendar, W., Klymak, J.M. and Foreman, M.G.G., Tidal generation of large sub-mesoscale eddy dipoles. *Ocean Sci.* **2011**, *7*, 487–502.
- Capuano, T., Sabrina, S., Xavier, C. and Blanke, B., Mesoscale and submesoscale processes in the Southeast Atlantic and their impact on the regional thermohaline structure. *J. Geophys. Res. Oceans* **2018**, *123*, 1937–1961.
- Castaing, P., Courantologie de dérive dans les zones côtières à l'aide de bouées positionnées par satellite (Système ARGOS), in *Proceedings of XVIIIème Journées de l'hydraulique. Marseille*, 1984, pp. I.4.1–I.4.8.
- Chant, R., Wilkin, J., Zhang, W., Choi, B.J., Hunter, E., Castelao, R., Glenn, S., Jurisa, J., Schofield, O., Houghton, R., Kohut, J., Frazer, T. and Moline, M., Dispersal of the Hudson river plume in the New York Bight: Synthesis of observational and numerical studies during LaTTE. *Biol. Sci.* **2008**, *21*, 148–161.
- Chao, S.Y., Wind-driven motion near inner shelf fronts. *J. Geophys. Res. Oceans* **1987**, *92*, 3849–3860.
- Chao, S.Y., Wind-driven motion of estuarine plumes. *J. Phys. Oceanogr.* **1988**, *18*, 1144–1166.
- Chapman, D.C., Numerical treatment of cross-shelf open boundaries in a barotropic coastal ocean model. *J. Phys. Oceanogr.* **1985**, *15*, 1060–1075.
- Charria, G., Lazure, P., Cann, B.L., Serpette, A., Reverdin, G., Louazel, S., Batifoulier, F., Dumas, F., Pichon, A. and Morel, Y., Surface layer circulation derived from Lagrangian drifters in the Bay of Biscay. *J. Marine Syst.* **2013**, *109–110*, S60–S76. XII International Symposium on Oceanography of the Bay of Biscay.
- Choi, B.J. and Wilkin, J.L., The effect of wind on the dispersal of the Hudson river plume. *J. Phys. Oceanogr.* **2007**, *37*, 1878–1897.
- Costoya, X., Fernández-Nóvoa, D. and Gómez-Gesteira, M., Loire and Gironde turbid plumes: Characterization and influence on thermohaline properties. *J. Sea Res.* **2017**, *130*, 7–16. Changing Ecosystems in the Bay of Biscay: Natural and Anthropogenic Effects.
- D'Asaro, E., Lee, C., Rainville, L., Harcourt, R. and Thomas, L., Enhanced turbulence and energy dissipation at ocean fronts. *Science* **2011**, *332*, 318–322.
- de Kok, J., Baroclinic eddy formation in a Rhine plume model. *J. Marine Syst.* **1997**, *12*, 35–52.
- Debreu, L., Marchesiello, P., Penven, P. and Cambon, G., Two-way nesting in split-explicit ocean models: algorithms, implementation and validation. *Ocean Model.* **2012**, *s 49–50*, 1–21.
- Ertel, H., Ein neuer hydrodynamischer Erhaltungssatz. *Naturwissenschaften* **1942**, *30*, 543–544.
- Evans Contreras, M., Pizarro, O., Dewitte, B., Sepúlveda, H. and Renault, L., Subsurface mesoscale eddy generation in the ocean off central Chile. *J. Geophys. Res. Oceans* **2019**, *124*, 5700–5722.
- Fong, D.A. and Geyer, W.R., Response of a river plume during an upwelling favorable wind event. *J. Geophys. Res. Oceans* **2001**, *106*, 1067–1084.
- Garvine, R.W., Penetration of buoyant coastal discharge onto the continental shelf: A numerical model experiment. *J. Phys. Oceanogr.* **1999**, *29*, 1892–1909.
- Gohin, F., Annual cycles of chlorophyll-a, non-algal suspended particulate matter, and turbidity observed from space and in-situ incoastal waters. *Ocean Sci.* **2011**, *7*, 705–732.
- Gröbelbauer, H.P., Fanneløp, T.K. and Britter, R.E., The propagation of intrusion fronts of high density ratios. *J. Fluid Mech.* **1993**, *250*, 669–687.

- Gula, J., Molemaker, M. and McWilliams, J., Topographic generation of submesoscale centrifugal instability and energy dissipation. *Nat. Commun.* **2016**, *7*, 12811.
- Guo, X. and Valle-Levinson, A., Tidal effects on estuarine circulation and outflow plume in the Chesapeake Bay. *Cont. Shelf Res.* **2007**, *27*, 20–42.
- Halverson, M.J. and Pawlowicz, R., Estuarine forcing of a river plume by river flow and tides. *J. Geophys. Res. Oceans* **2008**, *113*, C09033.
- Haynes, P. and Shuckburgh, E., Effective diffusivity as a diagnostic of atmospheric transport: 1. Stratosphere. *J. Geophys. Res. Atmos.* **2000**, *105*, 22777–22794.
- Hetland, R.D., Relating river plume structure to vertical mixing. *J. Phys. Oceanogr.* **2005**, *35*, 1667–1688.
- Hetland, R.D., Suppression of baroclinic instabilities in buoyancy-driven flow over sloping bathymetry. *J. Phys. Oceanogr.* **2017**, *47*, 49–68.
- Hickey, B.M., Pietrafesa, L.J., Jay, D.A. and Boicourt, W.C., The Columbia river plume study: Subtidal variability in the velocity and salinity fields. *J. Geophys. Res. Oceans* **1998**, *103*, 10339–10368.
- Horner-Devine, A., The bulge circulation in the Columbia river plume. *Cont. Shelf Res.* **2009**, *29*, 234–251.
- Horner-Devine, A.R., Hetland, R.D. and MacDonald, D.G., Mixing and transport in coastal river plumes. *Ann. Rev. Fluid Mech.* **2015**, *47*, 569–594.
- Hoskins, B., The role of potential vorticity in symmetric stability and instability. *Q. J. R. Meteor. Soc.* **1974**, *100*, 480–482.
- Hoskins, B.J. and Pedder, M.A., The diagnosis of middle latitude synoptic development. *Q. J. R. Meteor. Soc.* **1980**, *106*, 707–719.
- Hunter, E.J., Chant, R.J., Wilkin, J.L. and Kohut, J., High-frequency forcing and subtidal response of the Hudson river plume. *J. Geophys. Res. Oceans* **2010**, *115*, 1–16.
- Isobe, A., Ballooning of river-plume bulge and its stabilization by tidal currents. *J. Phys. Oceanogr.* **2005**, *35*, 2337–2351.
- Iwanaka, Y. and Isobe, A., Tidally induced instability processes suppressing river plume spread in a nonrotating and nonhydrostatic regime. *J. Geophys. Res. Oceans* **2018**, *123*, 3545–3562.
- Kang, D., Energetics of eddy-mean flow interactions in the gulf stream region. *J. Phys. Oceanogr.* **2015**, *45*, 1103–1120.
- Kantha, L.H. and Clayson, C.A., An improved mixed layer model for geophysical applications. *J. Geophys. Res. Oceans* **1994**, *99*, 25235–25266.
- Kelly-Gerrey, B., Hydes, D., Jégou, A., Lazure, P., Fernand, L., Puillat, I. and Garcia-Soto, C., Low salinity intrusions in the western English channel. *Cont. Shelf Res.* **2006**, *26*, 1241–1257.
- Kilcher, L.F. and Nash, J.D., Structure and dynamics of the Columbia river tidal plume front. *J. Geophys. Res.-Oceans* **2010**, *115*, C05S90.
- Lai, Z., Ma, R., Huang, M., Chen, C., Chen, Y., Xie, C. and Beardsley, R.C., Downwelling wind, tides, and estuarine plume dynamics. *J. Geophys. Res. Oceans* **2016**, *121*, 4245–4263.
- Lainé, A., Lapeyre, G. and Rivière, G., A quasigeostrophic model for moist storm tracks. *J. Atmos. Sci.* **2011**, *68*, 1306–1322.
- Lapeyre, G., Klein, P. and Hua, B.L., Oceanic restratification forced by surface frontogenesis. *J. Phys. Oceanogr.* **2006**, *36*, 1577–1590.
- Lavin, A., Valdès, L., Sánchez, F., Abaunza, P., Forest, A., Boucher, J., Lazure, P. and Jegou, A., The Bay of Biscay: the encountering of the ocean and the shelf. In *The Sea. Volume 14. Part B. The Global Coastal Ocean: Interdisciplinary Regional Studies and Synthesis*, edited by A. Robinson and K. Brink, chap. 24, pp. 933–999, 2006 (Harvard University Press: Harvard).
- Lazure, P., Garnier, V., Dumas, F., Herry, C. and Chifflet, M., Development of a hydrodynamic model of the Bay of Biscay. Validation of hydrology. *Cont. Shelf Res.* **2009**, *29*, 985–997. 100 Years of Research within the Bay of Biscay.
- Lazure, P. and Jegou, A.M., 3D modelling of seasonal evolution of Loire and Gironde plumes on Biscay Bay continental shelf. *Oceanol. Acta* **1998**, *21*, 165–177. International Conference on Oceanography of the Bay of Biscay.
- Le Boyer, A., Charria, G., Le Cann, B., Lazure, P. and Marié, L., Circulation on the shelf and the upper slope of the Bay of Biscay. *Cont. Shelf Res.* **2013**, *55*, 97–107.

- Lentz, S.J. and Helfrich, K.R., Buoyant gravity currents along a sloping bottom in a rotating fluid. *J. Fluid Mech.* **2002**, **464**, 251–278.
- Lentz, S. and Largier, J., The influence of wind forcing on the Chesapeake Bay buoyant coastal current*. *J. Phys. Oceanogr.* **2006**, **36**, 1305–1316.
- Li, M. and Rong, Z., Effects of tides on freshwater and volume transports in the Changjiang river plume. *J. Geophys. Res.-Oceans* **2012**, **117**, C06027.
- Lowe, R.J., Rottman, J.W. and Linden, P.F., The non-Boussinesq lock-exchange problem. Part 1. Theory and experiments. *J. Fluid Mech.* **2005**, **537**, 101–124.
- Maccready, P., Hetland, R. and Geyer, W., Long-term isohaline salt balance in an estuary. *Cont. Shelf Res.* **2002**, **22**, 1591–1601.
- MacDonald, D.G. and Geyer, W.R., Turbulent energy production and entrainment at a highly stratified estuarine front. *J. Geophys. Res. Oceans* **2004**, **109**, C05004.
- Marchesiello, P., McWilliams, J.C. and Shchepetkin, A., Open boundary conditions for long-term integration of regional oceanic models. *Ocean Model.* **2001**, **3**, 1–20.
- Marshall, D.P. and Adcroft, A.J., Parameterization of ocean eddies: Potential vorticity mixing, energetics and Arnold's first stability theorem. *Ocean Model.* **2010**, **32**, 188–204. The magic of modelling: A special volume commemorating the contributions of Peter D. Killworth – Part 2.
- Marshall, J., Jamous, D. and Nilsson, J., Entry, flux, and exit of potential vorticity in ocean circulation. *J. Phys. Oceanogr.* **2001**, **31**, 777–789.
- Marshall, J.C. and Nurser, A.J.G., Fluid dynamics of oceanic thermocline ventilation. *J. Phys. Oceanogr.* **1992**, **22**, 583–595.
- McWilliams, J.C., The emergence of isolated coherent vortices in turbulent flow. *J. Fluid Mech.* **1984**, **146**, 21–43.
- McWilliams, J.C., Submesoscale currents in the ocean. *Proc. R. Soc. A–Math. Phys. Eng. Sci.* **2016**, **472**, 20160117.
- Morel, Y. and McWilliams, J., Effects of isopycnal and diapycnal mixing on the stability of oceanic currents. *J. Phys. Oceanogr.* **2001**, **31**, 2280–2296.
- Nash, J., Kilcher, L. and Moum, J., Structure and composition of a strongly stratified, tidally pulsed river plume. *J. Geophys. Res.* **2009**, **114**, C00B12.
- Nof, D. and Pichevin, T., The ballooning of outflows. *J. Phys. Oceanogr.* **2001**, **31**, 3045–3058.
- O'Donnell, J., The dynamics of estuary plumes and fronts. In *Contemporary Issues in Estuarine Physics*, edited by A. Valle-Levinson, chap. 8, pp. 186–246, 2010 (Cambridge University Press: Cambridge).
- Oort, A.H., Anderson, L.A. and Peixoto, J.P., Estimates of the energy cycle of the oceans. *J. Geophys. Res. Oceans* **1994**, **99**, 7665–7688.
- Orlanski, I., A simple boundary condition for unbounded hyperbolic flows. *J. Comp. Phys.* **1976**, **21**, 251–269.
- Palma, E. and Matano, R., An idealized study of near equatorial river plumes. *J. Geophys. Res. Oceans* **2017**, **122**, 3599–3620.
- Pan, J. and Jay, D., Effects of ambient velocity shear on nonlinear internal wave associated mixing at the Columbia river plume front. *J. Geophys. Res.* **2009**, **114**, C00B07.
- Pimenta, F., Kirwan, A. and Huq, P., On the transport of buoyant coastal plumes. *J. Phys. Oceanogr.* **2011**, **41**, 620–640.
- Pingree, R.D. and Le Cann, B., Structure, strength and seasonality of the slope currents in the Bay of Biscay region. *J. Mar. Bio. Assoc. UK* **1990**, **70**, 857–885.
- Pingree, R. and Sinha, B., Westward moving waves or eddies (Storms) on the subtropical/azores front near 32.5°N? interpretation of the eulerian currents and temperature records at moorings 155 (35.5°W) and 156 (34.4°W). *J. Marine Syst.* **2001**, **29**, 239–276.
- Puillat, I., Lazure, P., Jégou, A., Lampert, L. and Miller, P., Hydrographical variability on the French continental shelf in the Bay of Biscay, during the 1990s. *Cont. Shelf Res.* **2004**, **24**, 1143–1163.
- Rathan, S. and Raju, G.N., A modified fifth-order WENO scheme for hyperbolic conservation laws. *Comput. Math. Appl.* **2018**, **75**, 1531–1549.
- Rhines, P. and Schopp, R., The wind-driven circulation: Quasi-geostrophic simulations and theory for nonsymmetric winds. *J. Phys. Oceanogr.* **1991**, **21**, 1438–1469.

- Rubio, A., Caballero, A., Orfila, A., Hernández-Carrasco, I., Ferrer, L., González, M., Solabarrieta, L. and Mader, J., Eddy-induced cross-shelf export of high Chl-a coastal waters in the SE Bay of Biscay. *Remote Sens. Environ.* **2018**, **205**, 290–304.
- Schiller, R.V., Kourafalou, V.H., Hogan, P. and Walker, N.D., The dynamics of the Mississippi River plume: Impact of topography, wind and offshore forcing on the fate of plume waters. *J. Geophys. Res. Oceans* **2011**, **116**, C06029.
- Schubert, W., Ruprecht, E., Hertenstein, R., Ferreira, R.N., Taft, R., Rozoff, C., Ciesielski, P. and Kuo, H.C., English translations of twenty-one of Ertel's papers on geophysical fluid dynamics. *Meteorol. Z.* **2004**, **13**, 527–576.
- Shchepetkin, A. and McWilliams, J., The regional oceanic modeling system (ROMS): A split-explicit, free-surface, topography-following- coordinate ocean model. *Ocean Model.* **2005**, **9**, 347–404.
- Sheng, J., Dynamics of a buoyancy-driven coastal jet: The Gaspé current. *J. Phys. Oceanogr.* **2001**, **31**, 3146–3162.
- Simpson, J., Brown, J., Matthews, J. and Allen, G., Tidal straining, density currents, and stirring in the control of estuarine stratification. *Estuaries* **1990**, **13**, 125–132.
- Spall, M. and Price, J., Mesoscale variability in Denmark strait: The PV outflow hypothesis. *J. Phys. Oceanogr.* **1998**, **28**, 1598–1623.
- Stamper, M. and Taylor, J., The transition from symmetric to baroclinic instability in the Eady model. *Ocean Dyn.* **2016**, **67**, 65–80.
- Stone, P.H., On non-geostrophic baroclinic stability. *J. Atmos. Sci.* **1966**, **23**, 390–400.
- Teles-Machado, A., Peliz, A., McWilliams, J.C., Cardoso, R.M., Soares, P.M.M. and Miranda, P.M.A., On the year-to-year changes of the Iberian Poleward current. *J. Geophys. Res. Oceans* **2015**, **120**, 4980–4999.
- Thomas, L.N., Destruction of potential vorticity by winds. *J. Phys. Oceanogr.* **2005**, **35**, 2457–2466.
- Thomas, L. and Ferrari, R., Friction, frontogenesis, and the stratification of the surface mixed layer. *J. Phys. Oceanogr.* **2008**, **38**, 2501–2518.
- Thomas, L.N. and Lee, C.M., Intensification of ocean fronts by down-front winds. *J. Phys. Oceanogr.* **2005**, **35**, 1086–1102.
- Thomas, L., Tandon, A. and Mahadevan, A., *Submesoscale Processes and Dynamics. Geophysical Monograph Series*, Vol. 177, 2008. (Washington, DC: American Geophysical Union).
- Thomas, L., Taylor, J., Ferrari, R. and Joyce, T., Symmetric instability in the Gulf stream. *Deep-Sea Res. Pt. II-Top. Stud. Oceanogr.* **2013**, **91**, 96–110.
- Umlauf, L. and Burchard, H., Second-order turbulence closure models for geophysical boundary layers. A review of recent work. *Cont. Shelf Res.* **2005**, **25**, 795–827.
- Vandermeirsch, F., Charraudeau, M., Bonnat, A., Fichaut, M., Maillard, C., Gaillard, F. and Autret, E., Bay of Biscay's temperature and salinity climatology, in *XII International Symposium on Oceanography of the Bay of Biscay, 4–6 mai 2010, Plouzané, France*, 2010.
- Vic, C., Berger, H., Treguier, A.M. and Couvelard, X., Dynamics of an equatorial river plume: Theory and numerical experiments applied to the Congo plume case. *J. Phys. Oceanogr.* **2014**, **44**, 940.
- Visser, A., Souza, A., Hessner, K. and Simpson, J., The influence of water column stratification on tidal current profile in a ROFI system. *Oceanol. Acta* **1994**, **17**, 369–381.
- Voropayev, S. and Filippov, I., Development of a horizontal jet in homogeneous and stratified fluids. Laboratory experiment. *J. Fluid Mech.* **1985**, **21**, 964–972.
- Walters, R.A. and Heston, C., Removing tidal-period variations from time-series data using low-pass digital filters. *J. Phys. Oceanogr.* **1982**, **12**, 112–115.
- Warner, J.C., Geyer, W.R. and Lerczak, J.A., Numerical modeling of an estuary: A comprehensive skill assessment. *J. Geophys. Res. Oceans* **2005**, **110**, C05001.
- Yankovsky, A. and Chapman, D., A simple theory for the fate of buoyant coastal discharges. *J. Phys. Oceanogr.* **1997**, **27**, 1386–1401.
- Yelekci, O., Submesoscale dynamics in the Bay of Biscay continental shelf. Ph.D. Thesis, Pierre and Marie-Curie University 2017PA066529, 2017.

Appendix. Potential vorticity flux budget terms

We begin with the potential vorticity equation

$$\partial_t q = \text{ADV} + \text{FRIC} + \text{DIAB} + \text{Pres}. \quad (\text{A.1})$$

The different components can be expressed as

$$\begin{aligned} \text{ADV} = & (f + \partial_x v - \partial_y u) \partial_z (-\mathbf{u} \cdot \nabla b) \\ & + \partial_z b \partial_x (-\mathbf{v} \cdot \nabla v - fu) - \partial_z b \partial_y (-\mathbf{u} \cdot \nabla u + fv) \\ & + \partial_y b \partial_z (-\mathbf{u} \cdot \nabla u + fv) - \partial_x b \partial_z (-\mathbf{v} \cdot \nabla v - fu) \\ & + \partial_z u \partial_y (-\mathbf{u} \cdot \nabla b) - \partial_z v \partial_x (-\mathbf{u} \cdot \nabla b), \end{aligned} \quad (\text{A.2})$$

$$\begin{aligned} \text{FRIC} = & \partial_z b \left[\partial_x \left(\frac{Dv}{Dt} + \frac{1}{\rho_0} \partial_y P + fu \right) - \partial_y \left(\frac{Du}{Dt} + \frac{1}{\rho_0} \partial_x P - fv \right) \right] \\ & - \partial_y b \partial_z \left(\frac{Du}{Dt} + \frac{1}{\rho_0} \partial_x P - fv \right) - \partial_x b \partial_z \left(\frac{Dv}{Dt} + \frac{1}{\rho_0} \partial_y P + fu \right), \end{aligned} \quad (\text{A.3})$$

$$\text{DIAB} = (f + \partial_x v - \partial_y u) \partial_z \left(\frac{Db}{Dt} \right) + \partial_z u \partial_y \left(\frac{Db}{Dt} \right) - \partial_z v \partial_x \left(\frac{Db}{Dt} \right), \quad (\text{A.4})$$

$$\text{Pres} = \partial_z b \left[\partial_x \left(\frac{1}{\rho_0} \partial_y P \right) - \partial_y \left(\frac{1}{\rho_0} \partial_x P \right) \right] - \partial_y b \partial_z \left(\frac{1}{\rho_0} \partial_x P \right) - \partial_x b \partial_z \left(\frac{1}{\rho_0} \partial_y P \right), \quad (\text{A.5})$$

where $D/Dt = \partial_t + \mathbf{u} \cdot \nabla$.

Now, we integrate the potential vorticity equation (A.1) over a volume varying in time

$$\partial_t \int_{V(t)} q \, dV = \int_{V(t)} (\text{ADV} + \text{FRIC} + \text{DIAB} + \text{Pres}) \, dV + \text{BVP}, \quad (\text{A.6})$$

where

$$\text{BVP} = \int_{A(t)} q \mathbf{u}_A \cdot d\mathbf{A} \quad (\text{A.7})$$

is the lateral boundary values here the bounding isopycnes. Further, \mathbf{u}_A is the velocity along the bounding isopycnes and A is the bounding surface.

3.3 Conclusions et Perspectives

Dans ce chapitre, une étude des instabilités géostrophiques et ageostrophiques et des processus de mélange vertical a été réalisée dans le cas d'un panache de rivière idéalisé. Cette approche vient compléter notre compréhension des processus au sein de panaches de rivières et préciser le rôle de telles structures sur le mélange vertical en milieu côtier, élément clé, par exemple, pour l'activité de l'écosystème côtier. L'étude simplifiée d'un panache fluvial dans un océan stable et homogène permet de comprendre, tout en limitant les degrés de liberté, le régime de circulation et les non-linéarités (instabilités et mélange vertical) liés aux différents forçages fluviaux ou atmosphériques. La circulation ageostrophique et les instabilités sont liées à de grands nombres de Rossby et à des mouvements non linéaires qui entraînent une forte divergence de flux ³ typiquement dans les régions frontales.

Les instabilités (géostrophiques et ageostrophiques) coexistent et sont colocalisées dans différentes régions d'un panache de rivière (le bulge et le courant côtier) selon la nature et l'intensité du forçage atmosphérique ou fluvial. Les critères de vorticité isopycniques Hoskins et Charney-Stern nous permettent d'évaluer de nombreuses instabilités dans les deux régions d'un panache de rivière :

- Dans un panache de rivière forcé à débit modéré, les instabilités existent mais peuvent prendre plus de temps à se développer sans forçage externe (vents, marées,...).
- Un débit plus élevé tend à favoriser les instabilités de cisaillement vertical, les instabilités symétriques dans le noyau du bulge et les bords du panache de rivière (forte courbure et débits cisailés). Les instabilités baroclines et barotropes coexistent et s'intensifient également près de la base du panache fluvial et dans les deux régions.
- Des vents favorables au "downwelling" déclenchent des instabilités de cisaillement frontales symétriques, baroclines et barotropes. Le bulge est quasi supprimé lorsque les vents sont à leur maximum.

³La divergence de flux horizontaux est une approximation de la vitesse verticale dans un modèle numérique d'équations primitives hydrostatique.

- Près de l'embouchure de l'estuaire, la marée M2 tend à favoriser les instabilités symétriques, barotropes et baroclines. Les oscillations de marée favorisent l'existence de nombreux fronts près de la côte (dans la région du bulge).
- Des instabilités agéostrophiques se développent dans les régions frontales où de grands nombres de Rossby et de petits nombres de Richardson peuvent être observés. Un débit fluvial élevé génère un filament dans le noyau du bulge (en raison d'une forte recirculation) où les mouvements ageostrophiques peuvent être importants.

Les processus de mélange vertical sont liés au bilan de stratification. Le budget de stratification dans un panache de rivière est paramétré par le mélange de vorticité potentielle et les processus frontogénétiques. La frontogenèse est due à l'agitation (confluence des tourbillons, dynamique frontale) et le mélange de vorticité potentielle résulte du mélange vertical de la quantité de mouvement et de la masse. Les processus dominants dans un panache de rivière rencontrant un océan homogène sont la frontogenèse et le mélange advectif. Ces processus peuvent être importants dans le champ proche d'un panache de rivière en présence de marée, ou dans la région de champ lointain dans d'autres expériences de sensibilité.

Ces constatations sont sujettes à de nombreuses limites et questions. La limitation de cette étude est attribuée à la résolution horizontale qui limite les processus physiques rencontrés dans un front océanique (ici front de salinité). Une très haute résolution (< 100 m) et une approximation non hydrostatique permettraient de mieux représenter le moment angulaire d'une particule quittant un estuaire et la dynamique frontale. Les questions restantes pour mieux comprendre les instabilités et les processus de mélange vertical dans un panache de rivière sont les suivantes :

- Comment l'approximation non-hydrostatique permettrait de mieux comprendre l'interaction d'un panache de rivière stratifié et cisailé verticalement avec le milieu ambiant dans un estuaire ou à l'embouchure de celui-ci ?
- Quelles sont les instabilités induites par cette interaction et leurs échelles spatio-temporelles ?

- Quel est l'apport de ces instabilités dans le mélange turbulent de la masse et de la quantité de mouvement ?

3.4 Notes on chapter 3

In this chapter, different results have been analyzed in terms of idealized river plumes simulations. The results depicted here are related to PV (Potential vorticity) dynamics and unstable flows. However, this study is limited due to different reasons:

1. The isopycnal PV can be biased by the sigma-coordinates and therefore this representation can be different on an interpolated vertical grid or a geopotential coordinate numerical model.
2. The vertical buoyancy flux and shear production terms show a high spatial variability which is difficult to gain insight from in regards to instabilities generation. However, These terms have been averaged meridionally; and reveals that the net impact of these terms confirms the existence of barotropic, baroclinic and vertical shear instabilities (figure not shown).
3. The BVP (boundary value problem) and frictional PV fluxes are almost compensated in the absence of winds. This effect can be due to: (i) the absence of interaction between the base of the plume and the topography, (ii) the absence of wind activity at the surface and (iii) the numerical model advection schemes and the turbulent closure scheme (interior mixing).
4. The instabilities shown in this study are potentially existing (necessary condition), but the sufficient conditions have not been analyzed. The sufficient conditions rely on primitive equations linear stability analysis which can be done in future studies for the coastal current of the Gironde plume.
5. In Figures 24 and 25, The tide simulation exhibits an abrupt decrease at the end of the studied period, which is related to the filter.

Chapter 4

Vertical shear processes in river plumes

In this chapter, an idealized study of a vertically sheared and stratified plume is presented. In this study, the instabilities and turbulent mixing are analyzed in this plume in regard to different physical processes (shear intensity, stratification thickness and the bottom slope). The main results have been submitted to Ocean Modelling journal.

4.1 Introduction

Ce chapitre sera consacré aux instabilités de cisaillement vertical et au mélange vertical dans des régions du panache fluvial comme l'estuaire et le champ proche du panache à l'embouchure de la rivière. Je définirai dans un premier temps une situation de référence où les conditions initiales de cisaillement vertical et de stratification sont choisies à partir de la littérature sur ces processus dans différents panaches de rivière.

A partir de cette situation de référence, j'étudierai la sensibilité à plusieurs paramètres: (i) - l'intensité du cisaillement vertical, (ii) - l'épaisseur de la couche d'eau douce, (iv) - la courbure de la base du panache et (v) - la pente du fond.

La stratégie adoptée ici est la définition de simulations en approximation non-

hydrostatique et en 2 dimensions (modèle Fluid2D)¹ pour explorer les instabilités de cisaillement vertical (type Kelvin-Helmholtz et Holmboe) dans un contexte côtier. Ces instabilités représentent également le lien entre les ondes internes, omniprésentes dans un panache interagissant avec un fond et la marée, et la turbulence 3D.

Dans ce contexte, j'évaluerai la nature de ces instabilités en décrivant leurs échelles spatio-temporelles. Ensuite, je m'intéresserai à leurs évolutions en fonction de différents paramètres bathymétriques et hydrologiques. L'étude de ces instabilités sera basée sur l'analyse de stabilité linéaire qui décrit leur amplitude, leur croissance et leur énergie cinétique turbulente.

Enfin, j'analyserai le mélange turbulent induit par ces différentes instabilités en caractérisant leurs coefficients de mélange et de masse, leur transport vers la turbulence et leur efficacité de mélange. Ces diagnostics seront comparés au mélange turbulent total afin d'en déduire leurs contributions respectives.

Cette étude a été soumise au journal scientifique Ocean Modelling et le contenu de cet article est présenté dans la section suivante.

4.2 Article: Vertical shear processes in river plumes: Instabilities and turbulent mixing

¹Nous remercions Guillaume Roulet d'avoir mis à disposition ce modèle numérique qui a permis la réalisation de cette étude

Vertical shear processes in river plumes: Instabilities and turbulent mixing

Adam Ayouche^{a,b}, Xavier Carton^a, Guillaume Charria^a

^aLaboratory for Ocean Physics and Satellite remote sensing (LOPS), UMR6523, Ifremer, Univ. Brest, CNRS, IRD, Brest, France

^bCorresponding author: Adam Ayouche, adam.ayouche@ensta-bretagne.org

Abstract

We address here the problem of vertical shear flow instabilities at the base of a river plume and their consequences in terms of turbulent energy production and of mixing. This study was carried out using 2D non-hydrostatic simulations and a stability linear analysis. The initial conditions used in these simulations were similar to those observed in river plumes, near the estuaries. The unstable stratified sheared flows follow three stages in their evolution: (i) the generation of billows induced by vertical shear instabilities, (ii) their intensification and (iii) their elongation. The elongation of the generated billows is related to the strain intensity which depends on the physical setting (velocity shear, stratification thickness and bottom slope). Two vertical shear instabilities were found in our study: the Holmboe and Kelvin-Helmholtz instabilities. The Kelvin-Helmholtz instability has a smaller growth time and longer wavelengths; the Holmboe instability is characterized by longer growth time and shorter wavelengths. The Kelvin-Helmholtz instability is intensified when the bottom is sloping and for large shears. The Holmboe instability is stronger when the stratification thickness is reduced compared to the shear thickness, and when the bottom is sloping. For mixing, the flow can be: (i) pre-turbulent, (ii) quasi-turbulent or (iii) turbulent. The pre-turbulent flow corresponds to more mass mixing than momentum mixing and to more Eddy Kinetic Energy dissipation than Eddy Available Potential Energy dissipation. Such a flow is encountered over a flat bottom whatever the initial shear. The quasi-turbulent and turbulent flows are

reached when the bottom is sloping, and when the stratification thickness is reduced. Using turbulent mixing statistics (mixing coefficients, mixing efficiency, EKE and EAPE dissipation rates), we showed that despite their slow growth, Holmboe instabilities contribute more efficiently to the turbulent mixing than Kelvin-Helmholtz instabilities. The Holmboe instabilities are the only source of turbulent mixing when sharp density gradients are observed (small buoyancy thickness experiment). Our simulations highlight the efficient contribution of the Holmboe instability on the turbulent mixing.

Keywords: River plumes, Kelvin-Helmholtz instability, Holmboe instability, Turbulent mixing, dissipation rates

1. Introduction

2 The Kelvin-Helmholtz (hereafter KH) instability was first introduced by
3 Helmholtz in 1868 (Helmholtz, 1868). He considered that the assumption of
4 a fluid free from friction is not true in its interior. Indeed, using analogy with
5 electricity, he showed that the flow of two neighboring fluids results in a surface
6 separation. This surface separation evolves as a discontinuity in the velocity field
7 in the neighboring fluids. The surface discontinuity was considered as a surface
8 of gyration where moments of rotation are generated by frictional processes.
9 Thomson (1871) showed that under the action of wind waves, disturbances can
10 be observed below the ocean surface, which evolve into small waves, which travel
11 fast and finally cease, except when the disturbing force (the wind) continues to
12 act. These growing waves are manifestations of the Kelvin-Helmholtz instabil-
13 ity; they can roll up into vortices with horizontal axis, named “billows”. This
14 instability was studied with a mathematical model having two fluid layers with
15 uniform and distinct velocities and densities. This study was then generalized
16 by Taylor (1931) and Goldstein and Taylor (1931) using an arbitrary vertical
17 velocity profile in a continuously stratified fluid. The flow instability equation
18 was obtained from the linearization of the three-dimensional non hydrostatic
19 equations. A condition for instability was obtained, based on the Richardson

20 number: the minimum Richardson number should be lower than a threshold of
21 0.25.

22 The KH instability exists in different geophysical and astrophysical flows. In
23 the Jupiter atmosphere, the interaction between the solar wind and the mag-
24 netosphere favors the development of vortices (Delamere and Bagenal, 2010,
25 2013; Zhang et al., 2018). These vortices result from a KH instability initiated
26 in the subsolar region and advected by magnetospheric flows to the dusk sec-
27 tor. Magnetic KH instability and its features (vortices) have also been observed
28 at the surface of a fast coronal mass ejecta in the Sun (Foullon et al., 2011).
29 The unstable flow nonlinearities favor the transport of momentum, plasma, and
30 energy both in large scale and in micro-scale turbulence. In the atmosphere,
31 KH vortices are observed in the upper troposphere and above the tropopause
32 (Browning, 1971; Singh et al., 1999). These vortices have diameters larger than
33 200 m and a characteristic period of 12 minutes. They are related to maxima
34 in the vertical wind shear.

35 In the ocean, KH vortices are high frequency and small scale features that
36 have been studied for a wide range of flow conditions, in stratified shear flows.
37 These vortices result from successive processes: (i) a primary Kelvin-Helmholtz
38 instability, (ii) a vortex merger and (iii) secondary Kelvin-Helmholtz instabil-
39 ities. The primary Kelvin-Helmholtz instability is generated at the interface
40 between two neighboring fluids (Holt, 1998; Li and Yamazaki, 2001; Morin
41 et al., 2004). These authors used field measurements, numerical simulations
42 and laboratory experiments to observe such instabilities. Primary KH instabil-
43 ities have been observed in a tilted tank (in the spanwise direction), with fluid
44 in the two layers unequally distant from the shear interface (Holt, 1998). The
45 author indicates that the primary KH instability is delayed in the asymmetric
46 case compared with the symmetric configuration. KH vortices, a result of a
47 primary KH instability, have been identified in the seasonal thermocline off San
48 Diego, California in 1988 (Li and Yamazaki, 2001). These authors found, using
49 turbulent velocity measurements, that these vortices have a horizontal scale of
50 about 3.5 m. Primary instability waves have been observed in a stratified flow

51 in the Knight inlet (Morin et al., 2004). These authors conducted laboratory
52 experiments with two reservoirs containing fluids of (slightly) different densities,
53 flowing over a 2D sill in a rectangular channel. They deduced that the shear in-
54 terface fluctuations are due to internal seiche and to primary Kelvin-Helmholtz
55 instabilities. The KH billows (resulting from primary KH instabilities) at the
56 interface of a stratified shear flow can then undergo a merging process (Brandt
57 and Nomura, 2007; Dixit and Govindarajan, 2013).

58 The merging process of a pair of Gaussian vortices has been studied in differ-
59 ent stratification conditions. In a weak stratification, vortex merger proceeds via
60 several stages: a diffusive/axisymmetrization phase, a convective/deformation
61 phase, a convective/entrainment phase and a final diffusive/axisymmetrization
62 phase (Brandt and Nomura, 2007). In these stages, the interaction between
63 vorticity gradients and the rate of strain is central. Brandt and Nomura suggest
64 that their effects on stratification is controlled by the ratio between the growth
65 of cores (billows cores) to viscous effects (quantified by the Reynolds number).
66 In contrast, in intermediate to high stratification, vortex merger is not always
67 possible as strong baroclinic vorticity prevents it and induces low diffusivity; the
68 drift of the vorticity centroid can be observed (Dixit and Govindarajan, 2013).
69 Billow merger or drift are followed by the growth of higher order harmonics
70 associated with a secondary Kelvin-Helmholtz instability (Palmer et al., 1994;
71 Morin et al., 2004). The secondary KH instability arises in the vicinity of the
72 KH billows. When the density interface is sharp enough, another secondary
73 instability appears: the Holmboe instability (Ortiz et al., 2002; Alexakis, 2005;
74 Zagvozkin et al., 2019). The unstable shear flow, when the density stratification
75 length scale is much smaller than the shear length scale, undergoes a Kelvin-
76 Helmholtz instability with a steady vortex formed at the middle of the interface;
77 it is accompanied by a Holmboe instability with waves traveling along the in-
78 terfacial boundary (Zagvozkin et al., 2019). In general, different regions can
79 be defined in an unstable shear flow: (i) a region with neutral gravity waves,
80 (ii) a region where two Holmboe modes propagates in the opposite direction,
81 (iii) a region where KH instability exists and (iv) a region with singular neu-

82 tral modes (Alexakis, 2005). After the onset of vertical shear instabilities (KH
83 and Holmboe), a transition to turbulence occurs (Holt, 1998; Li and Yamazaki,
84 2001; Morin et al., 2004; Thorpe, 2012). KH instability favors entrainment be-
85 tween the neighboring layers and therefore mixing (Morin et al., 2004). The
86 turbulent patches thus formed are characterized by a spectral slope of -2 ; they
87 are limited by mixing occurrence in the sloping direction (Holt, 1998; Li and
88 Yamazaki, 2001). In laminar and turbulent flows, the KH vortices can develop
89 and pre-existing turbulence may affect the onset of Kelvin-Helmholtz instability
90 (Thorpe, 2012).

91 In river plumes, the KH instability can be observed in estuaries and the
92 near-field region (near the river mouth). This instability can be generated by
93 many physical effects: winds, river discharge and tides. Tedford et al. (2009)
94 observed a one-sided instability (KH instability) in the Frazer River estuary
95 using an echo sounder. They compared field measurements with the Taylor-
96 Goldstein equation modes. They suggested that the interaction between river
97 discharge and tides produces KH instability above or below the density inter-
98 face. In their study, mixing and turbulence result from strong tidal velocities
99 near the bed and from shear instabilities. These instabilities have also been
100 studied along the North Passage of the Yangtze river estuary using a high res-
101 olution nonhydrostatic model (Shi et al., 2019). The authors found that the
102 interaction between freshwater discharge and tides tempers the duration and
103 length scale of the KH vortices. Moreover, in their study KH instability induces
104 high mixing efficiency with maximum mixing rates of $5 \times 10^{-6} \text{ J m}^{-2} \text{ s}^{-1}$. These
105 turbulent fine structures influence the behavior of a tidal plume (Iwanaka and
106 Isobe, 2018). Iwanaka and Isobe (2018) conducted field surveys near a river
107 mouth and used a nonhydrostatic model; they showed that small horizontal
108 scale features ($< 100 \text{ m}$) can be observed in the tidal plume. They related these
109 small eddies to inertial and Kelvin-Helmholtz instabilities. They indicated that
110 such instabilities act like friction that prevents the tidal plume from expanding
111 offshore. In different oceanic regions, the KH instability induces mixing and
112 turbulent processes (Smyth and Moum, 2012). In numerous studies, the verti-

113 cal diffusivity, reached when KH vortices are observed, lies between 10^{-4} and
114 $10^{-3} \text{ m}^2.\text{s}^{-1}$ (van Haren and Gostiaux, 2010; Horner-Devine et al., 2015). In
115 highly stratified river plumes, the size of KH billows (Ozmidov scale) is $O(10$
116 $\text{cm})$ (Horner-Devine et al., 2015). Thus, these small scale eddies can be diffi-
117 cult to observe. In most river plumes, the KH billows occupy less than 10% of
118 the interfacial volume but they achieve significant mixing (Horner-Devine et al.,
119 2015).

120 In the present work, a 2D nonhydrostatic model is used to perform idealized
121 numerical simulations of stratified shear flows characteristic of river plumes. We
122 will address the following issues:

- 123 • What is the evolution of a sheared river plume base under different flow
124 parameters ?
- 125 • Which type of vertical shear instabilities can affect the plume base and
126 under which flow conditions ?
- 127 • What are the consequences of the vertical shear instabilities on vertical
128 turbulent mixing ?

129 The paper will be organised as follows: the model equations, configuration,
130 simulations and methods will be described in section 2; the 2D structure and life
131 cycle of the plume and its interface will be presented in section 3.1, the vertical
132 shear instabilities affecting it, in section 3.2 and the turbulent mixing and its
133 efficiency that those instabilities induce, in section 3.3. The main results will
134 be discussed in section 4 and conclusions will be provided in section 5.

135 2. Materials and Methods

136 2.1. Model configuration

137 The simulations are performed using the Fluid2d numerical model. Fluid2d
138 is a versatile Python-Fortran CFD (Computational Fluid Dynamics) model pro-
139 vided by <https://mespages.univ-brest.fr/roullet/fluid2d/index.html>. Fluid2d is

140 dedicated to simulate a large range of 2D flows. It is defined on a C-Arakawa
 141 grid where tracers (buoyancy, vorticity) are discretized at model cell centers.
 142 Velocity components and stream functions are discretized at cell edges and cell
 143 corners respectively. The time discretization scheme is explicit. In our study,
 144 velocity and density equations in the (x-z) plane, under the non-hydrostatic
 145 (NH) approximation, are used. In this approximation, we consider an incom-
 146 pressible and stratified fluid with no Coriolis effect. No explicit viscosity, nor
 147 explicit diffusivity are used here. The NH Boussinesq equations are written as:

$$\partial_x u + \partial_z w = 0 \quad (1)$$

$$\frac{D\mathbf{u}}{Dt} = -\nabla p + b\mathbf{k} \quad (2)$$

$$\frac{Db}{Dt} = 0 \quad (3)$$

148 where $\mathbf{u} = u\mathbf{i} + w\mathbf{k}$ (\mathbf{i} and \mathbf{k} are the horizontal and vertical unit vectors,
 149 respectively) is the velocity vector, p is the pressure scaled by a mean density
 150 ρ_0 , b is the buoyancy and $\frac{D}{Dt} = \partial_t + \mathbf{u} \cdot \nabla$ is the material derivative.

151 The first NH equation indicates that the velocity is derived from a stream-
 152 function with $w = \partial_x \psi$ and $u = -\partial_z \psi$. Therefore we deduce the vorticity as
 153 $\omega = \partial_x w - \partial_z u = \nabla^2 \psi$. The latter lead to the vorticity and buoyancy equations
 154 summarized below:

$$\partial_t \omega + J(\psi, \omega) = \partial_x b \quad (4)$$

$$\partial_t b + J(\psi, b) = -N^2 \partial_x \psi \quad (5)$$

$$\partial_{xx}^2 \psi + \partial_{yy}^2 \psi = \omega \quad (6)$$

155 where ω is the vorticity, b is the buoyancy field, J the Jacobian operator,
 156 N^2 is the Brunt Vaisala frequency and ψ is the streamfunction.

157 The model uses a third order Runge-Kutta (Stably Strongly Preserving
 158 scheme) as a time stepping scheme. The advection scheme is a fifth order
 159 upwind for both tracers and momentum which has the advantage of a built-in
 160 dissipation. Neither explicit viscosity nor diffusivity is used here. The grid size
 161 is 512*2048 in the (z-x) plane and the time step is 0.01 second. The horizontal
 162 and vertical extents of the model grid are 40 m and 10 m respectively. A peri-
 163 odic boundary condition is applied in the x direction and a free-slip boundary
 164 in the vertical direction. The model runs for 4 modeled minutes with outputs
 165 every quarter of a second. The model has no external forcing, nor Coriolis effect.
 166 The Coriolis effect could be added but in our case it is not mandatory, since the
 167 simulation time is far below the inertial period.

168 2.2. Model experiments

169 Here, a description of the different experiments performed in this study is
 170 provided. Starting from the reference case, sensitivity experiments are carried
 171 out, which involve different flow parameters or topographic ridges. In all exper-
 172 iments, the initial conditions are a shear-stratified flow; the background velocity
 173 and buoyancy vertical profiles are

$$B = N_0^2 h_b \tanh\left(\frac{z - z_0}{h_b}\right) \quad (7)$$

$$U = -S_0 h_s \tanh\left(\frac{z - z_0}{h_s}\right) \quad (8)$$

174 where h_s is the thickness of the shear layer and h_b is the thickness of the
 175 stratified layer (figure 1). We assume that the thickness is identical for both of
 176 these fields ($h_b = h_s$), except in experiment 3, where the stratification thickness
 177 is much smaller than the shear layer thickness ($h_b = \frac{h_s}{1000}$). The thickness
 178 retained in these experiments is 2 m which corresponds to an average value of
 179 the freshwater thickness in river plumes in previous studies (Granskog et al.,
 180 2005; Hetland, 2005; Ayouche et al., 2020). z_0 is the vertical location of the
 181 interface taken here as mid-depth.

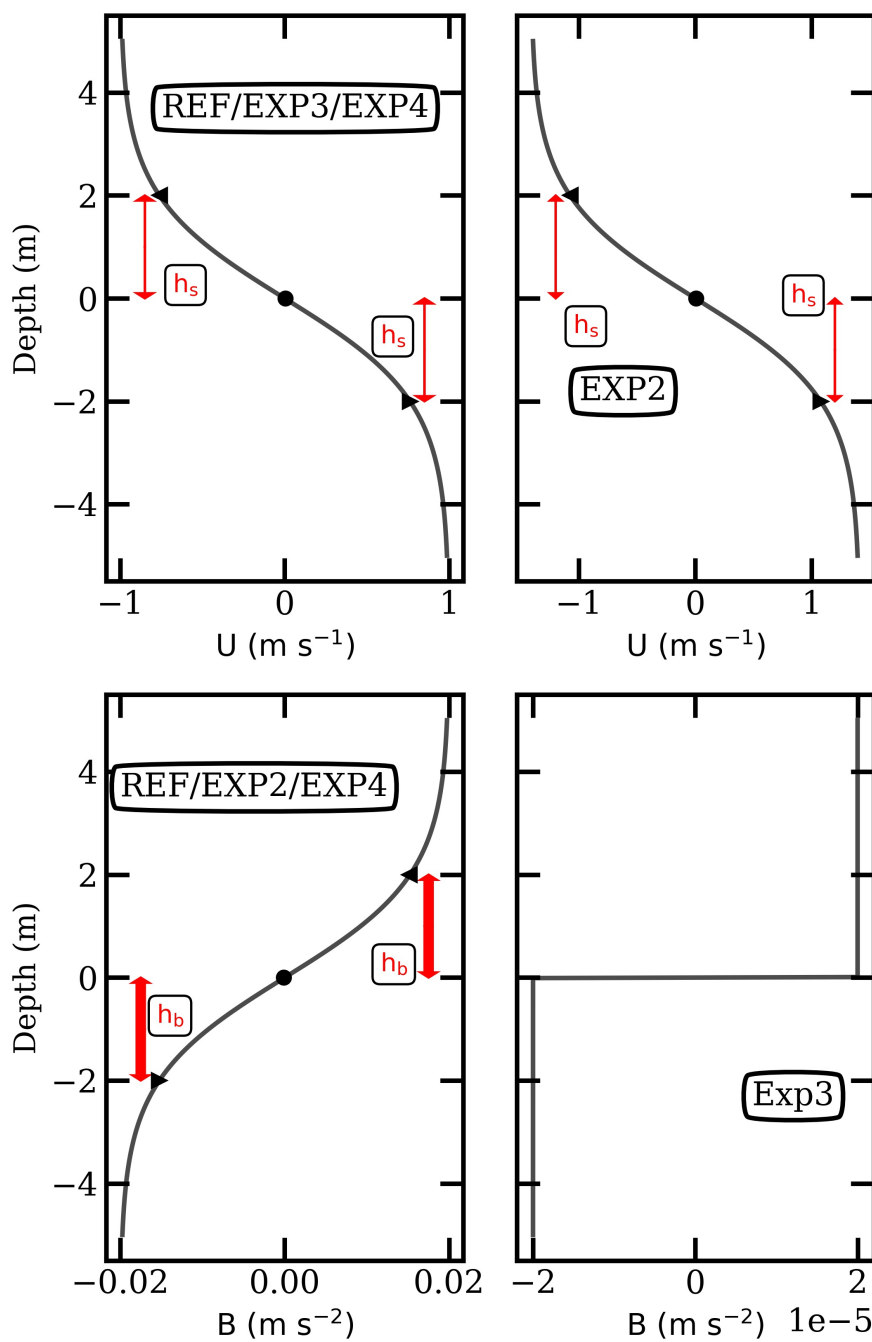


Figure 1: The initial conditions for all the experiments: (top row) - Streamwise velocity, (bottom row) - Buoyancy

182 N_0^2 is the Brunt Vaisala frequency computed as

$$N_0^2 = \frac{g\Delta\rho}{\rho_0 H} \quad (9)$$

183 where H is the total water depth (here 10 m), g is the acceleration gravity,
 184 ρ_0 is a mean density (here as 1025 kg.m^{-3}), $\Delta\rho$ is a density difference between
 185 two layers taken here as 15 kg.m^{-3} (Horner-Devine et al., 2015) which leads
 186 to a Brunt Vaisala frequency of 0.01 s^{-2} . This parameter is fixed for all the
 187 experiments shown here.

188
 189 A total of 4 experiments have been carried out in this study. Between these
 190 experiments, we also vary S_0 , the square root of the vertical shear $S^2 = (\partial_z u)^2 +$
 191 $(\partial_z w)^2$. Most experiments use a flat bottom except the last experiment where
 192 topographic ridges are introduced. The bottom shape z_b of the last experiment
 193 is written as:

$$z_b(x) = \begin{cases} 1.5 \times (1 - \cos(\pi \frac{x-5}{5})), & \text{if } 5 \leq x \leq 35 \\ -\frac{H}{2}, & \text{otherwise} \end{cases}$$

194 A white noise is added to the initial vorticity to trigger the instability. The
 195 initial minimum Richardson number is below the critical threshold (0.25) which
 196 ensures the generation of vertical shear instabilities. Table 1 summarizes the
 197 simulations performed in this study.

Experiments	Initial shear (s^{-2})	Initial stratification (s^{-2})	Minimum Richardson number	Interface	Bottom	Boundaries
Reference	0.25	0.01	0.04	plane ($h_b = h_s$)	flat	Periodic in x + Rigid in z
Exp 2	0.5	0.01	0.02	plane ($h_b = h_s$)	flat	Periodic in x + Rigid in z
Exp 3	0.25	0.01	0.04	plane ($h_b = \frac{h_s}{1000}$)	flat	Periodic in x + Rigid in z
Exp 4	0.25	0.01	0.04	plane ($h_b = h_s$)	sloping	Periodic in x + Rigid in z

Table 1: Simulations parameters

198 2.3. Diagnostics for stratified sheared flows structure and dynamics

199 Since we wish to examine the life cycle of the billows at the interface of
 200 the stratified sheared flow, we will define several diagnostics. Each billow will

201 be characterized by: (i) its centroid position (x_c, z_c) , (ii) its radius and (iii)
 202 its aspect ratio. We define the eometrical moments of vorticity as in Dritschel
 203 (1998) and we write

$$J_{mn} = \int \int_D x^m z^n \omega(x, z) dx dz \quad (10)$$

204 The centroid of each billow is defined as

$$x_c = \frac{J_{10}}{J_{00}}, z_c = \frac{J_{01}}{J_{00}} \quad (11)$$

205 The billow semi-major axis a and semi-minor axis b are defined as in Le Dizès
 206 and Verga (2002) and we write

$$a^2 = \frac{J_{20} \cos^2(\phi) - J_{11} \sin(2\phi) + J_{02} \sin^2(\phi)}{J_{00}}, b^2 = \frac{J_{02} \cos^2(\phi) - J_{11} \sin(2\phi) + J_{20} \sin^2(\phi)}{J_{00}} \quad (12)$$

207 where the rotation angle and the radius of each billow are expressed as

$$\phi = \frac{1}{2} \arctan\left(\frac{2J_{11}}{J_{20} - J_{02}}\right), r = \frac{\sqrt{\pi ab}}{\pi} \quad (13)$$

208 We quantify the average radius of the identified billows for each experiment.
 209 Then, we represent the moving average (over 30 seconds) of the billows aspect
 210 ratio $\frac{b}{a}$.

211 The spatial distribution of the Okubo-Weiss parameter (Okubo, 1970; Weiss,
 212 1991) will be computed as:

$$OW = s_n^2 + s_s^2 - \omega^2 \quad (14)$$

213 where ω is the vorticity, $s_n = -2\partial_z w$ is the normal strain and $s_s = \partial_x w + \partial_z u$
 214 is the tangential strain.

215 The Okubo-Weiss parameter will identify regions where the vorticity domi-
 216 nates ($OW < 0$) and regions where the strain dominates ($OW > 0$).

217 Then, we will compute the surface average of the strain intensity $s^2 = s_n^2 + s_s^2$,
 218 and the strain direction $\alpha_{\text{strain}} = \arctan\left(\frac{s_n}{s_s}\right)$ in regions where OW is positive.

219 The moving average (over 30 seconds) of these strain diagnostics will be
220 compared to the aspect ratio.

221 2.4. Diagnostics for instabilities

222 A decomposition of the flow will be performed. The mean flow is the back-
223 ground state (initial conditions) and perturbations are obtained for the velocity
224 components (u and w) and the buoyancy field as

$$b'(x, z, t) = b(x, z, t) - b(x, z, t = 0) = b(x, z, t) - B(x, z) \quad (15)$$

$$u'(x, z, t) = u(x, z, t) - u(x, z, t = 0) = u(x, z, t) - U(x, z) \quad (16)$$

$$w'(x, z, t) = w(x, z, t) - w(x, z, t = 0) = w(x, z, t) \quad (17)$$

225 A measure of the turbulence intensity in the stratified shear flow is the eddy
226 kinetic energy which is expressed as

$$\text{EKE}(t) = \frac{1}{2LH_c} \int_0^L \int_0^{H_c} (u'(x, z, t)^2 + w'(x, z, t)^2) dx dz \quad (18)$$

227 where L is the horizontal length of the domain and H_c is the critical layer
228 as defined in appendix Appendix A.

229 Then, a linear stability analysis is performed using the non-hydrostatic (NH)
230 approximation. The linear analysis stability is performed to identify the nature
231 of the instability, its growth, its phase speed and its critical layer depth. The
232 EKE of each identified instability is also computed. Full details about this linear
233 stability analysis are given in Appendix A.

234 2.5. Diagnostics for turbulent mixing

235 The turbulent mixing will be quantified first by the vertical eddy viscosity
236 K_m and by the vertical diffusivity K_b (Nakano and Yoshida, 2019):

$$K_m = -\frac{1}{LH_c} \int_0^L \int_0^{H_c} \frac{u'w'}{\partial_z U} dx dz \quad (19)$$

$$K_b = -\frac{1}{LH_c} \int_0^L \int_0^{H_c} \frac{w'b'}{\partial_z B} dx dz \quad (20)$$

237 Then, the vertical EKE dissipation ϵ (Yang et al., 2019) and the vertical
238 buoyancy dissipation ϵ_b will be evaluated as:

$$\epsilon = -\frac{1}{LH_c} \int_0^L \int_0^{H_c} \frac{u'w'}{\partial_z U} ((\partial_z u')^2 + (\partial_z w')^2) dx dz \quad (21)$$

$$\epsilon_b = -\frac{1}{LH_c} \int_0^L \int_0^{H_c} \frac{w'b'}{\partial_z B} (\partial_z b')^2 dx dz \quad (22)$$

239 The turbulent Prandtl number will be then deduced from the vertical diffu-
240 sivity and the vertical eddy viscosity as $P_r = \frac{K_m}{K_b}$.

241 We will evaluate the irreversible mixing efficiency $\Gamma_i = \frac{\Gamma}{1+\Gamma}$ (Kaminski and
242 Smyth, 2019), where Γ is the mixing efficiency deduced from $K_b = \Gamma \frac{\epsilon}{\partial_z B}$ (Yang
243 et al., 2019). This irreversible mixing efficiency will be computed for each ver-
244 tical shear instability (Holmboe and Kelvin-Helmholtz) using modal decompo-
245 sitions of the vertical EKE dissipation and the vertical diffusivity that we write
246 as:

$$\tilde{K}_b = -\frac{1}{LH_c} \int_0^L \int_0^{H_c} \frac{\text{Re}(\tilde{w}\tilde{b}^*)}{\partial_z B} dx dz \quad (23)$$

$$\tilde{\epsilon} = -\frac{1}{LH_c} \int_0^L \int_0^{H_c} \frac{\text{Re}(\tilde{u}\tilde{w}^*)}{\partial_z U} (\partial_z \tilde{u} \partial_z \tilde{u}^* + \partial_z \tilde{w} \partial_z \tilde{w}^*) dx dz \quad (24)$$

247 We will consider the mixing as efficient if Γ_i is larger than 0.2 (Osborn,
248 1980).

249 3. Results

250 3.1. Structure and dynamics of stratified sheared flows

251 Here, we present and analyse the time evolution of the stratified-sheared
252 interface. The interface corresponds to a river plume base. The centroid of
253 vorticity is computed with different parameters (average radius of billows, ratio

254 of centroid distance over the average radius, magnitude of the strain and its
255 direction, and Okubo-Weiss parameter) to describe the dynamical processes
256 governing the evolution of the coherent vortices formed at the plume base. We
257 carry out several sensitivity experiments to understand the dynamics of the
258 antisymmetric sheared flow in different settings.

259 3.1.1. Reference configuration

260 Figure 2 shows the time evolution of the buoyancy and vorticity fields at
261 different stages of the reference simulation. During the first period of this sim-
262 ulation (for $8 < t \leq 54$ seconds), the anti-symmetric shear causes the buoyant
263 plume interface to deform, and crests and troughs are generated. The advec-
264 tion of water parcels across the interface produces vorticity that evolves from
265 a noisy field at the beginning, to a wavy stripe engulfing the sheared interface
266 (see equation 4). Then (for $87 \leq t \leq 130$ seconds), the crest of perturbation
267 moves upward; this forms a flow constriction in the upper layer. The flow con-
268 striction accelerates the flow in the upper layer and a roll-up of the shear layer
269 is observed which generates small eddies (billows). These billows are two small
270 cyclonic eddies, with an average radius of 3.8 m, and their roll-ups favor fluid
271 entrainment between the two layers. Finally (at $t \sim 240$ seconds), the two cy-
272 clonic billows elongate; this elongation triggers the development of small scale
273 filaments at their rims and in their cores.

274 The billows have strong vorticity which competes with the fluid strain. This
275 competition can be evaluated with the Okubo-Weiss (OW) parameter (figure
276 3a). The vorticity dominates ($OW < 0$) in the sheared layer during the gen-
277 eration, the intensification and the elongation of the billows. Meanwhile, the
278 strain dominance ($OW > 0$) is patchy during the period of generation of the
279 billows (at $t \sim 54$ and 87 seconds). Intense strain is found at the edges of small
280 filaments located in the upper layer (2 m below the surface) and in the lower
281 layer (2 m above the bottom). During this period (for $t < 100$ seconds), the
282 strain is mostly tangential ($\alpha_{\text{strain}} \sim -0.1$ rad) and remains constant (its inten-
283 sity $\sim 0.02 \text{ s}^{-2}$), as shown in figure 3b. This indicates that during this period,

284 the vorticity favors the generation of the billows; and thus the strain influence
285 is not prominent.

286 Then, the billows roll up and are intensified (at $t \sim 130$ seconds). The
287 strain remains dominant at the same locations as in the previous periods. It
288 is prominent in small scale features in the core of the billows, and in the thin
289 tilted interface formed between the billow cores: the braid. During the period of
290 intensification of the billows (at $t > 100$ seconds), the strain intensity increases
291 sharply and reaches a maximum ($\sim 0.045 \text{ s}^{-2}$) at $t \sim 150$ seconds. The strain
292 is mostly tangential during this period as its direction is nearly horizontal. This
293 tangential strain induces an elongation of both billows in the horizontal direction
294 since their aspect ratio increases sharply up to values ~ 0.15 .

295 The billows reach their full extension during the last period (at $t \sim 240$
296 seconds). The spatial distribution of the strain dominance is localized in small
297 filaments in the core of the billows and between them. Since the elongation
298 of each billow reaches half of the horizontal domain length, each billow is con-
299 strained by the other; then, their aspect ratio decreases notably (at $t > 150$
300 seconds) and therefore the tangential strain ($\alpha_{\text{strain}} \sim -0.1 \text{ rad}$) slackens.

301 3.1.2. Sensitivity to the vertical shear (Exp2)

302 In this simulation, the (initial) vertical shear is twice that of the reference
303 experiment. Figure 4 shows the time evolution of the vorticity and buoyancy
304 fields. During the first period (for $8 < t \leq 54$ seconds), the sharp interface
305 evolves quickly and by the end of this period, buoyant crests appear. The vor-
306 ticity field is noisy and intense and, at the end, turbulent structures are observed
307 in the sheared interface. Then (for $87 \leq t \leq 130$ seconds), the perturbed inter-
308 face evolves to form two, intense, cyclonic billows which begin to roll and due to
309 the fluid acceleration in the upper layer and the induced tangential strain, they
310 extend in the horizontal direction. These two billows have a radius $\sim 3.8 \text{ m}$.
311 Finally (at $t \sim 240$ seconds), these two cyclonic billows elongate in the tangen-
312 tial direction and their extent reaches half of the domain length, respectively.
313 Filaments and strong vorticity are observed in their core and at their rims.

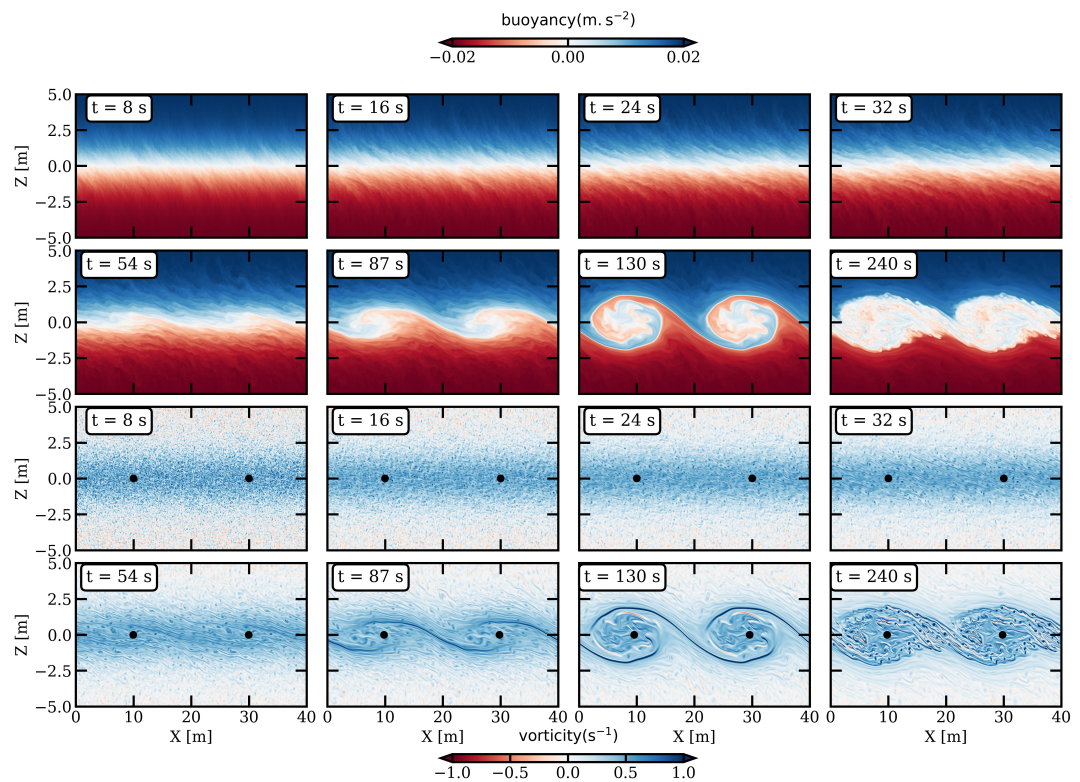


Figure 2: Snapshots in the Reference Experiment of: buoyancy field (top two rows), vorticity field (bottom two rows). The black dots in the vorticity field indicate the vorticity centroid of each billow.

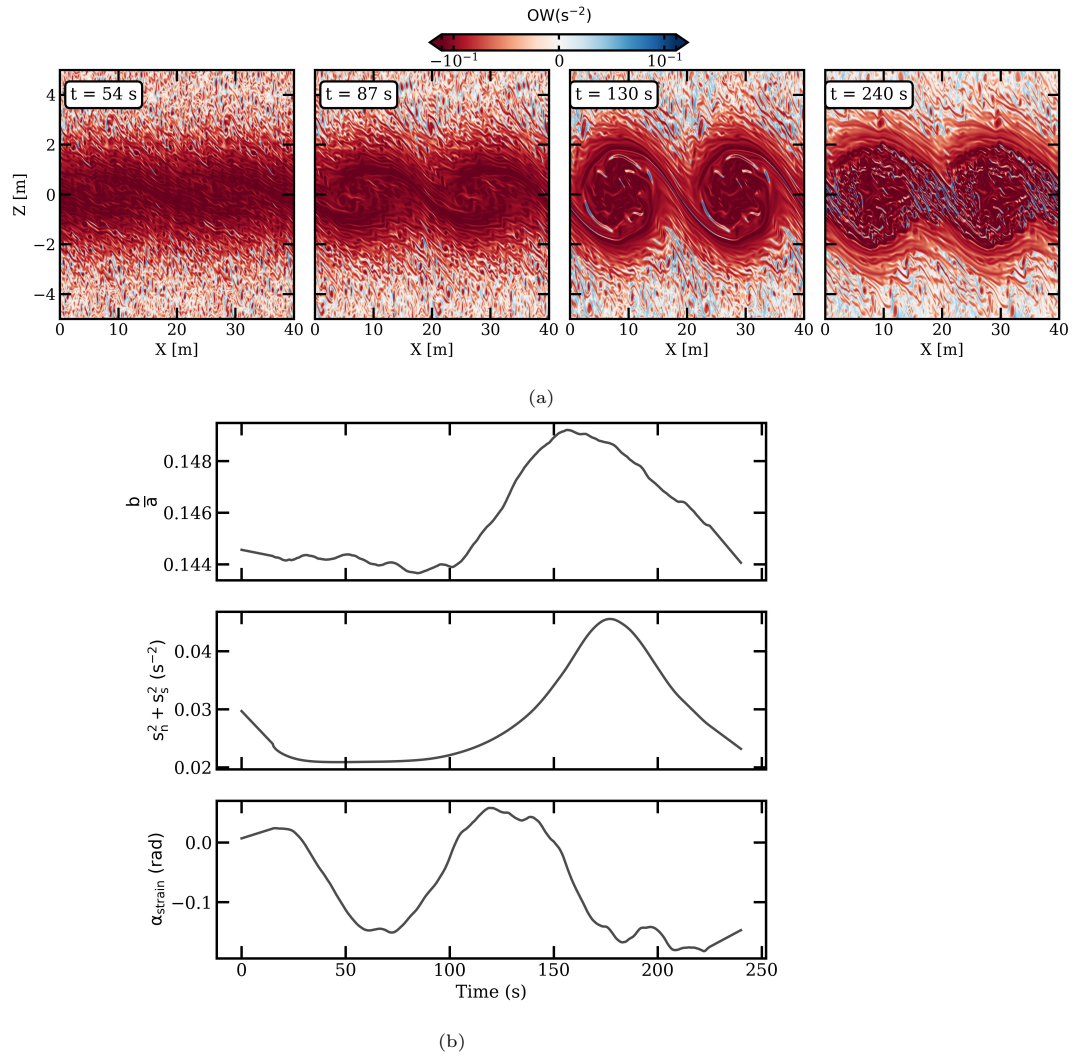


Figure 3: (a) - Snapshots of the Okubo-Weiss parameter in the Reference Experiment. (b) - Time evolution (Reference Experiment) of the aspect ratio of the two billows (top row), the intensity of the strain (second row) and its direction (bottom row).

314 In this experiment, during the generation of vortices ($t \sim 54$ seconds) the
315 Okubo-Weiss parameter is weakly positive locally in the top and bottom layers
316 around small filaments; and negative in the sheared layer (figure 5a). Prior to
317 this period (at $t \leq 54$ seconds), the tangential strain ($\alpha_{\text{strain}} \sim 0$ rad) inten-
318 sity remains weak (figure 5b). This indicates that during this period, the flow
319 develops intense vorticity that will contribute to the two billow cores.

320 Then (at $t \sim 87$ seconds), the vortices are formed and roll up. The strain
321 dominance increases in the upper and lower layers, in small strips in the inner
322 core of the billows, and along the braid. This induces a sharp increase in the
323 intensity of the tangential strain ($\alpha_{\text{strain}} \sim 0.1$ rad) reaching values up to 0.05
324 s^{-2} at $t \sim 100$ seconds. The sharp increase of the tangential strain induces a
325 deformation of both billows as indicated by the sharp growth of their aspect
326 ratio (a maximum ~ 0.1525).

327 Lastly ($t \sim 130$ and 240 seconds), the vortices are elongated and intensified.
328 Their elongation and intensification induce straining in their cores and along the
329 interface separating the billows. The vorticity is still dominant in the sheared
330 layer. During this period (at $t > 100$ seconds), the billows aspect ratio is neither
331 decreasing nor increasing. This is due to the generation of strong vorticity
332 complemented with a tangential elongation of both vortices. The two elongated
333 billows cover the length of the domain, and therefore limit the growth of the
334 strain. The intensity of the strain decreases during this period. The strain
335 remains tangential as its direction is ~ 0 rad.

336 Thus, the billow radii in this simulation are identical to those of the reference
337 experiment. Despite this similarity, the vortices are formed earlier here and the
338 growth of their aspect ratio here is larger than in the reference experiment.
339 This is due to the intensity of the tangential strain, mainly, that reaches 0.05
340 s^{-2} compared to 0.04 s^{-2} in the reference configuration. The stronger shear
341 favors the earlier generation of billows.

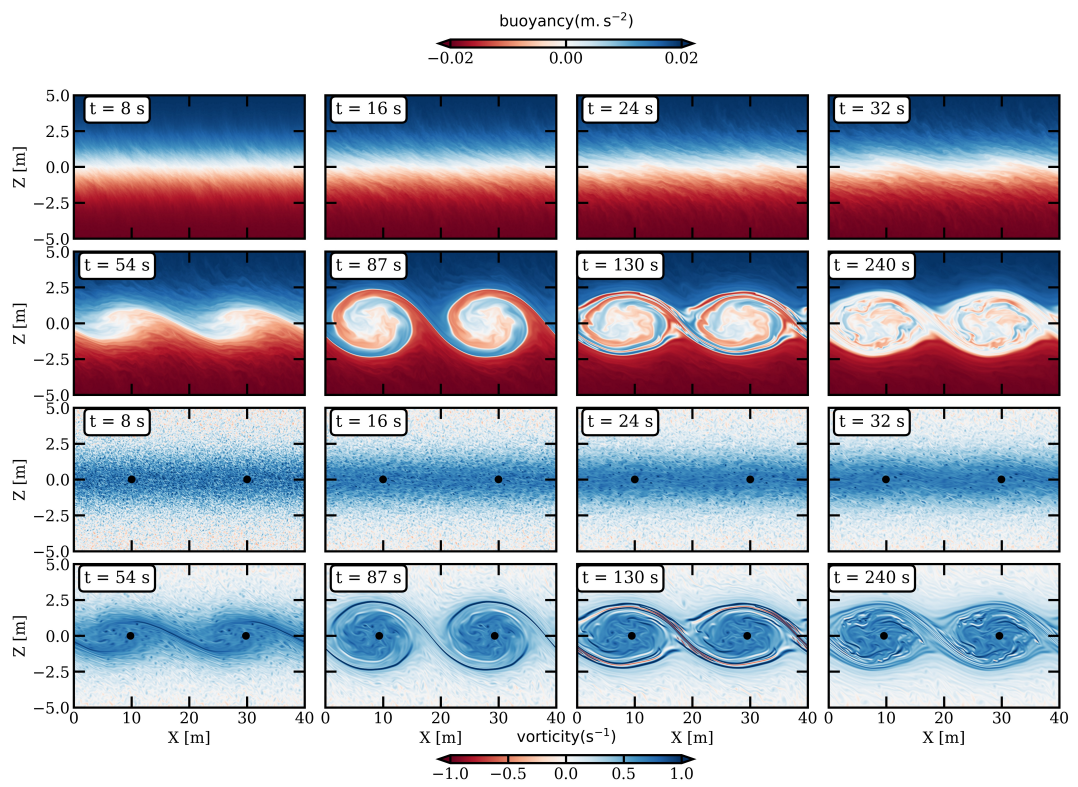


Figure 4: As Figure 2 for experiment 2.

342 *3.1.3. Sensitivity to the thickness of the interface (Exp3)*

343 In this simulation, the stratification thickness is much smaller than the shear
344 thickness (see table 1). Figure 6 shows snapshots of the spatial distribution of
345 buoyancy and vorticity fields. During the first period (for $8 < t \leq 54$ seconds),
346 small perturbations form at the thin buoyant interface. By the end of this
347 period, the small perturbations evolve as two crests propagating in the opposite
348 direction of the two troughs. Then (for $87 \leq t \leq 130$ seconds), the perturbations
349 evolve as two cyclonic billows that elongate in the direction of the sheared flow.
350 Finally ($t \sim 240$ seconds), the billows reach their full horizontal extent and
351 filaments develop in their cores. The average radius of these billows is ~ 3.8 m.

352 During the linear stage of the instability (at $t \sim 54$ seconds), the vorticity
353 dominates the strain almost everywhere in the domain, except in local strips
354 in the top and bottom layers (figure 7a). The billows are not definitely formed
355 yet and their aspect ratio remains weakly varying (~ 0.145), as shown in figure
356 7b. The billows aspect ratio varies with a decreasing strain intensity during this
357 period. The strain is tangential (its direction is ~ 0 rad).

358 Then (at $t \sim 87$ seconds), the sheared layer rolls up and two distinct billows
359 are formed. The billows induce intense vorticity in the sheared layer and along
360 the braid ($OW < 0$). The billows also lead to an intensified straining in the
361 upper and bottom layers. The aspect ratio of the two billows grows and reaches
362 values ~ 0.11). Despite the growth of their aspect ratio, the intensity of the
363 strain varies weakly ($\sim 0.02 \text{ s}^{-2}$) with a tangential direction (~ 0.1 rad).

364 Finally (at $t \sim 130$ and 240 seconds), the billows intensify and elongate.
365 During this period, the vorticity is still dominant in the sheared layer. Mean-
366 while, the strain dominance is noticeable above and below the sheared layer.
367 The billow aspect ratio increases (at $t > 150$ seconds) and weakly intensifies the
368 tangential strain ($\sim 0.02 \text{ s}^{-2}$).

369 Thus, in comparison to the reference simulation, the average radius of the
370 billows remains the same. Despite this similarity, their aspect ratio is larger
371 and the tangential strain is less dominant. The reduced stratification thickness

372 helps in the earlier growth of billows. Meanwhile, it induces less strain in the
373 core of the billows and along the braid.

374 3.1.4. Sensitivity to topographic ridges (Exp4)

375 Figure 8 shows the time evolution of the (plane) buoyant interface above
376 topographic ridges. Firstly (for $8 \leq t \leq 54$ seconds), the antisymmetric sheared
377 flow and its interaction with ridges cause the deformation of the plume base.
378 This deformation yields to three distinct cyclonic billows of different sizes (av-
379 erage radius ~ 3 m). These three billows mutually interact which alters their
380 respective shapes. These billows also interact with the topographic ridges which
381 favors their stretching. Then (for $87 \leq t \leq 240$ seconds), the sheared flow evolves
382 in different chaotic vortices and anticyclonic filaments are generated at their
383 edges due to their mutual interactions; and their stretching above the ridges.

384 Next, we evaluate the spatial distribution of the Okubo-Weiss parameter
385 (figure 9a). First (at $t \sim 54$ seconds), the vorticity dominates in the sheared
386 layer albeit some straining in the core of the billows. During this period ($t \leq 54$
387 seconds), the intensity of the strain increases sharply ($\sim 0.01 \text{ s}^{-2}$), as shown in
388 figure 9b. The growth of the strain exhibits an elongation of the billows in the
389 tangential direction (aspect ratio ~ 0.2). After this period ($t > 54$ seconds), the
390 elongation of the eddies is nor increasing nor decreasing due to: (i) the mutual
391 interactions between the billows, (ii) the billows vertical extent which constricts
392 the regions where the strain dominates; and therefore this latter weakens, and
393 (iii) the continuous interaction between the billows and the topographic ridges.

394 Thus, in comparison with the reference configuration, the interaction be-
395 tween topographic ridges and the anti-symmetric shear flow favors the develop-
396 ment of three distinct cyclonic billows. The average billow size is small com-
397 pared with the reference configuration due to their mutual interaction and their
398 stretching above the ridges. The tangential strain is also noticeable above the
399 ridges which increases its intensity compared with the reference configuration.

3.2. Modal analysis and instability growth

In this section, we evaluate the most unstable modes of the stratified-sheared river plume base. Those unstable modes are categorized as Holmboe and Kelvin-Helmholtz instabilities as described in section 2.4. Their growth, vertical structure and the time evolution of their turbulent energies are computed. We explore the sensitivity of these instabilities to the various parameters.

3.2.1. Reference configuration

Two vertical shear instabilities are investigated here, the Kelvin-Helmholtz and the Holmboe instabilities. The vertical shear instabilities exist since the necessary condition for their development (Richardson number smaller than 0.25) is satisfied already in the initial conditions. The Kelvin-Helmholtz instability is characterized by large growth rate and zero phase velocity. The Holmboe instability has a nonzero phase velocity and smaller growth rates.

We use the linear stability theory to investigate these instabilities (figure 10a). This analysis predicts that Kelvin-Helmholtz instability occurs for large wavelengths ($k \sim 0.23 \text{ m}^{-1}$, $\lambda = \frac{2\pi}{k} \sim 27 \text{ m}$). The Holmboe instability occurs for smaller wavelengths ($k \sim 5.4 \text{ m}^{-1}$, $\lambda \sim 1 \text{ m}$). The identification of Holmboe instability has been investigated using the bifurcation theory as shown in figure B.14 and as explained in Appendix B.

The most unstable mode for the Kelvin-Helmholtz instability has a growth time scale ~ 17.6 seconds. The Holmboe instability unstable mode develops slowly with a growth period ~ 88.4 seconds. The Holmboe waves have a phase speed of 2.4 cm s^{-1} .

Next, we explore the vertical structure of the magnitude of the streamwise velocity for the Kelvin-Helmholtz and Holmboe instabilities (figure 10b,c). The Kelvin-Helmholtz mode has a constant velocity at the surface and near the bottom. In this mode, the streamwise velocity is maximal ($\sim 10 \text{ cm s}^{-1}$) at the sheared interface or at the critical layer (around mid-depth) surrounded with minima ($\sim 3.3 \text{ cm s}^{-1}$) at the upper and lower density interfaces. These minima have the same amplitude and are symmetric with respect to the critical layer

430 depth. The Holmboe mode is characterized by a local minimum ($\sim 22.3 \text{ cm s}^{-1}$)
431 observed at the critical layer. This local minimum is found in a thin layer (of
432 a few cm) surrounded by two secondary lobes. The upper lobe flows slightly
433 faster than the lower lobe.

434 Now, we evaluate the horizontally and vertically (from the surface to the crit-
435 ical layer) averaged Eddy Kinetic Energy (EKE) for the Total, Kelvin-Helmholtz
436 and Holmboe perturbations (figure 11a). Early time ($0 < t \leq 50$ seconds) is
437 associated with a slight increase of the total EKE which characterizes the onset
438 of the instability. Then (at $50 < t \leq 150$ seconds), a sharp increase of the total
439 and KH EKE is observed indicating that the instability fully develops into two
440 distinct cyclonic billows, and the initiation of their elongations. Then a decrease
441 of the total and KH EKE is observed since the billows are well developed and
442 dissipation can occur.

443 The KH mode turbulent energy represents an important fraction of the total
444 EKE ($\sim 10\%$). The Holmboe instability, characterized by smaller wavelengths,
445 develops when the KH instability slackens or relaxes. The EKE associated
446 with Holmboe instability is much smaller (10^4 smaller) than the KH EKE.
447 This indicates that the KH instability is the dominant nonlinear process in the
448 reference simulation.

449 3.2.2. Sensitivity to the vertical shear (*Exp2*)

450 In this case, the KH instability develops for larger wavelengths ~ 27 m and
451 a growth time ~ 11.4 seconds (figure 10a). Meanwhile, the Holmboe instability
452 develops for smaller wavelengths ~ 2 m ($k \sim 2.9 \text{ m}^{-1}$) and a slower growth
453 time of 112 seconds. The Holmboe instability induces turbulent waves that
454 travel slowly with a phase speed $\sim 0.7 \text{ cm s}^{-1}$.

455 Now, we analyze the vertical structure of the streamwise velocity for each
456 instability (figure 10b,c). For the Kelvin-Helmholtz instability, the streamwise
457 velocity is uniform in the top and bottom 2 m. This velocity diminishes in the
458 upper density interface with a local minimum of 3.5 cm s^{-1} . In the shear layer
459 (between -2 and 2 m), the flow is faster with a maximum of 9 cm s^{-1} . It is

460 again slower in the lower density interface. This shows that the KH instability
 461 is intensified in the shear layer while it slackens at both density interfaces.
 462 Meanwhile, the vertical structure of the Holmboe mode has a minimum (~ 15
 463 cm s^{-1}) at the critical layer (depth ~ 5 m) surrounded by two lobes. The
 464 lower lobe travels faster than the upper lobe. The Holmboe instability results
 465 therefore in two waves traveling at different speeds around the critical layer.

466 Finally, we examine the time evolution of the EKE for the total perturba-
 467 tions, and the KH and Holmboe decompositions (figure 11b). The total and
 468 KH EKE starts increasing when the generation of the KH instability starts (at
 469 $t > 40$ seconds). Then, these turbulent energies reach a maximum around 90
 470 seconds once the billows are fully formed. After this peak, the total and KH
 471 EKE increase again during two distinct periods (for $125 < t \leq 150$ seconds,
 472 and between 175 and 200 seconds). These peaks correspond to the elongation
 473 of the billows and their intensification. Their intensification leads to the devel-
 474 opment of small scale features in their cores which may also increase the EKE.
 475 The Holmboe energy increases during periods when the total and KH energies
 476 weaken. The KH instability represents the dominant process in this experiment
 477 (it is stronger than the Holmboe instability by 10^3).

478 Thus, compared to the reference configuration, the stronger shear: (i) speeds
 479 up the growth of the KH instability, (ii) retards the growth of the Holmboe in-
 480 stability, (iii) increases the wavelength of the Holmboe instability, (iv) enhances
 481 by an order of magnitude the energetic contribution of Holmboe instabilities
 482 and (v) diminishes the propagation of Holmboe waves with a lower layer (near
 483 the critical layer) traveling faster than the upper layer.

484 3.2.3. Sensitivity to the thickness of the interface (Exp3)

485 When the thickness of the buoyant layer is small compared with the shear
 486 thickness, the KH and Holmboe instabilities co-exist. The KH instability is
 487 characterized by larger wavelength ($\lambda \sim 27$ m) and faster growth time ~ 15
 488 seconds (figure 10a). The Holmboe instability grows slowly (~ 663 seconds)
 489 and with a smaller wavelength ~ 5 m. The Holmboe waves propagate with a

490 phase speed $\sim 2 \text{ cm s}^{-1}$.

491 Now, we evaluate the vertical structure of the Holmboe and KH instabilities
 492 (figure 10b,c). The streamwise velocity increases in the shear layer with a max-
 493 imum of 8 cm s^{-1} , and it is slower at the upper and lower shear interfaces (\sim
 494 4 cm s^{-1}). The streamwise velocity for the Holmboe mode is minimal (~ 0.05
 495 cm s^{-1}) around the critical layer. Two layers are observed around this critical
 496 layer propagating at different speeds. The upper layer moves slightly faster than
 497 the lower layer.

498 To quantify the turbulent activity, we plot the time evolution of the EKE
 499 for the total, KH and Holmboe perturbations (figure 11c). The total and KH
 500 EKE increase after the onset of the vertical shear instabilities (at $t > 50$ sec-
 501 onds). They reach a maximum at $t \sim 100$ seconds once the cyclonic billows
 502 are generated. Then, they increase again after 150 seconds to reach a second
 503 maximum at $t \sim 180$ seconds. These second maxima correspond to the elonga-
 504 tion and intensification of the billows. Holmboe EKE increases during periods
 505 of relaxation of both the total and KH EKE. Holmboe instability may exist in
 506 this case but its contribution is weak (10^2 times smaller than the KH energy).

507 Thus, compared with the reference simulation, a small buoyancy thickness:
 508 (i) speeds up the generation of the KH instability, (ii) slows down the devel-
 509 opment of the Holmboe instability, (iii) increases the spatial wavelength of the
 510 Holmboe instability and (iv) slightly diminishes the propagation speed of the
 511 Holmboe waves.

512 3.2.4. Sensitivity to topographic ridges (Exp4)

513 In the presence of topographic ridges, the KH and Holmboe instabilities co-
 514 exist. The KH instability grows quickly in time (at ~ 14 seconds) and develops
 515 spatially with a wavelength $\sim 27 \text{ m}$ (figure 10a). The Holmboe instability
 516 grows with a shorter wavelength $\sim 1 \text{ m}$. Its growth period is ~ 46 seconds. The
 517 Holmboe instability waves propagate slowly, with a phase speed $\sim 0.5 \text{ cm s}^{-1}$.

518 Then, we evaluate the vertical structure of the KH and Holmboe instabilities
 519 in terms of the streamwise velocity magnitude (figure 10b,c). The streamwise

520 velocity of the Kelvin Helmholtz mode of instability increases in the shear layer
 521 ($\sim 12.5 \text{ cm s}^{-1}$) and slackens at the edges of this layer. The Holmboe instability
 522 mode has a streamwise velocity weakening at the critical layer and strengthening
 523 above and below this layer with the same speed ($\sim 60 \text{ cm s}^{-1}$).

524 Finally, we analyze the total, KH and Holmboe EKE during the simulated
 525 period (figure 11d). The total EKE grows rapidly; it reaches a maximum at $t \sim$
 526 50 seconds. Similarly, the KH EKE increases rapidly due to the fast generation
 527 of billows. Then ($t > 100$ seconds), the total EKE decreases due to frictional
 528 processes induced by the interaction between billows and the topographic ridges.
 529 The latter is also observed for the KH EKE. Meanwhile, the Holmboe EKE
 530 grows during periods of relaxation/decrease of the KH instability but with a
 531 smaller contribution (10^3 smaller).

532 Thus, in comparison to the reference simulation, the topographic ridges: (i)
 533 strengthens the KH and Holmboe instabilities growth due to the interaction
 534 of the sheared flow with topographic ridges which accelerates the fluid, (ii)
 535 dissipates the KH instability through frictional processes and (iii) slows down
 536 the Holmboe induced waves and renders their wavelength.

537 3.3. Turbulent mixing

538 In this section, we characterize the turbulent mixing by : (i) the EKE pro-
 539 duction, (ii) the buoyancy and EKE dissipate rates, and (iii) mixing statistics.

540 3.3.1. Reference configuration

541 First, we evaluate the time evolution of the mass and momentum mixing
 542 coefficients, and their dissipation rates (figure 12a). After the onset of the
 543 instability (at $t > 50$ seconds), the turbulent mixing of mass and momentum
 544 sharply increase until it reaches a maximum at $t \sim 120$ seconds. This maximum
 545 corresponds to the generation of the billows which favor fluid entrainment and
 546 therefore mixing between the upper and lower layers. Since turbulent energy
 547 is produced via mixing, an energy sink is necessary. Dissipative processes (of
 548 EKE and EAPE/buoyancy) contribute to this sink. The EKE and buoyancy

549 dissipation rates reach a maximum (at $t \sim 150$ seconds) when the sources of
 550 EKE weaken.

551 Once the billows are formed, they elongate and intensify (for $150 < t \leq$
 552 175 seconds). Their elongation and intensification strengthens the water recir-
 553 culation in their cores and thus the mixing of mass and momentum increases.
 554 During this period, the dissipation rates of EKE and of buoyancy increase.

555 Finally (for $t > 175$ seconds), the EKE production by mass and momen-
 556 tum mixing decreases. This is also accompanied by smaller dissipation rates of
 557 buoyancy and EKE. This is due to the full elongation of vortices which induces
 558 less turbulence and therefore the production and dissipation of turbulent energy
 559 drop.

560 To quantify the turbulent mixing, we plot the mass and momentum mixing
 561 coefficients, the buoyancy and EKE vertical dissipation rates, the turbulent
 562 Prandtl number and the irreversible mixing efficiency (figure 13). The turbulent
 563 Prandtl number is ~ 0.2 , much less than unity (figure 13e). This indicates that
 564 the flow is in a pre-turbulent phase. This state is due to large mass mixing
 565 $K_b \sim 3.4 \times 10^{-3} \text{m}^2 \text{s}^{-1}$ compared with the momentum mixing $K_m \sim 7.2 \times$
 566 $10^{-4} \text{m}^2 \text{s}^{-1}$ (figure 13a,b). The pre-turbulent flow and its mixing coefficients
 567 are largely due to high EKE dissipation $\epsilon \sim 2 \times 10^{-4} \text{m}^2 \text{s}^{-3}$ compared with weak
 568 EAPE dissipation $\epsilon_b \sim 7 \times 10^{-6} \text{m}^2 \text{s}^{-3}$ (figure 13c,d). The pre-turbulent flow is
 569 influenced by the KH and Holmboe instabilities. They influence the turbulent
 570 mixing, as can be quantified with the irreversible mixing efficiency. Here, the
 571 Holmboe instability is more efficient ($\Gamma_i \sim 1 > 0.2$) in mixing the mass and
 572 momentum than the Kelvin-Helmholtz instability ($\Gamma_i \sim 0.9 > 0.2$), as shown in
 573 figure 13f.

574 3.3.2. Sensitivity to the vertical shear (Exp2)

575 The enhanced shear favors an early growth of the mass and momentum
 576 mixing due to the rapid generation of instabilities (figure 12b).

577 The momentum mixing increases (at $t > 50$ seconds) once the shear layer
 578 deforms. It reaches a maximum early (at $t \sim 60$ seconds) of $\sim 4 \times 10^{-3} \text{m}^2 \text{s}^{-1}$.

579 The dissipation of EKE reaches a maximum (at $t \sim 60$ seconds) of $\sim 5 \times 10^{-4}$
 580 $\text{m}^2 \text{s}^{-3}$. After this period (for $t > 60$ seconds), the momentum mixing decreases.
 581 Mass mixing shows variations similar to those of momentum mixing, though
 582 an order of magnitude larger. Meanwhile, the buoyancy dissipation increases
 583 sharply, with a maximum $\sim 5 \times 10^{-5} \text{m}^2 \text{s}^{-3}$ occurring at $t \sim 100$ seconds,
 584 during periods when mass mixing relaxes.

585 In this experiment, the flow is in a pre-turbulent phase since the turbulent
 586 Prandtl number is ~ 0.2 (figure 13e); momentum mixing $\sim 1.6 \times 10^{-3} \text{m}^2 \text{s}^{-1}$
 587 dominates over mass mixing $\sim 1.6 \times 10^{-4} \text{m}^2 \text{s}^{-1}$ (figure 13a,b). This pre-
 588 turbulent flow also corresponds to stronger EKE dissipation ($3 \times 10^{-4} \text{m}^2 \text{s}^{-3}$)
 589 than buoyancy dissipation ($2.5 \times 10^{-5} \text{m}^2 \text{s}^{-3}$) (figure 13c,d). Turbulent mixing
 590 is influenced by the two instabilities, as measured by their mixing efficiencies.
 591 The Kelvin-Helmholtz instability contributes more to the mixing ($\Gamma_i \sim 0.9 >$
 592 0.2) than the Holmboe instability ($\Gamma_i \sim 0.4 > 0.2$) (figure 13f).

593 Thus, in comparison with the reference configuration, the enhanced shear: (i)
 594 speeds up the mixing of the mass and momentum, (ii) does not change the nature
 595 of the flow (pre-turbulent), (iii) strengthens the momentum mixing and the
 596 induced EKE dissipation rates, (iv) weakens the mass mixing and strengthens
 597 the EAPE dissipation rates and (iv) intensifies the mixing efficiency induced by
 598 the Kelvin-Helmholtz instability and decreases the mixing efficiency induced by
 599 the Holmboe instability.

600 3.3.3. Sensitivity to the thickness of the interface (Exp3)

601 When the stratification thickness is reduced compared to the shear thickness,
 602 the momentum mixing increases sharply (at $t > 50$ seconds). It reaches a
 603 maximum $4 \times 10^{-3} \text{m}^2 \text{s}^{-1}$ at $t \sim 75$ seconds. The production of EKE is
 604 balanced by a growth of EKE dissipation, reaching values $\sim 2.5 \times 10^{-4} \text{m}^2 \text{s}^{-3}$.
 605 Once the billows are generated ($75 < t \leq 150$ seconds), momentum mixing
 606 and its induced dissipation decrease. Then (for $t > 150$ seconds), both the
 607 sink and the shear production of turbulent energy increase again due to the
 608 elongation of billows which induce a strong recirculation and also favor mixing

609 and dissipation.

610 Mass mixing shapes the EKE production in the same way as momentum
611 mixing, with a maximum $\sim 4.5 \times 10^{-4} \text{ m}^2 \text{ s}^{-1}$ at $t \sim 75$ seconds. Meanwhile,
612 the sink of EAPE through buoyancy increases during periods when the mass
613 mixing relaxes or decreases. Buoyancy dissipation is not important in this case
614 ($\sim 10^{-12} \text{ m}^2 \text{ s}^{-3}$); momentum dissipation is then the sole turbulent energy sink.

615 The flow is in a turbulent phase as $P_r \sim 10$ (figure 13e). The turbulent
616 flow induces more momentum mixing $\sim 3 \times 10^{-3} \text{ m}^2 \text{ s}^{-1}$ than mass mixing
617 $\sim 2 \times 10^{-4} \text{ m}^2 \text{ s}^{-1}$ (figure 13a,b). The sink of turbulent energy is higher for
618 the momentum $\sim 10^{-4} \text{ m}^2 \text{ s}^{-3}$ than for the buoyancy $\sim 10^{-12} \text{ m}^2 \text{ s}^{-3}$ (figure
619 13c,d). The Holmboe instability contributes efficiently to the turbulent mixing
620 since $\Gamma_i \sim 0.6 > 0.2$. Meanwhile, the KH instability is not efficient $\Gamma_i \sim 0.01 <$
621 0.2 (figure 13f).

622 Thus, in comparison to the reference configuration, the reduced stratification
623 thickness: (i) increases the momentum mixing and decreases the mass mixing,
624 (ii) shapes the flow in a turbulent phase and (iii) relates the mixing efficiency
625 to the Holmboe instability.

626 3.3.4. Sensitivity to topographic ridges (Exp4)

627 Figure 12d shows the time evolution of the mass and momentum mixing
628 coefficients, the EKE and buoyancy dissipation rates. During the onset of the
629 instability (for $t < 100$ seconds), the momentum mixing and EKE dissipation
630 decrease due to the rapid generation of the billows and their interaction with
631 topographic ridges which favor frictional processes. Then (at $t > 100$ seconds),
632 the billows are fully developed and they engulf almost the entire vertical extent
633 of the domain. The latter induces a strong momentum mixing reaching $\sim 10^{-2}$
634 $\text{m}^2 \text{ s}^{-1}$ with EKE dissipation rate $\sim 5 \times 10^{-2} \text{ m}^2 \text{ s}^{-3}$. The interaction between
635 the topographic ridges and the shear flow induces mixing and EKE dissipation
636 through intense convection and/or bottom frictional processes.

637 Mass mixing varies as momentum mixing, and reaches values $\sim 2.5 \times 10^{-2}$
638 $\text{m}^2 \text{ s}^{-1}$. We can relate this to the vorticity and buoyancy torques in the vorticity

639 transport equation. The EAPE/buoyancy dissipation varies as the mass mixing
 640 ($\sim 2.5 \times 10^{-5} \text{ m}^2 \text{ s}^{-3}$) except during the onset of the instability ($t < 100$ seconds).
 641 The strong dissipation of buoyancy is likely due to the interaction between the
 642 flow and the bottom during this early period.

643 In this experiment, the flow is pre-turbulent as $P_r \sim 0.45$ (figure 13e). The
 644 latter is explained by higher mass mixing $\sim 2.5 \times 10^{-2} \text{ m}^2 \text{ s}^{-1}$ than momentum
 645 mixing $\sim 7.6 \times 10^{-3} \text{ m}^2 \text{ s}^{-1}$ (figure 13a,b). The sink of turbulent energy is higher
 646 for momentum $\sim 2.2 \times 10^{-3} \text{ m}^2 \text{ s}^{-3}$ than for buoyancy $\sim 2.4 \times 10^{-5} \text{ m}^2 \text{ s}^{-3}$ (figure
 647 13c,d). Both the KH and Holmboe instabilities are efficient ($\Gamma_i > 0.2$) in mixing
 648 the fluid; the Holmboe instability contributes more ($\Gamma_i \sim 1.1$) to the turbulent
 649 mixing than the KH instability ($\Gamma_i \sim 0.8$) (figure 13f).

650 Thus, in comparison with the reference configuration, the interaction be-
 651 tween the sheared flow and topographic ridges: (i) strengthens the momentum
 652 and mass turbulent mixing, (ii) slightly increases the turbulence in the flow
 653 however the pre-turbulent phase persists, (iii) favors EKE and EAPE/buoyancy
 654 dissipations and (iv) slightly increases the mixing efficiency of the Holmboe in-
 655 stabilities and decreases the mixing efficiency of the KH instabilities.

656 4. Discussion

657 4.1. The structure and dynamics of stratified sheared flows

658 In this paper, we have studied the structure and dynamics of stratified
 659 sheared flows via 2D non-hydrostatic numerical simulations. In these simu-
 660 lations, we analyzed the flow evolution in various physical configurations.

661 Firstly, we observed that the stratified sheared interface evolves in time
 662 from a wavy strip to billows. We carried out sensitivity experiments and we
 663 compared them to a reference simulation. In the flat bottom cases, we showed
 664 that the generated cyclonic billows have similar sizes. Their sizes are constrained
 665 by their interactions, the initial conditions and the horizontal length of the
 666 domain. An enhanced shear and a small buoyant interface trigger an earlier
 667 growth of these vortices. The recirculation inside their cores is intensified when

668 the initial shear is increased; this recirculation is weakened when the buoyant
669 interface is thin (compared with the shear layer thickness). This recirculation
670 favors the entrainment between the upper and bottom layers. We also noted
671 that topographic ridges favor the generation of smaller cyclonic billows with
672 anticyclonic filaments at their edges. In this latter case, the antisymmetric
673 shear flow induces noticeable turbulence in the domain.

674 Secondly, we examined the spatial distribution of the Okubo-Weiss parame-
675 ter for the different experiments. This tool has been used to identify mesoscale
676 eddies in previous studies (Le Vu et al., 2018; Ioannou et al., 2019; de Marez
677 et al., 2020; Ayouche et al., 2021b). In our experiments, the vorticity domi-
678 nates in the shear layer when the bottom is flat. The billows are generated in
679 the stratified sheared layer. Over topographic ridges, vorticity is also generated
680 due to frictional processes and to fluid acceleration. In this case, the vorticity
681 dominates mostly in the whole domain, once strong turbulence is generated.

682 Thirdly, we explored the spatial distribution, and in particular the predom-
683 inance, of the strain field. We showed that the flow is strained above and below
684 the sheared layer when the bottom is flat. This is due to the constriction of
685 the flow in these layers resulting in high/low pressure regions. In these cases,
686 the strain is also generated in the cores of the billows and along the braid. The
687 latter is due to the flow recirculation which may induce local straining. In these
688 experiments, the enhanced shear intensifies the strain in the upper and bottom
689 layers, and in the cores of billows due to increased fluid acceleration and recir-
690 culation. When the buoyant interface is thin compared to the sheared interface,
691 the straining becomes stronger in the upper and lower layers but weakens inside
692 the billows. This is due to the increased area above and below the buoyant
693 interface which results in more pressure forces and therefore in higher strain.
694 Meanwhile, when the bottom is wavy, the strain dominates locally at the edges
695 of the small billows and filaments and above the ridges. This is due to the inter-
696 action between the wavy bottom and the antisymmetric flow; this interaction
697 creates more turbulence later in the simulation.

698 Lastly, we showed that the strain is tangential when the bottom is flat since

699 only streamwise velocity is considered initially. We found that the tangential
700 strain is correlated with the horizontal elongation of the billows. The tangential
701 strain and the induced billows elongation are intensified when the shear in-
702 creases, and even more so as the buoyant interface is thin. Such findings can be
703 explained by the tangential force exerted by the enhanced shear on the billows
704 causing their deformation in the parallel direction to the flow (this tangential
705 force is amplified by the increased area when the buoyant interface is thin). This
706 has been also observed for the case of topographic ridges, tangential strain de-
707 forms these billows due to the local fluid acceleration induced by friction (above
708 the ridges) and the background shear (top layer).

709 The generated billows have an average aspect ratio below $\frac{1}{3}$; such an extreme
710 aspect ratio may lead to their splitting in the absence of background strain and
711 shear (Mitchell and Rossi, 2008). However, in our experiments the billows do
712 not split due to their mutual interactions and to the presence of a shear flow.
713 This small aspect ratio is related to the elongation/strain of the billows. In
714 particular, a single billow deforms into an elliptical vortex with filaments at
715 its rim in the presence of background shear (Guha et al., 2013). Nevertheless,
716 overall, the vorticity dominates the strain in the experiments with billows. This
717 has also been observed in other studies of Kelvin-Helmholtz billows (Fontane
718 and Joly, 2008).

719 4.2. Development and role of KH and Holmboe instabilities

720 We have analyzed the vertical shear instabilities in stratified sheared flows,
721 via the linear stability analysis based on 2D non-hydrostatic equations.

722 Firstly, we identified two vertical shear instabilities: Kelvin-Helmholtz and
723 Holmboe, in our flow configuration. The Kelvin-Helmholtz instability is charac-
724 terized as the most unstable mode by the linear analysis. The Kelvin Helmholtz
725 instability has a wavelength ~ 12 times the shear thickness in the studied cases.
726 The KH wavelength is typically an order of magnitude larger than the shear
727 layer thickness as shown in Smyth and Moum (2012). The wavelengths may
728 also be constrained by the domain geometry and the initial conditions. Ver-

729 tically, the KH instability has a larger magnitude in the shear layer with a
730 maximum reached at the critical layer (plume base). The Kelvin-Helmholtz in-
731 stability reaches its maximum amplitude within a time range between 11 and
732 18 seconds. Compared to the reference simulation, this instability grows faster
733 and intensifies (in terms of EKE): (i) when the shear increases, (ii) when the
734 shear flow interacts with topographic ridges and also (iii) for a small buoyancy
735 interface thickness.

736 Secondly, the Holmboe instability is characterized by smaller wavelengths
737 (between 1 and 5 m) and a longer growth time (between 40 and 663 seconds).
738 The smallest wavelength (~ 1 m) and the shortest growth time (~ 40 -80 sec-
739 onds) are found for the reference and wavy bottom experiments. Meanwhile,
740 the enhanced shear slows down the growth of the Holmboe instability (~ 112
741 seconds), and its wavelength is larger (~ 5 m). The small buoyancy thickness
742 induces a Holmboe instability with the slowest growth time (~ 663 seconds) and
743 with a wavelength ~ 2 m. The difference between the Kelvin-Helmholtz and
744 Holmboe instabilities is that the first is stationary (zero phase speed) and the
745 second is propagating (non-zero phase speed). The Holmboe instability is char-
746 acterized by two counter-propagating waves (lobes) above and below the plume
747 base. At the plume base, the magnitude of the streamwise velocity is mini-
748 mal (and maximal above and below) for the Holmboe instability; it is maximal
749 for the Kelvin-Helmholtz instability. In terms of turbulent energy, the Holm-
750 boe instability is intensified during periods of relaxation/decrease of the Kelvin
751 Helmholtz instability but with a smaller impact. Indeed, the KH EKE repre-
752 sents an important fraction ($\sim 10\%$) of the total turbulent energy. Holmboe
753 instability amplification occurs for a sharp buoyancy interface (small buoyancy
754 thickness) and in the presence of a wavy bottom.

755 Thus, we showed the existence of the primary Kelvin-Helmholtz and Holm-
756 boe instabilities in the studied experiments. We showed that the wavy bottom
757 and the small buoyancy thickness are propitious to the intensification of the
758 Holmboe instability. The Holmboe instability has a smaller wavelength and a
759 larger growth time compared with the Kelvin-Helmholtz instability as shown

760 in Alexakis (2005). Vertically, the Kelvin-Helmholtz instability has a larger in-
761 fluence in the sheared layer with a maximum at the base of the plume. This
762 result is similar to what has been observed at the base of a surface mixed layer
763 when a stratified flow interacts with the Ekman induced currents (Smyth and
764 Moum, 2012). The interaction between downwelling favorable winds and the
765 Gironde river plume favors the development of the Kelvin-Helmholtz instabil-
766 ity (Ayouché et al., 2020, 2021a). This instability has been also observed, and
767 simulated using a 3D NH numerical model, in the Yangtze river estuary due to
768 the interaction between tidal flood and high water slack. The Kelvin-Helmholtz
769 instability has also been observed and analyzed using the Taylor Goldstein equa-
770 tion in the Frazer river estuary. The authors found that during ebb tide and
771 high discharge events, the wavelength of such instability is ~ 24 m which is
772 similar to the value in our simulations. Meanwhile, the Holmboe instability is
773 characterized by two counter-propagating waves (nonzero phase speed) within
774 the critical layer (plume base). It grows also slowly compared to the KH in-
775 stability and with shorter wavelengths. The latter findings have been indicated
776 in previous studies (Smyth and Peltier, 1991; Ortiz et al., 2002; Alexakis, 2005;
777 Parker et al., 2020). Carpenter et al. (2010) used in-situ observations and the
778 linear analysis stability theory and indicated the coexistence of the KH and
779 Holmboe instabilities in the Frazer estuary. Their findings inferred that both
780 instabilities may coexist in stratified sheared flows such as river estuaries which
781 corroborates the results of our study.

782 4.3. Turbulent mixing: intensity and efficiency

783 We have studied the turbulent mixing via: (i) the mass and momentum
784 mixing coefficients, (ii) the EAPE and EKE dissipation rates and (iii) statistics.

785 We explored these diagnostics in a reference simulation and we carried out
786 different sensitivity experiments. In these experiments, the turbulent mixing
787 (mass and momentum) and dissipation rates (EKE and EAPE) increase after the
788 linear stage of the instability. Then, billows are generated inducing entrainment
789 between the upper and bottom layers in their cores. The entrainment between

790 these layers results in turbulent mixing of mass and momentum. This mixing
 791 is a source of turbulent energy and it is also linked to its sink (dissipation
 792 rates). The momentum mixing and EKE dissipation rate vary similarly during
 793 the generation, intensification and elongation of the billows; when the bottom
 794 is flat. This remains true for the wavy bottom due to frictional processes and
 795 enhanced turbulence; this turbulence generates smaller cyclonic billows above
 796 the bottom and anticyclonic filaments in the water column. Another source
 797 of turbulent energy is the mass mixing. The mass mixing increases once the
 798 billows are generated. This is due to the intensification of the stratification
 799 when the bottom and upper waters are mixed in the cores of the billows, when
 800 the bottom is flat. This is also observed when a stratified shear flow interacts
 801 with a wavy bottom resulting in smaller billows and filaments. This source of
 802 EKE is concomitant with a sink of EAPE. In these experiments, the sink of
 803 EAPE strengthens once the mass mixing weakens.

804 Then, we compared these experiments in terms of mixing statistics. We
 805 characterized the flow as either: (i) pre-turbulent ($P_r < 1$) or (iii) turbulent
 806 ($P_r > 1$). The flow is pre-turbulent in the reference simulation, when the shear
 807 increases and when the bottom is not flat. This is due to more mass mixing (\sim
 808 $10^{-4} - 10^{-2} \text{ m}^2 \text{ s}^{-1}$) than momentum mixing ($\sim 10^{-4} - 10^{-3} \text{ m}^2 \text{ s}^{-1}$). This is
 809 linked to higher EKE dissipation ($\sim 10^{-4} \text{ m}^2 \text{ s}^{-3}$) than EAPE dissipation (\sim
 810 $10^{-5} \text{ m}^2 \text{ s}^{-3}$). The enhanced shear participates in increasing the mixing (by
 811 an order of magnitude) and the induced dissipations (at least by a factor of 2).
 812 When the bottom is wavy, the flow is pre-turbulent; however turbulence state
 813 can be reached by the end of the simulation due to frictional processes. In this
 814 experiment, the momentum and mass mixing are intensified compared with the
 815 reference simulation. Frictional processes result from the interaction between
 816 the antisymmetric flow and the bottom; they induce more EKE dissipation (\sim
 817 $2 \times 10^{-2} \text{ m}^2 \text{ s}^{-3}$) than EAPE dissipation ($\sim 2 \times 10^{-5} \text{ m}^2 \text{ s}^{-3}$), despite the quasi-
 818 turbulence observed by the end of the simulation. The flow reaches a turbulent
 819 phase when the buoyancy thickness is small compared with the shear thickness.
 820 In this experiment, the momentum mixing ($\sim 2 \times 10^{-3} \text{ m}^2 \text{ s}^{-1}$) is stronger

821 than the mass mixing ($\sim 1.3 \times 10^{-4} \text{ m}^2 \text{ s}^{-1}$), due to the difference between the
 822 buoyancy and the shear thicknesses (leading to more entrainment in the shear
 823 layer than in the buoyant layer). The EKE dissipation is similar to that in the
 824 reference configuration, but the EAPE dissipation is weaker ($\sim 10^{-12} \text{ m}^2 \text{ s}^{-3}$)
 825 due to the small buoyant layer thickness. Previous studies in the Frazer river
 826 estuary have shown that the diffusivity mixing coefficients range between 10^{-4}
 827 and $10^{-3} \text{ m}^2 \text{ s}^{-1}$ which is similar to what we found in flat bottom experiments
 828 (MacDonald, 2003; Tedford et al., 2009). In the near field region of river plumes,
 829 EKE dissipation rates are intensified and reach values between 10^{-4} and 10^{-3}
 830 $\text{m}^2 \text{ s}^{-3}$ (MacDonald and Geyer, 2004; Kilcher et al., 2012; Horner-Devine et al.,
 831 2015). These values are similar to what has been simulated in our study: (i)
 832 lower values are expected in river estuaries (flat bottom experiments) and (ii)
 833 higher values are expected in the near-field (wavy bottom experiment).

834 Finally, we analyzed the turbulent mixing efficiency to understand the in-
 835 fluence of the Holmboe and the Kelvin-Helmholtz instabilities. Despite their
 836 weaker growth time, the Holmboe instabilities contribute more efficiently to the
 837 turbulent mixing than KH instabilities except when the shear increases. Their
 838 mixing efficiency are less sensitive to the thickness of the stratified layer or to
 839 the tilt of the bottom ($\Gamma_i \sim 1$). The KH instabilities are more efficient when
 840 the shear increases ($\Gamma_i \sim 0.9$) and inefficient ($\Gamma_i \sim 0.01$) when the stratification
 841 thickness is reduced. The latter results indicate that both instabilities contribute
 842 to the turbulent mixing, except when the buoyant layer thickness is small com-
 843 pared with the shear layer thickness. Yet, Holmboe instability has a larger
 844 impact on turbulent mixing than KH instability, except when the initial shear
 845 increases (smaller Richardson number). Smyth et al. (2007) found a scaling of
 846 the Holmboe momentum and mass mixing coefficients as $K_m = 2.4 \times 10^{-4} h \Delta u$
 847 and $K_b = 0.8 \times 10^{-4} h \Delta u$ (where h is the shear thickness and Δu is the differ-
 848 ence between the maximum and minimum streamwise velocity). In our study,
 849 this would lead to $K_m = 10^{-3} \text{ m}^2 \text{ s}^{-1}$ and $K_b = 3.2 \times 10^{-4} \text{ m}^2 \text{ s}^{-1}$ (see table
 850 1 and Figure 1). These values are similar to our results in the case of a small
 851 density/buoyancy thickness; this is the case where only the Holmboe instability

852 mixes efficiently.

853 These findings confirm that Holmboe instabilities are potential sources of
854 turbulent mixing in the ocean (Smyth and Winters, 2003; Salehipour et al.,
855 2016). Smyth et al. (2005) showed that the collapse of KH billows explains the
856 generation of internal waves which supports their importance in the mixing of
857 the ocean.

858 5. Conclusions

859 In this study, we have studied the dynamics, instabilities and turbulent mix-
860 ing in stratified sheared flows. We idealized these flows based on typical condi-
861 tions of river estuaries and the near-field regions of river plumes. We analysed
862 four main physical cases, varying the parameters, we identified the dominant
863 instability in each case, its structure and growth rate. The buoyancy/mass mix-
864 ing and momentum mixing have been compared for all cases and our findings
865 have been compared with previous studies and observations (still considering
866 the limitations of our idealized model and configuration).

867

868 Clearly the main limitation in our study is the absence of 3D dynamics,
869 of a more complex and realistic topography and of neighboring dynamical fea-
870 tures such as filaments and eddies. Another limiting feature of our study is
871 the absence of Coriolis effect and the interaction between stratified sheared and
872 horizontal rotational flows, leading to geostrophic or ageostrophic instabilities
873 (baroclinic and symmetric). This underlines the need for a 3D non hydrostatic
874 model to expand the present study. The use of a 3D non hydrostatic model
875 will allow us to understand the link between internal waves and 3D vertical
876 shear instabilities. Furthermore, shear flow instabilities and internal waves are
877 important in coastal environment due to their impact on marine biology and on
878 sedimentation. Only a 3D model can address these impacts.

879

880 **Appendix A. The linear stability analysis**

881 We linearize the perturbations around a background state in the non hydro-
882 static (NH) Boussinesq equations. We consider the background state to be in a
883 steady regime and in hydrostatic balance.

884 The perturbation fields are written as:

$$(b', u', w', p') = (\hat{b}(z), \hat{u}(z), \hat{w}(z), \hat{p}(z)) \exp(\sigma t + ikx) \quad (\text{A.1})$$

885 where the real part of σ is the growth rate, $-\frac{\text{Im}(\sigma)}{k}$ is the phase speed and k
886 is the horizontal wavenumber. The hat fields are eigenfunctions.

887 These perturbations have been injected in the linearized NH equations com-
888 bined into pair of equations for the vertical velocity and the buoyancy field.

889 The matrix form of the pair of equations for the vertical velocity and the
890 buoyancy field is summarized below:

$$\sigma \begin{pmatrix} \frac{d^2}{dz^2} - k^2 & 0 \\ 0 & \text{I} \end{pmatrix} \begin{pmatrix} \hat{w} \\ \hat{b} \end{pmatrix} = \begin{pmatrix} -ikU(\frac{d^2}{dz^2} - k^2) + ikU_{zz} & -k^2 \cos(\alpha) + ik \sin(\alpha) \frac{d}{dz} \\ -B_z & -ikU \end{pmatrix} \begin{pmatrix} \hat{w} \\ \hat{b} \end{pmatrix} \quad (\text{A.2})$$

891 The subscript z indicates a vertical derivative and α characterizes the bottom
892 ridges angle. Here we write $\sin(\alpha) = \max(\partial_x z_b(x))$ and $\cos(\alpha) = \sqrt{1 - \sin(\alpha)^2}$.

893 Vertical boundaries conditions are $\hat{w} = \hat{b} = 0$

894 The Howard's semicircle theorem (Kochar and Jain, 1979) is used to get
895 only physical solutions bounded by the mean flow velocity extreme values:

$$(c_r - 0.5(U_{\min} + U_{\max}))^2 + c_i^2 \leq 0.5(U_{\max} - U_{\min}) \quad (\text{A.3})$$

896 where $c_r = -\frac{\text{Im}(\sigma)}{k}$ is the phase velocity and $c_i = \frac{\text{Re}(\sigma)}{k}$. The critical layer
897 depth is defined as the depth where $U = c_r$.

898 The vertical eigenfunction have been written for a specific horizontal wavenum-
899 ber as:

$$(\hat{b}(z), \hat{u}(z), \hat{w}(z), \hat{p}(z)) = A_m \exp(imz) \quad (\text{A.4})$$

900 where A_m is the mode amplitude and m is the vertical wavenumber.

901 Finally, the perturbations from the numerical simulations have been pro-
 902 jected onto an orthogonal basis $(\exp(i(kx + mz)))_{k,m}$ to get their modal decom-
 903 positions denoted as $(\tilde{u}, \tilde{w}, \tilde{b})$. We write the modal EKE as

$$\text{E}\tilde{\text{K}}\text{E} = 0.5 \int_0^L \int_0^{H_c} (\tilde{u} * \tilde{u}^* + \tilde{w} * \tilde{w}^*) dx dz \quad (\text{A.5})$$

904 where the subscript $*$ denotes the complex conjugate, L is the horizontal
 905 length of the domain and H_c is the critical depth.

906 Appendix B. Identification of the Holmboe mode: the bifurcation 907 theory

908 In order to identify the Holmboe mode characterized by a nonzero phase
 909 velocity, we use the bifurcation theory (Khavasi et al., 2014). This theory eval-
 910 uates the intersection between $\sigma_r = \text{Re}(\sigma)$, and positive/negative branches of
 911 $\sigma_i = \text{Im}(\sigma)$. Therefore, we use this theory to identify the Holmboe mode for
 912 each experiment; and it is represented with the vertical blue line in figure B.14.

913 Acknowledgments

914 This study is part of the COCTO project (SWOT science team program)
 915 funded by the CNES. The PhD Thesis of A. Ayouche is funded by Brittany
 916 region and Ifremer. Model simulations were performed using the HPC facilities
 917 DATARMOR of 'Pôle de Calcul Intensif pour la 704 Mer' at Ifremer, Brest,
 918 France. The authors thank Guillaume Roulet for providing the numerical model
 919 'Fluid2d'. Model outputs are available upon request.

920 References

921 Alexakis, A., 2005. On holmboe's instability for smooth shear
 922 and density profiles. *Physics of Fluids* 17, 084103. URL:
 923 <https://doi.org/10.1063/1.2001567>, doi:10.1063/1.2001567,
 924 arXiv:<https://doi.org/10.1063/1.2001567>.

- 925 Ayouche, A., Carton, X., Charria, G., Theetten, S., Ayoub, N., 2020. Insta-
926 bilities and vertical mixing in river plumes: application to the bay of biscay.
927 *Geophysical & Astrophysical Fluid Dynamics* 114, 650–689. URL: [https://](https://doi.org/10.1080/03091929.2020.1814275)
928 doi.org/10.1080/03091929.2020.1814275, doi:10.1080/03091929.2020.
929 1814275, arXiv:<https://doi.org/10.1080/03091929.2020.1814275>.
- 930 Ayouche, A., Charria, G., Carton, X., Ayoub, N., Theetten, S., 2021a. Non-
931 linear processes in the gironde river plume (north-east atlantic): Insta-
932 bilities and mixing. *Frontiers in Marine Science* 8, 810. URL: [https://](https://www.frontiersin.org/article/10.3389/fmars.2021.701773)
933 www.frontiersin.org/article/10.3389/fmars.2021.701773, doi:10.
934 3389/fmars.2021.701773.
- 935 Ayouche, A., De Marez, C., Morvan, M., L'Hegaret, P., Carton, X., Le Vu,
936 B., Stegner, A., 2021b. Structure and dynamics of the ras al hadd oceanic
937 dipole in the arabian sea. *Oceans* 2, 105–125. URL: [https://www.mdpi.com/](https://www.mdpi.com/2673-1924/2/1/7)
938 [2673-1924/2/1/7](https://www.mdpi.com/2673-1924/2/1/7), doi:10.3390/oceans2010007.
- 939 Brandt, L.K., Nomura, K.K., 2007. The physics of vortex merger and the effects
940 of ambient stable stratification. *Journal of Fluid Mechanics* 592, 413–446.
941 doi:10.1017/S0022112007008671.
- 942 Browning, K.A., 1971. Structure of the atmosphere in the vicin-
943 ity of large-amplitude kelvin-helmholtz billows. *Quarterly Jour-*
944 *nal of the Royal Meteorological Society* 97, 283–299. URL:
945 [https://rmets.onlinelibrary.wiley.com/doi/abs/10.1002/qj.](https://rmets.onlinelibrary.wiley.com/doi/abs/10.1002/qj.49709741304)
946 [49709741304,](https://doi.org/10.1002/qj.49709741304) doi:[https://doi.org/10.1002/qj.49709741304,](https://doi.org/10.1002/qj.49709741304)
947 [arXiv:https://rmets.onlinelibrary.wiley.com/doi/pdf/10.1002/qj.49709741304.](https://rmets.onlinelibrary.wiley.com/doi/pdf/10.1002/qj.49709741304)
- 948 Carpenter, J.R., Balmforth, N.J., Lawrence, G.A., 2010. Identify-
949 ing unstable modes in stratified shear layers. *Physics of Fluids* 22,
950 054104. URL: <https://doi.org/10.1063/1.3379845>, doi:10.1063/1.
951 3379845, arXiv:<https://doi.org/10.1063/1.3379845>.
- 952 Delamere, P.A., Bagenal, F., 2010. Solar wind interaction with jupiter's
953 magnetosphere. *Journal of Geophysical Research: Space Physics* 115,

- 954 A10201. URL: [https://agupubs.onlinelibrary.wiley.com/doi/abs/](https://agupubs.onlinelibrary.wiley.com/doi/abs/10.1029/2010JA015347)
955 10.1029/2010JA015347, doi:<https://doi.org/10.1029/2010JA015347>,
956 arXiv:<https://agupubs.onlinelibrary.wiley.com/doi/pdf/10.1029/2010JA015347>.
- 957 Delamere, P.A., Bagenal, F., 2013. Magnetotail structure of the giant
958 magnetospheres: Implications of the viscous interaction with the solar
959 wind. *Journal of Geophysical Research: Space Physics* 118, 7045–
960 7053. URL: [https://agupubs.onlinelibrary.wiley.com/doi/abs/](https://agupubs.onlinelibrary.wiley.com/doi/abs/10.1002/2013JA019179)
961 10.1002/2013JA019179, doi:<https://doi.org/10.1002/2013JA019179>,
962 arXiv:<https://agupubs.onlinelibrary.wiley.com/doi/pdf/10.1002/2013JA019179>.
- 963 Dixit, H.N., Govindarajan, R., 2013. Effect of density stratifica-
964 tion on vortex merger. *Physics of Fluids* 25, 016601. URL:
965 <https://doi.org/10.1063/1.4773445>, doi:10.1063/1.4773445,
966 arXiv:<https://doi.org/10.1063/1.4773445>.
- 967 Dritschel, D., 1998. On the persistence of non-axisymmetric vortices in inviscid
968 two-dimensional flows. *Journal of Fluid Mechanics - J FLUID MECH* 371,
969 141–155. doi:10.1017/S0022112098002080.
- 970 Fontane, J., Joly, L., 2008. The stability of the variable-density kelvin–helmholtz
971 billow. *Journal of Fluid Mechanics* 612, 237–260. doi:10.1017/
972 S0022112008002966.
- 973 Foullon, C., Verwichte, E., Nakariakov, V., Nykyri, K., Farrugia, C., 2011.
974 Magnetic kelvin-helmholtz instability at the sun. *The Astrophysical Journal*
975 *Letters* 729, L8. doi:10.1088/2041-8205/729/1/L8.
- 976 Goldstein, S., Taylor, G.I., 1931. On the stability of superposed streams
977 of fluids of different densities. *Proceedings of the Royal Society of*
978 *London. Series A, Containing Papers of a Mathematical and Physical*
979 *Character* 132, 524–548. URL: [https://royalsocietypublishing.](https://royalsocietypublishing.org/doi/abs/10.1098/rspa.1931.0116)
980 [org/doi/abs/10.1098/rspa.1931.0116](https://royalsocietypublishing.org/doi/abs/10.1098/rspa.1931.0116), doi:10.1098/rspa.1931.0116,
981 arXiv:<https://royalsocietypublishing.org/doi/pdf/10.1098/rspa.1931.0116>.

- 982 Granskog, M., Ehn, J., Niemelä, M., 2005. Characteristics and potential impacts
983 of under-ice river plumes in the seasonally ice-covered bothnian bay (baltic
984 sea). *Journal of Marine Systems* 53, 187–196. doi:10.1016/j.jmarsys.2004.
985 06.005.
- 986 Guha, A., Rahmani, M., Lawrence, G.A., 2013. Evolution of a barotropic
987 shear layer into elliptical vortices. *Phys. Rev. E* 87, 013020. URL:
988 <https://link.aps.org/doi/10.1103/PhysRevE.87.013020>, doi:10.1103/
989 PhysRevE.87.013020.
- 990 van Haren, H., Gostiaux, L., 2010. A deep-ocean kelvin-helmholtz
991 billow train. *Geophysical Research Letters* 37, L03605. URL:
992 [https://agupubs.onlinelibrary.wiley.com/doi/abs/10.1029/
993 2009GL041890](https://agupubs.onlinelibrary.wiley.com/doi/abs/10.1029/2009GL041890), doi:<https://doi.org/10.1029/2009GL041890>,
994 arXiv:<https://agupubs.onlinelibrary.wiley.com/doi/pdf/10.1029/2009GL041890>.
- 995 Helmholtz, P., 1868. Xliii. on discontinuous movements of flu-
996 ids. *The London, Edinburgh, and Dublin Philosophical Maga-
997 zine and Journal of Science* 36, 337–346. URL: [https://doi.
998 org/10.1080/14786446808640073](https://doi.org/10.1080/14786446808640073), doi:10.1080/14786446808640073,
999 arXiv:<https://doi.org/10.1080/14786446808640073>.
- 1000 Hetland, R.D., 2005. Relating river plume structure to vertical mix-
1001 ing. *Journal of Physical Oceanography* 35, 1667 – 1688. URL: [https:
1002 //journals.ametsoc.org/view/journals/phoc/35/9/jpo2774.1.xml](https://journals.ametsoc.org/view/journals/phoc/35/9/jpo2774.1.xml),
1003 doi:10.1175/JP02774.1.
- 1004 Holt, J.T., 1998. Experiments on kelvin-helmholtz bil-
1005 lows influenced by boundaries. *Geophysical & Astrophysi-
1006 cal Fluid Dynamics* 89, 205–233. URL: [https://doi.org/
1007 10.1080/03091929808203686](https://doi.org/10.1080/03091929808203686), doi:10.1080/03091929808203686,
1008 arXiv:<https://doi.org/10.1080/03091929808203686>.
- 1009 Horner-Devine, A.R., Hetland, R.D., MacDonald, D.G., 2015.

- 1010 Mixing and transport in coastal river plumes. Annual Re-
1011 view of Fluid Mechanics 47, 569–594. URL: [https://doi.](https://doi.org/10.1146/annurev-fluid-010313-141408)
1012 [org/10.1146/annurev-fluid-010313-141408](https://doi.org/10.1146/annurev-fluid-010313-141408), doi:10.1146/
1013 [annurev-fluid-010313-141408](https://doi.org/10.1146/annurev-fluid-010313-141408), arXiv:<https://doi.org/10.1146/annurev-fluid-010313-141408>.
- 1014 Ioannou, A., Stegner, A., Tuel, A., LeVu, B., Dumas, F., Speich,
1015 S., 2019. Cyclostrophic corrections of aviso/duacs surface veloci-
1016 ties and its application to mesoscale eddies in the mediterranean
1017 sea. Journal of Geophysical Research: Oceans 124, 8913–8932.
1018 URL: [https://agupubs.onlinelibrary.wiley.com/doi/abs/10.](https://agupubs.onlinelibrary.wiley.com/doi/abs/10.1029/2019JC015031)
1019 [1029/2019JC015031](https://doi.org/10.1029/2019JC015031), doi:<https://doi.org/10.1029/2019JC015031>,
1020 arXiv:<https://agupubs.onlinelibrary.wiley.com/doi/pdf/10.1029/2019JC015031>.
- 1021 Iwanaka, Y., Isobe, A., 2018. Tidally induced instability processes sup-
1022 pressing river plume spread in a nonrotating and nonhydrostatic
1023 regime. Journal of Geophysical Research: Oceans 123, 3545–3562.
1024 URL: [https://agupubs.onlinelibrary.wiley.com/doi/abs/10.](https://agupubs.onlinelibrary.wiley.com/doi/abs/10.1029/2017JC013495)
1025 [1029/2017JC013495](https://doi.org/10.1029/2017JC013495), doi:<https://doi.org/10.1029/2017JC013495>,
1026 arXiv:<https://agupubs.onlinelibrary.wiley.com/doi/pdf/10.1029/2017JC013495>.
- 1027 Kaminski, A.K., Smyth, W.D., 2019. Stratified shear instability in a field of
1028 pre-existing turbulence. Journal of Fluid Mechanics 862, 639–658. doi:10.
1029 [1017/jfm.2018.973](https://doi.org/10.1017/jfm.2018.973).
- 1030 Khavasi, E., Firoozabadi, B., Afshin, H., 2014. Linear analysis of the stabil-
1031 ity of particle-laden stratified shear layers. Canadian Journal of Physics 92,
1032 103–115. URL: <https://doi.org/10.1139/cjp-2013-0028>, doi:10.1139/
1033 [cjp-2013-0028](https://doi.org/10.1139/cjp-2013-0028), arXiv:<https://doi.org/10.1139/cjp-2013-0028>.
- 1034 Kilcher, L.F., Nash, J.D., Moum, J.N., 2012. The role of tur-
1035 bulence stress divergence in decelerating a river plume. Jour-
1036 nal of Geophysical Research: Oceans 117, C05032. URL:
1037 <https://agupubs.onlinelibrary.wiley.com/doi/abs/10.1029/>

- 1038 2011JC007398, doi:<https://doi.org/10.1029/2011JC007398>,
1039 arXiv:<https://agupubs.onlinelibrary.wiley.com/doi/pdf/10.1029/2011JC007398>.
- 1040 Kochar, G.T., Jain, R.K., 1979. Note on howard's semicircle theorem. *Journal*
1041 *of Fluid Mechanics* 91, 489–491. doi:10.1017/S0022112079000276.
- 1042 Le Dizès, S., Verga, A., 2002. Viscous interactions of two co-rotating vortices
1043 before merging. *Journal of Fluid Mechanics* 467, 389–410. doi:10.1017/
1044 S0022112002001532.
- 1045 Le Vu, B., Stegner, A., Arsouze, T., 2018. Angular momentum eddy detec-
1046 tion and tracking algorithm (ameda) and its application to coastal eddy
1047 formation. *Journal of Atmospheric and Oceanic Technology* 35, 739 –
1048 762. URL: [https://journals.ametsoc.org/view/journals/atot/35/4/
1049 jtech-d-17-0010.1.xml](https://journals.ametsoc.org/view/journals/atot/35/4/jtech-d-17-0010.1.xml), doi:10.1175/JTECH-D-17-0010.1.
- 1050 Li, H., Yamazaki, H., 2001. Observations of a kelvin-helmholtz billow
1051 in the ocean. *Journal of Oceanography* 57, 709–721. doi:10.1023/A:
1052 1021284409498.
- 1053 MacDonald, D.G., 2003. Mixing processes and hydraulic control in a highly
1054 stratified estuary. Technical Report. MASSACHUSETTS INST OF TECH
1055 CAMBRIDGE.
- 1056 MacDonald, D.G., Geyer, W.R., 2004. Turbulent energy pro-
1057 duction and entrainment at a highly stratified estuarine front.
1058 *Journal of Geophysical Research: Oceans* 109, C05004. URL:
1059 [https://agupubs.onlinelibrary.wiley.com/doi/abs/10.1029/
1060 2003JC002094](https://agupubs.onlinelibrary.wiley.com/doi/abs/10.1029/2003JC002094), doi:<https://doi.org/10.1029/2003JC002094>,
1061 arXiv:<https://agupubs.onlinelibrary.wiley.com/doi/pdf/10.1029/2003JC002094>.
- 1062 de Marez, C., Carton, X., L'Hégaret, P., Meunier, T., Stegner, A., Le Vu, B.,
1063 Morvan, M., 2020. Oceanic vortex mergers are not isolated but influenced
1064 by the β - effect and surrounding eddies. *Scientific Reports* 10, 2897 (10p.).
1065 doi:10.1038/s41598-020-59800-y.

- 1066 Mitchell, T.B., Rossi, L.F., 2008. The evolution of kirchhoff elliptic vortices.
1067 Physics of Fluids 20, 054103. URL: <https://doi.org/10.1063/1.2912991>,
1068 doi:10.1063/1.2912991, arXiv:<https://doi.org/10.1063/1.2912991>.
- 1069 Morin, V.M., Zhu, D.Z., Loewen, M.R., 2004. Supercritical exchange flow down
1070 a sill. Journal of Hydraulic Engineering 130, 521–531. doi:10.1061/(ASCE)
1071 0733-9429(2004)130:6(521).
- 1072 Nakano, H., Yoshida, J., 2019. A note on estimating eddy diffusivity for oceanic
1073 double-diffusive convection. Journal of Oceanography , 1–19.
- 1074 Okubo, A., 1970. Horizontal dispersion of floatable particles in the vicini-
1075 ty of velocity singularities such as convergences. Deep Sea Research and
1076 Oceanographic Abstracts 17, 445–454. URL: <https://www.sciencedirect.com/science/article/pii/0011747170900598>, doi:[https://doi.org/10.1016/0011-7471\(70\)90059-8](https://doi.org/10.1016/0011-7471(70)90059-8).
- 1079 Ortiz, S., Chomaz, J.M., Loiseleux, T., 2002. Spatial holm-
1080 boe instability. Physics of Fluids 14, 2585–2597. URL:
1081 <https://doi.org/10.1063/1.1485078>, doi:10.1063/1.1485078,
1082 arXiv:<https://doi.org/10.1063/1.1485078>.
- 1083 Osborn, T.R., 1980. Estimates of the local rate of vertical diffu-
1084 sion from dissipation measurements. Journal of Physical Oceanog-
1085 raphy 10, 83 – 89. URL: [https://journals.ametsoc.org/view/](https://journals.ametsoc.org/view/journals/phoc/10/1/1520-0485_1980_010_0083_eotlro_2_0_co_2.xml)
1086 journals/phoc/10/1/1520-0485_1980_010_0083_eotlro_2_0_co_2.xml,
1087 doi:10.1175/1520-0485(1980)010<0083:EOTLR0>2.0.CO;2.
- 1088 Palmer, T.L., Fritts, D.C., Andreassen, , Lie, I., 1994. Three-
1089 dimensional evolution of kelvin-helmholtz billows in stratified
1090 compressible flow. Geophysical Research Letters 21, 2287–
1091 2290. URL: [https://agupubs.onlinelibrary.wiley.com/doi/](https://agupubs.onlinelibrary.wiley.com/doi/abs/10.1029/94GL01714)
1092 [abs/10.1029/94GL01714](https://agupubs.onlinelibrary.wiley.com/doi/abs/10.1029/94GL01714), doi:<https://doi.org/10.1029/94GL01714>,
1093 arXiv:<https://agupubs.onlinelibrary.wiley.com/doi/pdf/10.1029/94GL01714>.

- 1094 Parker, J.P., Caulfield, C.P., Kerswell, R.R., 2020. The viscous holmboe insta-
1095 bility for smooth shear and density profiles. *Journal of Fluid Mechanics* 896,
1096 A14. doi:10.1017/jfm.2020.340.
- 1097 Salehipour, H., Caulfield, C.P., Peltier, W.R., 2016. Turbulent mixing due
1098 to the holmboe wave instability at high reynolds number. *Journal of Fluid*
1099 *Mechanics* 803, 591–621. doi:10.1017/jfm.2016.488.
- 1100 Shi, J., Tong, C., Zheng, J., Zhang, C., Gao, X., 2019. Kelvin-helmholtz billows
1101 induced by shear instability along the north passage of the yangtze river
1102 estuary, china. *Journal of Marine Science and Engineering* 7. URL: <https://www.mdpi.com/2077-1312/7/4/92>, doi:10.3390/jmse7040092.
- 1104 Singh, S., Mahajan, K.K., Choudhary, R.K., Nagpal, O.P.,
1105 1999. Detection of kelvin-helmholtz instability with the in-
1106 dian mesosphere-stratosphere-troposphere radar: A case study.
1107 *Journal of Geophysical Research: Atmospheres* 104, 3937–3945.
1108 URL: [https://agupubs.onlinelibrary.wiley.com/doi/abs/](https://agupubs.onlinelibrary.wiley.com/doi/abs/10.1029/98JD02675)
1109 [10.1029/98JD02675](https://doi.org/10.1029/98JD02675), doi:<https://doi.org/10.1029/98JD02675>,
1110 arXiv:<https://agupubs.onlinelibrary.wiley.com/doi/pdf/10.1029/98JD02675>.
- 1111 Smyth, W., Moum, J., 2012. Ocean mixing by kelvin-helmholtz instability.
1112 *Oceanography* 25, 140–149. doi:10.5670/oceanog.2012.49.
- 1113 Smyth, W.D., Carpenter, J.R., Lawrence, G.A., 2007. Mixing in sym-
1114 metric holmboe waves. *Journal of Physical Oceanography* 37, 1566 –
1115 1583. URL: [https://journals.ametsoc.org/view/journals/phoc/37/6/](https://journals.ametsoc.org/view/journals/phoc/37/6/jpo3037.1.xml)
1116 [jpo3037.1.xml](https://journals.ametsoc.org/view/journals/phoc/37/6/jpo3037.1.xml), doi:10.1175/JP03037.1.
- 1117 Smyth, W.D., Nash, J.D., Moum, J.N., 2005. Differential diffusion in break-
1118 ing kelvin-helmholtz billows. *Journal of Physical Oceanography* 35, 1004 –
1119 1022. URL: [https://journals.ametsoc.org/view/journals/phoc/35/6/](https://journals.ametsoc.org/view/journals/phoc/35/6/jpo2739.1.xml)
1120 [jpo2739.1.xml](https://journals.ametsoc.org/view/journals/phoc/35/6/jpo2739.1.xml), doi:10.1175/JP02739.1.

- 1121 Smyth, W.D., Peltier, W.R., 1991. Instability and transition in finite-amplitude
1122 kelvin–helmholtz and holmboe waves. *Journal of Fluid Mechanics* 228,
1123 387–415. doi:10.1017/S0022112091002756.
- 1124 Smyth, W.D., Winters, K.B., 2003. Turbulence and mixing in holmboe
1125 waves. *Journal of Physical Oceanography* 33, 694 – 711. URL: https://journals.ametsoc.org/view/journals/phoc/33/4/1520-0485_2003_33_694_tamihw_2.0.co_2.xml,
1126 doi:10.1175/1520-0485(2003)33<694:
1127 TAMIHW>2.0.CO;2.
- 1129 Taylor, G.I., 1931. Effect of variation in density on the stability of superposed
1130 streams of fluid. *Proceedings of the Royal Society of London. Series A, Con-*
1131 *taining Papers of a Mathematical and Physical Character* 132, 499–523. URL:
1132 <http://www.jstor.org/stable/95674>.
- 1133 Tedford, E.W., Carpenter, J.R., Pawlowicz, R., Pieters, R., Lawrence,
1134 G.A., 2009. Observation and analysis of shear instability in the
1135 fraser river estuary. *Journal of Geophysical Research: Oceans* 114,
1136 C11006. URL: [https://agupubs.onlinelibrary.wiley.com/doi/abs/](https://agupubs.onlinelibrary.wiley.com/doi/abs/10.1029/2009JC005313)
1137 [10.1029/2009JC005313](https://doi.org/10.1029/2009JC005313), doi:<https://doi.org/10.1029/2009JC005313>,
1138 arXiv:<https://agupubs.onlinelibrary.wiley.com/doi/pdf/10.1029/2009JC005313>.
- 1139 Thomson, W., 1871. Hydrokinetic solutions and observations. *Philosophical*
1140 *Magazine* 42, 362–377. doi:10.1017/CB09780511694523.031.
- 1141 Thorpe, S.A., 2012. On the kelvin–helmholtz route to turbulence. *Journal of*
1142 *Fluid Mechanics* 708, 1–4. doi:10.1017/jfm.2012.383.
- 1143 Weiss, J., 1991. The dynamics of enstrophy transfer in two-dimensional hy-
1144 drodynamics. *Physica D: Nonlinear Phenomena* 48, 273–294. URL: <https://www.sciencedirect.com/science/article/pii/016727899190088Q>,
1145 doi:[https://doi.org/10.1016/0167-2789\(91\)90088-Q](https://doi.org/10.1016/0167-2789(91)90088-Q).
- 1147 Yang, Q., Nikurashin, M., Sasaki, H., Sun, H., Tian, J., 2019. Dissipation of

- 1148 mesoscale eddies and its contribution to mixing in the northern south china
1149 sea. *Scientific Reports* 9, 556. doi:10.1038/s41598-018-36610-x.
- 1150 Zagvozkina, T., Vorobei, A., Lyubimova, T., 2019. Kelvin-helmholtz and holm-
1151 boe instabilities of a diffusive interface between miscible phases. *Phys. Rev.*
1152 *E* 100, 023103. URL: [https://link.aps.org/doi/10.1103/PhysRevE.100.](https://link.aps.org/doi/10.1103/PhysRevE.100.023103)
1153 023103, doi:10.1103/PhysRevE.100.023103.
- 1154 Zhang, B., Delamere, P.A., Ma, X., Burkholder, B., Wiltberger, M.,
1155 Lyon, J.G., Merkin, V.G., Sorathia, K.A., 2018. Asymmetric kelvin-
1156 helmholtz instability at jupiter's magnetopause boundary: Implications
1157 for corotation-dominated systems. *Geophysical Research Letters* 45,
1158 56–63. URL: [https://agupubs.onlinelibrary.wiley.com/doi/abs/](https://agupubs.onlinelibrary.wiley.com/doi/abs/10.1002/2017GL076315)
1159 [10.1002/2017GL076315](https://doi.org/10.1002/2017GL076315), doi:<https://doi.org/10.1002/2017GL076315>,
1160 arXiv:<https://agupubs.onlinelibrary.wiley.com/doi/pdf/10.1002/2017GL076315>.

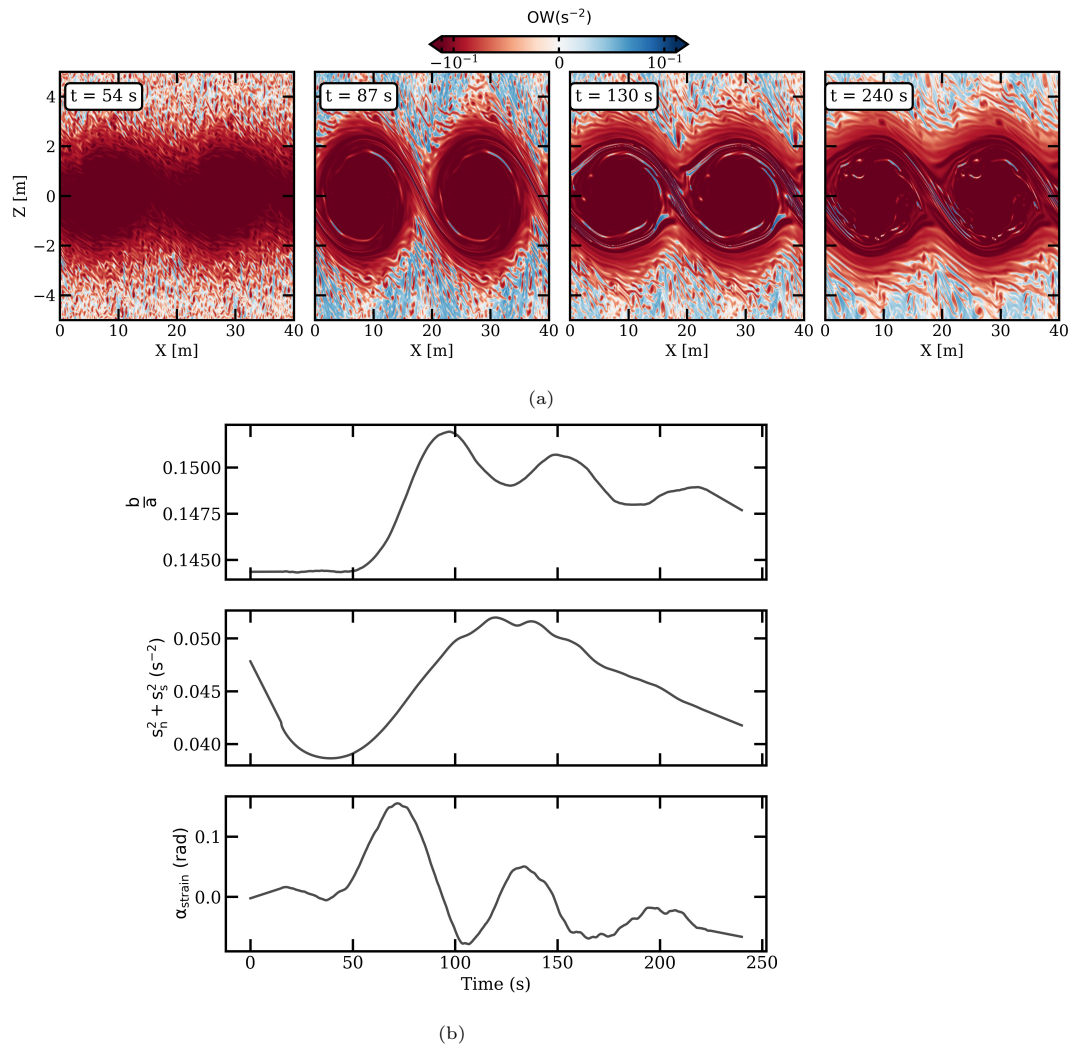


Figure 5: As Figure 3 for experiment 2.

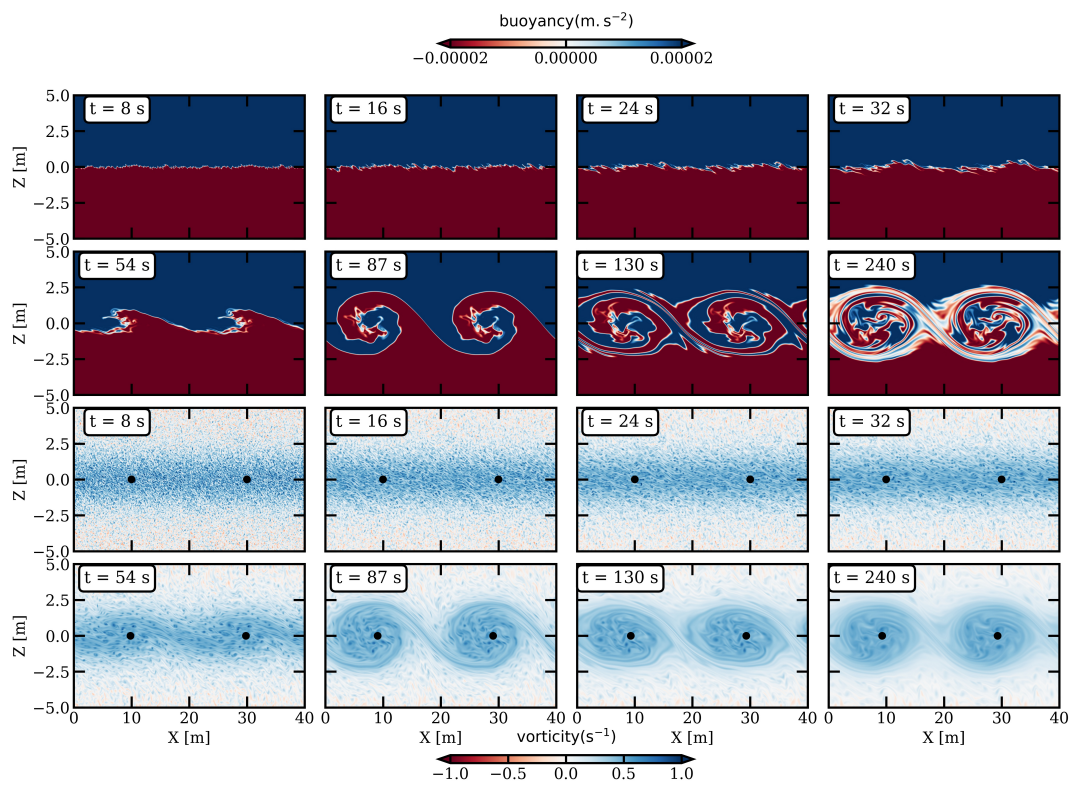


Figure 6: As Figure 2 for experiment 3.

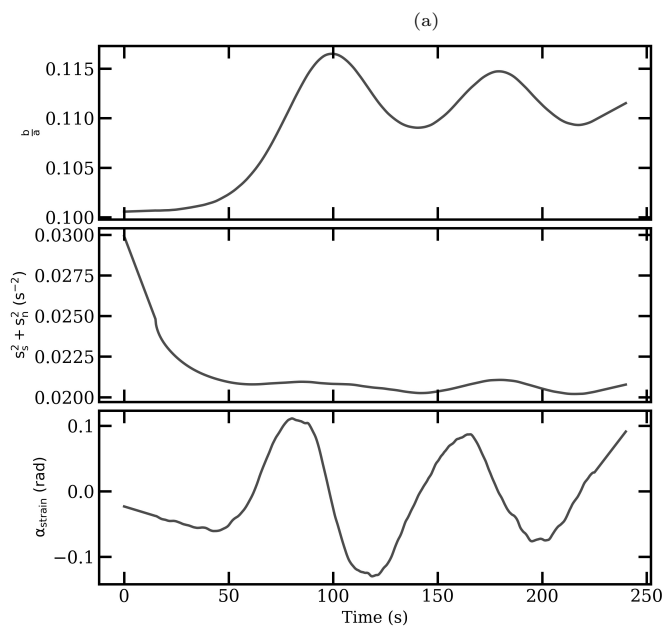
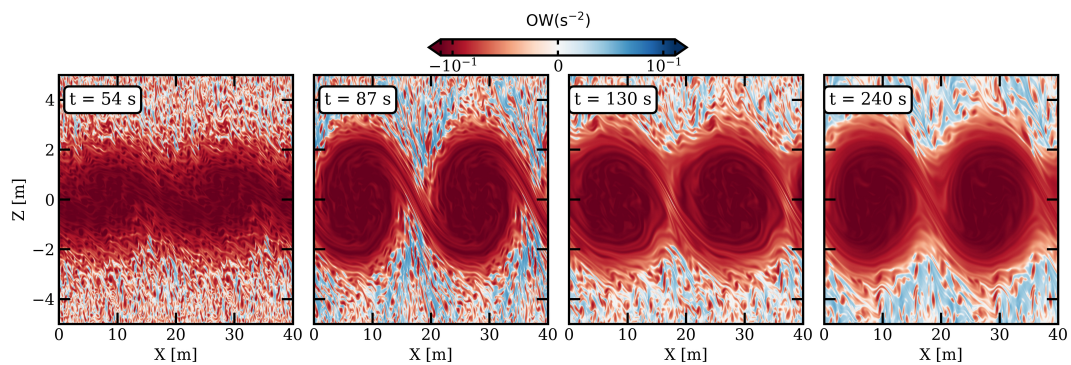


Figure 7: As Figure 3 for experiment 3.

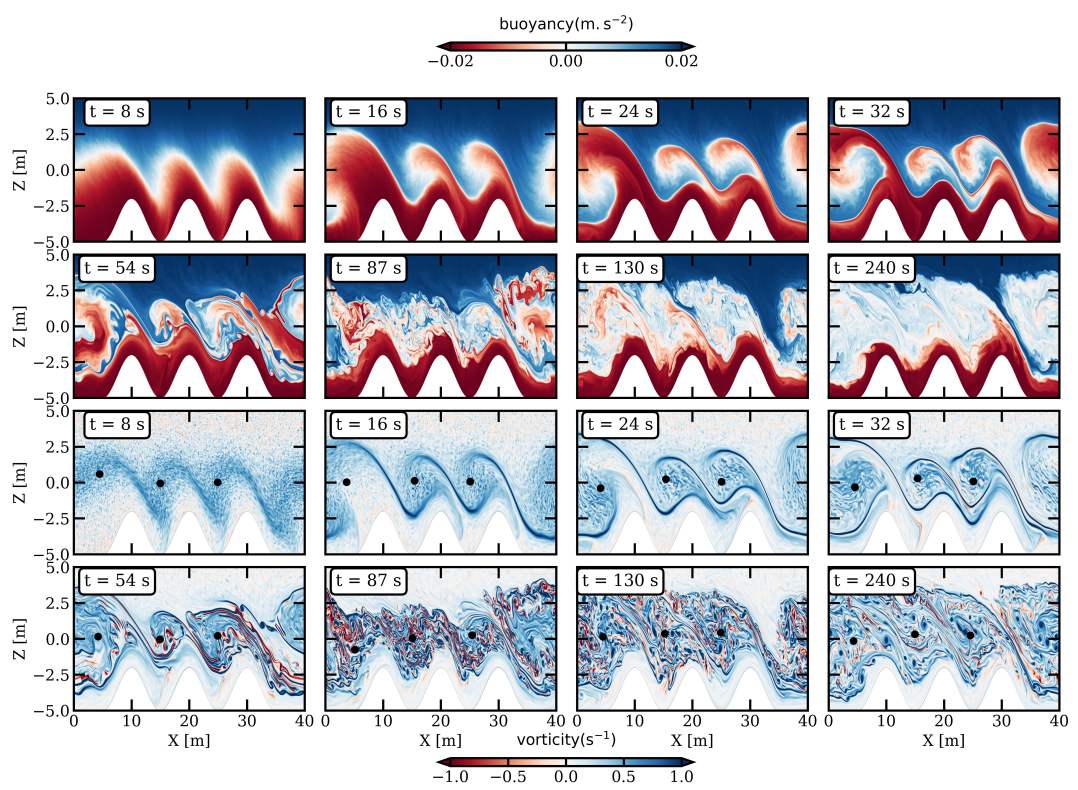
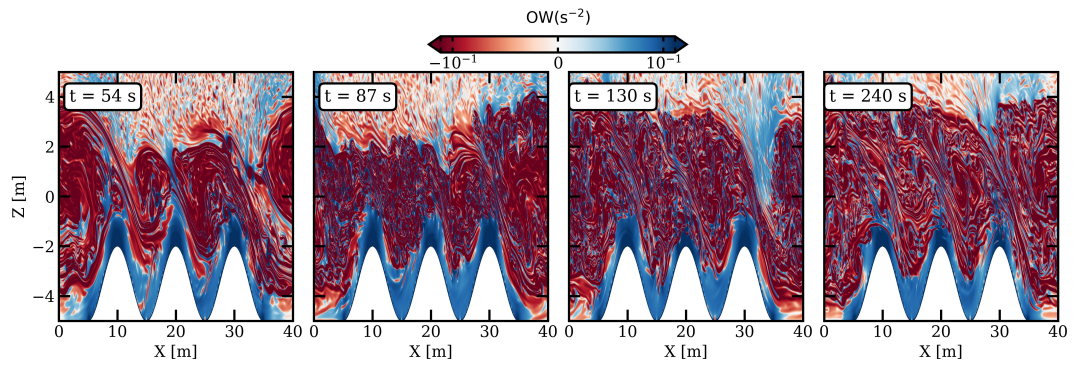
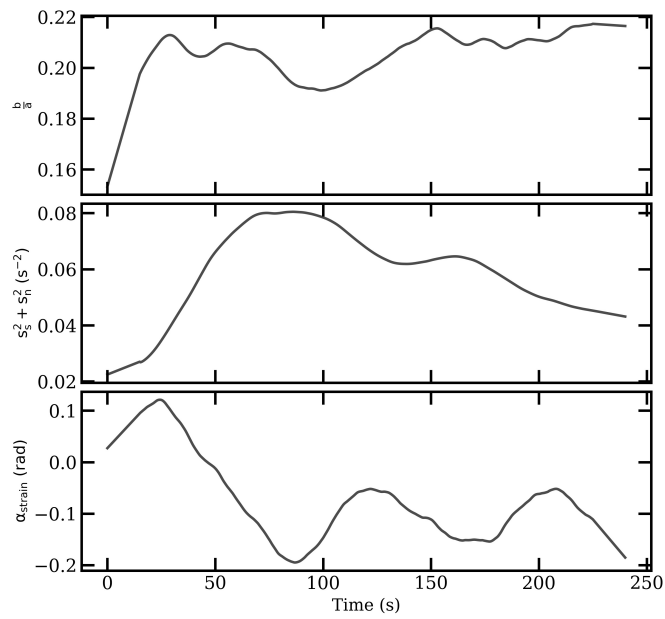


Figure 8: As Figure 2 for experiment 4.



(a)



(b)

Figure 9: As Figure 3 for experiment 4.

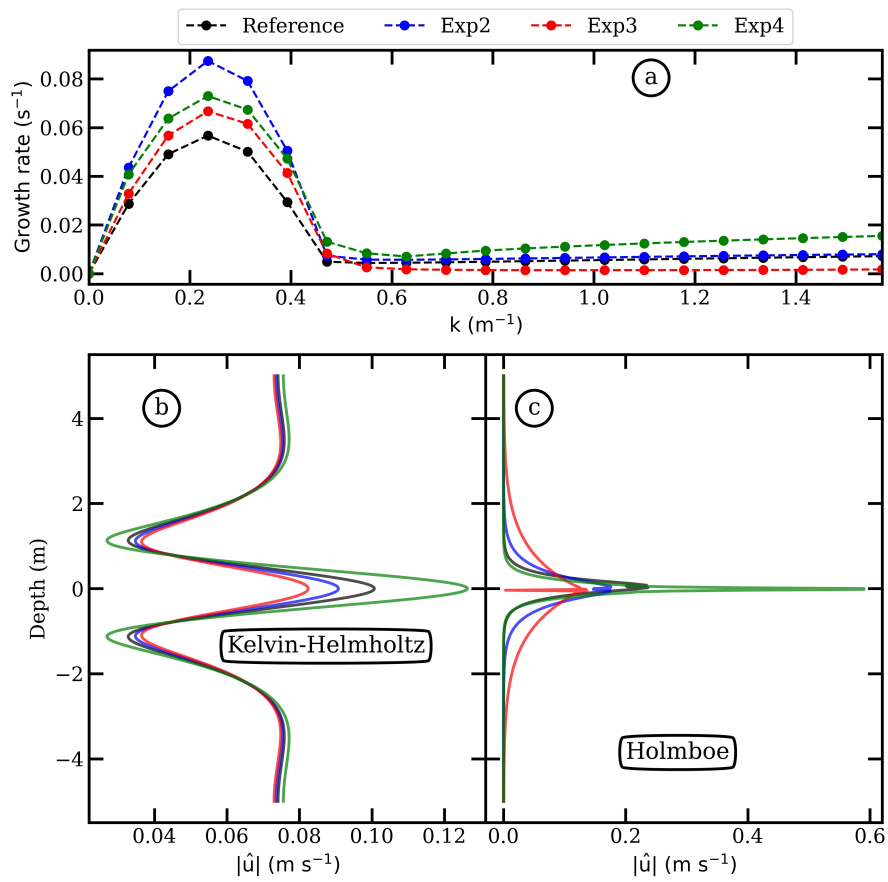


Figure 10: (a) the growth rate, (b) -the vertical magnitude of the streamwise velocity for the Kelvin-Helmholtz mode and (c) the vertical magnitude of the streamwise velocity for the Holmboe mode, for the reference and sensitivity experiments.

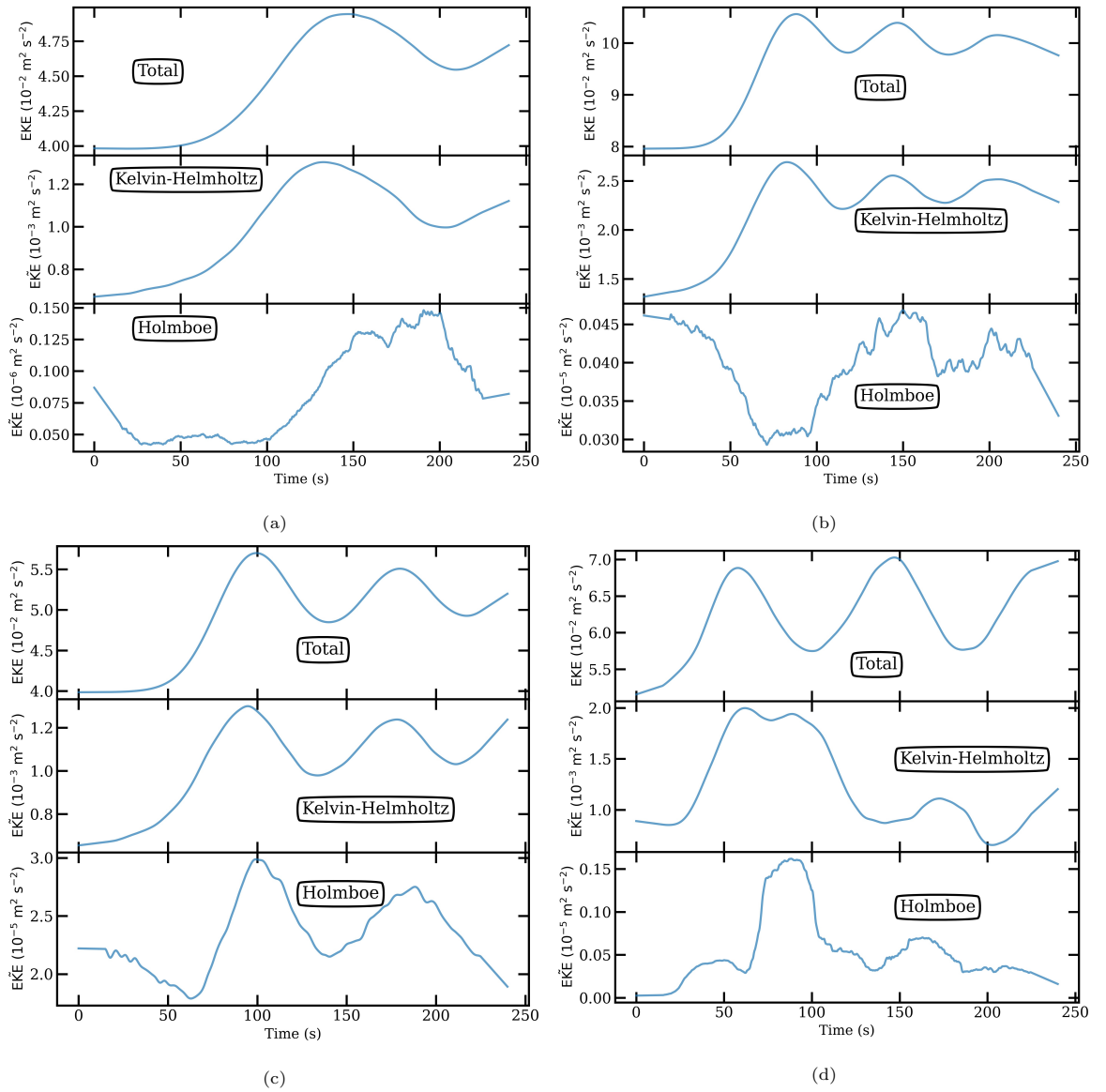


Figure 11: The total and modal decompositions of the EKE for the reference configuration (a), the experiment 2 (b), the experiment 3 (c) and the experiment 4 (d).

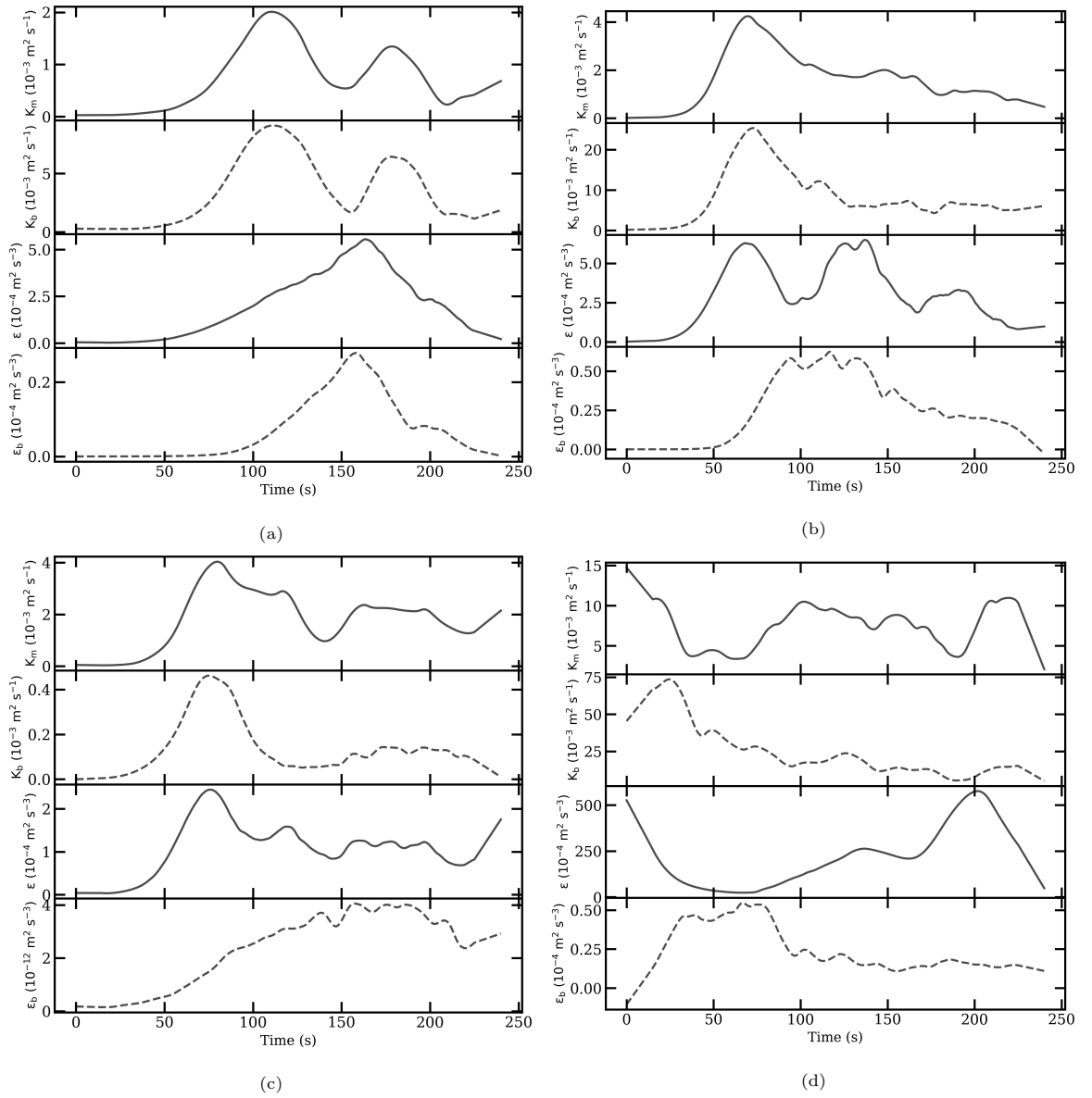


Figure 12: Vertical eddy viscosity (black solid line), vertical diffusivity (black dashed line), vertical dissipation of EKE (black solid line) and of buoyancy (black dashed line) for the reference configuration (a), the experiment 2 (b), the experiment 3 (c) and the experiment 4 (d).

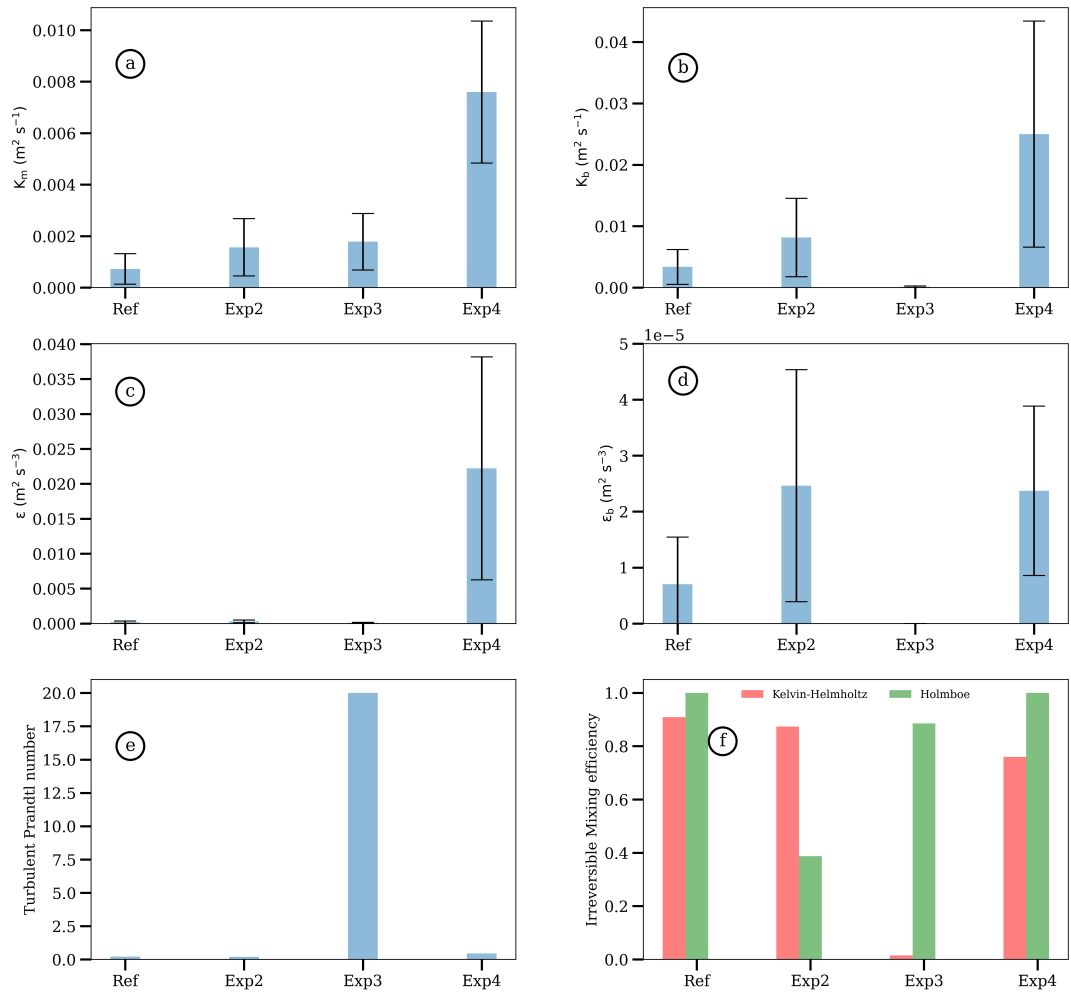


Figure 13: Statistics and error bars (vertical segments at the end of the colored lines) for all experiments : (a) vertical eddy viscosity, (b) vertical diffusivity, (c) vertical EKE dissipation, (d) vertical buoyancy dissipation, (e) turbulent Prandtl number, and (f) irreversible mixing efficiency for KH (red) and Holmboe (green) instabilities.

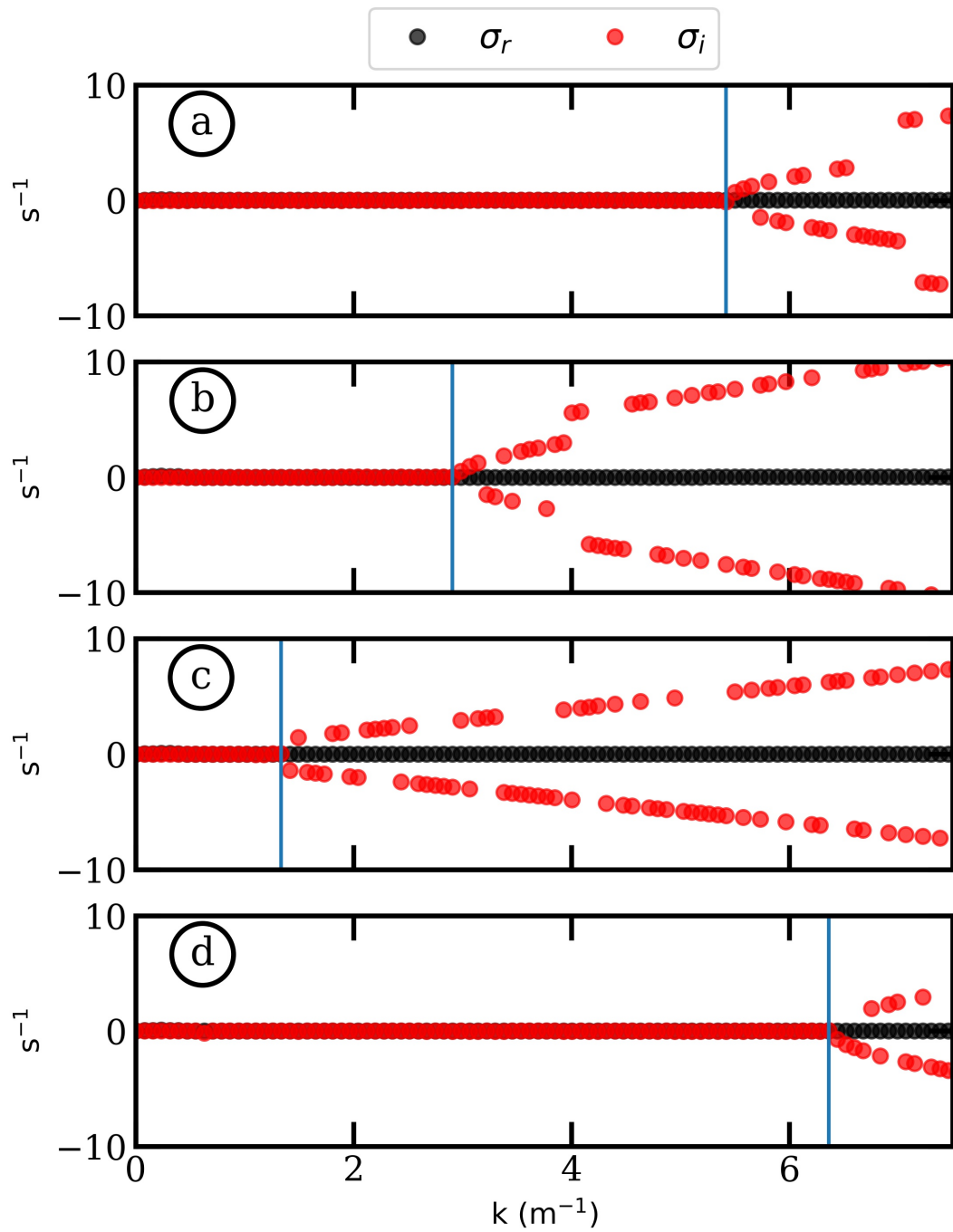


Figure B.14: The bifurcation theory for the Reference simulation (a), experiment 2 (b), experiment 3 (c), and experiment 4 (d). The blue solid vertical line indicate the identified Holmboe mode.

4.3 Conclusions et Perspectives

Dans ce chapitre, je me suis intéressé à des processus agéostrophiques de cisaillement vertical dans un panache de rivière. Cette étude repose sur l'approximation non-hydrostatique indispensable pour une représentation adéquate de processus non-linéaires rapides² et à très petites échelles³.

Dans cette étude, j'ai défini un panache de rivière de référence en deux dimensions à partir de paramètres observés dans des études préalables. J'ai ensuite évalué la sensibilité de ce panache à divers paramètres physiques: l'épaisseur de la couche stratifiée, l'intensité de cisaillement et la nature du fond.

Tout d'abord, j'ai montré la génération de petits tourbillons⁴ dans la couche stratifiée et cisailée. L'existence de ces tourbillons est régie par la définition des conditions initiales qui respectent le critère de Richardson: $R_i < 0.25$. Ces tourbillons anticycloniques se déforment dans un plan tangentiel sous des contraintes d'étirement cisailé; quand le fond est plat. Dans le cas d'un fond incliné, les tourbillons cycloniques générés sont de plus petites tailles et se dissipent très rapidement suite à l'accélération de l'écoulement. L'étirement cisailé est sensible aux différents paramètres physiques: plus intense quand le fond est incliné, suivi de quand l'épaisseur de la stratification est réduite et enfin quand le cisaillement initial augmente.

Puis, j'ai relié la génération de ces tourbillons à des instabilités de cisaillement vertical: Holmboe et Kelvin-Helmholtz. Ces instabilités se développent à la base du panache et sont caractérisées par des taux de croissance variant entre quelques secondes et quelques minutes.

Enfin, j'ai caractérisé le mélange turbulent en masse et quantité de mouvement et la dissipation d'énergie turbulente (potentielle et cinétique). Ces derniers résultats ont été comparés et validés par rapport à des simulations/observations précédentes. Dans ces simulations, j'ai démontré que les instabilités d'Holmboe sont une source efficace pour le mélange turbulent dans un estuaire ou à son embouchure.

²de l'ordre de quelques minutes

³de l'ordre de quelques mètres

⁴rayon ~ 4 m

Dans le contexte de ces études idéalisées, je m'interroge sur:

- L'existence d'instabilités de cisaillement vertical dans le panache de la Gironde dans un contexte réaliste.
- Le lien, la croissance et la nature entre diverses instabilités (symétriques, baroclines, barotropes et cisaillement vertical).
- Le mélange induit par l'interaction entre le panache de la Gironde et les forçages (marées, vents et flux atmosphériques) à la surface et dans l'océan intérieur.

4.4 Notes on chapter 4

In this chapter, I studied the KH and Holmboe instabilities in 2D idealized simulations corresponding to stratified-sheared flows in the near-field region of the plume. However, this study points out several limitations:

1. Studying the difference between 2D and 3D idealized simulations will improve our understanding about the Holmboe and KH instabilities development (e.g., energy cascade).
2. Considering in-situ observations in different plumes with different forcing conditions will shape our knowledge about these instabilities and their impact on the plume mixing (e.g., internal waves dynamics)
3. Performing 3D realistic simulations in non-hydrostatic approximation within different oceans and different plumes may also contribute to understand the interaction between the Coriolis effect, sheared flows, winds, tides and air-sea fluxes; and their induced dynamics (e.g., mixing and instabilities).

Chapter 5

River plumes in turbulent ocean

In this chapter, a realistic study of the Gironde river plume is presented. In this study, the dynamics, instabilities and mixing is analyzed in this plume in regard to realistic bathymetry and realistic physical processes (river discharge, winds, tides and atmospheric fluxes). The main results have been published in the journal *Frontiers in Marine Science* journal.

5.1 Introduction

Dans ce chapitre, je m'intéresserai à l'étude du panache de la Gironde dans le Golfe de Gascogne. Cette étude se base sur des simulations numériques réalistes à haute résolution (400 m). J'ai restreint cette étude à deux situations hivernale (mois de Mars) et estivale (mois d'Août). Ces choix me permettront d'analyser la dynamique sous-mésoéchelle du panache de la Gironde en contrastant une situation à débit modéré (Mars) et à débit faible (Août).

La stratégie adoptée ici complémente les études précédentes. Dans les études précédentes, j'ai considéré l'interaction de plusieurs processus physiques (vents, marée, débit de rivière) avec un panache de rivière (type Gironde) tout en simplifiant la forme de la côte et la bathymétrie. Néanmoins, ces études ne permettent pas de comprendre la dynamique du panache de la Gironde dans un contexte réaliste côtier. A cet effet, l'interaction du panache de la Gironde avec la combinaison de plusieurs forçages (marée, vents, débit de rivière et flux atmosphériques), une

bathymétrie et une côte réaliste est très importante dans la compréhension de la dynamique côtière dans le Golfe de Gascogne. Afin de comprendre l'impact de ces panaches de rivière dans un environnement côtier réaliste, plusieurs questions vont être étudiées:

- Quelle est la nature (géostrophique et agéostrophique) de la dynamique du panache de la Gironde ?
- Quelle est la nature des instabilités dans le panache de la Gironde, leurs taux de croissance et leurs liens avec les forçages (marée, débit de rivière, vents...)?
- Quelle est l'impact des processus instables sur le mélange vertical dans le panache de la Gironde à la surface et dans l'océan intérieur ?

Cette étude a été soumise au journal scientifique *Frontiers in Marine Science* et le contenu de cet article est présenté dans la section suivante.

5.2 Article: Non-linear processes in the Gironde river plume (North-East Atlantic): Instabilities and mixing



Non-Linear Processes in the Gironde River Plume (North-East Atlantic): Instabilities and Mixing

Adam Ayouche^{1*}, Guillaume Charria¹, Xavier Carton¹, Nadia Ayoub² and Sébastien Theetten¹

¹ Laboratory for Ocean Physics and Satellite remote sensing (LOPS), UMR6523, Ifremer, Univ. Brest, CNRS, IRD, Brest, France, ² Laboratoire d'Etudes en Géophysique et Océanographie Spatiales (LEGOS), UMR5566, Université de Toulouse, CNRS, CNES, IRD, Toulouse, France

Instability and mixing are ubiquitous processes in river plumes but their small spatial and temporal scales often limit their observation and analysis. We investigate flow instability and mixing processes in the Gironde river plume (Bay of Biscay, North-East Atlantic ocean) in response to air-sea fluxes, tidal currents, and winds. High-resolution numerical simulations are conducted in March (average river discharge) and in August (low discharge) to explore such processes. Two areas of the Gironde river plume (the bulge and the coastal current) experience different instabilities: barotropic, baroclinic, symmetric, and/or vertical shear instabilities. Energy conversion terms reveal the coexistence of barotropic and baroclinic instabilities in the bulge and in the coastal current during both months. These instabilities are intensified over the whole domain in August and over the inner-shelf in March. The Hoskins criterion indicates that symmetric instability exists in most parts of the plume during both periods. The evolution of the Gironde plume with the summer stratification, tidal currents and winds favors its development. During both seasons, ageostrophic flow and large Rossby numbers characterize rapidly-growing and small-scale frontal baroclinic and symmetric instabilities. The transition between these instabilities is investigated with an EKE decomposition on the modes of instability. In the frontal region of the plume, during both months, symmetric instabilities grow first followed by baroclinic and mixed ones, during wind bursts and/or high discharge events. In contrast, when the wind is weak or relaxing, baroclinic instabilities grow first followed by symmetric and then mixed ones. Their growth periods range from a few hours to a few days. Mixing at the ocean surface is analyzed via Potential Vorticity (PV) fluxes. The net injection of PV at the ocean surface occurs at submesoscale buoyant fronts of the Gironde plume during both months. Vertical mixing at these fronts has similar magnitude as the wind-driven and surface buoyancy fluxes. During both months, the frontal region of the plume is restratified during wind relaxation events and/or high river discharge events through frontogenetic processes. Conversely, wind bursts destratify the frontal plume interior through non-conservative PV fluxes.

Keywords: river plumes, buoyant fronts, (sub)mesoscale instabilities, PV mixing, stratification, Gironde river, Bay of Biscay

OPEN ACCESS

Edited by:

Alexander Yankovsky,
University of South Carolina,
United States

Reviewed by:

Nuno Vaz,
University of Aveiro, Portugal
Peng Cheng,
Xiamen University, China

*Correspondence:

Adam Ayouche
adam.ayouche@ensta-bretagne.org

Specialty section:

This article was submitted to
Coastal Ocean Processes,
a section of the journal
Frontiers in Marine Science

Received: 28 April 2021

Accepted: 07 June 2021

Published: 30 June 2021

Citation:

Ayouché A, Charria G, Carton X,
Ayoub N and Theetten S (2021)
Non-Linear Processes in the Gironde
River Plume (North-East Atlantic):
Instabilities and Mixing.
Front. Mar. Sci. 8:701773.
doi: 10.3389/fmars.2021.701773

1. INTRODUCTION

The Bay of Biscay is a semi-enclosed region in the northeastern Atlantic ocean where ocean flows with different spatial and temporal scales interact and are constrained by a complex bathymetry (a wide continental shelf, several canyons along the slope). The bay receives freshwater from three main rivers (the Loire, the Gironde, and the Adour). The purpose of this paper is to investigate the instability of the Gironde river plume and the associated mixing processes.

The Bay of Biscay is the seat to multiple oceanic phenomena as described in Koutsikopoulos et al. (1998) and Le Boyer et al. (2013). The continental shelf and the open ocean have different dynamics; regional modeling reveals weak cross-slope exchanges (Xu et al., 2015; Graham et al., 2018; Rubio et al., 2018; Akpınar et al., 2020). Over the continental shelf, river runoffs induce density currents and salinity fronts (Lazure and Jegou, 1998; Puillat et al., 2004). The residual circulation over the shelf is due to wind and tidal forcings, leading to density gradients. On the continental slope, nonlinear processes favor the generation of mesoscale [scales $\sim O(10\text{--}100\text{ km})$] and submesoscale [scales $\sim O(1\text{--}10\text{ km})$] structures (Charria et al., 2017; Yelekçi et al., 2017). The open ocean circulation is marked by long-living mesoscale eddies, mainly generated along the continental slope. Such eddies can be shed by the Iberian Poleward current, which flows over canyons (Pingree and Le Cann, 1989; Pingree and Le Cann, 1990; Frouin et al., 1990; Pingree et al., 1999; Garcia-Soto et al., 2002; Serpette et al., 2006; Le Cann and Serpette, 2009).

Using submesoscale permitting numerical models, small-scale oceanic features have been observed in the Bay of Biscay with a seasonal variability (Charria et al., 2017). At the end of winter, the most intense surface features result from mixed layer baroclinic instabilities. These features also display an interannual variability due to winter atmospheric conditions (Charria et al., 2017). In this macro-tidal bay, tides also play a role in the growth of small scale features. For example, Karagiorgos et al. (2020) showed that the semidiurnal tidal harmonics intensify the submesoscale activity in summer, in particular near the Ushant front. Tidal and buoyant fronts are ubiquitous in the Bay of Biscay. Buoyant fronts are observed over the continental shelf due to the interaction between the Loire and Gironde river plumes and the open ocean (Yelekçi et al., 2017). This frontal activity is intense in winter due to the river influence over the inner-shelf. The Loire, Gironde, and Adour rivers are an important source of freshwater, they represent more than 75% of the total river runoff in the bay, with an annual river discharge of $900\text{ m}^3\text{ s}^{-1}$; their plumes reach a noticeable alongshore extension during downwelling favorable wind events (Lazure et al., 2009; Costoya et al., 2017).

When the freshwater flows from the estuary to the open ocean, a river plume is formed. The structure and extent of the river plume result from the river discharge, the local topography, and the influence of winds, tides, and of the Coriolis force. It can be studied in two steps: (1) the offshore spreading and its curvature which lead to the generation of an anticyclonic bulge and (2) the development of a coastal current, both interacting with the topography (Yankovsky and Chapman, 1997). Concerning the

bulge, Nof and Pichevin (2001) studied the ballooning of buoyant outflows near a river mouth using numerical and analytical simulations. For large Rossby number outflows, they found that a ballooning anticyclonic gyre forms, which traps most of the freshwater. When the Rossby number of the outflow is smaller than unity, the coastal current transports most of the freshwater which does not accumulate in the bulge. Frictionless processes alter the Potential Vorticity (PV) of the bulge. Isobe (2005) finds that the bulge ballooning is due to near inertial disturbances near the river mouth; these instabilities develop in the anticyclonic gyre fed by an inflow of freshwater. Such instabilities grow in the absence of wind or ambient currents whereas tides stabilize their growth offshore, and also modify the plume structure near the river mouth (Horner-Devine, 2009). When winds are weak, tidal plumes can form as the river plume interacts with tides; this is observed for the Columbia River. In the presence of stronger winds, river plume spreading is sensitive to the wind direction (Kourafalou et al., 1996a,b; Liu et al., 2008; Kastner et al., 2018). When winds are downwelling favorable, low surface salinity waters are advected to the southwest. In contrast, upwelling favorable winds favor large exports of low-salinity water offshore. Under the influence of external forcings, river plumes undergo geostrophic and non-geostrophic instabilities.

Geostrophic and non-geostrophic instabilities can develop in river plumes under favorable conditions. The numerical modeling of the Mississippi-Atchafalaya river plume has revealed that baroclinic instabilities are not observed when the width of the coastal current is too small compared to the local deformation radius and inertial length scale (Hetland, 2017). This study however mentioned that baroclinic unstable flows can be observed in the presence of tides and during winds relaxation periods or through a transition from symmetric instabilities. This instability can also occur as frontal disturbances due to a small salinity anomaly or strong stratification (Jia and Yankovsky, 2012). They indicate that barotropic and baroclinic instabilities can coexist. In this latter study, baroclinic instability played the leading role and could be inhibited with a gentle bottom slope. The onset of such instabilities can also occur after a downwelling favorable wind event (Lv et al., 2020). This study, using numerical simulations, showed that a downwelling favorable wind strengthens the stratification and that symmetric instabilities are generated. After a wind event, the stratification weakens and baroclinic instabilities prevail. For the specific case of the Bay of Biscay, the interaction between the Gironde river plume, tides and winds promote the existence of different instabilities which coexist in different regions of the plume (Ayouché et al., 2020). This study showed that semi-diurnal tides lead to the coexistence of symmetric, barotropic, and baroclinic instabilities in the near field of the plume. Southwesterly winds promote the coexistence of frontal symmetric, baroclinic, and barotropic instabilities in the far field region of the plume. In addition, when the river plume is not constrained by external forcings (high discharge only $\sim 10,000\text{ m}^3\text{ s}^{-1}$), it undergoes symmetric and mixed barotropic/baroclinic instabilities where the Rossby number is large.

River plumes are not only propitious to the development of such instabilities but also play a major role in the exchange

of freshwater with the salty open ocean which induces vertical mixing within different regions of the plume.

In river plumes, a competition between the growth of fronts and local mixing is observed in different regions. The freshwater volume retained behind the front is inversely proportional to mixing rates, near the river mouth (Hetland, 2010). The near-field plume is sensitive to tides and to estuarine discharge. Larger river discharges lead to a decrease in plume mixing, limiting its lateral expansion and inhibiting shear mixing (Cole and Hetland, 2016). Tidal rectification is also a possible mechanism for transport and/or mixing as suggested by Wu and Wu (2018). Tides also lead to the development of Kelvin-Helmholtz billows in the bottom boundary layer which enhance mixing between freshwater and ambient salty waters near the river mouth (MacDonald and Geyer, 2004; Kilcher and Nash, 2010). In the far-field region of the plume the net mixing is less sensitive to tides and more sensitive to increased river discharge in the absence of winds through shear mixing (Cole and Hetland, 2016). In the presence of winds, mixing is efficient in both near field and far field regions (Hetland, 2005). In idealized simulations of the Gironde River plume, interior mixing was evaluated with a restratification budget based on PV mixing (Ayouché et al., 2020). They showed that frontogenetic processes govern the restratification in the near field region of the plume when forced by tides or a high river discharge ($\sim 10,000 \text{ m}^3 \text{ s}^{-1}$). Frontogenesis is enhanced in the coastal current of the plume when interacting with downwelling favorable winds and the PV is eroded through surface frictionless processes.

Following these previous studies, we analyze the plume dynamics, its instabilities and the associated mixing in the case of the Gironde River. We use diagnostics based on potential vorticity budget and on a Fourier decomposition of the Eddy Kinetic Energy (EKE).

Numerical realistic simulations (with a submesoscale resolving model) are performed with a specific focus on the Gironde river plume. The study is organized around the following four main questions:

1. What are the 3D structure and dynamics of Gironde river plume in high resolution realistic simulations?
2. Which instability processes affect this river plume (nature, mechanism, intensity, and growth)?
3. What are the processes responsible for potential vorticity removal or injection at the ocean boundary layers (surface and bottom) in the river plume?
4. What are the processes explaining the stratification weakening or intensification in the plume?

The paper is organized as follows: the model configuration, simulations and methods are described in section 2. The model validation is presented in section 3. The 3D structure and dynamics of Gironde river plume are detailed in section 4.1. The instabilities are analyzed in sections 4.2 and 4.3; the potential vorticity mixing at the ocean boundaries is analyzed in section 4.4 and the processes explaining the stratification destruction or intensification are explored in section 4.5. The main results are then discussed (section 5) before the main conclusions and perspectives are given.

2. MATERIALS AND METHODS

2.1. Model Configuration

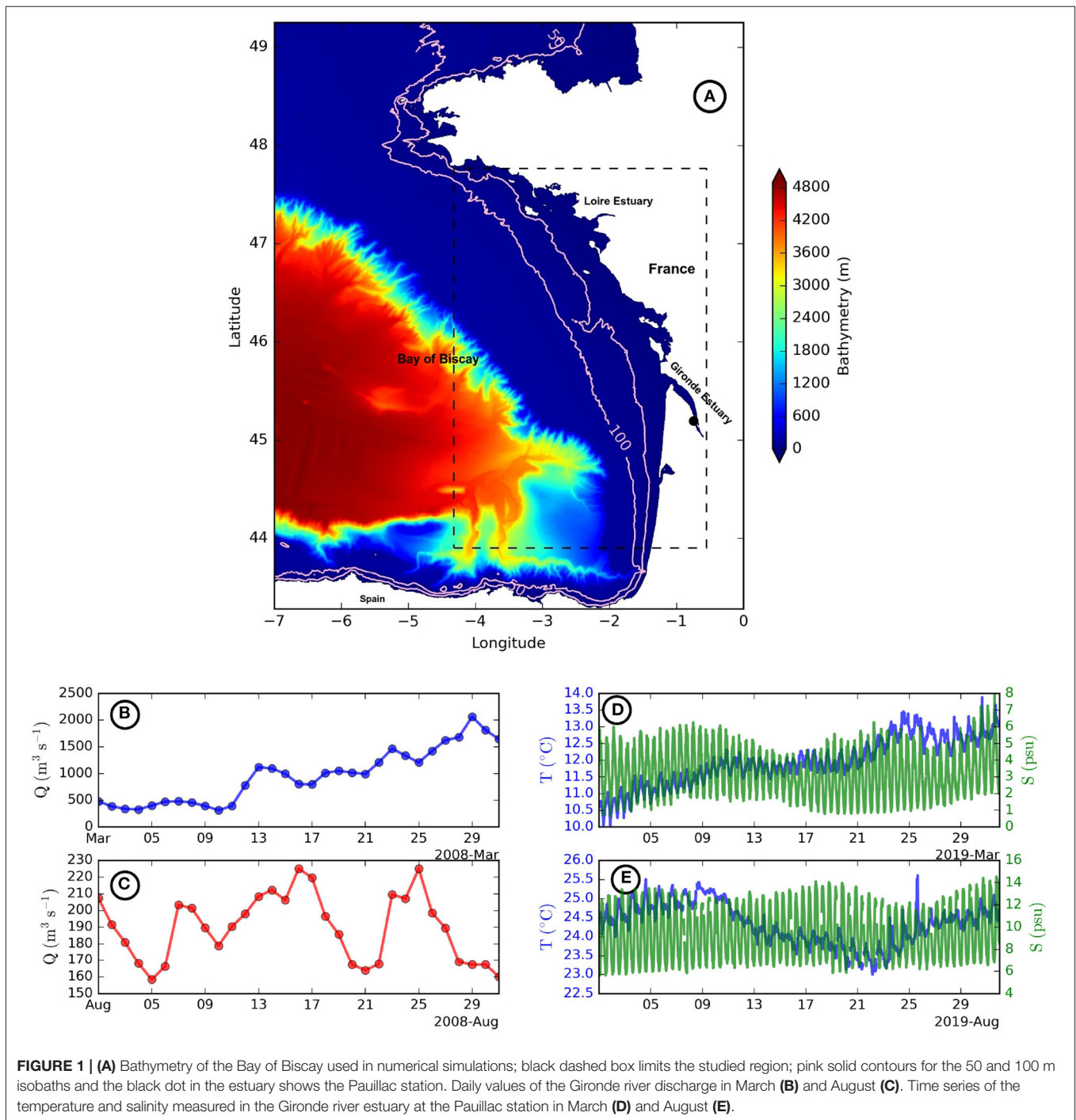
The numerical model used for our realistic simulations is the CROCO model (based on the ROMS model) (Shchepetkin and McWilliams, 2005; Debreu et al., 2012). CROCO is a free-surface, hydrostatic, primitive equation ocean model. Sigma coordinates are used in the vertical with 40 vertical levels. These levels are stretched at the surface with $\theta_s = 5$ and at the bottom with $\theta_b = 0.4$. The bathymetry is a combination of HOMONIM bathymetry from the Shom (<https://data.shom.fr/>—100 m horizontal resolution) and of EMODNET bathymetry for regions E3 and E4 (<https://portal.emodnet-bathymetry.eu>—115 m horizontal resolution). The merged bathymetry was smoothed to limit pressure gradient errors. The minimum depth is 8 m (estuaries) and the maximum depth at the western boundary is $\sim 4,000$ m (Figure 1A). Orthogonal curvilinear horizontal coordinates are used with a horizontal resolution of 400 m. The model time step is 15 s with hourly model outputs.

The horizontal and vertical advection of momentum are performed with the Total Variation Diminishing scheme. The tracers horizontal and vertical advection schemes are with the Zico extension fifth order WENO scheme (a weighted ENO with improvements of the weights formula) (Rathan and Naga Raju, 2018). The tracer horizontal advection is rotated along isopycnals. The model turbulent closure scheme is KPP (Large et al., 1994). The background vertical diffusivities (for both momentum and tracers) are $Kv_b = 10^{-5} \text{ m}^2 \text{ s}^{-1}$ and $Kt_b = 10^{-6} \text{ m}^2 \text{ s}^{-1}$. Smagorinsky-like viscous and diffusive terms (with molecular viscosities and diffusivities) are implemented. The quadratic Von-Karman law (logarithmic law) is used for bottom friction with a bottom roughness $z_0 = 5$ mm.

Initial conditions and open boundaries are extracted from a daily average of the BACH1000, 1 km resolution, 100 sigma layers, MARS3D simulation (Charria et al., 2017; Akpınar et al., 2020). Open boundaries are parameterized using the Chapman (Chapman, 1985) and Flather scheme (Marchesiello et al., 2001) for 2D components (sea surface height and barotropic velocities). An Orlanski scheme is used for the 3D momentum and tracers (Orlanski, 1976). A sponge layer with 200 grid points is used.

Atmospheric forcing is provided by ERA-Interim (3 h) (Dee et al., 2011). The wind stress is computed from the C_d drag coefficient, model SST, and wind velocities at 10 m using the bulk formulae. The different components of the air-sea heat exchanges are parameterized using bulk definitions. The bulk formulation is based on air temperature, pressure, relative humidity at 2 m, rain and cloud coverage (ERA-Interim). The tidal sea surface elevation and currents with 15 harmonic constituents are imposed along the boundaries using the FES2014 ocean tide atlas (Lyard et al., 2020). In the result section, model outputs are detided using Godin filtering (Godin, 1972). In our study, 2 months (March and August 2008) have been simulated.

The freshwater source salinity and temperature for the Gironde river are estimated as monthly averages (March, August 2019) from the MAGEST *in situ* observing network time series (at 1 m depth; Figures 1D,E). Since no MAGEST data were available during the 2008 year, we chose the nearest year where



freshwater source salinity and temperature are available (the 2019 year). The Pauillac station was considered here (location shown in **Figure 1A**) for summer and winter simulations. For the Loire river, temperature and salinity are estimated from the BOBYCLIM climatology (<http://www.ifremer.fr/climatologie-gascogne/>; Vandermeirsch et al., 2010). River discharges are provided by Banque Hydro France for Dordogne, Garonne (Gironde as a combination of both Dordogne and Garonne rivers) and Loire rivers, and their daily values are shown in

Figures 1B,C. River inputs (discharge, freshwater source salinity, and temperature) are applied over one grid point at the end of the Gironde and Loire estuaries.

2.2. Methods of Analysis

2.2.1. River Plume Instabilities

The instability mechanisms are analyzed using the transfer of kinetic and potential energy from the mean to the turbulent flows. A scale decomposition is performed (into mean and

perturbations) on the velocity and buoyancy fields. We write $\mathbf{u} = \bar{\mathbf{u}} + \mathbf{u}'$ and $b = \bar{b} + b'$. Overbar and prime denote temporal mean over one day as follows $\overline{X(t)} = \frac{1}{T} \int_{t-T/2}^{t+T/2} X(t') dt'$ and perturbations relative to the mean flow, respectively. The horizontal (HRS) and vertical (VRS) shear stresses and the vertical buoyancy flux (VBF) (instantaneous values) are expressed as (Gula et al., 2016):

$$\text{HRS} = -u'^2 \partial_x \bar{u} - u'v'[\partial_y \bar{u} + \partial_x \bar{v}] - v'^2 \partial_y \bar{v} \quad (1)$$

$$\text{VRS} = -u'w' \partial_z \bar{u} - v'w' \partial_z \bar{v} \quad (2)$$

$$\text{VBF} = w'b' \quad (3)$$

Positive HRS, VRS, and VBF values indicate the potential presence of barotropic, vertical shear, and baroclinic instabilities, respectively. A positive HRS [transfer from MKE (mean kinetic energy) to EKE (eddy kinetic energy)] characterizes barotropic instability. A positive vertical buoyancy flux (VBF, transfer from potential to kinetic energy) reveals baroclinic instability. Mixed barotropic and baroclinic instabilities occur when VBF and HRS are positive at the same location. Kelvin-Helmholtz instability is characterized by a positive VRS. More generally, negative values of VBF, VRS, HRS represent a contribution from the perturbation to the mean flow (Kang, 2015; Contreras et al., 2019).

The change of sign of Ertel potential vorticity (Q) (or of its anomaly with respect to a state of rest) is used to indicate instability. Ertel potential vorticity is written as:

$$Q = \omega_a \cdot \nabla b \quad (4)$$

where $\omega_a = \nabla \wedge \mathbf{u} + f\mathbf{k}$ is the absolute vorticity and $b = -g \frac{\rho}{\rho_0}$ is the buoyancy (ρ_0 is the mean density in our domain).

To understand the relation between river plumes, stratification and shear mixing, we evaluate the Richardson Number:

$$R_i = \frac{N^2}{S^2} \quad (5)$$

where $N^2 = \partial_z b$ is the Brunt-Vaisala frequency and $S^2 = \partial_z u^2 + \partial_z v^2$ is the vertical shear of horizontal velocity. $R_i < 0.25$ indicates the possibility of Kelvin Helmholtz instability (which is one type of vertical shear instability).

The Hoskins (1974) criteria $fQ < 0$ and $R_i < 1$ indicate a potential existence of symmetric instability.

Eddy kinetic energy [$\text{EKE} = 0.5 * (u'^2 + v'^2)$] was decomposed over different modes of instability as suggested by Stone's theory (Stone, 1970). We decompose perturbations using Fourier analysis onto baroclinic (BC), symmetric (SI), mixed modes (MM; as in Stamper and Taylor, 2016); MM are a combination of SI and BC. We consider the baroclinic mode in the cross-shore direction (independent of the wavenumber l) and the symmetric mode in the along-shore direction (independent of the wavenumber k); the mixed mode is for both directions

(wavenumbers different than 0). We express the vertical averaged eddy kinetic energy associated with each mode as follows:

$$\overline{\text{EKE}}^z (k = 0, l \neq 0) = \frac{1}{2H} \int \int u'^2 + v'^2 dl dz \quad (6)$$

$$\overline{\text{EKE}}^z (l = 0, k \neq 0) = \frac{1}{2H} \int \int u'^2 + v'^2 dk dz \quad (7)$$

$$\overline{\text{EKE}}^z (k \neq 0, l \neq 0) = \frac{1}{2H} \int \int \int u'^2 + v'^2 dk dl dz \quad (8)$$

Where we express perturbations as:

$$\mathbf{u}', \mathbf{v}' = (\mathbf{u}(z), \mathbf{v}(z)) * \exp(\sigma t) * \exp i(kx + ly) \quad (9)$$

H represents the averaged depth of the base of the plume and is expressed as follows (Thomson and Fine, 2003):

$$\text{mld} = \frac{\int z N^2 dz}{\int N^2 dz} \quad (10)$$

For each instability, the growth rate σ of instability is expressed as:

$$\sigma = \frac{1}{2(t_i - t_{i-1})} \log\left(\frac{\text{EKE}_i}{\text{EKE}_{i-1}}\right) \quad (11)$$

The same decompositions are performed on the EAPE (Eddy Available Potential Energy) field (Rouillet et al., 2014)

$$\text{EAPE} = \frac{b'^2}{2N^2} \quad (12)$$

where b' is the buoyancy perturbation field.

2.2.2. Analysis of the River Plume Restratification

We evaluate the ocean restratification in terms of PV mixing and of frontogenesis/frontolysis (Marshall and Nurser, 1992; Marshall et al., 2001; Lapeyre et al., 2006; Thomas and Ferrari, 2008). To describe PV mixing near the surface, we write the evolution equation of PV:

$$\partial_t Q + \nabla \cdot \mathbf{J} = 0 \quad (13)$$

where the flux is written $\mathbf{J} = w\mathbf{q} + \nabla b \wedge \mathbf{F} - \omega_a \mathbf{D}$. The first term is advective stirring ($\mathbf{J}_a = w\mathbf{q}$), the second term is frictional mixing ($\mathbf{J}_f = \nabla b \wedge \mathbf{F}$) and last term is diabatic mixing ($\mathbf{J}_d = -\omega_a \mathbf{D}$). We write $\mathbf{D} = \frac{D\mathbf{b}}{Dt} = \partial_t \mathbf{b} + u \partial_x \mathbf{b} + v \partial_y \mathbf{b} + w \partial_z \mathbf{b}$. \mathbf{F} represents body forces in the Navier-Stokes equations as expressed in Marshall and Nurser (1992).

At the surface, advective stirring can be neglected (via the Haynes and McIntyre impermeability theorem) and we can write $\mathbf{J} = \mathbf{J}_f + \mathbf{J}_d = \mathbf{J}_{\text{wind}} + \mathbf{J}_{\text{ttw}} + \mathbf{J}_{\text{dbuoy}} + \mathbf{J}_{\text{bot}}$.

The frictional term is made of the wind contribution at the surface (\mathbf{J}_{wind}) and of the body force exerted by the bottom (\mathbf{J}_{bot}). The diabatic term is made of the surface buoyancy flux ($\mathbf{J}_{\text{dbuoy}}$) and of a wind-driven buoyancy flux term at fronts (\mathbf{J}_{ttw} ,

where τ_w stands for turbulent thermal wind), where Ekman transport can advect dense water over light one (e.g., Thomas and Ferrari, 2008). These four terms are expressed as follows:

$$J_{\text{wind}} = (f + \zeta_z) \frac{\text{EBF}}{H} \quad (14)$$

$$J_{\text{ttw}} = (f + \zeta_z) \frac{\text{EBF}_g}{H} \quad (15)$$

$$J_{\text{dbuoy}} = (f + \zeta_z) B_0 H \quad (16)$$

$$J_{\text{bot}} = \nabla b \wedge \mathbf{F}_b \cdot \mathbf{n} \quad (17)$$

where $\text{EBF} = (\rho f)^{-1} \boldsymbol{\tau}^w \wedge \mathbf{k} \cdot \nabla_h \mathbf{b}$ ($\boldsymbol{\tau}^w$ for the surface wind stress) is the Ekman Buoyancy flux. $\text{EBF}_g = -\nu \partial_z \mathbf{u} \cdot \partial_z \mathbf{u}_g$ is the geostrophic Ekman buoyancy flux. Geostrophic shear is deduced from thermal wind balance, using $\nu = 0.1 H u^*$, a scaling where $u^* = \sqrt{\frac{\|\boldsymbol{\tau}^w\|}{\rho}}$ is the wind frictional velocity (Wenegrat et al., 2018). B_0 is the surface buoyancy flux deduced from $D = \partial_z B$. \mathbf{F}_b represents the body force (the right hand side terms of the Navier-Stokes equations) at the bottom.

We focus on the restratification processes using a Budget of vertical density gradient (Brunt Vaisala frequency). This budget is related to PV fluxes (deduced from a volume integral of Equation 13) and frontogenesis [$\text{FRONT} = \partial_t(\zeta_z b)$, where ζ_z is the vertical component of the relative vorticity and b is the buoyancy]. This budget is defined as in Wenegrat et al. (2018) but we include the lateral transport of N^2 across the lateral boundaries since the computation domain is finite and subject to tides and river discharge from the estuary; it is written as:

$$\begin{aligned} \overline{\partial_t N^2} + \frac{\text{bvp}|_{z_b}^{z_t}}{h} = & -\frac{1}{fh} (\langle \text{FRONT} \rangle|_{z_b}^{z_t} + \langle J_d \rangle|_{z_b}^{z_t} \\ & + \langle J_f \rangle|_{z_b}^{z_t} + \langle J_a \rangle|_{z_b}^{z_t}) \end{aligned} \quad (18)$$

where $\overline{N^2} = \frac{\langle b(z=z_t) - b(z=z_b) \rangle}{h}$; bvp is the boundary value problem considered here for the advection of N^2 across the lateral boundaries (called Σ); it is expressed as $\text{bvp} = \frac{1}{\Sigma} \int \int \mathbf{u} \cdot \mathbf{n} N^2 d\Sigma$. h represented the thickness ($z_t - z_b$) of the layer where this budget is evaluated. The brackets ($\langle \rangle$) indicate a horizontal averaging over a domain. In our study, this budget is evaluated near the surface and in the frontal region of the Gironde plume.

3. MODEL VALIDATION

3.1. Frontal Dynamics

In this section, the modeled salinity is described for the two simulated months (March and August). Here the salinity evolution is not detailed. The horizontal salinity gradients are derived and compared with MODIS chlorophyll concentration gradients (with ~ 800 m spatial resolution); this comparison of two different tracers aims at comparing the fronts. Indeed, remotely sensed salinity is not available at high resolution.

First, the spatial distribution of the salinity is explored in the studied region (Figures 2A,B). The Gironde river plume is made

of two regions: a bulge (an anticyclonic gyre near the river mouth, also called the near field) and a coastal current (also called the far field). When the river discharge rate is nominal ($\sim 1,500 \text{ m}^3 \text{ s}^{-1}$), the Gironde river plume is well developed (for instance, in March 2008). Low salinity water from the estuary is advected offshore in the plume, and extends northward, up to a latitude $\sim 46.5^\circ \text{N}$, via the coastal current. Indeed, low salinity values (with values of about 30) characterize the river water in the open ocean, once it has exited the estuary. This plume remains close to the coast due to wind influence. By contrast, in August, the bulge is small because of the low river discharge ($200 \text{ m}^3 \text{ s}^{-1}$), and of strong westerlies. Indeed, these westerlies favor the development of a northward coastal current. They constrict the coastal current near the coast while it extends to the northern part of the domain. The plume is bounded by sharp salinity gradients with the high salinity shelf water (34–35 psu). These gradients are observed to oscillate with tides.

Figure 3 shows the horizontal salinity gradient and MODIS chlorophyll gradient in the studied region. The salinity gradient is mainly zonal as $\partial_x S > \partial_y S$. In March, salinity fronts are intense inside and outside of the Gironde estuary (Figure 3A). Near the Gironde river mouth, they remain close to the coast (longitude $\sim 1.5^\circ \text{W}$). These fronts are more sensitive to the average river discharge. The river discharge also feeds the coastal current where salinity fronts are intense. In the Gironde river plume, the zonal salinity gradient is largest in the estuary since the river discharge is low in August (Figure 3B). In the near field, the Gironde river plume front remains close to the coast (longitude $\sim 1.5^\circ \text{W}$). This plume extends to the north (up to a latitude $\sim 46.5^\circ \text{N}$) in the coastal current. Moderate winds and small river discharge constrict the coastal current near the coast. Beyond the river plume front, small scale filaments and eddies are observed.

Then, we compare these modeled salinity fronts to observed chlorophyll fronts (Figures 3C,D). In winter, cloud coverage does not allow the observation of the Gironde river plume (Figure 3C). Thus, comparisons are carried out outside of this region. South of the Gironde river plume (latitude between 44.5 and 45°N), the observed chlorophyll fronts and modeled salinity fronts locations are similar (longitude $\sim 1.6^\circ \text{W}$). On the northern side of the bay, the Loire river plume front (latitude $\sim 47^\circ \text{N}$) remains close to the coast in our numerical simulation and in the observed MODIS dataset. The modeled and observed river plume fronts are different in intensity. The location of salinity and chlorophyll fronts is similar outside of the Loire river plume. In August, the turbid Gironde river plume and salinity fronts are similar (Figure 3D). In the near field, the chlorophyll gradient maxima is close to the coast (longitude $\sim 1.5^\circ \text{W}$). Meanwhile, the chlorophyll front is at the same longitude in the coastal current.

Thus, our numerical simulations reproduce the frontal activity linked with the salinity gradients in the studied region. The main differences between the model and the data are that: (i) in the Gironde river plume, the coastal plume front is closer to the coast in numerical simulations, (ii) small scale eddies and filaments outside the Gironde river plume are not observed in the MODIS dataset. These differences can be due to: (i) different horizontal resolutions, (ii) MODIS chlorophyll data is influenced by biological processes, (iii) uncertainties in MODIS

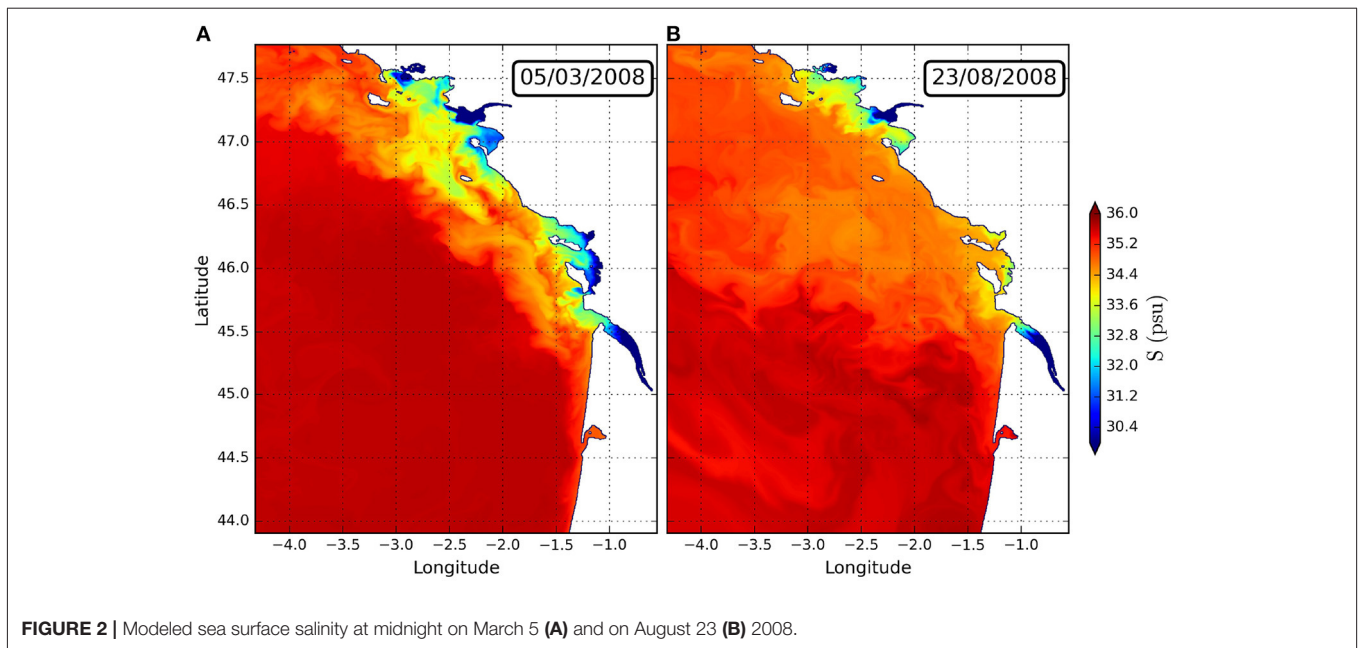


FIGURE 2 | Modeled sea surface salinity at midnight on March 5 (A) and on August 23 (B) 2008.

chlorophyll data due for instance to cloud coverage, or (iv) the fact that we include only the Loire and Gironde rivers in our numerical simulations. Other rivers, such as the Charente and the Sèvre-Niortaise, located between the Loire and Gironde rivers, may contribute to the total freshwater input and change slightly the coastal current front location due to their small discharges (between 12 and 40 m³ s⁻¹ in annual average).

3.2. Tidal Dynamics in the Model Simulations

Here, we compute the modeled and observed sea surface height (ssh) anomaly. The ssh anomaly (ssha) is computed as the perturbation from a time mean over the studied periods. Then, we decompose these signals into different tidal harmonics. This decomposition is performed on each tidal constituent and written as

$$\text{ssha}(t) = \sum_{i=0}^k a_i \cos(\omega_i t + \phi_i) \quad (19)$$

where a_i are the Fourier coefficients, ω_i is the angular frequency of harmonic i and ϕ_i is its phase.

These decomposed signals are extracted at four locations across the domain. These locations are listed in **Table 1**. In our numerical simulations, we consider the nearest immersed locations to observations. This validation is performed for semi-diurnal (M2, S2, and N2) and for diurnal (K1, O1, Q1) tidal constituents. The amplitudes and phase lags averaged over all tidal gauges for observations and numerical model are first explored (**Figure 4**). The main differences are observed for the semi-diurnal components with an amplitude overestimated by the model of the M2 and N2 harmonics (+~10 cm in August and March) and an underestimation of the S2 harmonic (-5 to 10 cm) (**Figure 4A**). Simulated diurnal components are close to

observations with differences around 1 cm (an underestimation by the model of the O1 harmonic amplitudes by 1 cm, an overestimation of the K1 harmonics by 1–2 cm for both months, with differences of 0.5–1 cm for Q1 harmonic).

In March, the model overestimates the phase lags of several tidal constituents: S2 by 1°, N2 by 1°, and O1 by 2° (**Figure 4B**). It underestimates the M2 by 1°, K1 by 2°, and Q1 by 10° tidal constituents in phase lags. In contrast, during August the model underestimates the S2 by 30°, N2 by 100°, O1 by 5°, and Q1 by 10° tide harmonics as phases lags. But it overestimates the phase lags of the M2 by 20° and K1 by 10° harmonics. In order to evaluate these discrepancies two statistical indicators are defined, the root mean square error (RMSE) and the Willmott refined index (d_i) that we write as

$$\text{RMSE} = \sqrt{\frac{1}{n} \sum_1^n (P_i - O_i)^2} \quad (20)$$

$$d_i = 1 - \frac{\sum_1^n |P_i - O_i|}{2 \sum_1^n |O_i - \bar{O}_i|} \quad (21)$$

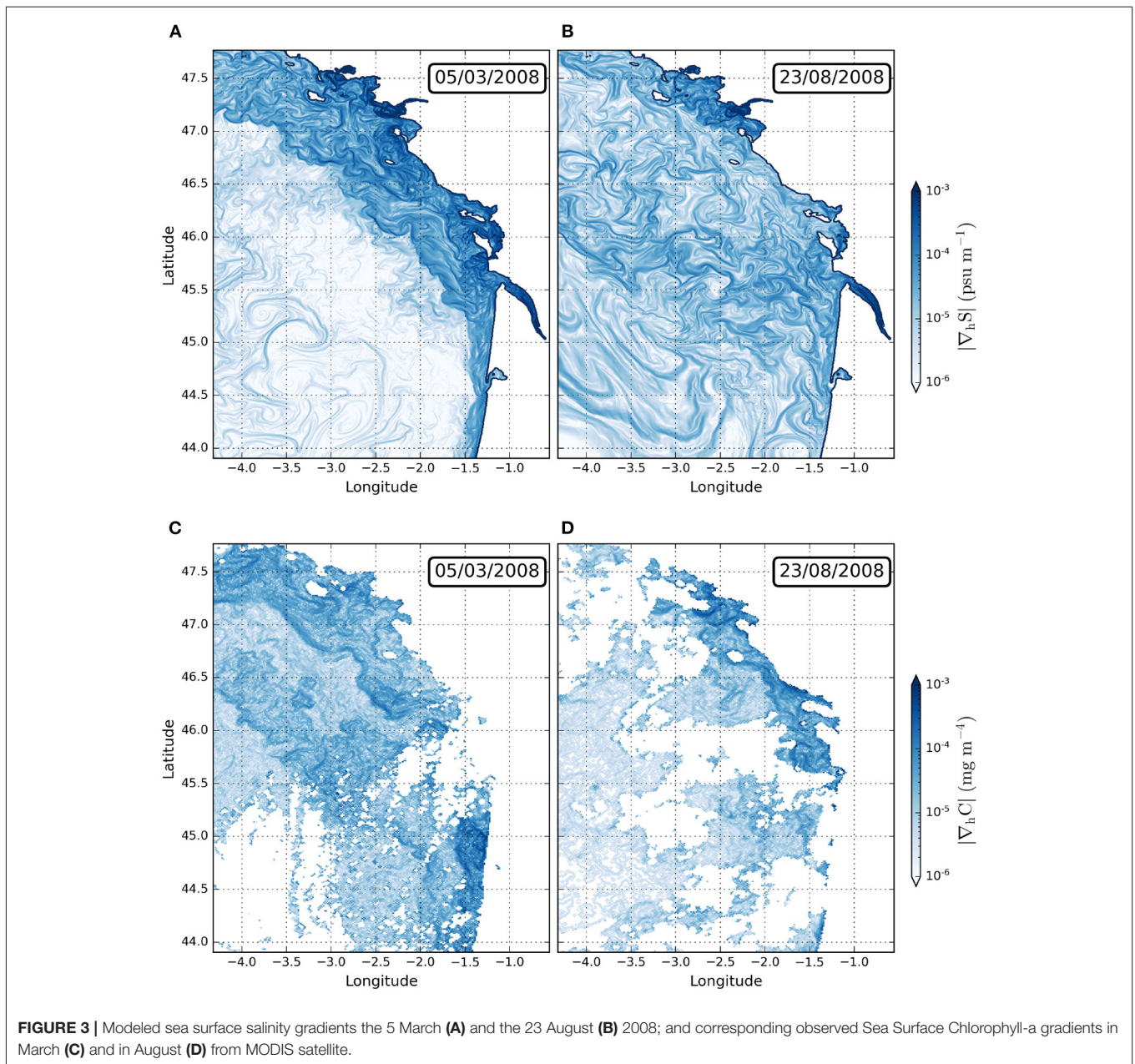
when $\sum_1^n |P_i - O_i| \leq 2 \sum_1^n |O_i - \bar{O}_i|$

$$d_i = \frac{2 \sum_1^n |O_i - \bar{O}_i|}{\sum_1^n |P_i - O_i|} \quad (22)$$

when $\sum_1^n |P_i - O_i| > 2 \sum_1^n |O_i - \bar{O}_i|$

where the overbar denotes a time average over the studied period and n refers to the number of values for the observed and modeled time series.

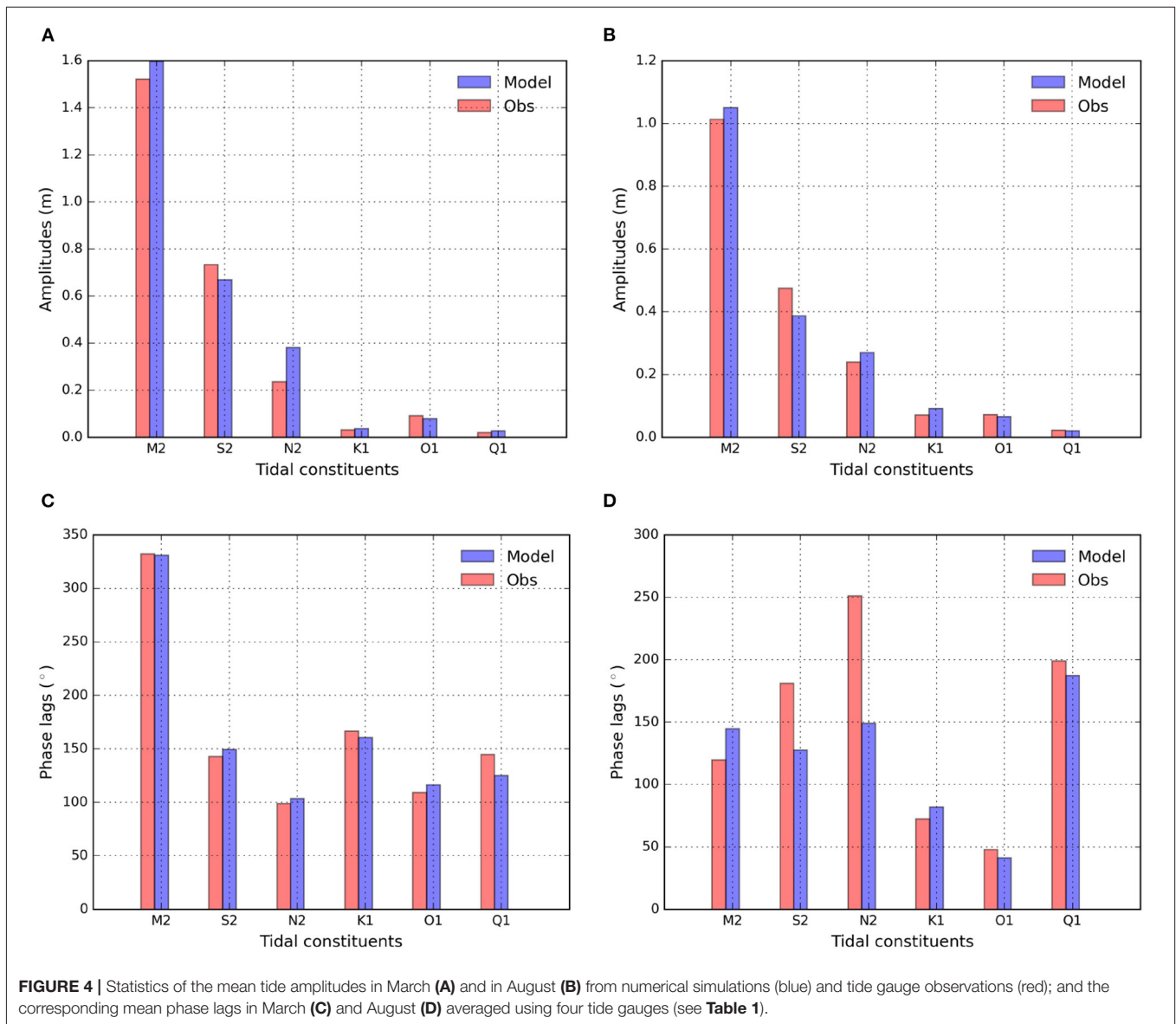
The RMSE evaluates the bias between the modeled (P_i) and the observed (O_i) ssh anomaly signals. The refined Willmott

**TABLE 1** | Geographic location of each tide gauge in the studied domain.

Tide gauges	Latitude [° N]	Longitude[° E]
Arcachon eyrac (Station 1)	44.7	-1.2
Port bloc (Station 2)	46.0	-1.1
Herbaudiere (Station 3)	47.0	-2.2
Saint nazaire (Station 4)	47.3	-2.2

index characterizes the performance of the model to predict the observed values and it is bounded between -1 and 1 (Willmott et al., 2012). The refined Willmott index is less sensitive to

outliers. These indicators are computed for each tide gauge and constituent. The RMSE of ssh anomaly is <12 cm at each station for the semi-diurnal tidal constituents in March and August (Figures 5A,B). This indicator is above 10 cm for the N2 harmonic during these periods. The RMSE between observations and model ssh anomaly is between 0.5 and 2 cm at each location in March and August for the diurnal tidal constituents. It reaches a maximum of 2 cm for the K1 harmonic near the Gironde (Station 2) and the Loire (Station 3) river plumes in August. The Willmott refined index indicates that the model performance at each location is good ($d_i \geq 0.7$) for most of the semi-diurnal and diurnal tidal constituents in March and August (Figures 5C,D). However, the agreement between the numerical and observations



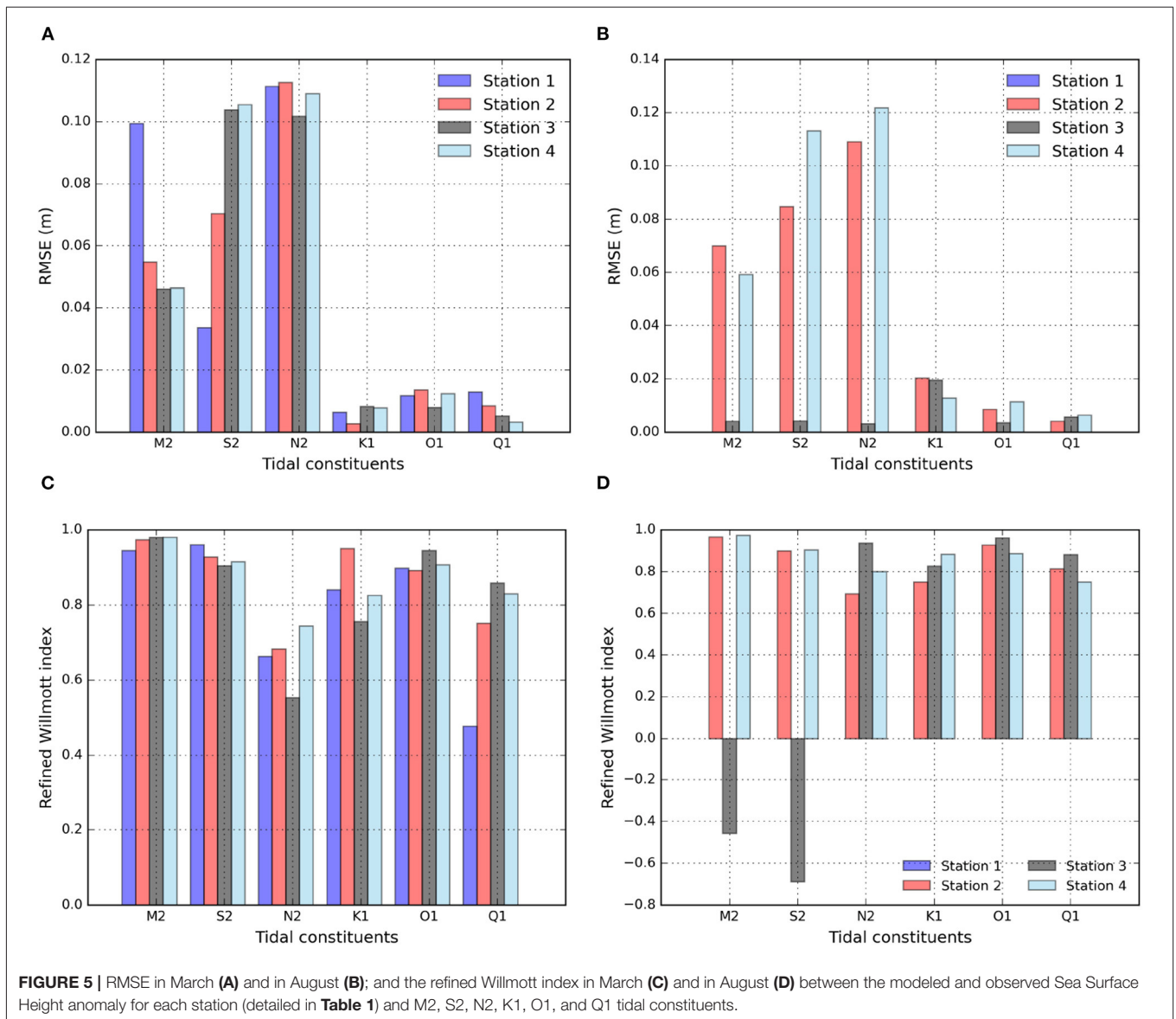
is correct ($0.5 \leq d_i < 0.7$) for the N2 harmonic at the 4 stations in March, and near the Gironde river plume (Station 2) in August. This satisfactory performance is also observed for the Q1 harmonic near the Gironde river plume (Station 1). A poor performance of the model ($0 \leq d_i < 0.5$) is observed for the Q1 harmonic at station 1 (near the Gironde river plume) in March. Finally, the model outperformed ($d_i < 0$) for the M2 and N2 harmonics near the Loire river plume (Station 3) in August.

The differences between observed and modeled sea level can be explained by: (i) the location of the tide gauges near the coast, or near islands, where the model grid is too coarse to resolve local processes, or (ii) the sensitivity to the bottom drag parameterization in the numerical model. Simulated tides are sensitive to the bathymetry, the bottom roughness and to the friction law (linear, quadratic, and logarithmic) (Toublanc et al., 2018; Piton et al., 2020).

Despite these differences and since the Bay of Biscay is energetic in M2 and S2 tidal harmonics, the numerical model performance is satisfactory for the simulations of tides.

3.3. Vertical Salinity Structure

Now, we evaluate the salinity distribution in the numerical simulations of March and August 2008, in order to explore the Gironde river plume dynamics. We use observations from cruises carried out during these periods. ECLAIR cruises (Huret et al., 2018) located in front of the Gironde estuary, and achieved in March (10–16th) and August (10–14th) 2008 constitute a unique and valuable dataset to validate the vertical salinity structure in our simulations. The vertical salinity profiles from 13 CTD stations are compared with collocated modeled profiles (Figure 6). During the ECLAIR1 cruise in March 2008, a river plume with a limited offshore extent was observed despite the



high river discharge season. Profiles 2 and 4 (Figure 6) show comparable salinity values with a similar stratification (profile 2 has a lower salinity at the surface originated from the plume). The model overestimates the salinity (+0.1 in profile 2 in the surface layer; +0.1 in profile 4 outside the plume in a vertically mixed water column). In summer, during ECLAIR5, the modeled river plume extends offshore with several low salinity filaments. The river plume reaches a depth of about 30 m (profiles 7 and 13) in the numerical simulation, similar to the observed profiles. In the plume, low salinities between 34.4 and 34.6 are reproduced in the simulations. Deeper, below 40 m depth, the observed and simulated salinities are very close with values around 35.6. The large spatial and temporal variability of the river plume makes the comparison to *in-situ* observations complicated. However, the simulated salinity and vertical gradients are in good agreement with the observations which make us confident about the realism of our simulations of the plume.

4. ANALYSIS OF THE GIRONDE RIVER PLUME STRUCTURE, STABILITY, AND MIXING

4.1. Gironde River Plume Dynamics

The dynamics of the Gironde river plume is first analyzed using the local Rossby number ($R_o \sim \frac{\zeta_z}{f}$, where ζ_z is the vertical component of the relative vorticity and f the Coriolis parameter) at the surface; this is presented in Figure 7. This local Rossby number determines the geostrophic or ageostrophic nature of the velocity field of the Gironde river plume. In winter (March), the circulation is mostly anticyclonic in the plume ($\zeta_z < 0$) except : (i) at the river mouth (longitude $\sim 1.2^\circ\text{W}$ and latitude between 45.5 and 45.6°N), (ii) in the northern part of the coastal current (longitude $\sim 1.5^\circ\text{W}$ and latitude $\sim 46.2^\circ\text{N}$), and (iii) offshore of the plume front (longitude $\sim 1.5^\circ\text{W}$ and latitude between 45.75 and 46.2°N ; Figure 7, left). The circulation is ageostrophic [R_o

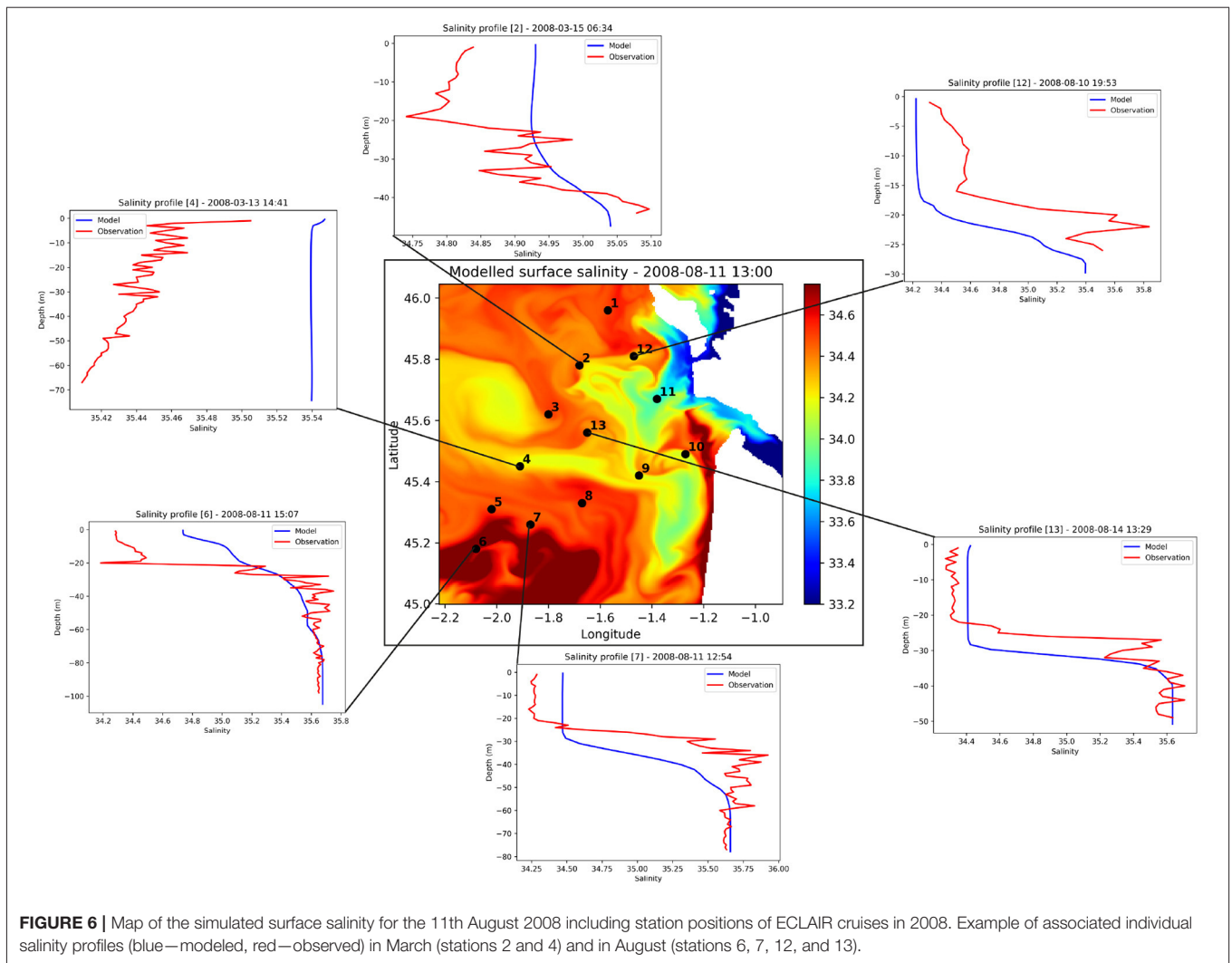


FIGURE 6 | Map of the simulated surface salinity for the 11th August 2008 including station positions of ECLAIR cruises in 2008. Example of associated individual salinity profiles (blue—modeled, red—observed) in March (stations 2 and 4) and in August (stations 6, 7, 12, and 13).

$\sim O(1)$] at these locations. Moreover, strong negative vorticity ($\frac{\zeta}{f} < -1$) is observed in the coastal current. Further offshore, over the continental shelf, the local Rossby number is small, indicating a geostrophic balance. In contrast, when the ocean is stratified (in August), the circulation remains anticyclonic in the river plume except : (i) at the northern corner of the river mouth (longitude $\sim 1.2^\circ\text{W}$ and latitude $\sim 45.6^\circ\text{N}$), (ii) near the coast south of the Gironde river plume (longitude between 1.2 and 1.5°W and latitude between 45 and 45.4°N), and (iii) at the offshore edge of the plume front (longitude $\sim 1.5^\circ\text{W}$ and latitude between 45.4 and 46.2°N ; **Figure 7**, right). This (cyclonic) circulation is ageostrophic at the northern (latitude between 45.75 and 46°N) and southern edges of the plume front and in a small filament south of the Gironde, along the coast and to the east. At the southern edge of the plume, a small ageostrophic cyclonic eddy can be observed (longitude $\sim 1.5^\circ\text{W}$ and latitude $\sim 45.4^\circ\text{N}$) due to recirculation processes. Over the continental shelf and outside of the Gironde river plume, the overall circulation is anticyclonic except at the rim of small

eddies and in filaments. The stratification in summer favors the development of anticyclonic eddies over the continental shelf.

Despite the existence of local ageostrophic motions in the Gironde river plume and over the continental shelf, on average (over the box in **Figure 7**), the global Rossby number is small ($R_o \sim 0.1$) both in March and August. This means that the global circulation over the continental shelf is mostly in geostrophic balance. Therefore, to understand the contrast between these motions, we represent in **Figure 8** the surface averaged time evolution of the wind stress intensity ($\tau = \sqrt{\tau_x^2 + \tau_y^2}$, where τ_x and τ_y are the cross-shore and along-shore wind stress components) and the vertical geostrophic shear. These terms are evaluated in frontal regions bounded by two isopycnals ($1,024$ and 1024.5 kg m^{-3} in August, $1,025$ and 1025.5 kg m^{-3} in March) and are written as

$$S_g^2 = \partial_z u_g^2 + \partial_z v_g^2 = \frac{\partial_y b^2 + \partial_x b^2}{f^2} \quad (23)$$

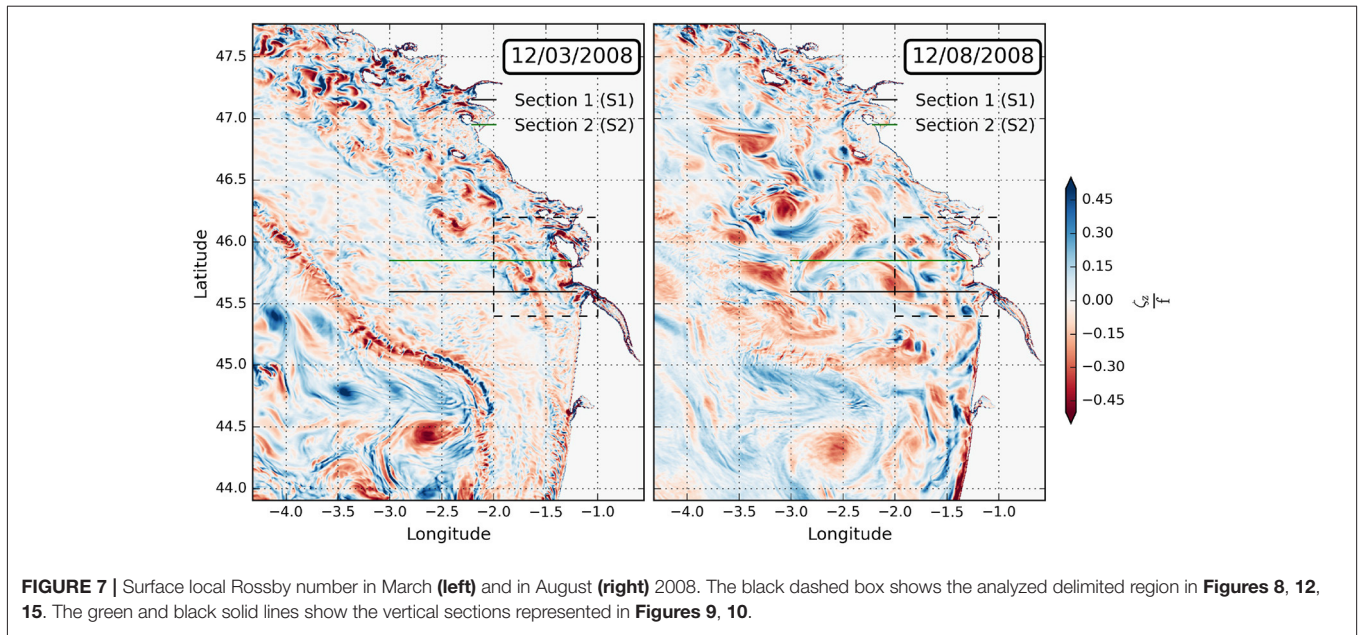


FIGURE 7 | Surface local Rossby number in March (left) and in August (right) 2008. The black dashed box shows the analyzed delimited region in **Figures 8, 12, 15**. The green and black solid lines show the vertical sections represented in **Figures 9, 10**.

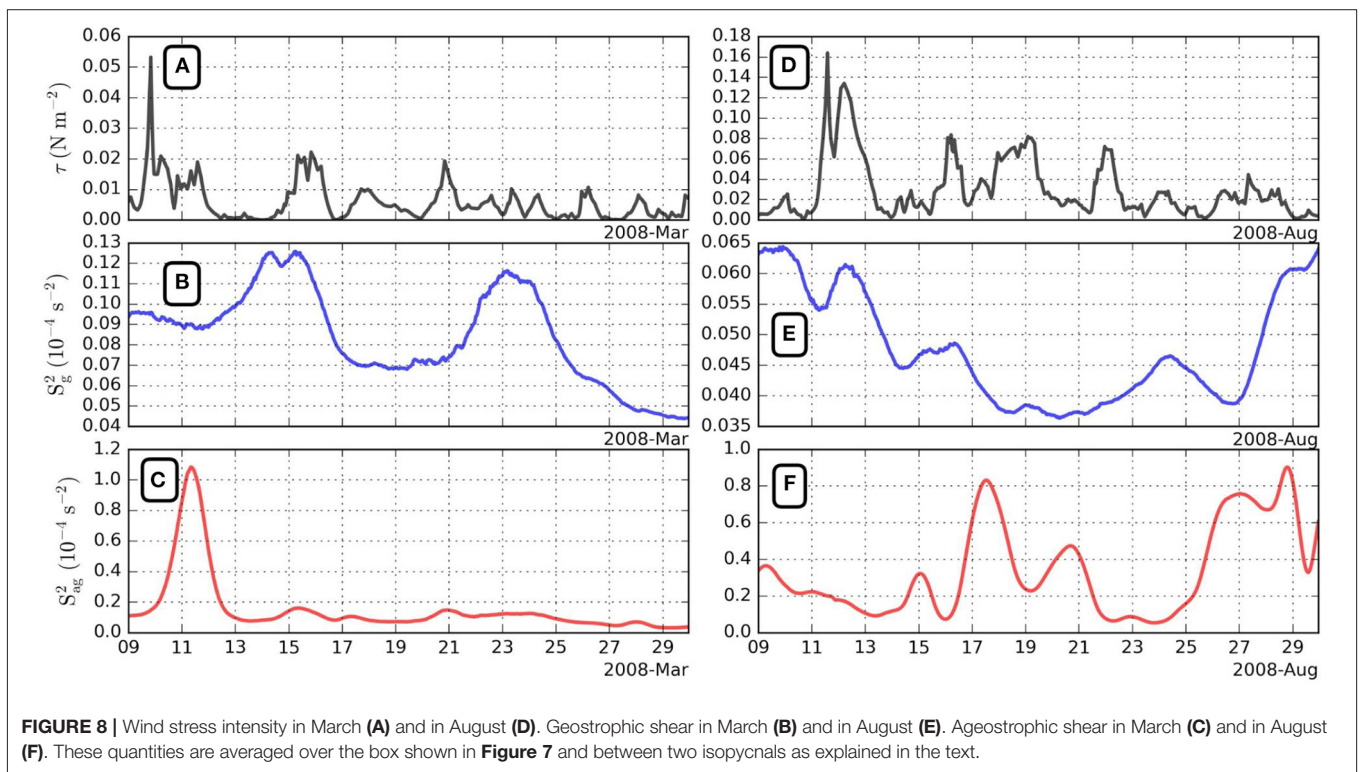


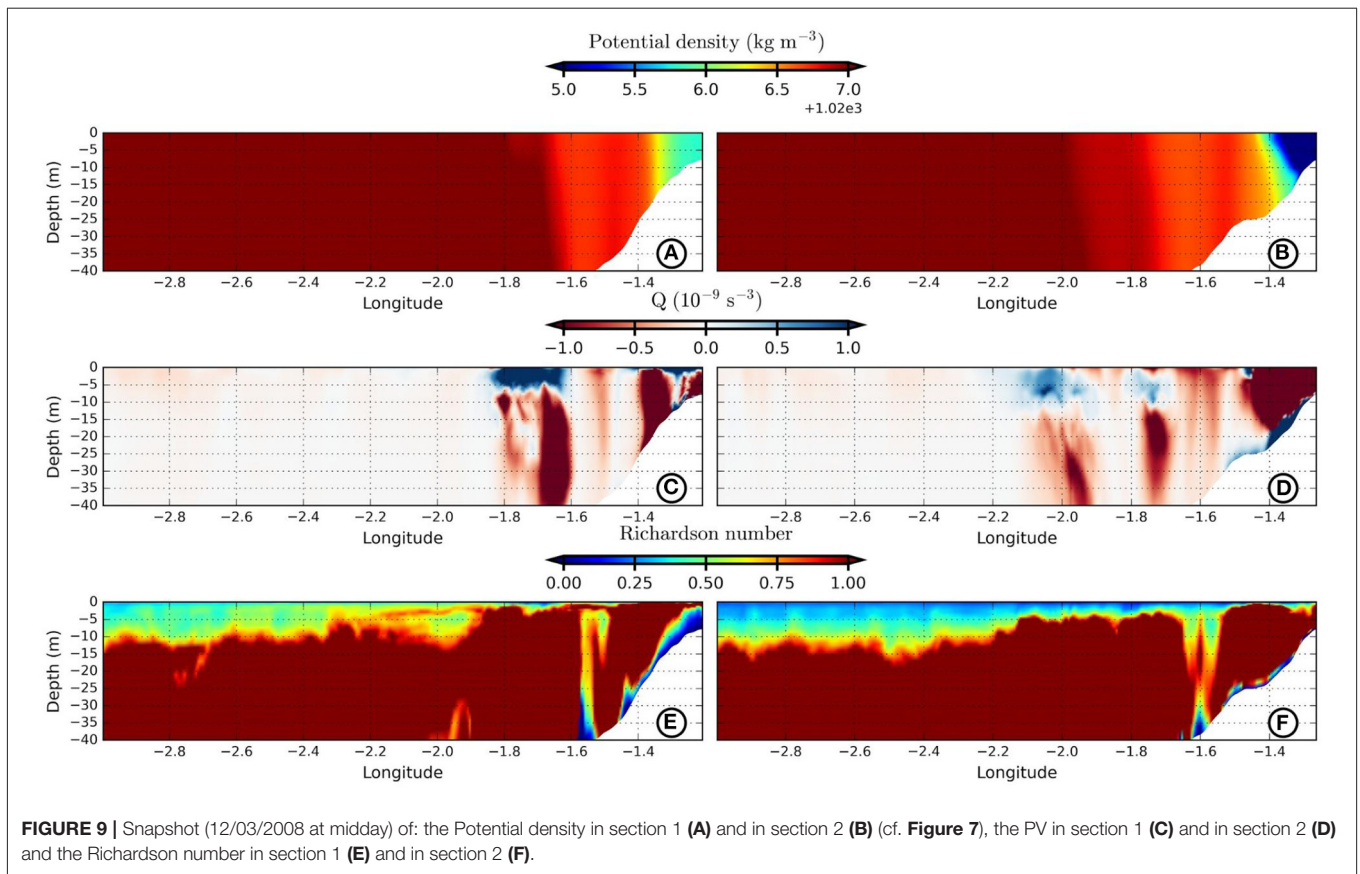
FIGURE 8 | Wind stress intensity in March (A) and in August (D). Geostrophic shear in March (B) and in August (E). Ageostrophic shear in March (C) and in August (F). These quantities are averaged over the box shown in **Figure 7** and between two isopycnals as explained in the text.

where $b = -g \frac{\rho}{\rho_0}$ is the buoyancy (g is the gravity acceleration, ρ is the potential density and ρ_0 is a mean density over the studied domain), and the vertical ageostrophic shear is written as

$$S_{ag}^2 = \partial_z(u - u_g)^2 + \partial_z(v - v_g)^2 \quad (24)$$

In March, a storm is observed during the first half of the month (between March 9th and 13th; **Figure 8A**). During this period

and after a lag of ~ 1 day, the vertical ageostrophic shear increases and the geostrophic shear remains steady (**Figures 8B,C**). Then (between 13 and 15th March), a wind relaxation event is observed during which the ageostrophic shear slackens and the geostrophic shear increases. Afterwards (between 15 and 21st March), the geostrophic shear weakens and remains steady during 3 days. Conversely, during the latter period, few moderate wind events are observed with few variations in the ageostrophic shear.



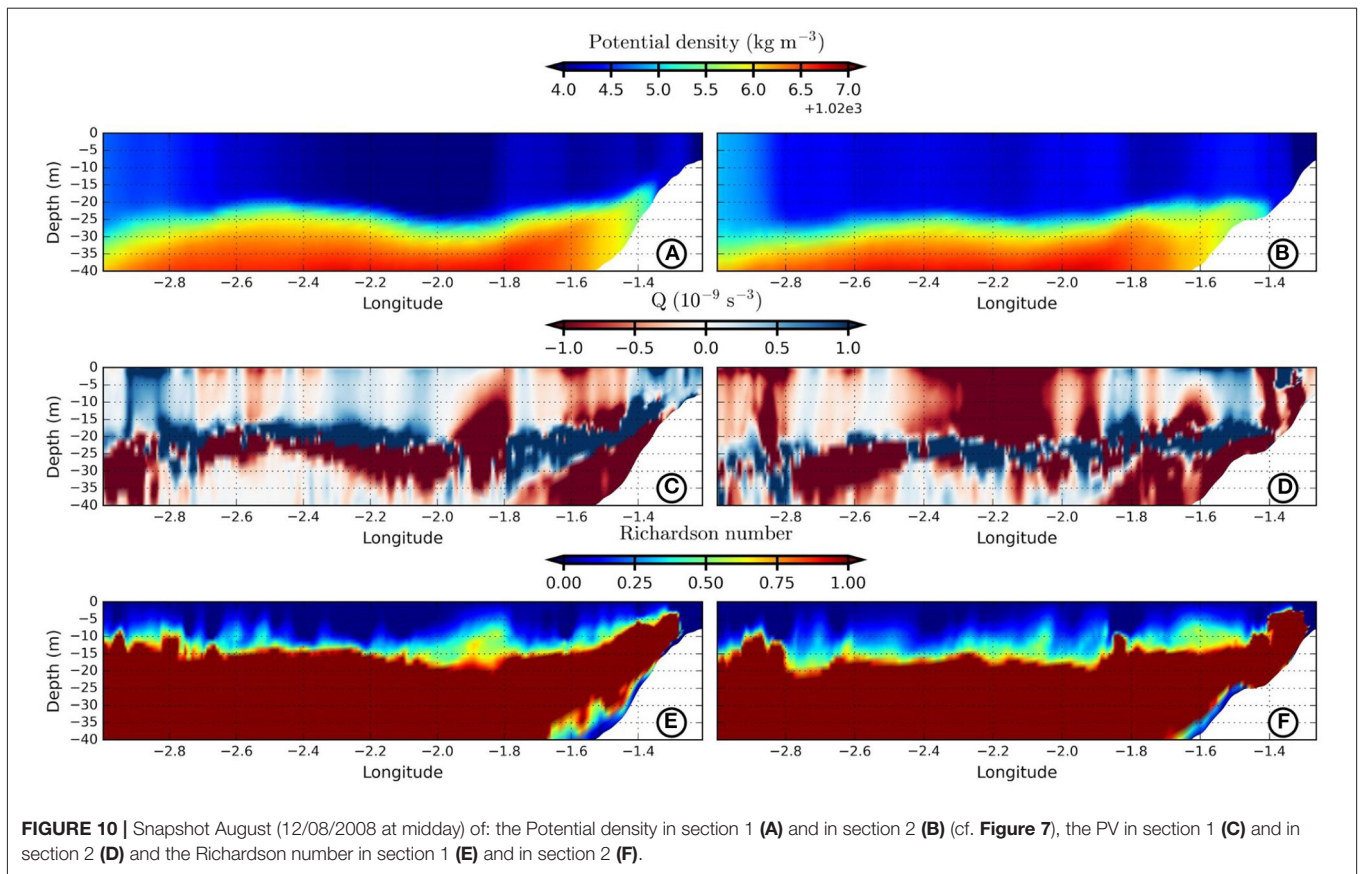
Following this period (between 21 and 23rd March), weak wind events are associated with the growth of geostrophic shear and weak ageostrophic shear. At the end of March, the geostrophic shear decreases noticeably and a weak maximum in the ageostrophic shear is observed. Geostrophic shear growth events are associated with wind relaxation and increase in river discharge ($Q \sim 1,000$ and $1,500 \text{ m}^3 \text{ s}^{-1}$, see Figure 1B). Meanwhile, the wind conditions in August 2008 are characterized by a series of strong wind events, with an intensity larger than the peak in March (an order of magnitude larger). Therefore, the ageostrophic component predominates largely over the geostrophic shear (an order of magnitude larger) due to these wind conditions and to the weak river discharge during this period ($Q \sim 200 \text{ m}^3 \text{ s}^{-1}$, see Figures 1C, 8D). The increase of the ageostrophic shear during this month is due to previous wind gusts (Figure 8F). Moreover, the geostrophic shear increases during wind relaxation events or when the ageostrophic shear slackens (Figure 8E). It remains quasi-steady during periods where the ageostrophic shear increases.

Thus, ageostrophic motions prevail in the frontal region of the plume due to (i) a local Rossby number $R_0 \sim O(1)$ and (ii) higher (two times larger in March or an order of magnitude larger in August) ageostrophic shear than the geostrophic shear (the geostrophic shear is an order of magnitude larger in March due to the average river discharge $>1,000 \text{ m}^3 \text{ s}^{-1}$). In the Bay of Biscay, ageostrophic motions are more noticeable in winter

(March) over the inner shelf (shallower than 100 m) and over the whole continental shelf in summer (August).

4.2. Generation and Occurrence of Instabilities in the Gironde River Plume

In this section, we perform diagnostics to identify and characterize instabilities in the Gironde river plume. First, we evaluate the existence of symmetric instabilities using the Hoskins stability criterion in the near field and the coastal current during March and August. The Hoskins stability criterion is based on negative PV values and a Richardson number smaller than one. Negative PV are related to different instabilities: gravitational, inertial (centrifugal), or symmetric. Gravitational instability requires unstable stratification (negative N^2) which is not the case here since the Richardson number is positive (Figures 9E,F). Centrifugal instability requires a negative absolute vorticity which is not the case here either (figure not shown). Hereafter, we will refer to negative PV (Hoskins criteria) as symmetric instabilities since it is mostly dominated by geostrophic and ageostrophic shears. In March, symmetric instabilities exist in different locations of the near field: (i) in the Gironde river plume (longitude between 1.25 and 1.4°W) from the surface to the bottom, (ii) at the offshore edge of the river plume front (longitude $\sim 1.5^\circ \text{W}$) where large (negative) values are observed near the surface (at 2 m depth), and (iii) offshore of the Gironde river plume (longitudes between 1.6



and 1.8°W) from 10 to 40 m depth (Figures 9C,E). In the plume interior, symmetric instabilities are generated via local flow interaction with moderate winds and river discharges inducing vertical sheared horizontal currents. In the offshore part of the plume front, they are also observed and intensified near the surface due to strong buoyancy/salinity gradients and high wind sheared flows since the vertical ageostrophic shear prevails there (see previous section). Offshore of the Gironde river plume, symmetric instabilities may exist from 10 m down to 40 m depth due to interior horizontal sheared currents and weak/homogenized stratification. Near the bottom, vertical shear instabilities may prevail, since the Richardson number is smaller than 0.25, due to high baroclinic tidal currents and steep bathymetric gradients which induce high sheared currents. In this region the freshwater density is lower than $1,026 \text{ kg m}^{-3}$ and the plume is bottom attached (isopycnals interact with the bottom) (Figure 9A).

In March, in the coastal current, symmetric instabilities also exist at different locations: (i) near the coast (longitude between 1.3 and 1.5°W) in almost the whole water column except in a small layer near the bottom, (ii) at the edge of the plume (longitude $\sim 1.6^{\circ}\text{W}$) between the surface and 25 m depth, and (iii) offshore of the plume (longitude between 1.7 and 2°W) between 15 and 40 m depth (Figures 9D,F). In the plume interior, symmetric instabilities are intensified near the surface (~ 5 m depth) via the interaction of the plume with winds, tidal currents and/or the coast. The plume interaction with winds

and baroclinic tidal currents enhances the sheared currents intensity and therefore the vertical components of the PV become dominant which induce negative PV. The interaction between the coast and the Gironde plume may also induce processes which may favor the development of such instabilities. At the edge of the plume, symmetric instabilities prevail on the upper 25 m due to frontogenetic processes inducing high salinity gradients, baroclinic tidal currents, and moderate winds favoring intense ageostrophic vertical shear. Meanwhile, offshore of the Gironde plume, these instabilities exist on the upper 10 m via the ageostrophic shear induced by moderate winds. Near the bottom in this region of the plume, since the freshwater interacts with the bottom with densities $< 1,026 \text{ kg m}^{-3}$ as seen in Figure 9B, vertical shear instabilities may dominate. The latter instabilities develop due to steep bottom slopes and baroclinic tidal currents which favor strong sheared flows.

In August, symmetric instabilities also exist at different locations of the near field region bounded by different isopycnals. In regions where the density is smaller than 1024.5 kg m^{-3} (Figure 10A), they exist at different longitudes: (i) between 1.4 and 1.6°W , (ii) between 1.8 and 2°W , and (iii) far offshore between 2.4 and 2.7°W . These instabilities span the vertical extent of the isopycnal layer, between the surface and 25 m depth (Figures 10C,E). Symmetric and vertical shear instabilities coexist from the surface down to ~ 10 m depth, since the Richardson number is smaller than 0.25 and the PV is negative, due to the wind activity inducing a high vertical shear. The river

discharge would have a weak influence on those instabilities since small values (\sim) $200 \text{ m}^3 \text{ s}^{-1}$ are observed during August. In this isopycnic layer and slightly beneath, symmetric instabilities exist also due to shear interior induced by strong frontogenetic processes generated by tidal currents and/or internal waves. Near the bottom, symmetric and vertical shear instabilities coexist due to strong bathymetric gradients and baroclinic tidal currents.

In the coastal current and during the same period, symmetric instabilities prevail in regions with smaller densities, $<1024.5 \text{ kg m}^{-3}$ as shown in **Figure 10B**, and at various zonal locations: (i) near the coast (longitude $\sim 1.4^\circ\text{W}$), (ii) between 1.6 and 1.8°W , (iii) between 1.9 and 2.4°W , and (iv) far offshore with longitudes $>2.8^\circ\text{W}$ (**Figures 10D,F**). These instabilities overwhelm almost the entire isopycnic layer and are more intense due to stronger wind bursts compared to a winter situation (an order of magnitude stronger). At the top 10 m, they coexist with vertical shear instabilities, since the Richardson number is smaller than 0.25, due to strong ageostrophic shear which engenders negative PV values. Symmetric instabilities also exist between 10 and 25 m depth in regards of the interaction between the ambient stratification and tidal currents which induce frontogenetic processes and therefore intense horizontal buoyancy gradients. Beneath this isopycnic layer and near the bottom, symmetric and vertical shear instabilities coexist ($R_i < 0.25$), from 1.4 to 1.6°W longitude, due to steep bottom slopes and tidal currents inducing high ageostrophic shear.

Energy conversion terms are evaluated near the surface, at 5 m depth, during both months to identify the existence and intensity of baroclinic, barotropic, and vertical shear instabilities (**Figure 11**). Positive HRS, VBF, and VRS indicate the existence of barotropic, baroclinic, and vertical shear instabilities, respectively. The VBF and HRS dominate over the VRS term near the river mouth (not shown—VRS values below 10^{-9} m s^{-3}).

In winter, barotropic and baroclinic instabilities coexist at a larger scale over the continental shelf at the rim of eddies and in filaments (**Figure 11A**). Over the continental shelf, winds play a major role in increasing the energy of the mean flow which feeds the perturbations, and therefore the generation of mixed barotropic/baroclinic instabilities is observed. Over the inner-shelf (above 100 m isobath), these mixed instabilities are more intense due to the interaction of density currents induced by Gironde plume and its front, tidal currents and wind bursts. Those interactions sustain the mean flow (buoyancy and momentum) with a high reservoir of energy which feed the perturbations and generate such instabilities.

In summer, mixed barotropic/baroclinic instabilities exist in the near field and the coastal current of the plume, and over the continental shelf (**Figure 11B**). Compared to winter, those instabilities are intensified over the whole domain. In the Gironde plume and since the river discharge is weak, the source of such instabilities is the interaction of the ocean surface layer with tidal currents and wind activity. Those interactions alter the stratification and the momentum which induce perturbations essential to the generation of mixed barotropic/baroclinic instabilities. Over the continental shelf, the mean flow induced by eddies, wind bursts, and internal waves favor the development of these instabilities.

Since the wind and tides contribute to the generation of baroclinic and symmetric instabilities, the relation between these two instabilities in frontal regions of the plume will be explored in the following section.

4.3. Plume Instability

The development of instability can be monitored using the evolution of the energy from buoyancy and momentum perturbations. We then decompose the Eddy Kinetic Energy (EKE) and Eddy Available Potential Energy (EAPE) in three main contributions from: symmetric, baroclinic, and mixed instabilities (**Figure 12**).

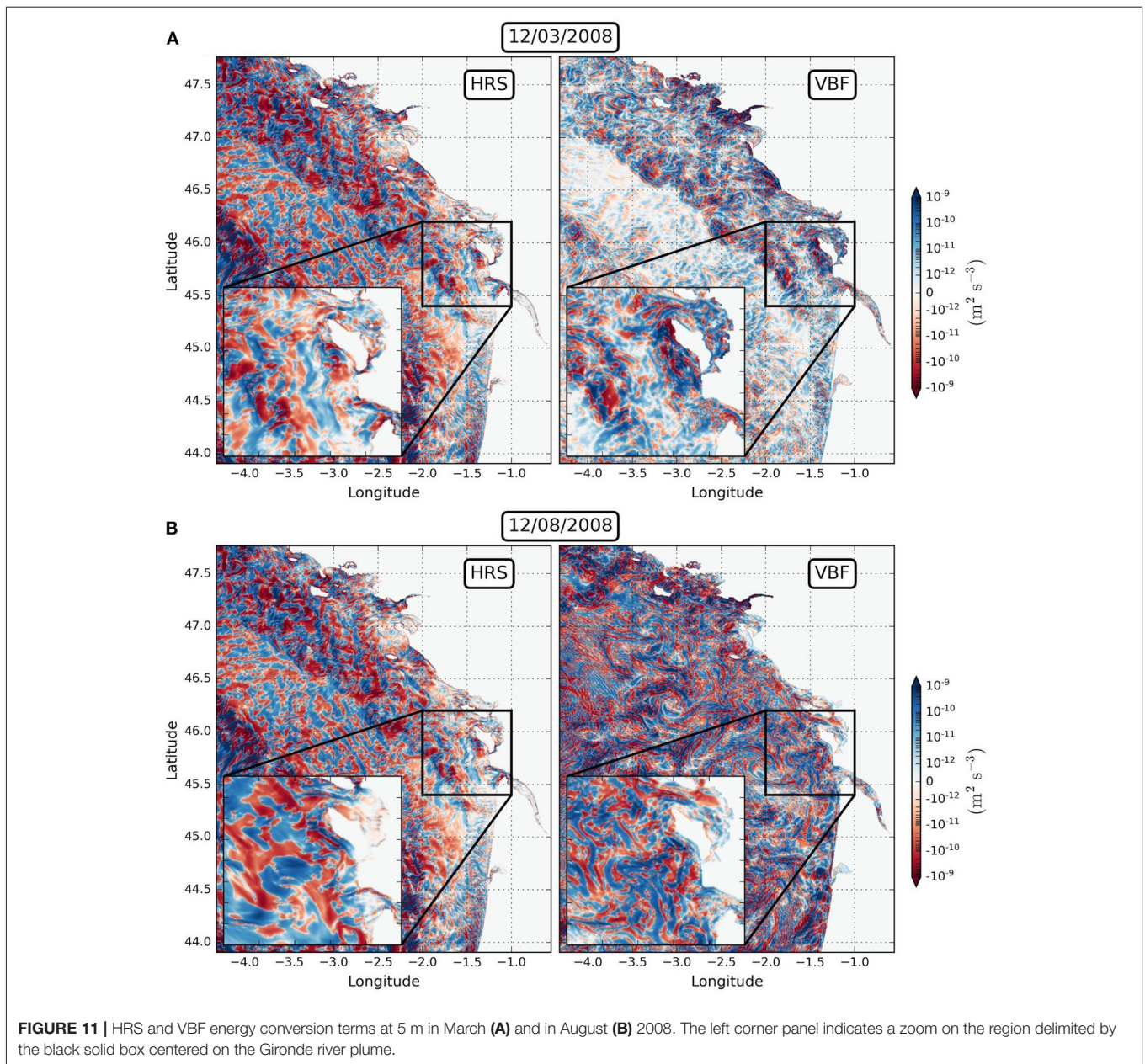
In winter, the mixed modes are dominant in both decompositions of EKE and EAPE; they are one order of magnitude larger than the symmetric and baroclinic modes during the first 8 days (see **Figures 12A–C**).

Meanwhile, during the last 2 days of this analyzed period, the three modes feed equally and weakly the perturbations in the 3D eddying state. Through this decomposition, two events are noticed which occur during the second half of March (on the 16th and the 17th). During these periods, peaks in EAPE precede peaks in EKE with a lag of about half a day. The lag is similar for the symmetric and baroclinic modes.

Conversely in August, the symmetric, baroclinic, and mixed modes supply EKE and EAPE significantly with a predominance of the mixed perturbations (**Figures 12D–F**). During this period, three major events can be observed in the EKE decomposition. The first event occurs around August 12th. On this day, the mixed mode grows first with a significant amplitude followed by symmetric and then baroclinic modes. Then, a second event occurs almost 2 days later when the symmetric mode grows first followed by baroclinic and then mixed modes. On August 16th, symmetric and mixed modes contribute equally and nearly at the same time followed by baroclinic modes. Finally, after this active period the three unstable modes have developed nonlinearly and reach a 3D eddying state. In contrast, in the EAPE decomposition only the first event is noticeable. It occurs almost a day later. Similarly to the EKE decomposition, mixed modes increase first followed by symmetric and then baroclinic modes. The lag between EKE and EAPE suggests that a transfer of energy occurs within the same instability mode.

The development of these instabilities is related to the wind activity. A lagged cross-correlation between the EKEs and the wind stress intensity (~ 0.7) reveals that the instabilities develop after wind events within a lag $\sim 18 \text{ h}$ in summer and ~ 3 days in winter (figure not shown). These lags are different due to a larger wind stress intensity in summer (an order of magnitude larger compared to winter).

Growth rates can be deduced from the evolution of EKE (see Equation 11). Estimated growth rates (**Figure 13**) range from 0.02 to 0.12 h^{-1} (i.e., time scales ranging from 8 to 50 h). In March, the second event grows faster and contributes more to the increase of the EKE (**Figure 13A**). Meanwhile in summer (**Figure 13B**), growth rates are higher for symmetric and baroclinic instabilities (between 0.04 and 0.08 h^{-1} for symmetric instabilities and between 0.04 and 0.1 h^{-1} for baroclinic instabilities). On the opposite, in winter, mixed and



symmetric instabilities have higher growth rates (between 0.04 and 0.1 h^{-1} for mixed instabilities and between 0.04 and 0.12 h^{-1} for symmetric instabilities).

4.4. Mixing at Ocean Boundaries

To explore the mixing in different ocean layers, the potential vorticity (PV) mixing in Gironde river is first evaluated in the surface and bottom boundary layers, where the isopycnals can outcrop. We averaged over 10 days (between the 10th and the 20th of each month) the surface wind-driven, buoyancy, thermal turbulent wind, and bottom PV fluxes. These fluxes have been evaluated between two outcropping isopycnals (at the surface and at the bottom): between $1,025$ and 1025.5 kg m^{-3} in March and

between $1,024$ and 1024.5 kg m^{-3} in August. **Figure 14** shows the spatial distribution of these fluxes during the two periods.

In March, surface buoyancy fluxes always remove PV from the ocean surface ($-J_{\text{dbuoy}} < 0$) except at some locations: (i) at the Gironde river mouth (longitude $\sim 1.5^\circ \text{W}$ and latitude $\sim 45.6^\circ \text{N}$) and (ii) at the northern edge of the coastal current (longitude $\sim 1.5^\circ \text{W}$ and latitude $\sim 46.2^\circ \text{N}$) (**Figure 14A**). The wind-driven PV fluxes ($-J_{\text{dwind}}$) inject and remove potential vorticity from the surface depending on the location. They strongly remove PV at the northern edge of the coastal current and at the offshore edge of the plume. On the opposite, near the river mouth and in the inner edge of the plume front, wind-driven PV is injected. The thermal turbulent wind flux ($-J_{\text{ttw}}$) always injects PV at

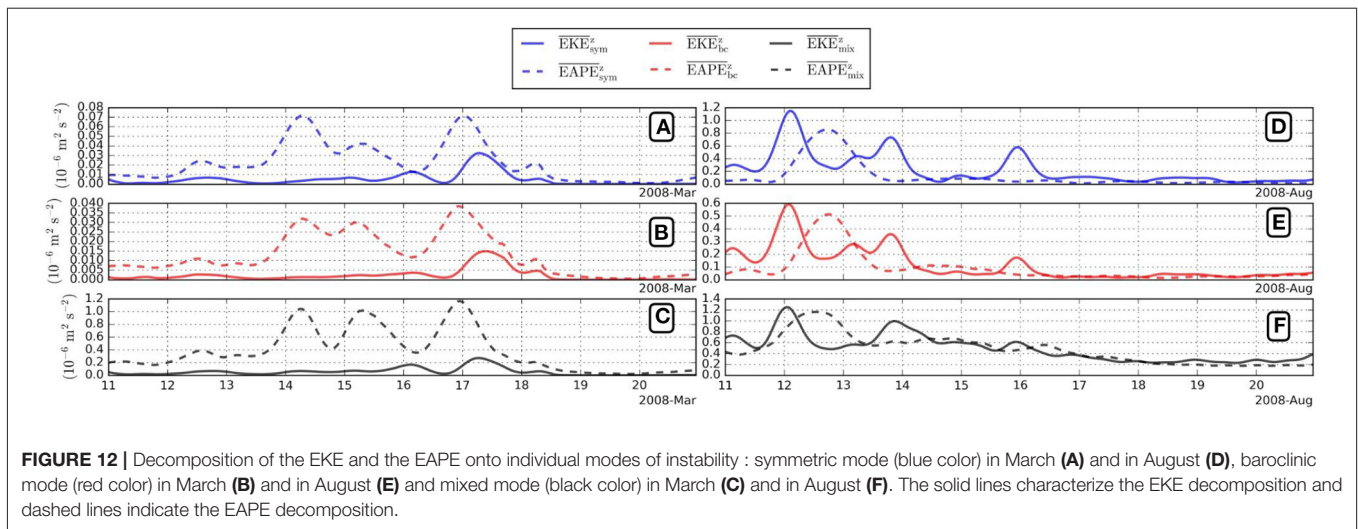


FIGURE 12 | Decomposition of the EKE and the EAPE onto individual modes of instability : symmetric mode (blue color) in March (A) and in August (D), baroclinic mode (red color) in March (B) and in August (E) and mixed mode (black color) in March (C) and in August (F). The solid lines characterize the EKE decomposition and dashed lines indicate the EAPE decomposition.

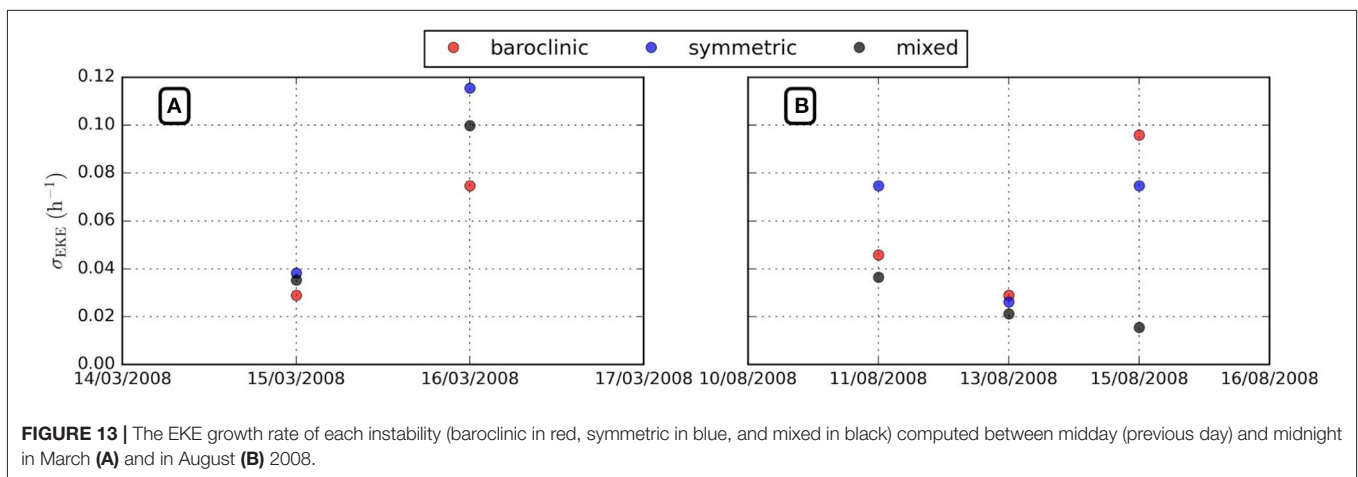


FIGURE 13 | The EKE growth rate of each instability (baroclinic in red, symmetric in blue, and mixed in black) computed between midday (previous day) and midnight in March (A) and in August (B) 2008.

the ocean surface, suggesting the importance of buoyant fronts induced by the Gironde river in the PV budget. These fluxes have comparable magnitudes ($\sim 10^{-12} \text{ m s}^{-4}$); this shows their importance in the freshwater mixing of the Gironde river plume. The bottom fluxes are not important during this period; their magnitudes are smaller ($\sim 10^{-14} < 10^{-12} \text{ m s}^{-4}$) than those of the surface fluxes (not shown).

In August, positive and negative surface buoyancy fluxes associated with PV are also observed (Figure 14B). They remove PV from the ocean surface ($-\text{Jdbuoy} < 0$): (i) near the river mouth, (ii) at the plume front, and (iii) over the continental shelf. In the latter region, the surface buoyancy PV fluxes show positive and negative patterns in the zonal direction. The wind-driven flux changes sign meridionally at the plume front and over the continental shelf. The thermal turbulent wind fluxes always inject PV in plume fronts when the river discharge is average, in the strong salinity gradients and in filaments over the continental shelf. These fluxes have the same magnitude; they are important sources of mixing at the ocean surface. The bottom PV flux is weak except in small positive strips north and south of the Gironde mouth and near the Loire river plume (not shown).

4.5. Frontal Vertical Mixing in the Water Column

Stratification budgets are analyzed in the plume frontal region (Figure 15) in a range of isopycnic layers previously defined (cf section 2.2.2). These budgets are evaluated between 5 and 10 m depth. The stratification budget is related to frontogenesis/frontolysis (intensification/weakening of salinity/density gradients), non-conservative PV fluxes (PV mixing) and advective PV fluxes (stirring processes). Non-conservative PV fluxes are the combination between frictional PV fluxes (related to momentum mixing) and diabatic PV fluxes (related to mass/buoyancy mixing). The bvp term was also considered to close the stratification budget (Figures 15B,D). This boundary term was not neglected since we considered that the finite computation domain is subject to tides and river discharge from the estuary. We compare the time variations of N^2 and the total term (sum of bvp and time variations of N^2). In the total term, the time variations of N^2 dominate except during episodic periods in winter (March 13th and 17th, Figure 1B) and summer (after August 19th, Figure 1C) where the bvp may have an important impact due to an increase of the river discharge.

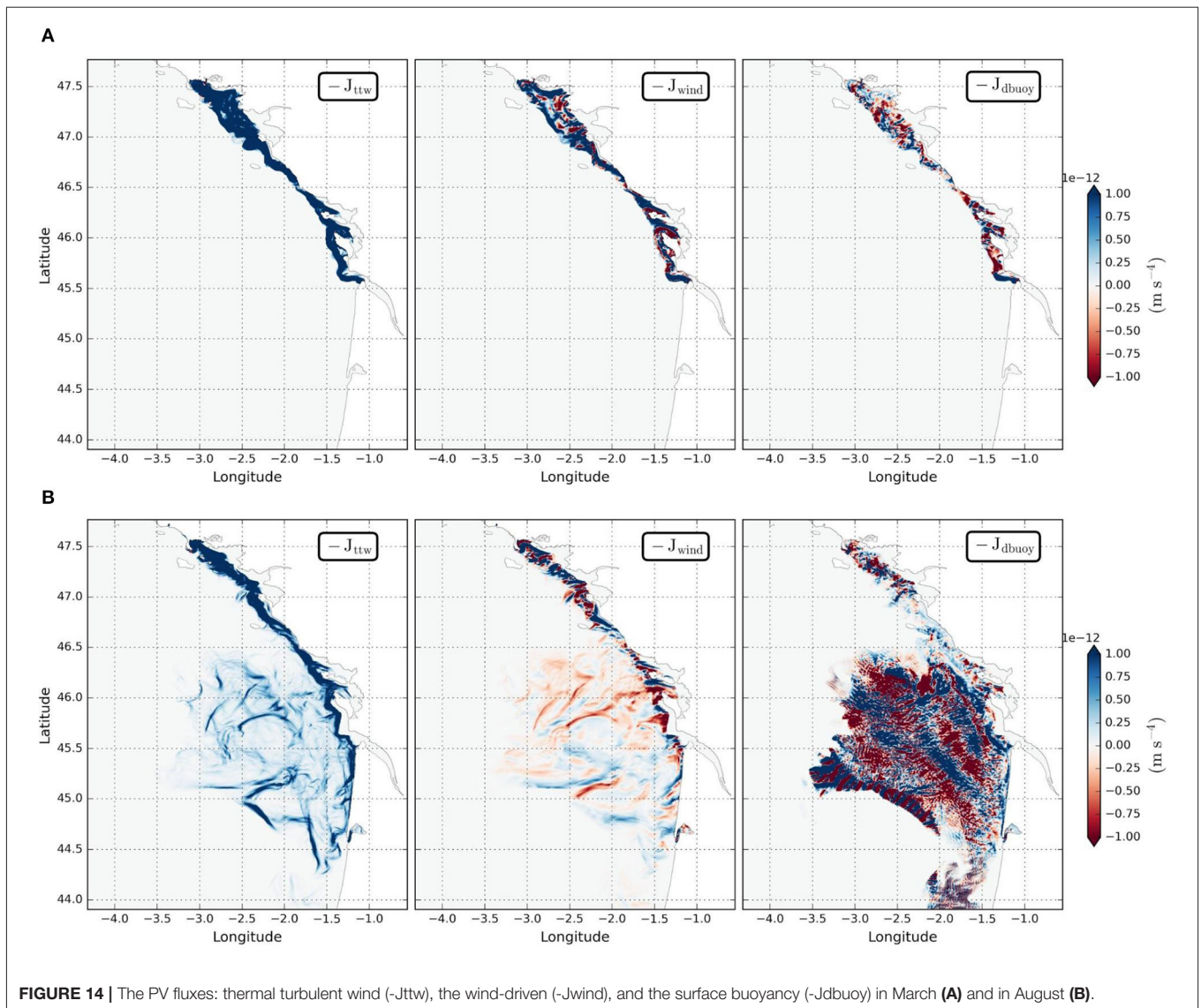
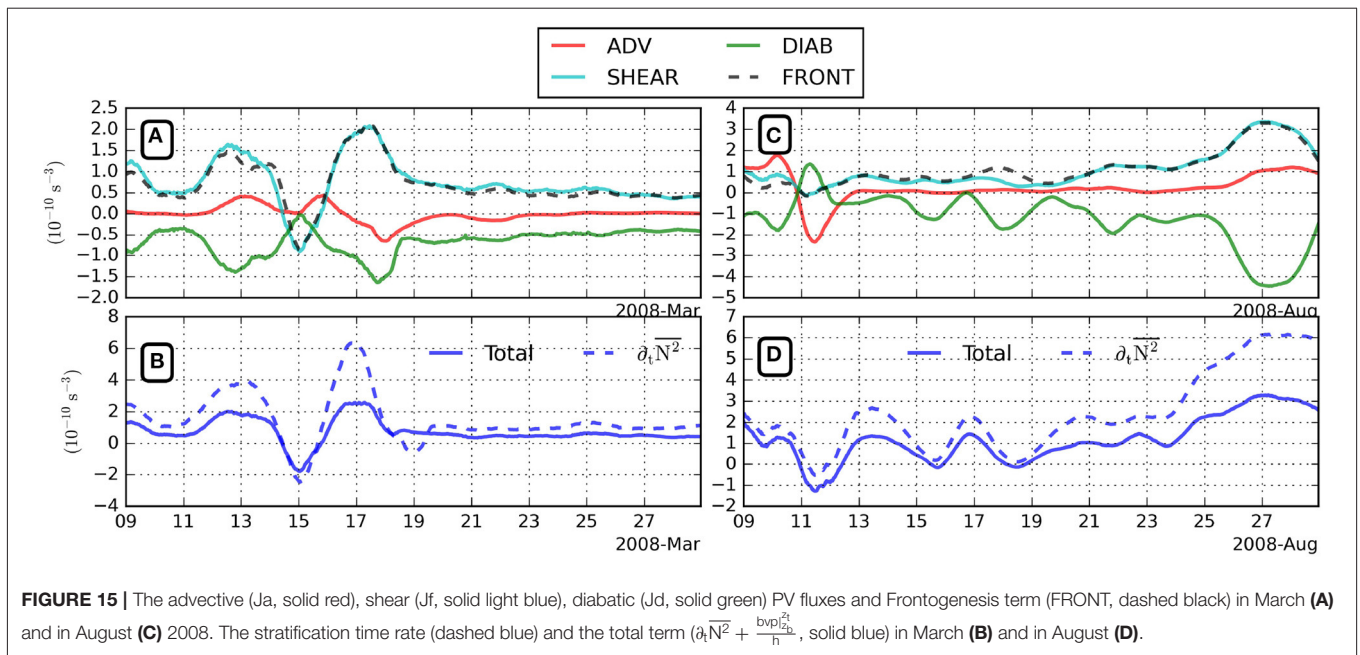


FIGURE 14 | The PV fluxes: thermal turbulent wind ($-J_{ttw}$), the wind-driven ($-J_{wind}$), and the surface buoyancy ($-J_{dbuoy}$) in March **(A)** and in August **(B)**.

Hereafter, we will consider the total term to characterize the time rate of the stratification in the plume frontal region.

In winter, two events of restratification and one event of destratification are observed (**Figure 15B**). The first restratification event occurs between March 12th and 14th. This event is associated with an increase of the river discharge and a wind relaxation after a wind burst. Frontogenesis (positive FRONT values) and weak positive advective PV fluxes (positive ADV values) then control the intensification of the stratification. Non conservative PV fluxes as a combination of shear and diabatic mixing, are mutually compensated and do not contribute to the restratification process of the water column between March 12th and 14th (**Figure 15A**). Destratification occurs between March 14th and 16th during a higher river discharge (around $1,000 \text{ m}^3 \text{ s}^{-1}$) period but it is mainly due to an increase of the wind stress. During this event, non conservative fluxes and frontolysis (negative FRONT values) contribute to

the destratification of the water column. Following the latter event (between March the 16th and 18th), a restratification occurs again driven by frontogenesis and slightly positive non conservative fluxes; the latter fluxes are associated with the wind relaxation after the second wind burst and with a high river discharge. After the last restratification event, the stratification variations decrease (or nearly constant) leading to a homogenized water column. The homogenization of the water column happens after the generation of instabilities (**Figures 12A–C**) and during moderate wind events (**Figure 8A**). It is mostly related to upwelling-favorable winds (figure not shown) which favor the flattening of isopycnals ($EAPE \sim 0$) and therefore the homogenization of the water column. Similar events are also observed in summer when the river discharge remains small (around $200 \text{ m}^3 \text{ s}^{-1}$). A destratification event develops between August 10th and 12th (**Figure 15C**) associated with an increase of the wind stress. This process is governed



by negative advective PV fluxes and a weak frontolysis. The non conservative PV fluxes are weakly positive (Figure 15D). Following this destratification, two successive restratification events (13th and 17th August) occur. During these events, frontogenesis is the major contributor since non conservative fluxes (shear and diabatic mixing) are small and negative. This weak frontogenesis occurs during wind relaxation after wind gusts. It is also related to the weak summer river discharge ($\sim 200 \text{ m}^3 \text{ s}^{-1}$). Advective (stirring) processes are then close to zero. Finally, between August 24th and the 29th, a noticeable restratification event is observed with an increase of the PV from 10^{-10} s^{-3} to more than $3 \times 10^{-10} \text{ s}^{-3}$. This increase is concomitant with a river discharge increase (from 160 to $230 \text{ m}^3 \text{ s}^{-1}$) and a weak wind stress. At that time, vertical advective PV fluxes and frontogenesis are the main sources of this restratification since non conservative fluxes are almost balanced or are weakly negative.

5. DISCUSSION

5.1. Gironde River Plume Fronts

Our high resolution numerical simulation reveals (sub)mesoscale features in the Gironde river plume and over the continental shelf. The shape of the plume appears more complex than previously simulated (Lazure and Jegou, 1998). River plume fronts have been explored in our simulations using the sea surface salinity gradients which characterize buoyant plumes (Vic et al., 2014; Ayouche et al., 2020). Salinity and chlorophyll fronts show similar locations in the Gironde and in the Loire river plumes. The extension of these plumes has been explored using satellite SST data (2002–2014) in previous studies (Costoya et al., 2016). The former authors showed that the locations of the Gironde and Loire river plumes fronts remain close to the coast which is

similar to our findings in this study. These fronts can be pushed shoreward by wind and tides, then suppressing the ballooning of the outflow (Nof and Pichevin, 2001; Isobe, 2005; Ayouche et al., 2020). In the northward coastal current of the Gironde river plume, winds may constrain the plume near the coast both in summer and in winter. Ayouche et al. (2020) showed that in idealized simulations referring to the Gironde river plume, downwelling favorable winds pushed the plume toward the coast and this might be the case in our simulations during episodic wind regimes. The river plume can also be detected from sea surface temperature in winter (Costoya et al., 2016; Yelekçi et al., 2017) when the strong river discharge strengthens the stratification; the mixed layer is then more sensitive to air-sea fluxes. Fronts in winter remain confined over the inner shelf. Their extent is limited offshore at the 100 m isobath, as shown by remote sensing observations (Yelekçi et al., 2017). Plume fronts are less prominent in summer due the weaker river discharges.

5.2. River Plume Dynamics

Inside the river plume, the circulation is mainly in geostrophic balance as observed (Mazzini et al., 2019; Alory et al., 2021) and modeled in other buoyant plumes (Nof and Pichevin, 2001; Ou et al., 2009; Schiller et al., 2011). Locally, the circulation in the river plume is ageostrophic [$R_0 \sim O(1)$]. This ageostrophic circulation corresponds to the strongly sheared flows near the plume front (with strong curvature). Isobe (2005) shows that in the bulge, the inertial oscillations are locally constrained by the tidal dynamics. In our simulations, such a mechanism may be at work in the near-field. The friction with the coast and its geometry induce strong negative vorticity ($\frac{\zeta_T}{f} < -1$) in the coastal current due to strong sheared flows. This ageostrophic circulation has been highlighted in idealized simulations (Ayouche et al., 2020; Lv et al., 2020) and is reproduced in the present

realistic simulations. These high Rossby number flows appear during high discharge conditions or during strong wind events. Over the continental shelf and outside the river plume, the ageostrophic circulation remains weak in winter. In summer, at the rim of eddies and in filaments, strong ageostrophic circulation is observed related to a local secondary circulation (McWilliams, 2017).

The local ageostrophic circulation and its contrast with geostrophic processes have been explored in the frontal region of the Gironde river plume. This contrast has been analyzed in terms of vertical shears and linked to the wind stress intensity. We find that wind gusts (high to moderate winds) generate ageostrophic shear in the plume after a period of time (of the order of a day) during both seasons. In contrast, when the wind stress intensity is weak the geostrophic shear predominates. We emphasize the key role of the average river discharge during weak wind events to enhance density currents and therefore their induced vertical geostrophic shear. The wind-driven and geostrophic shear processes are important in the cross-shelf circulation of a coastally trapped plume (Moffat and Lentz, 2012). The river discharge induces alongshore geostrophic currents which carry out the downcoast freshwater transport in the northern Hemisphere (Horner-Devine et al., 2015). The interaction between surface intensified river plumes and downwelling favorable winds induces geostrophic sheared flows (weak to moderate winds) in regions of strong horizontal density gradients (Spall and Thomas, 2016). In their study, high wind conditions induced circulation that prevails over the density current (Spall and Thomas, 2016). In our study, intense winds induce ageostrophic sheared currents that dominate over the density current which is similar to their key findings.

The Gironde river plume transports nutrients, sediments, and pollutants to the open ocean. Once it interacts with the open ocean, a flow barrier is formed: the plume front. This plume front is characterized by intense chlorophyll concentration and salinity/density gradients. Our study reveals also the existence of frontal ageostrophic dynamics related to winds. Such frontal dynamics and hydrology favor the concentration of phytoplankton which feeds marine organisms such as zooplankton and fish (Acha et al., 2004; Morgan et al., 2005). The concentration of nutrients and light fluctuations is sensitive to the nature of the front (convergent or divergent) and therefore influence the size of phytoplankton (Marañón et al., 2012; Marañón et al., 2015). The interactions between the frontal plume dynamics and marine biology using high resolution numerical modeling is a topic of interest for future studies to understand the biophysical dynamics in the Bay of Biscay.

5.3. Development of Instabilities in the River Plume

Energy conversion terms reveal that mixed baroclinic/barotropic instabilities, characterized by positive VBF and HRS, coexist in the near-field and the far-field of the Gironde plume. Such instabilities have a large signature over the inner-shelf (shallower than 100 m) in winter and summer.

In our realistic simulations, we have shown that the generation of such instabilities is due to the interaction between external forcings (tides and winds) and density currents in winter and mostly due to the interaction between external forcings and the surface ocean layer in summer since the river discharge is weak during this period. The combination between the Gironde discharge, tides and winds favors the development of such instabilities in the near and far fields of the plume. Our results confirm what has been shown in previous idealized simulations (Jia and Yankovsky, 2012; Ayouché et al., 2020).

Symmetric instabilities have also been investigated using the Hoskins and Richardson number criteria. These instabilities develop in different regions of the plume, the bulge and the coastal current, when the PV is negative and the Richardson number is smaller than 1. They are generated through the impact of winds on the bulge and coastal current. Symmetric instabilities in our realistic simulations remain close to the coast in winter and extend from the coast to the continental shelf in summer. These instabilities may overwhelm the water column in the bottom-attached plume interior in March and August. In August, symmetric instabilities remain near the surface locally over the continental shelf. Such instabilities have been studied previously in idealized simulations (Ayouché et al., 2020; Lv et al., 2020). In plumes frontal regions interacting with downwelling favorable winds, symmetric instabilities are triggered and restratify the plume interior (Lv et al., 2020). In idealized simulations referring to a Gironde river plume, downwelling winds trigger frontal symmetric instabilities in the coastal current of the plume and semidiurnal tides (M2) favor the generation of these instabilities in the bulge (Ayouché et al., 2020).

Vertical shear instabilities are also simulated ($R_i < 0.25$) near the bottom of the Gironde plume near (bulge) and far (coastal current) fields due to their interaction with steep bottom slopes and strong tidal currents. Their existence in the near field of the plume have been attributed to strong tidal horizontal currents near the bottom (MacDonald and Geyer, 2004; Kilcher and Nash, 2010).

The previous results highlight the possible coexistence of baroclinic and symmetric instabilities in the Gironde plume regions when R_i is smaller than one. Symmetric instabilities can be replaced by baroclinic instabilities when the Richardson number R_i is $O(1)$. To investigate the relation between these instabilities, an EKE modal decomposition has been achieved in frontal regions where large Rossby numbers are observed locally. These instabilities have short growth time ranging from a few hours to a few days. In winter, they occur after moderate wind bursts, during relaxation events, with a transition from symmetric to baroclinic instability. Indeed, symmetric instabilities grow first followed by mixed instabilities and then baroclinic instabilities after different wind events. During this period, the turbulent activity is transferred from the EAPE to the EKE for each instability (baroclinic, symmetric, and mixed). This transition corroborates the classical Lorentz cycle (Lorenz, 1955). The origin of such instabilities is due to the interaction between density currents and the wind activity in the Gironde plume.

In summer, these instabilities also occur after wind events. The growth time is slightly weaker than in winter, due to low

river discharge, but it keeps the same order of magnitude. These growths have been associated with three wind events. During the first event (moderate winds), symmetric instabilities grow first followed by baroclinic and then mixed instabilities. During the other two events, the wind is weak and therefore baroclinic instabilities grow first followed by symmetric and mixed instabilities. During this month, a transfer occurs from the EKE to the EAPE for each instability and this might be due to the presence of internal waves and their interactions with the Gironde plume. In our simulations, these decompositions reveal that frontal baroclinic instability exists through a transition from symmetric instabilities. The EKE decomposition indicates that mixed instabilities (symmetric and baroclinic instabilities) also exist but with a slower growth.

Baroclinic instabilities may exist during wind relaxation events or through a symmetric instability transition (Hetland, 2017; Lv et al., 2020). Following Stone (1970) classification, the presence of Richardson numbers between 0.84 and 1 locally in the plume during both simulated periods may explain the development of mixed baroclinic/symmetric instabilities. Another classification allows exploring the growth of non-geostrophic baroclinic instabilities based on the slope Burger number (Qu and Hetland, 2020). In further studies, the exploration of the slope Burger number in realistic simulations would help to detail the instability growth rate sensitivity.

5.4. Mixing in Ocean Boundary Layers

In our study, we retain non-linearities in the computation of PV fluxes since ageostrophic circulation is important at the river plume front compared with previous studies which neglected these non-linearities (Wenegrat et al., 2018). The three main sources of PV mixing at the surface of the ocean are buoyancy, thermal turbulent wind and wind-driven fluxes. These fluxes are similar in intensity during both months; this emphasizes their importance in the frontal region PV budget of the Gironde river plume. The main source of PV mixing at the surface of the ocean are buoyancy/salinity fronts since thermal wind fluxes always inject the PV during both periods. They are localized in the frontal region at the edge of the plume for both periods and at the rim of eddies and in filaments over the continental shelf in summer. Thermal turbulent wind PV fluxes are related to density currents that are enhanced during average to high river discharge periods, typically in winter. The latter results are limited to the bounding isopycnals defining the frontal region. Thermal turbulent wind PV fluxes are also enhanced during wind relaxation periods when the geostrophic shear increases, and when the ageostrophic circulation weakens (during both periods). This result has also been observed in the far field of the Chesapeake Bay plume during weak wind periods (Mazzini et al., 2019).

The wind-driven and surface buoyancy fluxes inject and extract PV from the frontal region of the river plume. In winter, these fluxes remain close to the coast. Surface buoyancy fluxes are injecting PV closer to the river mouth due to some local warming from the Gironde estuary and at the northern edge of the coastal current due to air-sea fluxes. Such injections of surface buoyancy fluxes are also observed in summer due to warmer

temperature from the atmosphere and from the Gironde estuary. Extreme events can play a role in those surface buoyancy fluxes as observed during hurricanes. For example, Hurricane Irma in 2017 impacted the stability in the Amazon-Orinoco river plume by reducing the SST cooling and energizing the air-sea fluxes (Rudzin et al., 2020). Surface buoyancy fluxes are also observed over the continental shelf as patterns of positive and negative fluxes that result from the air-sea interactions and internal tides oscillations. Internal waves, due to strong semi-diurnal tidal currents (Pichon and Corréard, 2006), have been observed over the continental shelf of the Bay of Biscay in late summer and they are reproduced in our simulations.

Wind-driven fluxes are sensitive to the wind direction and intensity. They are highly variable in space and time in the frontal region of the plume. In winter, these fluxes inject PV at the inner edge of the plume front and remove potential vorticity north of the coastal current and at the offshore edge of the plume front. While in summer, injection and removal of PV vary along the front (meridional direction). Over the continental shelf, positive and negative fluxes are mainly compensated. The PV removal and injection vary depending on whether the wind is along-front or cross-front and on the induced frontal symmetric instabilities. The injection of PV by winds can be also observed during periods when the wind is weak and the geostrophic shear increases. The wind-driven removal/destruction of PV by winds has been observed in ocean fronts when the wind is downfront which induces an upward flux at the sea surface (Thomas, 2005). The latter have also been observed for weak to moderate downfront winds interacting with buoyant coastal plumes (Spall and Thomas, 2016).

Since the frontal region of the plume is interacting with the bottom most of the time in our simulation, bottom PV fluxes have been analyzed. They remain relatively weak and are not expected to contribute effectively to the PV mixing of the plume frontal region.

5.5. River Plume Interior Mixing

In the ocean interior, the mixing has been characterized by frontogenesis and PV mixing processes in the Gironde river plume frontal region. In winter, during river discharge intensification periods and/or wind relaxation events, the frontogenesis prevails and the plume interior restratification is intensified. In contrast, destratification is characterized by non conservative fluxes (diabatic and shear mixing) and frontolysis through wind intensification periods. These budgets have been evaluated in idealized simulations characterizing the Gironde river plume in a winter regime (Ayouché et al., 2020). In their study, they show that downwelling favorable winds with average discharge favor the destratification in the coastal current (far field) of the plume. The former authors also show that semi-diurnal tides generate intense fronts (frontogenesis) near the river mouth (near-field region) that restratify the plume. Conversely, in a stratified regime (summer season), weak restratification events are observed during wind relaxation due to the small river discharge. The destratification in summer is also linked to a high wind event inducing frontolysis and the growth of ageostrophic shear. Similar results have been

observed in idealized simulations in stratified buoyant coastal plumes where the wind stress is linked to the reduction of PV and therefore to destratification (Spall and Thomas, 2016; Lv et al., 2020). In their study, the restratification processes are observed during wind relaxation periods when the geostrophic shear becomes dominant.

6. CONCLUSION

The Gironde river plume appears as a complex system under the influence of varying forcings: the river discharge, wind stress fluctuations, tide related processes. The interaction of all these nonlinear processes strongly shapes the development of instabilities and the mixing efficiency in the river plume.

Based on high resolution numerical simulations, we highlighted the buoyant frontal activity at meso- and sub-mesoscale with a contrasted seasonal activity. This buoyant frontal dynamics is linked with geostrophic (driven by river discharge) and ageostrophic (associated with wind stress) motions. The geostrophic balanced circulation exists in the river plume interior (in the near field and the coastal current) whereas the ageostrophic circulation occurs locally in the frontal regions. Exploring two seasons (winter and summer), numerical simulations indicate that ageostrophic features are more intense over the inner shelf (shallower than 100 m) in winter and extend to the whole continental shelf in summer. Our understanding of geostrophic and ageostrophic dynamics is giving insights for future observations of coastal ocean submesoscale through satellite altimetry (e.g., SWOT mission).

These nonlinear processes favor the development and coexistence of instabilities (baroclinic, frontal symmetric, and barotropic) in different regions of the river plume. We simulated these instabilities. We observed baroclinic and symmetric instabilities in frontal regions. Such instabilities are growing in a mixed mode (co-existing) or through a transition sequence between symmetric and baroclinic instabilities linked with wind events. These instabilities can also develop in the near field or the coastal current (with a signature in energy and PV fluxes). Other instabilities such as barotropic instability are also found to coexist with baroclinic and symmetric instabilities, in the near field and the coastal current due to the interaction between Gironde river plume and moderate to high wind gusts, tidal currents and river discharge growth.

The potential source of the mixing in river plumes is sustained through different processes (ocean fronts, air/sea interactions, and wind dynamics). Based on our simulations, the mixing appears mainly linked to the frontal dynamics at the edge

of the river plume. The analysis of PV fluxes in the ocean interior and at the surface at small temporal (hourly fields) and spatial (400 m resolution) scales allows quantifying the mixing. PV fluxes are driven by density currents (frontogenesis), heat fluxes, internal waves and wind forcings (non conservative, i.e., shear and diabatic, mixing processes). The estimate of the PV budget relies on approximations and hypotheses (see section 2.2.2). Besides, mixing processes in the simulations are highly sensitive to model parameterizations. Therefore, future efforts should be oriented toward *in situ* measurements that would help us to assess or tune some model parameterizations and to test some of our hypotheses. In the near future, *in situ* experiments will be proposed to measure the turbulent mixing (i.e., turbulence microstructure measurements) to improve model parametrization for the river plume in tidally-driven coastal environments.

DATA AVAILABILITY STATEMENT

The raw data supporting the conclusions of this article will be made available by the authors, without undue reservation.

AUTHOR CONTRIBUTIONS

AA, GC, and XC designed the study. AA, GC, XC, and NA contributed to the writing. AA performed most of the analyses. ST develops the previous CROCO configuration used for this analysis. All authors contributed to the article and approved the submitted version.

FUNDING

This work has been driven with the support of Brittany region. This study is part of the COCTO project (SWOT science team program) funded by the CNES. The Ph.D. thesis of A. Ayouché was funded by Brittany region and Ifremer. Model simulations were carried out with GENCI (French National High-Performance Computing Organization) computational resources administered at the CINES (National Computing Center for Higher Education).

ACKNOWLEDGMENTS

The authors thank Sabine Schmidt for providing the MAGEST *in situ* observations. MAGEST Verdon station was part of the DIAGIR project.

REFERENCES

- Acha, E. M., Mianzan, H. W., Guerrero, R. A., Favero, M., and Bava, J. (2004). Marine fronts at the continental shelves of austral South America - Physical and ecological processes. *J. Mar. Syst.* 44, 83–105. doi: 10.1016/j.jmarsys.2003.09.005
- Akpınar, A., Charria, G., Theetten, S., and Vandermeirsch, F. (2020). Cross-shelf exchanges in the northern Bay of Biscay. *J. Mar. Syst.* 205:103314. doi: 10.1016/j.jmarsys.2020.103314
- Alory, G., Da-Allada, C. Y., Djakouré, S., Dadou, I., Jouanno, J., and Loemba, D. P. (2021). Coastal upwelling limitation by onshore geostrophic flow in the gulf of guinea around the Niger river plume. *Front. Mar. Sci.* 7:1116. doi: 10.3389/fmars.2020.607216
- Ayouché, A., Carton, X., Charria, G., Theetten, S., and Ayoub, N. (2020). Instabilities and vertical mixing in river plumes: application

- to the Bay of Biscay. *Geophys. Astrophys. Fluid Dyn.* 114, 650–689. doi: 10.1080/03091929.2020.1814275
- Chapman, D. C. (1985). Numerical treatment of cross-shelf open boundaries in a barotropic coastal ocean model. *J. Phys. Oceanogr.* 15, 1060–1075. doi: 10.1175/1520-0485(1985)015<1060:NTOCSO>2.0.CO;2
- Charria, G., Theetten, S., Vandermeersch, F., Yeleği, O., and Audiffren, N. (2017). Interannual evolution of (sub)mesoscale dynamics in the Bay of Biscay. *Ocean Sci.* 13, 777–797. doi: 10.5194/os-13-777-2017
- Cole, K. L., and Hetland, R. D. (2016). The effects of rotation and river discharge on net mixing in small-mouth kelvin number plumes. *J. Phys. Oceanogr.* 46, 1421–1436. doi: 10.1175/JPO-D-13-0271.1
- Contreras, M., Pizarro, O., Dewitte, B., Sepulveda, H. H., and Renault, L. (2019). Subsurface mesoscale eddy generation in the ocean off central Chile. *J. Geophys. Res.* 124, 5700–5722. doi: 10.1029/2018JC014723
- Costoya, X., Fernández-Nóvoa, D., deCastro, M., and Gómez-Gesteira, M. (2017). Loire and Gironde turbid plumes: Characterization and influence on thermohaline properties. *J. Sea Res.* 130, 7–16. doi: 10.1016/j.seares.2017.04.003
- Costoya, X., Fernández-Nóvoa, D., deCastro, M., Santos, F., Lazure, P., and Gómez-Gesteira, M. (2016). Modulation of sea surface temperature warming in the Bay of Biscay by Loire and Gironde rivers. *J. Geophys. Res.* 121, 966–979. doi: 10.1002/2015JC011157
- Debreu, L., Marchesiello, P., Penven, P., and Cambon, G. (2012). Two-way nesting in split-explicit ocean models: algorithms, implementation and validation. *Ocean Model.* 49–50, 1–21. doi: 10.1016/j.ocemod.2012.03.003
- Dee, D. P., Uppala, S. M., Simmons, A. J., Berrisford, P., Poli, P., Kobayashi, S., et al. (2011). The era-interim reanalysis: configuration and performance of the data assimilation system. *Q. J. R. Meteorol. Soc.* 137, 553–597. doi: 10.1002/qj.828
- Frouin, R., Fiúza, A. F. G., Ambar, I., and Boyd, T. J. (1990). Observations of a Poleward surface current off the coasts of Portugal and Spain during winter. *J. Geophys. Res.* 95, 679–691. doi: 10.1029/JC095iC01p00679
- García-Soto, C., Pingree, R. D., and Valdés, L. (2002). Navidad development in the southern Bay of Biscay: Climate change and Swoddy structure from remote sensing and *in situ* measurements. *J. Geophys. Res.* 107, 28–1–28–29. doi: 10.1029/2001JC001012
- Godin, G. (1972). *The Analysis of Tides*. Toronto, ON; Buffalo, NY: University of Toronto Press.
- Graham, J. A., Rosser, J. P., O’Dea, E., and Hewitt, H. T. (2018). Resolving shelf break exchange around the European northwest shelf. *Geophys. Res. Lett.* 45, 12,386–12,395. doi: 10.1029/2018GL079399
- Gula, J., Molemaker, M., and McWilliams, J. (2016). Topographic generation of submesoscale centrifugal instability and energy dissipation. *Nat. Commun.* 7:12811. doi: 10.1038/ncomms12811
- Hetland, R. (2005). Relating river plume structure to vertical mixing. *J. Phys. Oceanogr.* 35, 1667–1688. doi: 10.1175/JPO2774.1
- Hetland, R. D. (2010). The effects of mixing and spreading on density in near-field river plumes. *Dyn. Atmos. Oceans* 49, 37–53. doi: 10.1016/j.dynatmoce.2008.11.003
- Hetland, R. D. (2017). Suppression of baroclinic instabilities in buoyancy-driven flow over sloping bathymetry. *J. Phys. Oceanogr.* 47, 49–68. doi: 10.1175/JPO-D-15-0240.1
- Horner-Devine, A. (2009). The bulge circulation in the Columbia river plume. *Contin. Shelf Res.* 29, 234–251. doi: 10.1016/j.csr.2007.12.012
- Horner-Devine, A. R., Hetland, R. D., and MacDonald, D. G. (2015). Mixing and transport in coastal river plumes. *Annu. Rev. Fluid Mech.* 47, 569–594. doi: 10.1146/annurev-fluid-010313-141408
- Hoskins, B. J. (1974). The role of potential vorticity in symmetric stability and instability. *Q. J. R. Meteorol. Soc.* 100, 480–482. doi: 10.1002/qj.49710042520
- Huret, M., Bourriau, P., Doray, M., Gohin, F., and Petitgas, P. (2018). Survey timing vs. ecosystem scheduling: degree-days to underpin observed interannual variability in marine ecosystems. *Prog. Oceanogr.* 166, 30–40. doi: 10.1016/j.pocean.2017.07.007
- Isobe, A. (2005). Ballooning of river-plume bulge and its stabilization by tidal currents. *J. Phys. Oceanogr.* 35, 2337–2351. doi: 10.1175/JPO2837.1
- Jia, Y., and Yankovsky, A. (2012). The impact of ambient stratification on freshwater transport in a river plume. *J. Mar. Res.* 70, 69–92. doi: 10.1357/002224012800502408
- Kang, D. (2015). Energetics of eddy-mean flow interactions in the Gulf Stream region. *J. Phys. Oceanogr.* 45, 1103–1120. doi: 10.1175/JPO-D-14-0200.1
- Karagiorgos, J., Vervatis, V., and Sofianos, S. (2020). The impact of tides on the Bay of Biscay dynamics. *J. Mar. Sci. Eng.* 8:617. doi: 10.3390/jmse8080617
- Kastner, S. E., Horner-Devine, A. R., and Thomson, J. (2018). The influence of wind and waves on spreading and mixing in the Fraser river plume. *J. Geophys. Res.* 123, 6818–6840. doi: 10.1029/2018JC013765
- Kilcher, L. F., and Nash, J. D. (2010). Structure and dynamics of the Columbia river tidal plume front. *J. Geophys. Res.* 115:C05S90. doi: 10.1029/2009JC006066
- Kourafalou, V. H., Lee, T. N., Oey, L.-Y., and Wang, J. D. (1996a). The fate of river discharge on the continental shelf: 2. transport of coastal low-salinity waters under realistic wind and tidal forcing. *J. Geophys. Res.* 101, 3435–3455. doi: 10.1029/95JC03025
- Kourafalou, V. H., Oey, L.-Y., Wang, J. D., and Lee, T. N. (1996b). The fate of river discharge on the continental shelf: 1. modeling the river plume and the inner shelf coastal current. *J. Geophys. Res.* 101, 3415–3434. doi: 10.1029/95JC03024
- Koutsikopoulos, C., Beilouis, P., Leroy, C., and Taillefer, F. (1998). Temporal trends and spatial structures of the sea surface temperature in the Bay of Biscay. *Oceanol. Acta* 21, 335–344. doi: 10.1016/S0399-1784(98)80020-0
- Lapeyre, G., Klein, P., and Hua, B. L. (2006). Oceanic restratification forced by surface frontogenesis. *J. Phys. Oceanogr.* 36, 1577–1590. doi: 10.1175/JPO2923.1
- Large, W. G., McWilliams, J. C., and Doney, S. C. (1994). Oceanic vertical mixing: A review and a model with a nonlocal boundary layer parameterization. *Rev. Geophys.* 32, 363–403. doi: 10.1029/94RG01872
- Lazure, P., Garnier, V., Dumas, F., Herry, C., and Chifflet, M. (2009). Development of a hydrodynamic model of the Bay of Biscay. Validation of hydrology. *Contin. Shelf Res.* 29, 985–997. doi: 10.1016/j.csr.2008.12.017
- Lazure, P., and Jegou, A.-M. (1998). 3d modelling of seasonal evolution of Loire and Gironde plumes on Biscay bay continental shelf. *Oceanol. Acta* 21, 165–177. doi: 10.1016/S0399-1784(98)80006-6
- Le Boyer, A., Charria, G., Cann, B., Lazure, P., and Marié, L. (2013). Circulation on the shelf and the upper slope of the Bay of Biscay. *Contin. Shelf Res.* 55, 97–107. doi: 10.1016/j.csr.2013.01.006
- Le Cann, B. and Serpette, A. (2009). Intense warm and saline upper ocean inflow in the Southern Bay of Biscay in Autumn–winter 2006–2007. *Contin. Shelf Res.* 29, 1014–1025. doi: 10.1016/j.csr.2008.11.015
- Liu, W.-C., Chen, W.-B., Cheng, R. T., and Hsu, M.-H. (2008). Modelling the impact of wind stress and river discharge on Danshuei river plume. *Appl. Math. Model.* 32, 1255–1280. doi: 10.1016/j.apm.2007.03.009
- Lorenz, E. N. (1955). Available potential energy and the maintenance of the general circulation. *Tellus* 7, 157–167. doi: 10.3402/tellusa.v7i2.8796
- Lv, R., Cheng, P., and Gan, J. (2020). Adjustment of river plume fronts during downwelling-favorable wind events. *Contin. Shelf Res.* 202:104143. doi: 10.1016/j.csr.2020.104143
- Lyard, F. H., Allain, D. J., Cancet, M., Carrère, L., and Picot, N. (2020). FES2014 global ocean tides atlas: design and performances. *Ocean Sci. Discuss.* 2020, 1–40. doi: 10.5194/os-2020-96
- MacDonald, D. G., and Geyer, W. R. (2004). Turbulent energy production and entrainment at a highly stratified estuarine front. *J. Geophys. Res.* 109:C05004. doi: 10.1029/2003JC002094
- Marañón, E., Cermeño, P., Latasa, M., and Tardonléké, R. D. (2012). Temperature, resources, and phytoplankton size structure in the ocean. *Limnol. Oceanogr.* 57, 1266–1278. doi: 10.4319/lo.2012.57.5.1266
- Marañón, E., Cermeño, P., Latasa, M., and Tardonléké, R. D. (2015). Resource supply alone explains the variability of marine phytoplankton size structure. *Limnol. Oceanogr.* 60, 1848–1854. doi: 10.1002/lno.10138
- Marchesiello, P., McWilliams, J. C., and Shchepetkin, A. (2001). Open boundary conditions for long-term integration of regional oceanic models. *Ocean Model.* 3, 1–20. doi: 10.1016/S1463-5003(00)00013-5
- Marshall, J., Jamous, D., and Nilsson, J. (2001). Entry, flux, and exit of potential vorticity in ocean circulation. *J. Phys. Oceanogr.* 31, 777–789. doi: 10.1175/1520-0485(2001)031<0777:EFABOP>2.0.CO;2
- Marshall, J. C., and Nurser, A. J. G. (1992). Fluid dynamics of oceanic thermocline ventilation. *J. Phys. Oceanogr.* 22, 583–595. doi: 10.1175/1520-0485(1992)022<0583:FDוות>2.0.CO;2
- Mazzini, P. L. F., Chant, R. J., Scully, M. E., Wilkin, J., Hunter, E. J., and Nidzieko, N. J. (2019). The impact of wind forcing on the thermal wind shear of a river plume. *J. Geophys. Res.* 124, 7908–7925. doi: 10.1029/2019JC015259

- McWilliams, J. C. (2017). Submesoscale surface fronts and filaments: secondary circulation, buoyancy flux, and frontogenesis. *J. Fluid Mech.* 823, 391–432. doi: 10.1017/jfm.2017.294
- Moffat, C., and Lentz, S. (2012). On the response of a buoyant plume to downwelling-favorable wind stress. *J. Phys. Oceanogr.* 42, 1083–1098. doi: 10.1175/JPO-D-11-015.1
- Morgan, C., De Robertis, A., and Zabel, R. (2005). Columbia River plume fronts. I. Hydrography, zooplankton distribution, and community composition. *Mar. Ecol. Prog. Ser.* 299, 19–31. doi: 10.3354/meps299019
- Nof, D., and Pichevin, T. (2001). The ballooning of outflows. *J. Phys. Oceanogr.* 31, 3045–3058. doi: 10.1175/1520-0485(2001)031<3045:TBOO>2.0.CO;2
- Orlanski, I. (1976). A simple boundary condition for unbounded hyperbolic flows. *J. Comput. Phys.* 21, 251–269. doi: 10.1016/0021-9991(76)90023-1
- Ou, S., Zhang, H., and Wang, D.-x. (2009). Dynamics of the buoyant plume off the Pearl river estuary in summer. *Environ. Fluid Mech.* 9, 471–492. doi: 10.1007/s10652-009-9146-3
- Pichon, A., and Corréard, S. (2006). Internal tides modelling in the Bay of Biscay: comparisons with observations. *Sci. Mar.* 70, 65–88. doi: 10.3989/scimar.2006.70s165
- Pingree, R., and Le Cann, B. (1989). Celtic and armorican slope and shelf residual currents. *Prog. Oceanogr.* 23, 303–338. doi: 10.1016/0079-6611(89)90003-7
- Pingree, R., Sinha, B., and Griffiths, C. (1999). Seasonality of the European slope current (Goban spur) and ocean margin exchange. *Contin. Shelf Res.* 19, 929–975. doi: 10.1016/S0278-4343(98)00116-2
- Pingree, R. D., and Le Cann, B. (1990). Structure, strength and seasonality of the slope currents in the Bay of Biscay region. *J. Mar. Biol. Assoc. United Kingdom* 70, 857–885. doi: 10.1017/S0025315400059117
- Piton, V., Herrmann, M., Lyard, F., Marsaleix, P., Duhaut, T., Allain, D., et al. (2020). Sensitivity study on the main tidal constituents of the gulf of Tonkin by using the frequency-domain tidal solver in t-UGOM. *Geosci. Model Dev.* 13, 1583–1607. doi: 10.5194/gmd-13-1583-2020
- Puillat, I., Lazure, P., Jégou, A., Lampert, L., and Miller, P. (2004). Hydrographical variability on the French continental shelf in the Bay of Biscay, during the 1990s. *Contin. Shelf Res.* 24, 1143–1163. doi: 10.1016/j.csr.2004.02.008
- Qu, L., and Hetland, R. (2020). Nongeostrophic baroclinic instability over sloping bathymetry: Buoyant flow regime. *J. Phys. Oceanogr.* 50, 1937–1956. doi: 10.1175/JPO-D-19-0145.1
- Rathan, S., and Naga Raju, G. (2018). A modified fifth-order weno scheme for hyperbolic conservation laws. *Comput. Math. Appl.* 75, 1531–1549. doi: 10.1016/j.camwa.2017.11.020
- Roulet, G., Capet, X., and Maze, G. (2014). Global interior eddy available potential energy diagnosed from Argo floats. *Geophys. Res. Lett.* 41, 1651–1656. doi: 10.1002/2013GL059004
- Rubio, A., Caballero, A., Orfila, A., Hernández-Carrasco, I., Ferrer, L., González, M., et al. (2018). Eddy-induced cross-shelf export of high CHL-a coastal waters in the se Bay of Biscay. *Remote Sens. Environ.* 205, 290–304. doi: 10.1016/j.rse.2017.10.037
- Rudzin, J. E., Chen, S., Sanabia, E. R., and Jayne, S. R. (2020). The air-sea response during hurricane Irma's (2017) rapid intensification over the amazon-orinoco river plume as measured by atmospheric and oceanic observations. *J. Geophys. Res.* 125:e2019JD032368. doi: 10.1029/2019JD032368
- Schiller, R. V., Kourafalou, V. H., Hogan, P., and Walker, N. D. (2011). The dynamics of the Mississippi river plume: Impact of topography, wind and offshore forcing on the fate of plume waters. *J. Geophys. Res.* 116:C06029. doi: 10.1029/2010JC006883
- Serpette, A., Cann, B., and Colas, F. (2006). Lagrangian circulation of the north Atlantic central water over the abyssal plain and continental slopes of the Bay of Biscay: description of selected mesoscale features. *Sci. Mar.* 70, 27–42. doi: 10.3989/scimar.2006.70s127
- Shchepetkin, A. F., and McWilliams, J. C. (2005). The regional oceanic modeling system (ROMS): a split-explicit, free-surface, topography-following-coordinate oceanic model. *Ocean Model.* 9, 347–404. doi: 10.1016/j.ocemod.2004.08.002
- Spall, M. A., and Thomas, L. N. (2016). Downfront winds over buoyant coastal plumes. *J. Phys. Oceanogr.* 46, 3139–3154. doi: 10.1175/JPO-D-16-0042.1
- Stamper, M., and Taylor, J. (2016). The transition from symmetric to Baroclinic instability in the eady model. *Ocean Dyn.* 67, 65–80. doi: 10.1007/s10236-016-1011-6
- Stone, P. H. (1970). On non-geostrophic Baroclinic stability: Part II. *J. Atmos. Sci.* 27, 721–726. doi: 10.1175/1520-0469(1970)027<0721:ONGBSP>2.0.CO;2
- Thomas, L., and Ferrari, R. (2008). Friction, frontogenesis, and the stratification of the surface mixed layer. *J. Phys. Oceanogr.* 38, 2501–2518. doi: 10.1175/2008JPO3797.1
- Thomas, L. N. (2005). Destruction of potential vorticity by winds. *J. Phys. Oceanogr.* 35, 2457–2466. doi: 10.1175/JPO2830.1
- Thomson, R. E., and Fine, I. V. (2003). Estimating mixed layer depth from oceanic profile data. *J. Atmos. Ocean. Technol.* 20, 319–329. doi: 10.1175/1520-0426(2003)020<0319:EMLDFO>2.0.CO;2
- Toublanc, F. T., Ayoub, N., Lyard, F., Marsaleix, P., and Allain, D. (2018). Tidal downscaling from the open ocean to the coast: a new approach applied to the Bay of Biscay. *Ocean Model.* 124, 16–32. doi: 10.1016/j.ocemod.2018.02.001
- Vandermeersch, F., Charraudeau, M., Bonnat, A., Fichaut, M., Maillard, C., Gaillard, F., et al. (2010). “Bay of Biscay's temperature and salinity climatology,” in *XII International Symposium on Oceanography of the Bay of Biscay* (Plouzané).
- Vic, C., Berger, H., Tréguier, A.-M., and Couvelard, X. (2014). Dynamics of an equatorial river plume: theory and numerical experiments applied to the Congo plume case. *J. Phys. Oceanogr.* 44, 980–994. doi: 10.1175/JPO-D-13-0132.1
- Wenegrat, J. O., Thomas, L. N., Gula, J., and McWilliams, J. C. (2018). Effects of the submesoscale on the potential vorticity budget of ocean mode waters. *J. Phys. Oceanogr.* 48, 2141–2165. doi: 10.1175/JPO-D-17-0219.1
- Willmott, C. J., Robeson, S. M., and Matsuura, K. (2012). A refined index of model performance. *International J. Climatol.* 32, 2088–2094. doi: 10.1002/joc.2419
- Wu, T., and Wu, H. (2018). Tidal mixing sustains a bottom-trapped river plume and buoyant coastal current on an energetic continental shelf. *J. Geophys. Res.* 123, 8026–8051. doi: 10.1029/2018JC014105
- Xu, W., Miller, P. I., Quartly, G. D., and Pingree, R. D. (2015). Seasonality and interannual variability of the European slope current from 20years of altimeter data compared with *in situ* measurements. *Remote Sens. Environ.* 162, 196–207. doi: 10.1016/j.rse.2015.02.008
- Yankovsky, A., and Chapman, D. (1997). A simple theory for the fate of buoyant coastal discharges. *J. Phys. Oceanogr.* 27, 1386–1401. doi: 10.1175/1520-0485(1997)027<1386:ASTFTF>2.0.CO;2
- Yelekçi, Ö., Charria, G., Capet, X., Reverdin, G., Sudre, J., and Yahia, H. (2017). Spatial and seasonal distributions of frontal activity over the French continental shelf in the Bay of Biscay. *Contin. Shelf Res.* 144, 65–79. doi: 10.1016/j.csr.2017.06.015

Conflict of Interest: The authors declare that the research was conducted in the absence of any commercial or financial relationships that could be construed as a potential conflict of interest.

Copyright © 2021 Ayouché, Charria, Carton, Ayoub and Theetten. This is an open-access article distributed under the terms of the Creative Commons Attribution License (CC BY). The use, distribution or reproduction in other forums is permitted, provided the original author(s) and the copyright owner(s) are credited and that the original publication in this journal is cited, in accordance with accepted academic practice. No use, distribution or reproduction is permitted which does not comply with these terms.

5.3 Conclusions et Perspectives

Dans ce chapitre, je me suis intéressé à la dynamique, aux instabilités et au mélange vertical dans le panache de la Gironde dans un environnement réaliste (Golfe de Gascogne). Dans ce dernier, plusieurs forçages interagissent (flux atmosphériques, vents et marées) avec une bathymétrie complexe et des panaches de rivières sujets à un débit variable. Dans ce contexte, j'ai réalisé des simulations réalistes avec le modèle numérique CROCO. Celles-ci représentent des situations de débit modéré (Mars) et faible (Août). Dans cette optique, j'ai démontré:

- L'existence d'une circulation agéostrophique le long du front du panache de la Gironde, liée à la dynamique du vent.
- La génération d'instabilités mixtes baroclines/barotropes dans le panache de la Gironde.
- La génération d'instabilités frontales agéostrophiques symétriques, baroclines et mixtes baroclines/symétriques avec des taux de croissance variant entre quelques heures et quelques jours.
- L'injection de mélange en vorticité potentielle à la surface de l'océan par le biais de fronts de densité/salinité.
- L'injection/érosion de mélange en vorticité potentielle à la surface de l'océan, liée à une dynamique de vent intermittente (changement de direction du vent) et des flux de flotabilité (échanges atmosphère-océan, dynamique estivale d'ondes internes).
- L'intensification de la stratification engendrée par la frontogénèse et sa destruction liée à des processus non-conservatifs (mélange diabatique et par cisaillement).

Les études menées au cours de ma thèse présentent plusieurs limites et perspectives. Dans le sixième chapitre, je résumerai les résultats de chaque étude, ensuite je donnerai une conclusion transverse à ces chapitres et je fournirai des perspectives pour de futures études.

5.4 Notes on Chapter 5

In Chapter 5, realistic numerical simulations were performed in the Bay of Biscay during March and August. The Gironde plume was studied in terms of instabilities generation and existence, and mixing budget. This study shows different results regarding the mixing processes and instabilities nature in the Gironde plume. However, it depicts few limitations:

1. Symmetric instabilities are related to wind activity. However, negative PV reveals also the existence of other instabilities such as Gravitational and inertial instabilities. Nevertheless, in our case the latter instabilities are not predominating since symmetric instabilities are related to the vertical shear processes induced by wind gusts.
2. Modal decomposition of the EKE (eddy kinetic energy) have been performed over a domain encompassing both the bulge and the coastal current of the Gironde plume. This decomposition has been performed in the zonal and meridional directions. This choice is motivated by the dominance of the coastal current in the analysis domain. The coastal current is parallel to the coast and therefore globally this decomposition holds. However, local decomposition of the EKE should account for the preferential direction of the buoyancy gradients (curvature flows).
3. The spatial variability of the vertical buoyancy and the shear production terms shows noisy patterns and therefore the net impact is not clear. A meridional average of these terms reveals that despite the spatial variability, barotropic and baroclinic instabilities (co)exist near the mouth of the estuary and in the coastal current (figure not shown).
4. Surface buoyancy PV fluxes in summer reveals strong non-linearities that might be related to the Gironde plume, tidal oscillations and air-sea fluxes. To understand the origin of such oscillations, this term should be decomposed in different terms (heat fluxes, plume buoyancy fluxes, precipitation and evaporation...).

5. As in chapter 3, Interior mixing budget is sensitive to the choice of advection and turbulent closure schemes.

"If you optimize everything, you will
always be unhappy."

Donald Knuth

Chapter 6

Conclusions and Perspectives

In this final chapter, I discuss the issues, the limitations, and the major results of my work. An individual summary of each chapter is given. Then, I detail general conclusions of this dissertation before highlighting a few perspectives which could provide a basis for future work.

6.1 the PhD objectives and Workflow

The main objective of this dissertation was to improve our understanding of (sub)mesoscale processes in the coastal environment, and more specifically in river plumes. This objective was recalled, detailed and addressed in chapters 3, 4 and 5. The questions derived from this objective were the following:

1. What are the evolution of the vertical and horizontal structures of river plumes and the nature of their **dynamics** ?
2. What are the nature, intensity and location of the different **instabilities** (geostrophic and ageostrophic) in river plumes ?
3. Can we identify different processes altering the **vertical mixing** within different regions in river plumes and relate them to the turbulent energy exchanges ?

I approached these issues by quantifying several physical quantities and performing diagnostics: (i) - Potential Vorticity (PV) and Eddy Kinetic Energy conversion

terms, (ii) - Stratification budgets in the ocean interior and at its boundaries and (iii) - modal decompositions of EKE and EAPE using Fourier analysis. These diagnostics are well suited for high Rossby number flows ($R_o \sim O(1)$) such as submesoscale processes dominating at the rim of eddies, filaments and fronts [McWilliams, 2016, Gula et al., 2016]. These methods are implemented in a set of idealized and realistic simulations, with a specific focus on the Gironde river plume, using the Coastal and Regional COmmunity (CROCO) numerical model [Shchepetkin and McWilliams, 2005, Debreu et al., 2012].

I tackled also non-linear vertical shear processes in river plumes using 2D non-hydrostatic (NH) model Fluid2D with the perspective of: (i) - identifying and characterizing coherent vortices in vertical stratified and sheared flows, (ii) - achieving modal decompositions via a linear analysis stability (based on the NH primitive equations) to highlight the nature and spatio-temporal scale of instabilities and (iii) - the induced turbulent mixing and transport.

A summary of the idealized numerical study of the Gironde river plume will be first discussed (chapter 3). The non-linear vertical shear processes (chapter 4) will be discussed. Then, the interactions between the Gironde river plume and a turbulent ocean will be summarized (chapter 5). Finally, overall conclusions and perspectives will be drawn.

6.2 Summary of Chapter 3

In Chapter 3, I studied the dynamics, instabilities and mixing processes in an idealized Gironde river plume. This study considers a Gironde river plume with freshwater properties (river discharge, freshwater salinity and temperature) corresponding to a winter regime close to observations, expanding in an ocean initially at rest. This situation was used to first define a reference simulation, with a Gironde river plume unforced by surrounding currents or eddies. In this reference¹ simulation, I studied the plume interactions with tides and downwelling-favorable winds independently. In addition, and in order to highlight the impact of the river discharge, I compared

¹The bathymetry varies zonally with a typical slope of the inner-shelf of the Bay of Biscay

the idealized Gironde river plume to an idealized version of the Mississippi River, with a high discharge rate ($Q \sim 10000 \text{ m}^3 \text{ s}^{-1}$).

I found the (co)existence of (geostrophic and ageostrophic) instabilities in the bulge (reproduced during the simulated period in the absence of winds) and in the coastal current. The localization and intensity of these instabilities are influenced by atmospheric forcing, tides and river discharge rate:

- In an unforced Gironde plume, instabilities tend to grow slowly.
- Downwelling-favorable winds suppress the growth of the bulge, and favor the development of frontal symmetric, baroclinic and barotropic instabilities.
- M2 Tides favor symmetric, barotropic and baroclinic instabilities near the mouth of the estuary. They also stabilize the growth of the bulge.
- A high discharge plume is subject to vertical shear and symmetric instabilities in the core of the bulge. Baroclinic and barotropic instabilities coexist and intensify near the base of the plume (in the coastal current and the bulge).

Then, I performed a buoyancy budget near the base of the plume. The changes in stratification are related to the momentum and density mixing, and to frontogenetic processes. Frontogenetic processes are linked to salinity gradients; in regions where salinity gradients are intense, restratification occurs by frontogenesis. The latter have been simulated in the coastal current in the case of a downwelling-favorable wind, and near the mouth of the estuary in the case of M2 tides.

This study points out quite a few limitations and questions. These limitations and questions are summarized below:

Issues and limitations of Chapter 3

- What is the contribution of non-hydrostatic processes^a to the dynamics of a river plume (at the estuary and near the mouth of the river)^b ?
- Which instabilities exist in the Gironde river plume, in a realistic case, with current and eddy interactions: what are their nature, interactions, growth rate and intensity ?
- What is the impact of realistic atmospheric forcings, tides and river discharge in the mixing of the Gironde plume interior and at the surface ?

^avertical shear instabilities and turbulent mixing of mass and momentum

^bhigh resolution simulations with a horizontal resolution \sim to few meters or less, would be necessary to address this point

6.3 Summary of Chapter 4

In chapter 4, I discussed the instabilities and turbulent mixing in 2D idealized non-hydrostatic simulations of vertically sheared stratified flows. These simulations pertain to a river estuary and to the near-field region of a river plume. I defined a reference simulation and studied its sensitivity to different parameters: initial shear, stratification thickness and the bottom slope.

I found that small anticyclonic vortices² are generated at the plume base, when the bottom is flat. The reduced stratification and the enhanced shear favor an earlier development of these vortices. These vortices elongate in the flow direction due to a shear/tangential strain. The intensity of the strain is intensified when the stratification thickness (see figure 1 of chapter 4) is reduced; and when the initial shear enhances (stronger flow velocity). In the case of a sloping bottom, small cyclonic vortices are generated above the bottom and dissipate rapidly through an enhanced flow acceleration.

The generated vortices in our simulations result from a primary Kelvin-Helmholtz instability. The stationary³ primary Kelvin-Helmholtz instability develops at the

²Vortices radius $\sim 4\text{m}$

³zero phase speed

plume base. Its wavelength, $\sim 27\text{m}$, is limited by the horizontal length of the studied domain and the initial conditions. This wavelength remains similar regardless of the different simulation parameters. This instability reaches its maximal amplitude within a few seconds. The shortest growth period ~ 11 seconds is reached when the initial shear increases. Another propagating⁴ instability has been also analyzed: the Holmboe instability. This instability induces waves which propagate above and below the plume base. It develops with smaller wavelengths (between 1m and 5m) and grows with longer periods \sim a few minutes. The Holmboe instability intensifies when the bottom is inclined and when the stratification thickness is reduced.

The billows⁵ favor the entrainment between the upper and bottom layers which induces turbulent mixing and dissipative processes. I defined different turbulence phases in terms of the Prandtl number: (i) pre-turbulent ($P_r < 1$), (ii) quasi-turbulent ($P_r \sim 1$) and (iii) turbulent ($P_r > 1$). The pre-turbulent phase is reached in the reference and enhanced shear simulations. In this phase, the mass mixing overcomes the momentum mixing in relation with higher EKE than EAPE dissipation rates. Meanwhile, the quasi-turbulent and turbulent phases are reached when momentum mixing is more intense than mass mixing; this is the case for the sloping bottom and the reduced stratification simulations. In these latter cases, the level of turbulence is correlated with the intensification of the Holmboe instability. Indeed, the Holmboe and Kelvin-Helmholtz instabilities mix the fluid efficiently⁶ in our simulations. Yet, the Holmboe instabilities despite their longer growth periods are the most noticeable source of turbulent mixing. They are also the only source of turbulent mixing when the stratification is reduced; then the Kelvin-Helmholtz instability is inefficient⁷. These results have been compared and validated with previous studies and observations.

This study points out some unresolved questions and limitations:

⁴non-zero phase speed

⁵small-scale vortices

⁶mixing efficiency > 0.2

⁷mixing efficiency < 0.2

Issues and limitations of Chapter 4

- What is the link between 3D non-hydrostatic processes (instabilities and turbulent mixing) and the internal waves dynamics in curved flows such as river plumes?
- Do vertical shear instabilities exist in realistic Gironde river plume simulations in the limit of a hydrostatic approximation ?

6.4 Summary of Chapter 5

In this chapter, I have studied the interactions between the Gironde river (Bay of Biscay) and different forcings (winds, tides, air-sea fluxes) in a turbulent ocean. I have carried out submesoscale resolving numerical simulations with CROCO (hydrostatic approximation) in March and August. These months were chosen to analyze the contrast between average river discharges (winter) and weak river discharges (summer). Through some diagnostics suited to small scales features, I characterized the dynamics, instabilities and mixing processes in the Gironde river plume.

Firstly, I represented the distribution of geostrophic⁸ and ageostrophic⁹ motions in the Gironde plume. The winter and summer spatial distributions of the local Rossby number¹⁰ indicate that geostrophic motions occur in the plume interior; ageostrophic motions dominate at the plume front. In order to understand the dynamics of the Gironde plume front, I evaluated the temporal evolution of the geostrophic¹¹ and ageostrophic shears and their relation to the magnitude of the wind stress. In winter (March), the oceanic ageostrophic circulation is related to atmospheric storms. The geostrophic circulation induced by salinity gradients are related to the average river discharge ($Q > 1000 \text{ m}^3 \text{ s}^{-1}$) and to wind relaxation events. However in summer, the frontal circulation is mainly ageostrophic due to weak river discharge ($Q \sim 200 \text{ m}^3 \text{ s}^{-1}$) with moderate wind magnitude and variability.

⁸Rossby number < 1

⁹Rossby number $\sim O(1)$

¹⁰ $R_o \sim \frac{\zeta_z}{f}$

¹¹geostrophic shear is also defined as the intensity of the buoyancy/density gradients

Secondly, I identified different instabilities¹² in the Gironde river plume. In winter, the interaction between the average discharge, tidal currents and moderate winds induces intense vertical sheared horizontal currents; this favors the development of symmetric instabilities. These instabilities have been also observed during summer despite the weak river discharge. Mixed barotropic/baroclinic instabilities also exist in river plumes during both periods.

Thirdly, I studied the development¹³ of symmetric, baroclinic and mixed¹⁴ instabilities in the Gironde plume front. The mixed instabilities are the dominating instabilities at the plume front in winter. In summer mixed, baroclinic and symmetric instabilities are within the same range of intensity. These instabilities grow with a period between 8 and 50 hours; which validated their ageostrophic nature. Due to the low river discharge in summer, these instabilities grow slowly compared to winter. Their development is related to the wind activity in the Bay of Biscay.

Finally, I analyzed the mixing at the surface and in the ocean interior in the frontal region of the Gironde river plume. At the surface, mixing mainly occurs in the sheared flow of density currents; these currents are established via a balance between the freshwater outflow and Coriolis acceleration. Mixing also occurs around lenses of freshwater and filaments in summer. The wind and surface buoyancy fluxes are also sources of mixing despite their variability (injecting and removing buoyancy). The variability of mixing is due to air-sea fluxes, summer internal wave dynamics and the intermittent¹⁵ wind activity. Then, I performed a budget of stratification in the frontal region of the plume and near the surface (between 5m and 10m depth). This buoyancy budget, in summer and in winter, reveals that restratification¹⁶ is related to frontogenesis¹⁷, and destratification¹⁸ is related to non-conservative fluxes (diabatic fluxes and shear mixing). Frontogenesis occurs during wind relaxation events and is influenced by the river discharge; meanwhile non-conservative fluxes are a result of high/average wind activity regardless of the river discharge intensity.

¹²using Hoskins criteria and energy conversion terms

¹³intensity and growth

¹⁴mixed baroclinic/symmetric

¹⁵wind with variable regimes, leading to downwelling and upwelling

¹⁶intensification of stratification

¹⁷Frontogenesis induces intense salinity/density gradients

¹⁸destruction of stratification

In the next sections, I will depict the overall insights and perspectives of these chapters.

6.5 General Conclusions

In this thesis, I focused my interest on different non-linear processes¹⁹ occurring in river plumes:

1. The physical processes, due to the turbulent oceanic environment, which affect river plumes in particular in the Bay of Biscay.
2. The interactions between river plume dynamics and surrounded ocean processes which lead to balanced, or ageostrophic, instabilities.
3. These instabilities induce finer scale²⁰ structures which affect the vertical mixing hence the horizontal and vertical frontal structures of the plume.

River plumes are complex regions where numerous environmental processes interact: river discharge, wind, air-sea fluxes, tides and influence of the bottom slope. These environmental processes shape the river plume and alter its dynamics. First of all, I showed²¹ the impact of different environmental processes (downwelling-favorable winds, M2 tides and river discharge) on the Gironde river plume structure and dynamics, independently. This study reveals the dynamics of an anticyclonic gyre (the bulge) near the mouth of the estuary and a coastal current. The bulge grows offshore, fed by the river discharge, and partially leaking into a coastal density current; the bulge growth is thus faster and larger when the river discharge increases. Tides stabilize the growth of the bulge and numerous non-linear fronts are created near the estuary mouth due to tidal oscillations. Meanwhile, downwelling-favorable winds suppress the bulge and favor the alongshore extension of the coastal currents by tightening the streamlines and therefore accelerating the flow. Tides and winds trigger also the existence of ageostrophic dynamics in the plume (e.g., frontal region

¹⁹instabilities and mixing

²⁰mesoscale, submesoscale and microscale

²¹through 3D hydrostatic numerical idealized simulations

and near the mouth of the estuary). Yet, river waters exit through the estuary and feed the near-field (near-estuary) region, before reaching the deep open ocean. The near-estuary part of the plume is also subject to ageostrophic processes that are only partly (or not) simulated with hydrostatic numerical models. Therefore, using non-hydrostatic 2D simulations, I studied these processes in the estuary and the near-field of the plume. These processes (vertical stratified sheared flows) can be the result of: (i) intense river discharges, (ii) the interaction between weak/average river discharges and strong tidal currents and (iii) the interaction between weak/average river discharges and strong Ekman induced currents. Such processes lead to the generation of small billows at the base of the plume or above an inclined bottom. The billows generation and intensification is sensitive to the nature of the bottom, the intensity of the currents and/or the thickness of the stratified freshwater. Then, I studied the interaction between the combination of multiple environmental processes (variable river discharge, tidal currents, winds and air-sea fluxes) and the Gironde plume, using realistic simulations of the Bay of Biscay during different seasons (March and August months). The choice of these months was motivated by the analysis of the contrast between a low river discharge (August) and an average river discharge (March). This contrast reveals the intensification of salinity gradients in the Gironde plume in winter; meanwhile, in summer, it shows the existence of (sub)mesoscale features over the continental shelf. This study also highlights the contrast between geostrophic dynamics inside the plume and ageostrophic dynamics in the frontal region of the plume. Such ageostrophic dynamics were strongly correlated with the ageostrophic vertical shear resulting from the wind activity. Meanwhile, geostrophic dynamics in the plume front were dominating during wind relaxation events and/or river discharges peaks.

The interaction between environment processes and river plumes also favors the growth of different unstable motions: vertical shear instabilities, baroclinic instabilities, barotropic instabilities and/or symmetric instabilities. Mixed baroclinic/barotropic instabilities are highlighted in different regions of the plume. Mixed baroclinic/barotropic instabilities develop in the coastal current when the plume interacts with downwelling-favorable winds and near the mouth of the estuary due

to tides. The combination of different environmental processes (tides, winds, air-sea fluxes) in a realistic coastal ocean (the Bay of Biscay) favors the development of mixed baroclinic/barotropic instabilities near the mouth of the Gironde estuary and in the coastal current of the Gironde river plume. Symmetric instabilities are observed in the plume, near the estuary, when it interacts with tides and in the coastal current of the plume when it is forced with downwelling-favorable winds. The combination of different forcings (river discharge, tides, winds and air-sea fluxes) induces the development of frontal symmetric instabilities in the Gironde plume. These instabilities are linked to ageostrophic dynamics and to baroclinic instabilities. Frontal baroclinic, symmetric and mixed symmetric/baroclinic instabilities grow at a faster rate (between few hours to few days)²². Environmental processes such as winds, tides and river discharge may also induce vertical shear instabilities in the estuary and/or the near field of a river plume. They induce small vortices (billows) that mix the freshwater from the river and the salty water from the open ocean. However, their characterization in realistic environments is challenging due to their fast growth (\sim few seconds) but they have been simulated above the bottom near the mouth of the Gironde estuary (see chapter 5).

These instabilities induce fine scale features that affect the vertical mixing in different regions of the plume. In estuaries and near the mouth of the estuary, vertical shear instabilities induce turbulent mixing of the mass and momentum inside the core of the generated billows. This turbulent mixing and the induced EKE/EAPE dissipation rates have been characterized and validated with previous studies/observations. Holmboe instabilities are the key factor of mixing in these regions despite their slow growth. Once the freshwater exits from the estuary and encounters the Earth rotation, fronts are generated. These fronts are key injection of the mixing at the surface in the Bay of Biscay. Meanwhile, their surface interactions with air-sea fluxes and winds result in variable injection/removal of the mixing due to the intermittent directions of winds, internal waves dynamics, and the heating/cooling from the atmosphere. Near the surface, the intensification of these fronts is re-

²²These instabilities are ageostrophic since geostrophic instabilities require further time (\sim few weeks to months) to develop.



Figure 6-1: Summary of the main results of this thesis.

lated to frontogenesis. Meanwhile, destratification of these fronts results from the non-conservative fluxes of potential vorticity (diabatic and shear mixing).

In figure 6-1, I summarize the key findings of this thesis.

6.6 Perspectives

Different processes in this manuscript were analyzed in the context of issues related to the Bay of Biscay and its river plumes. However, they point out several limitations that would require further investigation:

- **Air-sea interactions.** The promising results in chapter 3 require further questioning. Indeed, I performed numerical idealized simulations referring to the Gironde river and considering numerous environmental processes (winds, tides). The interaction between the Gironde plume and each process has been studied. Yet, in this study, I omitted the influence of air-sea fluxes on the Gironde plume. This interaction deserves careful attention since the cooling or heating by the atmosphere in estuaries results in major effects such as unstable stratification that affect the plume dynamics, instabilities and induced mixing.
- **Plume-topography interactions.** In chapter 3, an idealized topography

was used with a smooth bottom slope representative of the Gironde river plume bathymetry. However, a representation of the bathymetry with obstacles should be included to improve the representation of the instabilities and of their induced mixing; this is important in particular for the Loire river plume. Also, studying bottom mixing, when the plume encounters the topography and interacts with tidal currents, can improve our understanding of the sediment transport and dynamics in the Gironde river plume.

- **Frontogenesis/Frontolysis budget.** In chapters 3 and 5, I characterize the interior mixing using a stratification budget in the frontal regions of the Gironde plume. This budget can be extended to different regions of a river plume using isopycnic or isohaline coordinates. The budget reveals that the intensification of the stratification is mainly related to frontogenesis. Frontogenesis explains the intensity of density/salinity gradients in fronts and deserves further investigation. Obtaining a detailed budget of frontogenesis in river plumes would emphasize the role of vortex stretching/squeezing and vortex tilting in strengthening/weakening the frontogenesis. This budget may also be obtained via idealized simulations with controlled environmental processes (tides, winds, air-sea fluxes) to understand their impacts; and realistic simulations to address more complete situations and seasonal variability.
- **3D Non-hydrostatic modelling.** In chapter 4, I simulated vertical shear processes (instabilities, mixing, dissipation) in estuaries and the near field regions of river plumes, using 2D non-hydrostatic simulations. I defined initial conditions representative of river plumes and studied the impact of different physical parameters: the shear, the freshwater thickness and the bottom slope. This study reveals the generation of the Kelvin-Helmholtz and Holmboe instabilities and their impact on the turbulent mixing and dissipation. However, in these simulations I did not consider the influence of the Coriolis force and the link between these instabilities and symmetric or baroclinic instabilities. The Coriolis effect can be added in a 3D non-hydrostatic simulation to clarify its impact. Moreover, 3D non-hydrostatic realistic and/or idealized

simulation would allow to study the link between vertical shear instabilities (Kelvin-Helmholtz and Holmboe) and internal waves dynamics.

- **Seasonal and interannual variability.** In chapter 5, I performed realistic simulations based on two months representing a contrast between summer (low Gironde river discharge) and winter (average Gironde river discharge). In this study, I analyzed the dynamics, instabilities and mixing of the Gironde river plume during these months. However, this study should be extended to further seasons and years to understand these issues in an extended period of time.
- **In-situ observations.** In chapters 3 and 5, in-situ measurements allow us to define the Gironde inputs such as river discharge, and the freshwater salinity and temperature. In-situ observations (chlorophyll surface concentration, salinity vertical profiles and tide gauges) were also used to validate numerical simulations in chapter 5. However, improvements might be needed in order to characterize submesoscale features and turbulence. These improvements lie in: (i) micro-profilers measurements in the Gironde estuary in complement to CTD measurements at high frequency and spatial samplings to characterize the turbulence induced by vertical shear instabilities, (ii) Aircraft infrared surface temperature future measurements (resolution of few meters) as used in the Gulf of Mexico [D'Asaro et al., 2020] will help to characterize the surface variability of the Gironde and Loire river plumes fronts. These measurements may be also used in coordination with the future SWOT altimeter data to more synoptically characterize submesoscale features in the Bay of Biscay.

This work outlines the complexity of coastal processes linked to river plumes and the impacts that they may have on the ecosystem.

Bibliography

- Akan, S. Moghimi, H. T. Özkan Haller, J. Osborne, and A. Kurapov. On the dynamics of the mouth of the columbia river: Results from a three-dimensional fully coupled wave-current interaction model. *Journal of Geophysical Research: Oceans*, 122(7):5218–5236, 2017. doi:<https://doi.org/10.1002/2016JC012307>. URL <https://agupubs.onlinelibrary.wiley.com/doi/abs/10.1002/2016JC012307>.
- A. Akpınar, G. Charria, S. Theetten, and F. Vandermeirsch. Cross-shelf exchanges in the northern bay of biscay. *Journal of Marine Systems*, 205:103314, 2020. ISSN 0924-7963. doi:<https://doi.org/10.1016/j.jmarsys.2020.103314>. URL <https://www.sciencedirect.com/science/article/pii/S0924796320300105>.
- A. Alexakis. On holmboe’s instability for smooth shear and density profiles. *Physics of Fluids*, 17(8):084103, 2005. doi:10.1063/1.2001567. URL <https://doi.org/10.1063/1.2001567>.
- G. Alory, C. Y. Da-Allada, S. Djakouré, I. Dadou, J. Jouanno, and D. P. Loemba. Coastal upwelling limitation by onshore geostrophic flow in the gulf of guinea around the niger river plume. *Frontiers in Marine Science*, 7:1116, 2021. ISSN 2296-7745. doi:10.3389/fmars.2020.607216. URL <https://www.frontiersin.org/article/10.3389/fmars.2020.607216>.
- A. Arakawa and V. R. Lamb. Computational design of the basic dynamical processes of the ucla general circulation model. In J. CHANG, editor, *General Circulation Models of the Atmosphere*, volume 17 of *Methods in Computational Physics: Advances in Research and Applications*, pages 173–265. Elsevier, 1977. doi:<https://doi.org/10.1016/B978-0-12-460817-7.50009-4>. URL <https://www.sciencedirect.com/science/article/pii/B9780124608177500094>.
- G. Avicola and P. Huq. Scaling analysis for the interaction between a buoyant coastal current and the continental shelf: Experiments and observations. *J. Phys. Oceanogr.*, 32(11):3233–3248, 2002. doi:10.1175/1520-0485(2002)032<3233:SAFTIB>2.0.CO;2. URL [https://doi.org/10.1175/1520-0485\(2002\)032<3233:SAFTIB>2.0.CO;2](https://doi.org/10.1175/1520-0485(2002)032<3233:SAFTIB>2.0.CO;2).
- A. Ayouche, X. Carton, G. Charria, S. Theettens, and N. Ayoub. Instabilities and vertical mixing in river plumes: application to the bay of biscay. *Geophysical & Astrophysical Fluid Dynamics*, 114(4-5):650–689, 2020. doi:10.1080/03091929.2020.1814275. URL <https://doi.org/10.1080/03091929.2020.1814275>.

- A. Ayouche, G. Charria, X. Carton, N. Ayoub, and S. Theetten. Non-linear processes in the gironde river plume (north-east atlantic): Instabilities and mixing. *Frontiers in Marine Science*, 8:810, 2021a. ISSN 2296-7745. doi:10.3389/fmars.2021.701773. URL <https://www.frontiersin.org/article/10.3389/fmars.2021.701773>.
- A. Ayouche, C. De Marez, M. Morvan, P. L'Hegaret, X. Carton, B. Le Vu, and A. Stegner. Structure and dynamics of the ras al hadd oceanic dipole in the arabian sea. *Oceans*, 2(1):105–125, 2021b. ISSN 2673-1924. doi:10.3390/oceans2010007. URL <https://www.mdpi.com/2673-1924/2/1/7>.
- L. Barry, G. Craig, and J. Thuburn. A gcm investigation into the nature of baroclinic adjustment. *J. Atmos. Sci. - J ATMOS SCI*, 57:1141–1155, 04 2000. doi:10.1175/1520-0469(2000)057<1141:AGIITN>2.0.CO;2.
- A. Beckmann and D. B. Haidvogel. Numerical simulation of flow around a tall isolated seamount. part i: Problem formulation and model accuracy. *Journal of Physical Oceanography*, 23(8):1736 – 1753, 1993. doi:10.1175/1520-0485(1993)023<1736:NSOFAA>2.0.CO;2. URL https://journals.ametsoc.org/view/journals/phoc/23/8/1520-0485_1993_023_1736_nsosfaa_2_0_co_2.xml.
- J. Botas, E. Fernández, A. Bode, and R. Anadón. A persistent upwelling off the central cantabrian coast (bay of biscay). *Est. Coast. Shelf Sci.*, 30:185–199, 02 1990. doi:10.1016/0272-7714(90)90063-W.
- L. K. Brandt and K. K. Nomura. The physics of vortex merger and the effects of ambient stable stratification. *Journal of Fluid Mechanics*, 592:413–446, 2007. doi:10.1017/S0022112007008671.
- L. Branscome, W. Gutowski, and D. Stewart. Effect of surface fluxes on the non-linear development of baroclinic waves. *J. Atmos. Sci.*, 46:460–475, 02 1989. doi:10.1175/1520-0469(1989)046<0460:EOSFOT>2.0.CO;2.
- K. Brink. Baroclinic instability of an idealized tidal mixing front. *J. Marine Res.*, 70:661–688, 07 2012. doi:10.1357/002224012805262716.
- K. Brink. Instability of a tidal mixing front in the presence of realistic tides and mixing. *J. Marine Res.*, 71, 05 2013. doi:10.1357/002224013807719473.
- K. A. Browning. Structure of the atmosphere in the vicinity of large-amplitude kelvin-helmholtz billows. *Quarterly Journal of the Royal Meteorological Society*, 97(413):283–299, 1971. doi:<https://doi.org/10.1002/qj.49709741304>. URL <https://rmets.onlinelibrary.wiley.com/doi/abs/10.1002/qj.49709741304>.
- A. Caballero, A. Pascual, G. Dibarboure, and M. Espino. Sea level and eddy kinetic energy variability in the bay of biscay, inferred from satellite altimeter data. *Journal of Marine Systems*, 72(1):116 – 134, 2008. ISSN 0924-7963. doi:<https://doi.org/10.1016/j.jmarsys.2007.03.011>. URL <http://www.sciencedirect.com/science/article/pii/S0924796307002412>. Oceanography of the Bay of Biscay.

- A. Caballero, L. Ferrer, A. Rubio, G. Charria, B. H. Taylor, and N. Grima. Monitoring of a quasi-stationary eddy in the bay of biscay by means of satellite, in situ and model results. *Deep-Sea Res. Pt. II-Topical Studies in Oceanography*, 106:23 – 37, 2014. ISSN 0967-0645. doi:<https://doi.org/10.1016/j.dsr2.2013.09.029>. URL <http://www.sciencedirect.com/science/article/pii/S0967064513003706>. Oceanography of the Bay of Biscay.
- W. Callendar, J. M. Klymak, and M. G. G. Foreman. Tidal generation of large submesoscale eddy dipoles. *Oc. Sci.*, 7(4):487–502, 2011. doi:[10.5194/os-7-487-2011](https://doi.org/10.5194/os-7-487-2011). URL <https://www.ocean-sci.net/7/487/2011/>.
- V. Canuto, A. Howard, Y. Cheng, and M. Dubovikov. Ocean turbulence. part i: One-point closure modeltextemdashmomentum and heat vertical diffusivities. *Journal of Physical Oceanography*, 31:1413–1426, 06 2001.
- T. Capuano, S. Sabrina, C. Xavier, and B. Blanke. Mesoscale and submesoscale processes in the southeast atlantic and their impact on the regional thermohaline structure. *J. Geophys. Res.-Oceans*, 123:1937–1961, 03 2018. doi:[10.1002/2017JC013396](https://doi.org/10.1002/2017JC013396).
- J. R. Carpenter, N. J. Balmforth, and G. A. Lawrence. Identifying unstable modes in stratified shear layers. *Physics of Fluids*, 22(5):054104, 2010. doi:[10.1063/1.3379845](https://doi.org/10.1063/1.3379845). URL <https://doi.org/10.1063/1.3379845>.
- P. Castaing. Courantologie de dérive dans les zones côtières à l’aide de bouées positionnées par satellite (Système ARGOS). *Proceedings of XVIIIème Journées de l’hydraulique. Marseille*, page I.4.1–I.4.8, 1984.
- R. Chant, J. Wilkin, W. Zhang, B.-J. Choi, E. Hunter, R. Castelao, S. Glenn, J. Jurisa, O. Schofield, R. Houghton, J. Kohut, T. Frazer, and M. Moline. Dispersal of the hudson river plume in the new york bight: Synthesis of observational and numerical studies during latte. *Biol. Sci.*, 21, 12 2008. doi:[10.5670/oceanog.2008.11](https://doi.org/10.5670/oceanog.2008.11).
- S.-Y. Chao. Wind-driven motion near inner shelf fronts. *J. Geophys. Res.-Oceans*, 92 (C4):3849–3860, 1987. doi:[10.1029/JC092iC04p03849](https://doi.org/10.1029/JC092iC04p03849). URL <https://agupubs.onlinelibrary.wiley.com/doi/abs/10.1029/JC092iC04p03849>.
- S.-Y. Chao. Wind-driven motion of estuarine plumes. *J. Phys. Oceanogr.*, 18(8): 1144–1166, 1988. doi:[10.1175/1520-0485\(1988\)018<1144:WDMOEP>2.0.CO;2](https://doi.org/10.1175/1520-0485(1988)018<1144:WDMOEP>2.0.CO;2). URL [https://doi.org/10.1175/1520-0485\(1988\)018<1144:WDMOEP>2.0.CO;2](https://doi.org/10.1175/1520-0485(1988)018<1144:WDMOEP>2.0.CO;2).
- D. C. Chapman. Numerical treatment of cross-shelf open boundaries in a barotropic coastal ocean model. *Journal of Physical Oceanography*, 15(8):1060 – 1075, 1985. doi:[10.1175/1520-0485\(1985\)015<1060:NTOCSO>2.0.CO;2](https://doi.org/10.1175/1520-0485(1985)015<1060:NTOCSO>2.0.CO;2). URL https://journals.ametsoc.org/view/journals/phoc/15/8/1520-0485_1985_015_1060_ntocso_2_0_co_2.xml.

- G. Charria, S. Theetten, F. Vandermeirsch, O. Yelekçi, and N. Audiffren. Interannual evolution of (sub)mesoscale dynamics in the bay of biscay. *Ocean Science*, 13(5):777–797, 2017. doi:10.5194/os-13-777-2017. URL <https://os.copernicus.org/articles/13/777/2017/>.
- G. Charria, P. Lazure, B. L. Cann, A. Serpette, G. Reverdin, S. Louazel, F. Batifoulier, F. Dumas, A. Pichon, and Y. Morel. Surface layer circulation derived from lagrangian drifters in the bay of biscay. *J. Mar. Sys.*, 109-110:S60 – S76, 2013. ISSN 0924-7963. doi:<https://doi.org/10.1016/j.jmarsys.2011.09.015>. URL <http://www.sciencedirect.com/science/article/pii/S0924796311002284>. XII International Symposium on Oceanography of the Bay of Biscay.
- B.-J. Choi and J. L. Wilkin. The effect of wind on the dispersal of the hudson river plume. *J. Phys. Oceanogr.*, 37(7):1878–1897, 2007. doi:10.1175/JPO3081.1. URL <https://doi.org/10.1175/JPO3081.1>.
- K. L. Cole and R. D. Hetland. The effects of rotation and river discharge on net mixing in small-mouth kelvin number plumes. *Journal of Physical Oceanography*, 46(5):1421 – 1436, 2016. doi:10.1175/JPO-D-13-0271.1. URL <https://journals.ametsoc.org/view/journals/phoc/46/5/jpo-d-13-0271.1.xml>.
- M. Contreras, O. Pizarro, B. Dewitte, H. H. Sepulveda, and L. Renault. Subsurface mesoscale eddy generation in the ocean off central chile. *Journal of Geophysical Research: Oceans*, 124(8):5700–5722, 2019. doi:<https://doi.org/10.1029/2018JC014723>. URL <https://agupubs.onlinelibrary.wiley.com/doi/abs/10.1029/2018JC014723>.
- X. Costoya, D. Fernández-Nóvoa, M. deCastro, F. Santos, P. Lazure, and M. Gómez-Gesteira. Modulation of sea surface temperature warming in the bay of biscay by loire and gironde rivers. *Journal of Geophysical Research: Oceans*, 121(1):966–979, 2016. doi:<https://doi.org/10.1002/2015JC011157>. URL <https://agupubs.onlinelibrary.wiley.com/doi/abs/10.1002/2015JC011157>.
- X. Costoya, D. Fernández-Nóvoa, M. deCastro, and M. Gómez-Gesteira. Loire and gironde turbid plumes: Characterization and influence on thermohaline properties. *Journal of Sea Research*, 130:7 – 16, 2017. ISSN 1385-1101. doi:<https://doi.org/10.1016/j.seares.2017.04.003>. URL <http://www.sciencedirect.com/science/article/pii/S1385110116302398>. Changing Ecosystems in the Bay of Biscay: Natural and Anthropogenic Effects.
- E. D’Asaro, C. Lee, L. Rainville, R. Harcourt, and L. Thomas. Enhanced turbulence and energy dissipation at ocean fronts. *Science*, 332(6027):318–322, 2011. ISSN 0036-8075. doi:10.1126/science.1201515. URL <https://science.sciencemag.org/content/332/6027/318>.
- E. A. D’Asaro, D. F. Carlson, M. Chamecki, R. R. Harcourt, B. K. Haus, B. Fox-Kemper, M. J. Molemaker, A. C. Poje, and D. Yang. Advances in observing and understanding small-scale open ocean circulation during the gulf of mexico research initiative era. *Frontiers in Marine Science*, 7:349, 2020. ISSN 2296-7745.

- doi:10.3389/fmars.2020.00349. URL <https://www.frontiersin.org/article/10.3389/fmars.2020.00349>.
- J. de Kok. Baroclinic eddy formation in a rhine plume model. *J. Mar. Sys.*, 12(1):35 – 52, 1997. ISSN 0924-7963. doi:[https://doi.org/10.1016/S0924-7963\(96\)00087-5](https://doi.org/10.1016/S0924-7963(96)00087-5). URL <http://www.sciencedirect.com/science/article/pii/S0924796396000875>.
- C. de Marez, X. Carton, P. L'Hégaret, T. Meunier, A. Stegner, B. Le Vu, and M. Morvan. Oceanic vortex mergers are not isolated but influenced by the β -effect and surrounding eddies. *Scientific Reports*, 10(1):2897 (10p.), February 2020. doi:10.1038/s41598-020-59800-y.
- L. Debreu, P. Marchesiello, P. Penven, and G. Cambon. Two-way nesting in split-explicit ocean models: algorithms, implementation and validation. *Ocean Modelling*, s 49–50:1–21, 06 2012. doi:10.1016/j.ocemod.2012.03.003.
- D. P. Dee, S. M. Uppala, A. J. Simmons, P. Berrisford, P. Poli, S. Kobayashi, U. Andrae, M. A. Balmaseda, G. Balsamo, P. Bauer, P. Bechtold, A. C. M. Beljaars, L. van de Berg, J. Bidlot, N. Bormann, C. Delsol, R. Dragani, M. Fuentes, A. J. Geer, L. Haimberger, S. B. Healy, H. Hersbach, E. V. Hólm, L. Isaksen, P. Kállberg, M. Köhler, M. Matricardi, A. P. McNally, B. M. Monge-Sanz, J.-J. Morcrette, B.-K. Park, C. Peubey, P. de Rosnay, C. Tavolato, J.-N. Thépaut, and F. Vitart. The era-interim reanalysis: configuration and performance of the data assimilation system. *Quarterly Journal of the Royal Meteorological Society*, 137(656):553–597, 2011. doi:<https://doi.org/10.1002/qj.828>. URL <https://rmets.onlinelibrary.wiley.com/doi/abs/10.1002/qj.828>.
- P. A. Delamere and F. Bagenal. Solar wind interaction with jupiter's magnetosphere. *Journal of Geophysical Research: Space Physics*, 115(A10):A10201, 2010. doi:<https://doi.org/10.1029/2010JA015347>. URL <https://agupubs.onlinelibrary.wiley.com/doi/abs/10.1029/2010JA015347>.
- P. A. Delamere and F. Bagenal. Magnetotail structure of the giant magnetospheres: Implications of the viscous interaction with the solar wind. *Journal of Geophysical Research: Space Physics*, 118(11):7045–7053, 2013. doi:<https://doi.org/10.1002/2013JA019179>. URL <https://agupubs.onlinelibrary.wiley.com/doi/abs/10.1002/2013JA019179>.
- P. Dirac. The lorentz transformation and absolute time. *Physica*, 19(1–12):888–896, 1953. doi:10.1016/S0031-8914(53)80099-6.
- H. N. Dixit and R. Govindarajan. Effect of density stratification on vortex merger. *Physics of Fluids*, 25(1):016601, 2013. doi:10.1063/1.4773445. URL <https://doi.org/10.1063/1.4773445>.
- D. Dritschel. On the persistence of non-axisymmetric vortices in inviscid two-dimensional flows. *Journal of Fluid Mechanics - J FLUID MECH*, 371:141–155, 09 1998. doi:10.1017/S0022112098002080.

- H. Ertel. Ein neuer hydrodynamischer erhaltungssatz. *Naturwissenschaften*, 30: 543–544, 1942.
- M. Evans Contreras, O. Pizarro, B. Dewitte, H. Sepúlveda, and L. Renault. Sub-surface mesoscale eddy generation in the ocean off central chile. *J. Geophys. Res.-Oceans*, 07 2019. doi:[10.1029/2018JC014723](https://doi.org/10.1029/2018JC014723).
- C. W. Fairall, E. F. Bradley, D. P. Rogers, J. B. Edson, and G. S. Young. Bulk parameterization of air-sea fluxes for tropical ocean-global atmosphere coupled-ocean atmosphere response experiment. *Journal of Geophysical Research: Oceans*, 101(C2):3747–3764, 1996. doi:<https://doi.org/10.1029/95JC03205>. URL <https://agupubs.onlinelibrary.wiley.com/doi/abs/10.1029/95JC03205>.
- R. Feynman and F. Vernon Jr. The theory of a general quantum system interacting with a linear dissipative system. *Annals of Physics*, 24:118–173, 1963. doi:[10.1016/0003-4916\(63\)90068-X](https://doi.org/10.1016/0003-4916(63)90068-X).
- D. A. Fong and W. R. Geyer. Response of a river plume during an upwelling favorable wind event. *J. Geophys. Res.-Oceans*, 106(C1):1067–1084, 2001. doi:[10.1029/2000JC900134](https://doi.org/10.1029/2000JC900134). URL <https://agupubs.onlinelibrary.wiley.com/doi/abs/10.1029/2000JC900134>.
- J. Fontane and L. Joly. The stability of the variable-density kelvin–helmholtz billow. *Journal of Fluid Mechanics*, 612:237–260, 2008. doi:[10.1017/S0022112008002966](https://doi.org/10.1017/S0022112008002966).
- C. Foullon, E. Verwichte, V. Nakariakov, K. Nykyri, and C. Farrugia. Magnetic kelvin-helmholtz instability at the sun. *The Astrophysical Journal Letters*, 729: L8, 02 2011. doi:[10.1088/2041-8205/729/1/L8](https://doi.org/10.1088/2041-8205/729/1/L8).
- R. Frouin, A. F. G. Fiúza, I. Ambar, and T. J. Boyd. Observations of a poleward surface current off the coasts of portugal and spain during winter. *Journal of Geophysical Research: Oceans*, 95(C1):679–691, 1990. doi:<https://doi.org/10.1029/JC095iC01p00679>. URL <https://agupubs.onlinelibrary.wiley.com/doi/abs/10.1029/JC095iC01p00679>.
- C. Garcia-Soto and R. D. Pingree. Late autumn distribution and seasonality of chlorophyll-a at the shelf-break/slope region of the armorican and celtic shelf. *J. Mar. Bio. Assoc. UK*, 78(1):17–33, 1998. doi:[10.1017/S002531540003993X](https://doi.org/10.1017/S002531540003993X).
- C. Garcia-Soto, R. D. Pingree, and L. Valdés. Navidad development in the southern bay of biscay: Climate change and swoddy structure from remote sensing and in situ measurements. *Journal of Geophysical Research: Oceans*, 107(C8):28–1–28–29, 2002. doi:<https://doi.org/10.1029/2001JC001012>. URL <https://agupubs.onlinelibrary.wiley.com/doi/abs/10.1029/2001JC001012>.
- R. W. Garvine. Radial spreading of buoyant, surface plumes in coastal waters. *Journal of Geophysical Research: Oceans*, 89(C2):1989–1996, 1984. doi:<https://doi.org/10.1029/JC089iC02p01989>. URL <https://agupubs.onlinelibrary.wiley.com/doi/abs/10.1029/JC089iC02p01989>.

- R. W. Garvine. A dynamical system for classifying buoyant coastal discharges. *Continental Shelf Research*, 15(13):1585–1596, 1995. ISSN 0278-4343. doi:[https://doi.org/10.1016/0278-4343\(94\)00065-U](https://doi.org/10.1016/0278-4343(94)00065-U). URL <https://www.sciencedirect.com/science/article/pii/027843439400065U>. Nearshore and Coastal Oceanography.
- R. W. Garvine. Penetration of Buoyant Coastal Discharge onto the Continental Shelf: A Numerical Model Experiment. *J. Phys. Oceanogr.*, 29(8):1892–1909, Aug 1999. doi:[10.1175/1520-0485\(1999\)029<1892:POBCDO>2.0.CO;2](https://doi.org/10.1175/1520-0485(1999)029<1892:POBCDO>2.0.CO;2).
- G. Godin. The analysis of tides. [*Toronto, Buffalo*] *University of Toronto Press [1972]*, xxi:264 pp, 01 1972.
- F. Gohin. Annual cycles of chlorophyll-a, non-algal suspended particulate matter, and turbidity observed from space and in-situ incoastal waters. *Oc. Sci.*, 7:705–732, 2011. doi:[10.5194/os-7-705-2011](https://doi.org/10.5194/os-7-705-2011).
- S. Goldstein and G. I. Taylor. On the stability of superposed streams of fluids of different densities. *Proceedings of the Royal Society of London. Series A, Containing Papers of a Mathematical and Physical Character*, 132(820):524–548, 1931. doi:[10.1098/rspa.1931.0116](https://doi.org/10.1098/rspa.1931.0116). URL <https://royalsocietypublishing.org/doi/abs/10.1098/rspa.1931.0116>.
- J. A. Graham, J. P. Rosser, E. O’Dea, and H. T. Hewitt. Resolving shelf break exchange around the european northwest shelf. *Geophysical Research Letters*, 45(22): 12,386–12,395, 2018. doi:<https://doi.org/10.1029/2018GL079399>. URL <https://agupubs.onlinelibrary.wiley.com/doi/abs/10.1029/2018GL079399>.
- M. Granskog, J. Ehn, and M. Niemelä. Characteristics and potential impacts of under-ice river plumes in the seasonally ice-covered bothnian bay (baltic sea). *Journal of Marine Systems*, 53:187–196, 05 2005. doi:[10.1016/j.jmarsys.2004.06.005](https://doi.org/10.1016/j.jmarsys.2004.06.005).
- H. P. Gröbelbauer, T. K. Fanneløp, and R. E. Britter. The propagation of intrusion fronts of high density ratios. *Journal of Fluid Mechanics*, 250:669–687, 1993. doi:[10.1017/S0022112093001612](https://doi.org/10.1017/S0022112093001612).
- A. Guha, M. Rahmani, and G. A. Lawrence. Evolution of a barotropic shear layer into elliptical vortices. *Phys. Rev. E*, 87:013020, Jan 2013. doi:[10.1103/PhysRevE.87.013020](https://doi.org/10.1103/PhysRevE.87.013020). URL <https://link.aps.org/doi/10.1103/PhysRevE.87.013020>.
- J. Gula, M. Molemaker, and J. McWilliams. Topographic generation of submesoscale centrifugal instability and energy dissipation. *Nature Communications*, 7:12811, 09 2016. doi:[10.1038/ncomms12811](https://doi.org/10.1038/ncomms12811).
- X. Guo and A. Valle-Levinson. Tidal effects on estuarine circulation and outflow plume in the chesapeake bay. *Cont. Shelf Res.*, 27:20–42, 01 2007. doi:[10.1016/j.csr.2006.08.009](https://doi.org/10.1016/j.csr.2006.08.009).

- M. J. Halverson and R. Pawlowicz. Estuarine forcing of a river plume by river flow and tides. *J. Geophys. Res.-Oceans*, 113(C9), 2008. doi:10.1029/2008JC004844. URL <https://agupubs.onlinelibrary.wiley.com/doi/abs/10.1029/2008JC004844>.
- A. Harten. High resolution schemes for hyperbolic conservation laws. *Journal of Computational Physics*, 49(3):357–393, 1983. ISSN 0021-9991. doi:[https://doi.org/10.1016/0021-9991\(83\)90136-5](https://doi.org/10.1016/0021-9991(83)90136-5). URL <https://www.sciencedirect.com/science/article/pii/0021999183901365>.
- P. Haynes and E. Shuckburgh. Effective diffusivity as a diagnostic of atmospheric transport: 1. stratosphere. *J. Geophys. Res.-Atmospheres*, 105(D18):22777–22794, 2000. doi:10.1029/2000JD900093. URL <https://agupubs.onlinelibrary.wiley.com/doi/abs/10.1029/2000JD900093>.
- P. Held, K. Bartholomä-Schrottke, and A. Bartholomä. Indications for the transition of kelvin-helmholtz instabilities into propagating internal waves in a high turbid estuary and their effect on the stratification stability. *Geo-Marine Letters*, 39: 149–159, 04 2019. doi:10.1007/s00367-019-00564-4.
- P. Helmholtz. Xliii. on discontinuous movements of fluids. *The London, Edinburgh, and Dublin Philosophical Magazine and Journal of Science*, 36(244):337–346, 1868. doi:10.1080/14786446808640073. URL <https://doi.org/10.1080/14786446808640073>.
- R. D. Hetland. Relating river plume structure to vertical mixing. *Journal of Physical Oceanography*, 35(9):1667 – 1688, 2005. doi:10.1175/JPO2774.1. URL <https://journals.ametsoc.org/view/journals/phoc/35/9/jpo2774.1.xml>.
- R. D. Hetland. The effects of mixing and spreading on density in near-field river plumes. *Dynamics of Atmospheres and Oceans*, 49(1):37–53, 2010. ISSN 0377-0265. doi:<https://doi.org/10.1016/j.dynatmoce.2008.11.003>. URL <https://www.sciencedirect.com/science/article/pii/S0377026508000699>.
- R. D. Hetland. Suppression of baroclinic instabilities in buoyancy-driven flow over sloping bathymetry. *Journal of Physical Oceanography*, 47(1):49 – 68, 2017. doi:10.1175/JPO-D-15-0240.1. URL <https://journals.ametsoc.org/view/journals/phoc/47/1/jpo-d-15-0240.1.xml>.
- B. M. Hickey, L. J. Pietrafesa, D. A. Jay, and W. C. Boicourt. The columbia river plume study: Subtidal variability in the velocity and salinity fields. *J. Geophys. Res.-Oceans*, 103(C5):10339–10368, 1998. doi:10.1029/97JC03290. URL <https://agupubs.onlinelibrary.wiley.com/doi/abs/10.1029/97JC03290>.
- J. T. Holt. Experiments on kelvin-helmholtz billows influenced by boundaries. *Geophysical & Astrophysical Fluid Dynamics*, 89(3-4):205–233, 1998. doi:10.1080/03091929808203686. URL <https://doi.org/10.1080/03091929808203686>.

- A. Horner-Devine. The bulge circulation in the columbia river plume. *Cont. Shelf Res.*, 29:234–251, 01 2009. doi:[10.1016/j.csr.2007.12.012](https://doi.org/10.1016/j.csr.2007.12.012).
- A. R. Horner-Devine, R. D. Hetland, and D. G. MacDonald. Mixing and transport in coastal river plumes. *Annual Review of Fluid Mechanics*, 47(1):569–594, 2015. doi:[10.1146/annurev-fluid-010313-141408](https://doi.org/10.1146/annurev-fluid-010313-141408). URL <https://doi.org/10.1146/annurev-fluid-010313-141408>.
- B. Hoskins. The role of potential vorticity in symmetric stability and instability. *Quart. J. Royal Meteor. Soc.*, 100:480 – 482, 07 1974. doi:[10.1002/qj.49710042520](https://doi.org/10.1002/qj.49710042520).
- B. J. Hoskins and M. A. Pedder. The diagnosis of middle latitude synoptic development. *Quart. J. Royal Meteor. Soc.*, 106(450):707–719, 1980. doi:[10.1002/qj.49710645004](https://doi.org/10.1002/qj.49710645004). URL <https://rmets.onlinelibrary.wiley.com/doi/abs/10.1002/qj.49710645004>.
- E. J. Hunter, R. J. Chant, J. L. Wilkin, and J. Kohut. High-frequency forcing and subtidal response of the hudson river plume. *J. Geophys. Res.-Oceans*, 115 (C7), 2010. doi:[10.1029/2009JC005620](https://doi.org/10.1029/2009JC005620). URL <https://agupubs.onlinelibrary.wiley.com/doi/abs/10.1029/2009JC005620>.
- M. Huret, P. Bourriau, M. Doray, F. Gohin, and P. Petitgas. Survey timing vs. ecosystem scheduling: Degree-days to underpin observed interannual variability in marine ecosystems. *Progress in Oceanography*, 166:30–40, 2018. ISSN 0079-6611. doi:<https://doi.org/10.1016/j.pocean.2017.07.007>. URL <https://www.sciencedirect.com/science/article/pii/S0079661117300824>. Multidisciplinary integrated surveys.
- A. Ioannou, A. Stegner, A. Tuel, B. LeVu, F. Dumas, and S. Speich. Cyclostrophic corrections of aviso/duacs surface velocities and its application to mesoscale eddies in the mediterranean sea. *Journal of Geophysical Research: Oceans*, 124(12):8913–8932, 2019. doi:<https://doi.org/10.1029/2019JC015031>. URL <https://agupubs.onlinelibrary.wiley.com/doi/abs/10.1029/2019JC015031>.
- A. Isobe. Ballooning of river-plume bulge and its stabilization by tidal currents. *J. Phys. Oceanogr. - J PHYS OCEANOGR*, 35, 12 2005. doi:[10.1175/JPO2837.1](https://doi.org/10.1175/JPO2837.1).
- Y. Iwanaka and A. Isobe. Tidally induced instability processes suppressing river plume spread in a nonrotating and nonhydrostatic regime. *Journal of Geophysical Research: Oceans*, 123(5):3545–3562, 2018. doi:<https://doi.org/10.1029/2017JC013495>. URL <https://agupubs.onlinelibrary.wiley.com/doi/abs/10.1029/2017JC013495>.
- Y. Jia and A. Yankovsky. The impact of ambient stratification on freshwater transport in a river plume. *Journal of Marine Research*, 70:69–92, 01 2012. doi:[10.1357/002224012800502408](https://doi.org/10.1357/002224012800502408).
- A. K. Kaminski and W. D. Smyth. Stratified shear instability in a field of pre-existing turbulence. *Journal of Fluid Mechanics*, 862:639–658, 2019. doi:[10.1017/jfm.2018.973](https://doi.org/10.1017/jfm.2018.973).

- D. Kang. Energetics of eddy–mean flow interactions in the gulf stream region. *J. Phys. Oceanogr.*, 45:1103–1120, 04 2015.
- L. H. Kantha and C. A. Clayson. An improved mixed layer model for geophysical applications. *Journal of Geophysical Research: Oceans*, 99(C12):25235–25266, 1994. doi:<https://doi.org/10.1029/94JC02257>. URL <https://agupubs.onlinelibrary.wiley.com/doi/abs/10.1029/94JC02257>.
- J. Karagiorgos, V. Vervatis, and S. Sofianos. The impact of tides on the bay of biscay dynamics. *Journal of Marine Science and Engineering*, 8(8):617, Aug 2020. ISSN 2077-1312. doi:[10.3390/jmse8080617](https://doi.org/10.3390/jmse8080617). URL <http://dx.doi.org/10.3390/jmse8080617>.
- S. E. Kastner, A. R. Horner-Devine, and J. Thomson. The influence of wind and waves on spreading and mixing in the fraser river plume. *Journal of Geophysical Research: Oceans*, 123(9):6818–6840, 2018. doi:<https://doi.org/10.1029/2018JC013765>. URL <https://agupubs.onlinelibrary.wiley.com/doi/abs/10.1029/2018JC013765>.
- B. Kelly-Gerreyn, D. Hydes, A. Jégou, P. Lazure, L. Fernand, I. Puillat, and C. Garcia-Soto. Low salinity intrusions in the western english channel. *Cont. Shelf Res.*, 26(11):1241 – 1257, 2006. ISSN 0278-4343. doi:<https://doi.org/10.1016/j.csr.2006.03.007>. URL <http://www.sciencedirect.com/science/article/pii/S0278434306000963>.
- E. Khavasi, B. Firoozabadi, and H. Afshin. Linear analysis of the stability of particle-laden stratified shear layers. *Canadian Journal of Physics*, 92(2):103–115, 2014. doi:[10.1139/cjp-2013-0028](https://doi.org/10.1139/cjp-2013-0028). URL <https://doi.org/10.1139/cjp-2013-0028>.
- L. F. Kilcher and J. D. Nash. Structure and dynamics of the columbia river tidal plume front. *J. Geophys. Res.-Oceans*, 115(C5), 2010. doi:[10.1029/2009JC006066](https://doi.org/10.1029/2009JC006066). URL <https://agupubs.onlinelibrary.wiley.com/doi/abs/10.1029/2009JC006066>.
- L. F. Kilcher, J. D. Nash, and J. N. Moum. The role of turbulence stress divergence in decelerating a river plume. *Journal of Geophysical Research: Oceans*, 117(C5):C05032, 2012. doi:<https://doi.org/10.1029/2011JC007398>. URL <https://agupubs.onlinelibrary.wiley.com/doi/abs/10.1029/2011JC007398>.
- G. T. Kochar and R. K. Jain. Note on howard’s semicircle theorem. *Journal of Fluid Mechanics*, 91(3):489–491, 1979. doi:[10.1017/S0022112079000276](https://doi.org/10.1017/S0022112079000276).
- V. H. Kourafalou, T. N. Lee, L.-Y. Oey, and J. D. Wang. The fate of river discharge on the continental shelf: 2. transport of coastal low-salinity waters under realistic wind and tidal forcing. *Journal of Geophysical Research: Oceans*, 101(C2):3435–3455, 1996a. doi:<https://doi.org/10.1029/95JC03025>. URL <https://agupubs.onlinelibrary.wiley.com/doi/abs/10.1029/95JC03025>.

- V. H. Kourafalou, L.-Y. Oey, J. D. Wang, and T. N. Lee. The fate of river discharge on the continental shelf: 1. modeling the river plume and the inner shelf coastal current. *Journal of Geophysical Research: Oceans*, 101(C2):3415–3434, 1996b. doi:<https://doi.org/10.1029/95JC03024>. URL <https://agupubs.onlinelibrary.wiley.com/doi/abs/10.1029/95JC03024>.
- C. Koutsikopoulos, P. Beillois, C. Leroy, and F. Taillefer. Temporal trends and spatial structures of the sea surface temperature in the bay of biscay. *Oceanologica Acta*, 21(2):335 – 344, 1998. ISSN 0399-1784. doi:[https://doi.org/10.1016/S0399-1784\(98\)80020-0](https://doi.org/10.1016/S0399-1784(98)80020-0). URL <http://www.sciencedirect.com/science/article/pii/S0399178498800200>. International Conference on Oceanography of the Bay of Biscay.
- Z. Lai, R. Ma, M. Huang, C. Chen, Y. Chen, C. Xie, and R. C. Beardsley. Downwelling wind, tides, and estuarine plume dynamics. *J. Geophys. Res.-Oceans*, 121(6):4245–4263, 2016. doi:[10.1002/2015JC011475](https://doi.org/10.1002/2015JC011475). URL <https://agupubs.onlinelibrary.wiley.com/doi/abs/10.1002/2015JC011475>.
- G. Lapeyre, P. Klein, and B. L. Hua. Oceanic restratification forced by surface frontogenesis. *J. Phys. Oceanogr.*, 36(8):1577–1590, 2006. doi:[10.1175/JPO2923.1](https://doi.org/10.1175/JPO2923.1). URL <https://doi.org/10.1175/JPO2923.1>.
- W. G. Large, J. C. McWilliams, and S. C. Doney. Oceanic vertical mixing: A review and a model with a nonlocal boundary layer parameterization. *Reviews of Geophysics*, 32(4):363–403, 1994. doi:<https://doi.org/10.1029/94RG01872>. URL <https://agupubs.onlinelibrary.wiley.com/doi/abs/10.1029/94RG01872>.
- A. Lavín, L. Valdès, F. Sánchez, P. Abaunza, A. Forest, J. Boucher, P. Lazure, and A. Jegou. The bay of biscay: the encountering of the ocean and the shelf. In A. Robinson and K. Brink, editors, *The Sea. Volume 14. Part B. The Global Coastal Ocean: Interdisciplinary Regional Studies and Synthesis*, chapter 24, pages 933–999. Harvard University Press, Harvard, 2006.
- P. Lazure, V. Garnier, F. Dumas, C. Herry, and M. Chifflet. Development of a hydrodynamic model of the bay of biscay. validation of hydrology. *Continental Shelf Research*, 29:985–997, 2009.
- P. Lazure and A.-M. Jegou. 3d modelling of seasonal evolution of loire and gironde plumes on biscay bay continental shelf. *Oceanologica Acta*, 21(2):165–177, 1998. ISSN 0399-1784. doi:[https://doi.org/10.1016/S0399-1784\(98\)80006-6](https://doi.org/10.1016/S0399-1784(98)80006-6). URL <https://www.sciencedirect.com/science/article/pii/S0399178498800066>. International Conference on Oceanography of the Bay of Biscay.
- A. Laine, G. Lapeyre, and G. Rivière. A quasigeostrophic model for moist storm tracks. *J. Atmos. Sci. - J ATMOS SCI*, 68:1306–1322, 06 2011. doi:[10.1175/2011JAS3618.1](https://doi.org/10.1175/2011JAS3618.1).

- A. Le Boyer, G. Charria, B. Le Cann, P. Lazure, and L. Marié. Circulation on the shelf and the upper slope of the bay of biscay. *Cont. Shelf Res.*, 55:97 – 107, 2013. ISSN 0278-4343. doi:<https://doi.org/10.1016/j.csr.2013.01.006>. URL <http://www.sciencedirect.com/science/article/pii/S0278434313000162>.
- B. Le Cann and A. Serpette. Intense warm and saline upper ocean inflow in the southern bay of biscay in autumn–winter 2006–2007. *Continental Shelf Research*, 29(8):1014–1025, 2009. ISSN 0278-4343. doi:<https://doi.org/10.1016/j.csr.2008.11.015>. URL <https://www.sciencedirect.com/science/article/pii/S027843430900020X>. 100 Years of Research within the Bay of Biscay.
- S. Le Dizès and A. Verga. Viscous interactions of two co-rotating vortices before merging. *Journal of Fluid Mechanics*, 467:389–410, 2002. doi:[10.1017/S0022112002001532](https://doi.org/10.1017/S0022112002001532).
- B. Le Vu, A. Stegner, and T. Arsouze. Angular momentum eddy detection and tracking algorithm (amedea) and its application to coastal eddy formation. *Journal of Atmospheric and Oceanic Technology*, 35(4):739 – 762, 2018. doi:[10.1175/JTECH-D-17-0010.1](https://doi.org/10.1175/JTECH-D-17-0010.1). URL <https://journals.ametsoc.org/view/journals/atot/35/4/jtech-d-17-0010.1.xml>.
- F. Lemarié, J. Kurian, A. Shchepetkin, M. Molemaker, F. Colas, and J. McWilliams. Are there inescapable issues prohibiting the use of terrain-following coordinates in climate models ? *Ocean Modelling*, 42:57–79, 12 2012. doi:[10.1016/j.ocemod.2011.11.007](https://doi.org/10.1016/j.ocemod.2011.11.007).
- S. Lentz and J. Largier. The influence of wind forcing on the chesapeake bay buoyant coastal current*. *J. Phys. Oceanogr.*, 36, 07 2006. doi:[10.1175/JPO2909.1](https://doi.org/10.1175/JPO2909.1).
- S. J. Lentz and K. R. Helfrich. Buoyant gravity currents along a sloping bottom in a rotating fluid. *J. Fluid Mech.*, 464:251–278, 2002. doi:[10.1017/S0022112002008868](https://doi.org/10.1017/S0022112002008868).
- H. Li and H. Yamazaki. Observations of a kelvin-helmholtz billow in the ocean. *Journal of Oceanography*, 57:709–721, 12 2001. doi:[10.1023/A:1021284409498](https://doi.org/10.1023/A:1021284409498).
- M. Li and Z. Rong. Effects of tides on freshwater and volume transports in the changjiang river plume. *J. Geophys. Res.-Oceans*, 117(C6), 2012. doi:[10.1029/2011JC007716](https://doi.org/10.1029/2011JC007716). URL <https://agupubs.onlinelibrary.wiley.com/doi/abs/10.1029/2011JC007716>.
- W.-C. Liu, W.-B. Chen, R. T. Cheng, and M.-H. Hsu. Modelling the impact of wind stress and river discharge on danshuei river plume. *App. Math. Model.*, 32(7):1255 – 1280, 2008. ISSN 0307-904X. doi:<https://doi.org/10.1016/j.apm.2007.03.009>. URL <http://www.sciencedirect.com/science/article/pii/S0307904X07001023>.

- E. N. Lorenz. Available potential energy and the maintenance of the general circulation. *Tellus*, 7(2):157–167, 1955. doi:10.3402/tellusa.v7i2.8796. URL <https://doi.org/10.3402/tellusa.v7i2.8796>.
- R. J. Lowe, J. W. Rottman, and P. F. Linden. The non-boussinesq lock-exchange problem. part 1. theory and experiments. *Journal of Fluid Mechanics*, 537: 101–124, 2005. doi:10.1017/S0022112005005069.
- R. Lv, P. Cheng, and J. Gan. Adjustment of river plume fronts during downwelling-favorable wind events. *Continental Shelf Research*, 202:104143, 2020. ISSN 0278-4343. doi:<https://doi.org/10.1016/j.csr.2020.104143>. URL <https://www.sciencedirect.com/science/article/pii/S0278434320300996>.
- F. H. Lyard, D. J. Allain, M. Cancet, L. Carrère, and N. Picot. Fes2014 global ocean tides atlas: design and performances. *Ocean Science Discussions*, 2020:1–40, 2020. doi:10.5194/os-2020-96. URL <https://os.copernicus.org/preprints/os-2020-96/>.
- P. Maccready, R. Hetland, and W. Geyer. Long-term isohaline salt balance in an estuary. *Cont. Shelf Res.*, 22:1591–1601, 07 2002. doi:10.1016/S0278-4343(02)00023-7.
- D. G. MacDonald. Mixing processes and hydraulic control in a highly stratified estuary. Technical report, MASSACHUSETTS INST OF TECH CAMBRIDGE, 2003.
- D. G. MacDonald and W. R. Geyer. Turbulent energy production and entrainment at a highly stratified estuarine front. *J. Geophys. Res.-Oceans*, 109 (C5), 2004. doi:10.1029/2003JC002094. URL <https://agupubs.onlinelibrary.wiley.com/doi/abs/10.1029/2003JC002094>.
- F. Madelain and E. Kerut. Evidence of mesoscale eddies in the northeast atlantic from a drifting buoy experiment. *Oceanologica Acta*, 1(2):159–168, 1978. URL <https://archimer.ifremer.fr/doc/00000/5226/>.
- P. Marchesiello, J. C. McWilliams, and A. Shchepetkin. Open boundary conditions for long-term integration of regional oceanic models. *Ocean Modelling*, 3(1):1–20, 2001. ISSN 1463-5003. doi:[https://doi.org/10.1016/S1463-5003\(00\)00013-5](https://doi.org/10.1016/S1463-5003(00)00013-5). URL <https://www.sciencedirect.com/science/article/pii/S1463500300000135>.
- D. P. Marshall and A. J. Adcroft. Parameterization of ocean eddies: Potential vorticity mixing, energetics and arnold’s first stability theorem. *Ocean Model.*, 32(3):188 – 204, 2010. ISSN 1463-5003. doi:<https://doi.org/10.1016/j.ocemod.2010.02.001>. URL <http://www.sciencedirect.com/science/article/pii/S1463500310000107>. The magic of modelling: A special volume commemorating the contributions of Peter D. Killworth – Part 2.

- J. Marshall, D. Jamous, and J. Nilsson. Entry, flux, and exit of potential vorticity in ocean circulation. *J. Phys. Oceanogr. - J PHYS OCEANOGR*, 31:777–789, 03 2001. doi:10.1175/1520-0485(2001)031<0777:EFAEOP>2.0.CO;2.
- J. C. Marshall and A. J. G. Nurser. Fluid dynamics of oceanic thermocline ventilation. *J. Phys. Oceanogr.*, 22(6):583–595, 1992. doi:10.1175/1520-0485(1992)022<0583:FDOOTV>2.0.CO;2. URL [https://doi.org/10.1175/1520-0485\(1992\)022<0583:FD00TV>2.0.CO;2](https://doi.org/10.1175/1520-0485(1992)022<0583:FD00TV>2.0.CO;2).
- P. L. F. Mazzini, R. J. Chant, M. E. Scully, J. Wilkin, E. J. Hunter, and N. J. Nidzieko. The impact of wind forcing on the thermal wind shear of a river plume. *Journal of Geophysical Research: Oceans*, 124(11):7908–7925, 2019. doi:<https://doi.org/10.1029/2019JC015259>. URL <https://agupubs.onlinelibrary.wiley.com/doi/abs/10.1029/2019JC015259>.
- J. C. McWilliams. The emergence of isolated coherent vortices in turbulent flow. *J. Fluid Mech.*, 146:21–43, 1984. doi:10.1017/S0022112084001750.
- J. C. McWilliams. Submesoscale currents in the ocean. *Proceedings of the Royal Society A: Mathematical, Physical and Engineering Sciences*, 472(2189):20160117, 2016. doi:10.1098/rspa.2016.0117. URL <https://royalsocietypublishing.org/doi/abs/10.1098/rspa.2016.0117>.
- J. C. McWilliams. Submesoscale surface fronts and filaments: secondary circulation, buoyancy flux, and frontogenesis. *Journal of Fluid Mechanics*, 823:391–432, 2017. doi:10.1017/jfm.2017.294.
- G. L. Mellor and T. Yamada. Development of a turbulence closure model for geophysical fluid problems. *Reviews of Geophysics*, 20(4):851–875, 1982. doi:<https://doi.org/10.1029/RG020i004p00851>. URL <https://agupubs.onlinelibrary.wiley.com/doi/abs/10.1029/RG020i004p00851>.
- T. B. Mitchell and L. F. Rossi. The evolution of kirchhoff elliptic vortices. *Physics of Fluids*, 20(5):054103, 2008. doi:10.1063/1.2912991. URL <https://doi.org/10.1063/1.2912991>.
- C. Moffat and S. Lentz. On the response of a buoyant plume to downwelling-favorable wind stress. *Journal of Physical Oceanography*, 42(7):1083 – 1098, 2012. doi:10.1175/JPO-D-11-015.1. URL <https://journals.ametsoc.org/view/journals/phoc/42/7/jpo-d-11-015.1.xml>.
- Y. Morel and J. McWilliams. Effects of isopycnal and diapycnal mixing on the stability of oceanic currents. *J. Phys. Oceanogr. - J PHYS OCEANOGR*, 31:2280–2296, 08 2001. doi:10.1175/1520-0485(2001)031<2280:EOIADM>2.0.CO;2.
- V. M. Morin, D. Z. Zhu, and M. R. Loewen. Supercritical exchange flow down a sill. *Journal of Hydraulic Engineering*, 130(6):521–531, 2004. doi:10.1061/(ASCE)0733-9429(2004)130:6(521).

- M. Morvan and X. Carton. Sub-mesoscale frontal instabilities in the omani coastal current. *Mathematics*, 8(4), 2020. ISSN 2227-7390. doi:10.3390/math8040562. URL <https://www.mdpi.com/2227-7390/8/4/562>.
- H. Nakano and J. Yoshida. A note on estimating eddy diffusivity for oceanic double-diffusive convection. *Journal of Oceanography*, pages 1–19, 2019.
- J. Nash and J. Moum. River plumes as a source of large-amplitude internal waves in the coastal ocean. *Nature*, 437:400–403, 2005.
- J. Nash, L. Kilcher, and J. Moum. Structure and composition of a strongly stratified, tidally pulsed river plume. *J. Geophys. Res*, 114, 08 2009. doi:10.1029/2008JC005036.
- D. Nof and T. Pichevin. The ballooning of outflows. *J. Phys. Oceanogr.*, 31(10): 3045–3058, 2001. doi:10.1175/1520-0485(2001)031<3045:TBOO>2.0.CO;2. URL [https://doi.org/10.1175/1520-0485\(2001\)031<3045:TBOO>2.0.CO;2](https://doi.org/10.1175/1520-0485(2001)031<3045:TBOO>2.0.CO;2).
- J. O’Donnell. The dynamics of estuary plumes and fronts. In A. Valle-Levinson, editor, *Contemporary Issues in Estuarine Physics*, chapter 8, pages 186–246. Cambridge University Press, Cambridge, 2010. doi:10.1017/CBO9780511676567.009.
- A. Okubo. Horizontal dispersion of floatable particles in the vicinity of velocity singularities such as convergences. *Deep Sea Research and Oceanographic Abstracts*, 17(3):445–454, 1970. ISSN 0011-7471. doi:[https://doi.org/10.1016/0011-7471\(70\)90059-8](https://doi.org/10.1016/0011-7471(70)90059-8). URL <https://www.sciencedirect.com/science/article/pii/0011747170900598>.
- A. H. Oort, L. A. Anderson, and J. P. Peixoto. Estimates of the energy cycle of the oceans. *J. Geophys. Res.-Oceans*, 99(C4):7665–7688, 1994. doi:10.1029/93JC03556. URL <https://agupubs.onlinelibrary.wiley.com/doi/abs/10.1029/93JC03556>.
- I. Orlanski. A simple boundary condition for unbounded hyperbolic flows. *Journal of Computational Physics*, 21(3):251–269, 1976. ISSN 0021-9991. doi:[https://doi.org/10.1016/0021-9991\(76\)90023-1](https://doi.org/10.1016/0021-9991(76)90023-1). URL <https://www.sciencedirect.com/science/article/pii/0021999176900231>.
- S. Ortiz, J.-M. Chomaz, and T. Loiseleux. Spatial holmboe instability. *Physics of Fluids*, 14(8):2585–2597, 2002. doi:10.1063/1.1485078. URL <https://doi.org/10.1063/1.1485078>.
- A. Osadchiv. Small mountainous rivers generate high-frequency internal waves in coastal ocean. *Scientific Reports*, 8:16609, 11 2018. doi:10.1038/s41598-018-35070-7.
- T. R. Osborn. Estimates of the local rate of vertical diffusion from dissipation measurements. *Journal of Physical Oceanography*, 10(1):83 – 89, 1980. doi:10.1175/1520-0485(1980)010<0083:EOTLRO>2.0.CO;2. URL https://journals.ametsoc.org/view/journals/phoc/10/1/1520-0485_1980_010_0083_eotlro_2_0_co_2.xml.

- S. Ou, H. Zhang, and D.-x. Wang. Dynamics of the buoyant plume off the pearl river estuary in summer. *Environmental Fluid Mechanics*, 9:471–492, 10 2009. doi:[10.1007/s10652-009-9146-3](https://doi.org/10.1007/s10652-009-9146-3).
- E. Palma and R. Matano. An idealized study of near equatorial river plumes. *J. Geophys. Res.-Oceans*, 122, 05 2017. doi:[10.1002/2016JC012554](https://doi.org/10.1002/2016JC012554).
- T. L. Palmer, D. C. Fritts, Andreassen, and I. Lie. Three-dimensional evolution of kelvin-helmholtz billows in stratified compressible flow. *Geophysical Research Letters*, 21(21):2287–2290, 1994. doi:<https://doi.org/10.1029/94GL01714>. URL <https://agupubs.onlinelibrary.wiley.com/doi/abs/10.1029/94GL01714>.
- J. Pan and D. Jay. Effects of ambient velocity shear on nonlinear internal wave associated mixing at the columbia river plume front. *J. Geophys. Res.*, 114, 06 2009. doi:[10.1029/2008JC004988](https://doi.org/10.1029/2008JC004988).
- J. P. Parker, C. P. Caulfield, and R. R. Kerswell. The viscous holmboe instability for smooth shear and density profiles. *Journal of Fluid Mechanics*, 896:A14, 2020. doi:[10.1017/jfm.2020.340](https://doi.org/10.1017/jfm.2020.340).
- A. Pichon and S. Corréard. Internal tides modelling in the bay of biscay: Comparisons with observations. *Scientia Marina*, 70:65–88, 2006.
- F. Pimenta, A. Kirwan, and P. Huq. On the transport of buoyant coastal plumes. *J. Phys. Oceanogr. - J PHYS OCEANOGR*, 41:620–640, 03 2011. doi:[10.1175/2010JPO4473.1](https://doi.org/10.1175/2010JPO4473.1).
- R. D. Pingree and B. Le Cann. Structure, strength and seasonality of the slope currents in the bay of biscay region. *J. Mar. Bio. Assoc. UK*, 70(4):857–885, 1990. doi:[10.1017/S0025315400059117](https://doi.org/10.1017/S0025315400059117).
- R. Pingree and B. Le Cann. Celtic and armorican slope and shelf residual currents. *Progress in Oceanography*, 23(4):303–338, 1989. ISSN 0079-6611. doi:[https://doi.org/10.1016/0079-6611\(89\)90003-7](https://doi.org/10.1016/0079-6611(89)90003-7). URL <https://www.sciencedirect.com/science/article/pii/0079661189900037>.
- R. Pingree and B. Le Cann. Three anticyclonic slope water oceanic eddies (swoddies) in the southern bay of biscay in 1990. *Deep Sea Research Part A. Oceanographic Research Papers*, 39(7):1147 – 1175, 1992. ISSN 0198-0149. doi:[https://doi.org/10.1016/0198-0149\(92\)90062-X](https://doi.org/10.1016/0198-0149(92)90062-X). URL <http://www.sciencedirect.com/science/article/pii/019801499290062X>.
- R. Pingree, B. Sinha, and C. Griffiths. Seasonality of the european slope current (goban spur) and ocean margin exchange. *Continental Shelf Research*, 19(7):929–975, 1999. ISSN 0278-4343. doi:[https://doi.org/10.1016/S0278-4343\(98\)00116-2](https://doi.org/10.1016/S0278-4343(98)00116-2). URL <https://www.sciencedirect.com/science/article/pii/S0278434398001162>.
- R. Pingree and B. Sinha. Westward moving waves or eddies (storms) on the subtropical/azores front near 32.5°n? interpretation of the eulerian currents and

- temperature records at moorings 155 (35.5°w) and 156 (34.4°w). *J. Mar. Sys.*, 29:239–276, 05 2001. doi:[10.1016/S0924-7963\(01\)00019-7](https://doi.org/10.1016/S0924-7963(01)00019-7).
- V. Piton, M. Herrmann, F. Lyard, P. Marsaleix, T. Duhaut, D. Allain, and S. Ouilon. Sensitivity study on the main tidal constituents of the gulf of tonkin by using the frequency-domain tidal solver in t-ugom. *Geoscientific Model Development*, 13(3):1583–1607, 2020. doi:[10.5194/gmd-13-1583-2020](https://doi.org/10.5194/gmd-13-1583-2020). URL <https://gmd.copernicus.org/articles/13/1583/2020/>.
- M. Pritchard and D. Huntley. Instability and mixing in a small estuarine plume front. *Estuarine, Coastal and Shelf Science*, 55(2):275–285, 2002. ISSN 0272-7714. doi:<https://doi.org/10.1006/ecss.2001.0902>. URL <https://www.sciencedirect.com/science/article/pii/S0272771401909023>.
- I. Puillat, P. Lazure, A. Jégou, L. Lampert, and P. Miller. Hydrographical variability on the french continental shelf in the bay of biscay, during the 1990s. *Continental Shelf Research*, 24(10):1143–1163, 2004. ISSN 0278-4343. doi:<https://doi.org/10.1016/j.csr.2004.02.008>. URL <https://www.sciencedirect.com/science/article/pii/S0278434304000330>.
- L. Qu and R. Hetland. Nongeostrophic baroclinic instability over sloping bathymetry: Buoyant flow regime. *Journal of Physical Oceanography*, 50(7):1937–1956, 2020. doi:[10.1175/JPO-D-19-0145.1](https://doi.org/10.1175/JPO-D-19-0145.1). URL <https://journals.ametsoc.org/view/journals/phoc/50/7/jpoD190145.xml>.
- S. Rathan and G. Naga Raju. A modified fifth-order weno scheme for hyperbolic conservation laws. *Computers Mathematics with Applications*, 75(5):1531–1549, 2018. ISSN 0898-1221. doi:<https://doi.org/10.1016/j.camwa.2017.11.020>. URL <https://www.sciencedirect.com/science/article/pii/S0898122117307344>.
- P. Rhines and R. Schopp. The wind-driven circulation: Quasi-geostrophic simulations and theory for nonsymmetric winds. *J. Phys. Oceanogr. - J PHYS OCEANOGR*, 21:1438–1469, 09 1991. doi:[10.1175/1520-0485\(1991\)021<1438:TWDCQG>2.0.CO;2](https://doi.org/10.1175/1520-0485(1991)021<1438:TWDCQG>2.0.CO;2).
- W. Rodi. Examples of calculation methods for flow and mixing in stratified fluids. *Journal of Geophysical Research: Oceans*, 92(C5):5305–5328, 1987. doi:<https://doi.org/10.1029/JC092iC05p05305>. URL <https://agupubs.onlinelibrary.wiley.com/doi/abs/10.1029/JC092iC05p05305>.
- G. Roulet, X. Capet, and G. Maze. Global interior eddy available potential energy diagnosed from argo floats. *Geophysical Research Letters*, 41(5):1651–1656, 2014. doi:<https://doi.org/10.1002/2013GL059004>. URL <https://agupubs.onlinelibrary.wiley.com/doi/abs/10.1002/2013GL059004>.
- A. Rubio, A. Caballero, A. Orfila, I. Hernández-Carrasco, L. Ferrer, M. González, L. Solabarrieta, and J. Mader. Eddy-induced cross-shelf export of high chl-a coastal waters in the se bay of biscay. *Rem. Sens. Env.*, 205:290 – 304, 2018.

- ISSN 0034-4257. doi:<https://doi.org/10.1016/j.rse.2017.10.037>. URL <http://www.sciencedirect.com/science/article/pii/S003442571730500X>.
- J. E. Rudzin, S. Chen, E. R. Sanabia, and S. R. Jayne. The air-sea response during hurricane irma's (2017) rapid intensification over the amazon-orinoco river plume as measured by atmospheric and oceanic observations. *Journal of Geophysical Research: Atmospheres*, 125(18):e2019JD032368, 2020. doi:<https://doi.org/10.1029/2019JD032368>. URL <https://agupubs.onlinelibrary.wiley.com/doi/abs/10.1029/2019JD032368>. e2019JD032368 2019JD032368.
- H. Salehipour, C. P. Caulfield, and W. R. Peltier. Turbulent mixing due to the holmboe wave instability at high reynolds number. *Journal of Fluid Mechanics*, 803:591–621, 2016. doi:[10.1017/jfm.2016.488](https://doi.org/10.1017/jfm.2016.488).
- R. V. Schiller, V. H. Kourafalou, P. Hogan, and N. D. Walker. The dynamics of the mississippi river plume: Impact of topography, wind and off-shore forcing on the fate of plume waters. *J. Geophys. Res.-Oceans*, 116 (C6), 2011. doi:[10.1029/2010JC006883](https://doi.org/10.1029/2010JC006883). URL <https://agupubs.onlinelibrary.wiley.com/doi/abs/10.1029/2010JC006883>.
- W. Schubert, E. Ruprecht, R. Hertenstein, R. N. Ferreira, R. Taft, C. Rozoff, P. Ciesielski, and H.-C. Kuo. English translations of twenty-one of ertel's papers on geophysical fluid dynamics. *Meteorologische Zeitschrift*, 13(6):527–576, 12 2004. doi:[10.1127/0941-2948/2004/0013-0527](https://doi.org/10.1127/0941-2948/2004/0013-0527). URL <http://dx.doi.org/10.1127/0941-2948/2004/0013-0527>.
- A. Serpette, B. Cann, and F. Colas. Lagrangian circulation of the north atlantic central water over the abyssal plain and continental slopes of the bay of biscay: description of selected mesoscale features. *Scientia Marina*, 70:27–42, 06 2006.
- A. F. Shchepetkin and J. C. McWilliams. The regional oceanic modeling system (roms): a split-explicit, free-surface, topography-following-coordinate oceanic model. *Ocean Modelling*, 9(4):347–404, 2005. ISSN 1463-5003. doi:<https://doi.org/10.1016/j.ocemod.2004.08.002>. URL <https://www.sciencedirect.com/science/article/pii/S1463500304000484>.
- J. Sheng. Dynamics of a buoyancy-driven coastal jet: The gaspé current. *Journal of Physical Oceanography*, 31(11):3146 – 3162, 2001. doi:[10.1175/1520-0485\(2001\)031<3146:DOABDC>2.0.CO;2](https://doi.org/10.1175/1520-0485(2001)031<3146:DOABDC>2.0.CO;2). URL https://journals.ametsoc.org/view/journals/phoc/31/11/1520-0485_2001_031_3146_doabdc_2.0.co_2.xml.
- J. Shi, C. Tong, J. Zheng, C. Zhang, and X. Gao. Kelvin-helmholtz billows induced by shear instability along the north passage of the yangtze river estuary, china. *Journal of Marine Science and Engineering*, 7(4), 2019a. ISSN 2077-1312. doi:[10.3390/jmse7040092](https://doi.org/10.3390/jmse7040092). URL <https://www.mdpi.com/2077-1312/7/4/92>.

- J. Shi, C. Tong, J. Zheng, C. Zhang, and X. Gao. Kelvin-helmholtz billows induced by shear instability along the north passage of the yangtze river estuary, china. *Journal of Marine Science and Engineering*, 7(4), 2019b. ISSN 2077-1312. doi:10.3390/jmse7040092. URL <https://www.mdpi.com/2077-1312/7/4/92>.
- J. Simpson, J. Brown, J. Matthews, and G. Allen. Tidal straining, density currents, and stirring in the control of estuarine stratification. *Estuaries*, 13:125–132, 06 1990. doi:10.2307/1351581.
- S. Singh, K. K. Mahajan, R. K. Choudhary, and O. P. Nagpal. Detection of kelvin-helmholtz instability with the indian mesosphere-stratosphere-troposphere radar: A case study. *Journal of Geophysical Research: Atmospheres*, 104(D4):3937–3945, 1999. doi:<https://doi.org/10.1029/98JD02675>. URL <https://agupubs.onlinelibrary.wiley.com/doi/abs/10.1029/98JD02675>.
- W. D. Smyth and W. R. Peltier. Instability and transition in finite-amplitude kelvin-helmholtz and holmboe waves. *Journal of Fluid Mechanics*, 228:387–415, 1991. doi:10.1017/S0022112091002756.
- W. D. Smyth and K. B. Winters. Turbulence and mixing in holmboe waves. *Journal of Physical Oceanography*, 33(4):694 – 711, 2003. doi:10.1175/1520-0485(2003)33<694:TAMIHW>2.0.CO;2. URL https://journals.ametsoc.org/view/journals/phoc/33/4/1520-0485_2003_33_694_tamihw_2.0.co_2.xml.
- W. D. Smyth, J. D. Nash, and J. N. Moum. Differential diffusion in breaking kelvin-helmholtz billows. *Journal of Physical Oceanography*, 35(6):1004 – 1022, 2005. doi:10.1175/JPO2739.1. URL <https://journals.ametsoc.org/view/journals/phoc/35/6/jpo2739.1.xml>.
- W. D. Smyth, J. R. Carpenter, and G. A. Lawrence. Mixing in symmetric holmboe waves. *Journal of Physical Oceanography*, 37(6):1566 – 1583, 2007. doi:10.1175/JPO3037.1. URL <https://journals.ametsoc.org/view/journals/phoc/37/6/jpo3037.1.xml>.
- W. Smyth and J. Moum. Ocean mixing by kelvin-helmholtz instability. *Oceanography*, 25:140–149, 06 2012. doi:10.5670/oceanog.2012.49.
- M. Spall and J. Price. Mesoscale variability in denmark strait: The pv outflow hypothesis. *J. Phys. Oceanogr.*, 28:1598–1623, 08 1998. doi:10.1175/1520-0485(1998)028<1598:MVIDST>2.0.CO;2.
- M. A. Spall and L. N. Thomas. Downfront winds over buoyant coastal plumes. *Journal of Physical Oceanography*, 46(10):3139 – 3154, 2016. doi:10.1175/JPO-D-16-0042.1. URL <https://journals.ametsoc.org/view/journals/phoc/46/10/jpo-d-16-0042.1.xml>.
- M. Stamper and J. Taylor. The transition from symmetric to baroclinic instability in the eady model. *Ocean Dyn.*, 11 2016. doi:10.1007/s10236-016-1011-6.

- P. H. Stone. On non-geostrophic baroclinic stability. *J. Atmos. Sci.*, 23(4):390–400, 1966. doi:10.1175/1520-0469(1966)023<0390:ONGBS>2.0.CO;2. URL [https://doi.org/10.1175/1520-0469\(1966\)023<0390:ONGBS>2.0.CO;2](https://doi.org/10.1175/1520-0469(1966)023<0390:ONGBS>2.0.CO;2).
- G. I. Taylor. Effect of variation in density on the stability of superposed streams of fluid. *Proceedings of the Royal Society of London. Series A, Containing Papers of a Mathematical and Physical Character*, 132(820):499–523, 1931. ISSN 09501207. URL <http://www.jstor.org/stable/95674>.
- E. W. Tedford, J. R. Carpenter, R. Pawlowicz, R. Pieters, and G. A. Lawrence. Observation and analysis of shear instability in the fraser river estuary. *Journal of Geophysical Research: Oceans*, 114(C11):006, 2009. doi:<https://doi.org/10.1029/2009JC005313>. URL <https://agupubs.onlinelibrary.wiley.com/doi/abs/10.1029/2009JC005313>.
- A. Teles-Machado, A. Peliz, J. C. McWilliams, R. M. Cardoso, P. M. M. Soares, and P. M. A. Miranda. On the year-to-year changes of the iberian poleward current. *J. Geophys. Res.-Oceans*, 120(7):4980–4999, 2015. doi:10.1002/2015JC010758. URL <https://agupubs.onlinelibrary.wiley.com/doi/abs/10.1002/2015JC010758>.
- L. Thomas and R. Ferrari. Friction, frontogenesis, and the stratification of the surface mixed layer. *J. Phys. Oceanogr.*, 38(11):2501–2518, 2008. doi:10.1175/2008JPO3797.1. URL <https://doi.org/10.1175/2008JP03797.1>.
- L. Thomas, A. Tandon, and A. Mahadevan. Submesoscale processes and dynamics. *Washington DC American Geophysical Union Geophysical Monograph Series*, 177, 01 2008. doi:10.1029/177GM04.
- L. Thomas, J. Taylor, R. Ferrari, and T. Joyce. Symmetric instability in the gulf stream. *Deep-Sea Res. Pt. II-Topical Studies in Oceanography*, 91:96–110, 07 2013. doi:10.1016/j.dsr2.2013.02.025.
- L. N. Thomas. Destruction of potential vorticity by winds. *J. Phys. Oceanogr.*, 35(12):2457–2466, 2005. doi:10.1175/JPO2830.1. URL <https://doi.org/10.1175/JPO2830.1>.
- L. N. Thomas and C. M. Lee. Intensification of ocean fronts by down-front winds. *J. Phys. Oceanogr.*, 35(6):1086–1102, 2005. doi:10.1175/JPO2737.1. URL <https://doi.org/10.1175/JPO2737.1>.
- R. E. Thomson and I. V. Fine. Estimating mixed layer depth from oceanic profile data. *Journal of Atmospheric and Oceanic Technology*, 20(2):319 – 329, 2003. doi:10.1175/1520-0426(2003)020<0319:EMLDFO>2.0.CO;2. URL https://journals.ametsoc.org/view/journals/atot/20/2/1520-0426_2003_020_0319_emldfo_2_0_co_2.xml.
- W. Thomson. Hydrokinetic solutions and observations. *Philosophical Magazine*, 42: 362–377, 1871. doi:10.1017/CBO9780511694523.031.

- S. A. Thorpe. On the kelvin–helmholtz route to turbulence. *Journal of Fluid Mechanics*, 708:1–4, 2012. doi:10.1017/jfm.2012.383.
- F. T. Toubanc, N. Ayoub, F. Lyard, P. Marsaleix, and D. Allain. Tidal downscaling from the open ocean to the coast: a new approach applied to the Bay of Biscay. *Ocean Modelling*, 124:16–32, April 2018. doi:10.1016/j.ocemod.2018.02.001. URL <https://hal.archives-ouvertes.fr/hal-02997777>.
- L. Umlauf and H. Burchard. Second-order turbulence closure models for geophysical boundary layers. a review of recent work. *Continental Shelf Research*, 25:795–827, 05 2005. doi:10.1016/j.csr.2004.08.004.
- G. K. Vallis. *Atmospheric and Oceanic Fluid Dynamics*. Cambridge University Press, Cambridge, U.K., 2006.
- H. M. van Aken. Surface currents in the bay of biscay as observed with drifters between 1995 and 1999. *Deep Sea Research Part I: Oceanographic Research Papers*, 49(6):1071 – 1086, 2002. ISSN 0967-0637. doi:[https://doi.org/10.1016/S0967-0637\(02\)00017-1](https://doi.org/10.1016/S0967-0637(02)00017-1). URL <http://www.sciencedirect.com/science/article/pii/S0967063702000171>.
- H. van Haren and L. Gostiaux. A deep-ocean kelvin-helmholtz billow train. *Geophysical Research Letters*, 37(3):L03605, 2010. doi:<https://doi.org/10.1029/2009GL041890>. URL <https://agupubs.onlinelibrary.wiley.com/doi/abs/10.1029/2009GL041890>.
- F. Vandermeirsch, M. Charraudeau, A. Bonnat, M. Fichaut, C. Maillard, F. Gailard, and E. Autret. Bay of Biscay’s temperature and salinity climatology. *XII International Symposium on Oceanography of the Bay of Biscay, 4-6 mai 2010, Plouzané, France*, 2010.
- C. Vic, H. Berger, A.-M. Treguier, and X. Couvelard. Dynamics of an equatorial river plume: Theory and numerical experiments applied to the congo plume case. *J. Phys. Oceanogr.*, 44:940, 12 2014. doi:10.1175/JPO-D-13-0132.1.
- A. Visser, A. Souza, K. Hessner, and J. Simpson. The influence of water column stratification on tidal current profile in a rofi system. *Oceanol. Acta*, 17:369–381, 01 1994.
- S. Voropayev and I. Filippov. Development of a horizontal jet in homogeneous and stratified fluids. laboratory experiment. *J. Fluid Mech.*, 21:964–972, 09 1985.
- R. A. Walters and C. Heston. Removing tidal-period variations from time-series data using low-pass digital filters. *J. Phys. Oceanogr.*, 12(1):112–115, 1982. doi:10.1175/1520-0485(1982)012<0112:RTPVFT>2.0.CO;2. URL [https://doi.org/10.1175/1520-0485\(1982\)012<0112:RTPVFT>2.0.CO;2](https://doi.org/10.1175/1520-0485(1982)012<0112:RTPVFT>2.0.CO;2).
- J. C. Warner, W. R. Geyer, and J. A. Lerczak. Numerical modeling of an estuary: A comprehensive skill assessment. *J. Geophys. Res.-Oceans*, 110(C5), 2005. doi:10.1029/2004JC002691. URL <https://agupubs.onlinelibrary.wiley.com/doi/abs/10.1029/2004JC002691>.

- J. Weiss. The dynamics of enstrophy transfer in two-dimensional hydrodynamics. *Physica D: Nonlinear Phenomena*, 48(2):273–294, 1991. ISSN 0167-2789. doi:[https://doi.org/10.1016/0167-2789\(91\)90088-Q](https://doi.org/10.1016/0167-2789(91)90088-Q). URL <https://www.sciencedirect.com/science/article/pii/016727899190088Q>.
- J. O. Wenegrat, L. N. Thomas, J. Gula, and J. C. McWilliams. Effects of the submesoscale on the potential vorticity budget of ocean mode waters. *Journal of Physical Oceanography*, 48(9):2141 – 2165, 2018. doi:10.1175/JPO-D-17-0219.1. URL <https://journals.ametsoc.org/view/journals/phoc/48/9/jpo-d-17-0219.1.xml>.
- D. C. Wilcox. Reassessment of the scale-determining equation for advanced turbulence models. *AIAA Journal*, 26(11):1299–1310, 1988. doi:10.2514/3.10041. URL <https://doi.org/10.2514/3.10041>.
- C. J. Willmott, S. M. Robeson, and K. Matsuura. A refined index of model performance. *International Journal of Climatology*, 32(13):2088–2094, 2012. doi:<https://doi.org/10.1002/joc.2419>. URL <https://rmets.onlinelibrary.wiley.com/doi/abs/10.1002/joc.2419>.
- T. Wu and H. Wu. Tidal mixing sustains a bottom-trapped river plume and buoyant coastal current on an energetic continental shelf. *Journal of Geophysical Research: Oceans*, 123(11):8026–8051, 2018. doi:<https://doi.org/10.1029/2018JC014105>. URL <https://agupubs.onlinelibrary.wiley.com/doi/abs/10.1029/2018JC014105>.
- W. Xu, P. I. Miller, G. D. Quartly, and R. D. Pingree. Seasonality and interannual variability of the european slope current from 20years of altimeter data compared with in situ measurements. *Remote Sensing of Environment*, 162(C):196–207, 2015. doi:10.1016/j.rse.2015.02.008.
- Q. Yang, M. Nikurashin, H. Sasaki, H. Sun, and J. Tian. Dissipation of mesoscale eddies and its contribution to mixing in the northern south china sea. *Scientific Reports*, 9:556, 01 2019. doi:10.1038/s41598-018-36610-x.
- A. E. Yankovsky and D. C. Chapman. A simple theory for the fate of buoyant coastal discharges. *Journal of Physical Oceanography*, 27(7):1386 – 1401, 1997. doi:10.1175/1520-0485(1997)027<1386:ASTFTF>2.0.CO;2. URL https://journals.ametsoc.org/view/journals/phoc/27/7/1520-0485_1997_027_1386_astftf_2.0.co_2.xml.
- O. Yelekci. *Submesoscale dynamics in the Bay of Biscay continental shelf*. PhD thesis, Pierre and Marie-Curie Univ, 2017. URL <http://www.theses.fr/2017PA066529>. 2017PA066529.
- O. Yelekçi, G. Charria, X. Capet, G. Reverdin, J. Sudre, and H. Yahia. Spatial and seasonal distributions of frontal activity over the french continental shelf in the bay of biscay. *Continental Shelf Research*, 144:65–79, 2017. ISSN 0278-4343. doi:<https://doi.org/10.1016/j.csr.2017.06.015>. URL <https://www.sciencedirect.com/science/article/pii/S0278434317303308>.

- T. Zagvozhkin, A. Vorobev, and T. Lyubimova. Kelvin-helmholtz and holmboe instabilities of a diffusive interface between miscible phases. *Phys. Rev. E*, 100:023103, Aug 2019. doi:10.1103/PhysRevE.100.023103. URL <https://link.aps.org/doi/10.1103/PhysRevE.100.023103>.
- B. Zhang, P. A. Delamere, X. Ma, B. Burkholder, M. Wiltberger, J. G. Lyon, V. G. Merkin, and K. A. Sorathia. Asymmetric kelvin-helmholtz instability at jupiter's magnetopause boundary: Implications for corotation-dominated systems. *Geophysical Research Letters*, 45(1):56–63, 2018. doi:<https://doi.org/10.1002/2017GL076315>. URL <https://agupubs.onlinelibrary.wiley.com/doi/abs/10.1002/2017GL076315>.
- Z. Zhang, M. Zhou, Y. Zhong, G. Zhang, S. Jiang, Y. Gao, R. Zhang, and W. O. Smith. Spatial variations of phytoplankton biomass controlled by river plume dynamics over the lower changjiang estuary and adjacent shelf based on high-resolution observations. *Frontiers in Marine Science*, 7:906, 2020. ISSN 2296-7745. doi:10.3389/fmars.2020.587539. URL <https://www.frontiersin.org/article/10.3389/fmars.2020.587539>.

Titre : Observabilité de surface et mélange vertical liés à la (sous)mésoéchelle en milieu côtier : application au golfe de Gascogne

Mots clés : dynamique à sousmésoéchelle, fronts, panache de la Gironde, instabilités, mélange vertical, dissipation

Résumé : L'objectif de cette thèse est l'analyse de la variabilité à sousmésoéchelle du panache de la Gironde. Dans la première partie, en utilisant des simulations numériques idéalisées j'ai démontré l'influence de différents forçages sur la dynamique, les instabilités et le mélange vertical du panache. Il est forcé par des vents de downwelling à évoluer en courant côtier instable. Sous l'influence de la marée, il se transforme en deux régions dynamiques : le bulge et un courant côtier. Dans cette situation, les instabilités mixtes baroclines/barotropes sont localement générées dans les deux régions. Les instabilités symétriques et de cisaillement vertical se développent alors à proximité de l'embouchure de l'estuaire. Dans cette étude, j'ai montré que la frontogénèse intensifie la stratification et les flux non conservatifs érodent la vorticité potentielle dans le cas de vents de downwelling.

Dans la seconde partie, je me suis intéressé à la dynamique d'un panache stratifié et cisailé sous l'influence de paramètres physiques. Ils donnent lieu à des instabilités de Kelvin-Helmholtz à petite échelle spatiale et de très courte période. Le mélange turbulent dans cette étude est sensible aux instabilités de Holmboe. Dans la dernière partie, l'interaction du panache dans un océan côtier turbulent a été étudiée avec des simulations réalistes. Dans la région frontale, la source de mélange à la surface est due aux gradients de densité/salinité. L'interaction du front avec les forçages induit des injections/érosions de vorticité potentielle liées à une dynamique variable et intermittente du vent, des flux atmosphériques et une dynamique d'ondes internes estivale.

Title : Surface observability and vertical mixing linked with (sub)mesoscale in a coastal region: Bay of Biscay application

Keywords : Submesoscale dynamics, fronts, Gironde river plume, instabilities, vertical mixing, dissipation

Abstract : The aim of this thesis is the analysis of the sub-mesoscale variability of the Gironde plume. In the first part, using idealized numerical simulations I demonstrated the influence of different forcings on the dynamics, instabilities and vertical mixing of the plume. It is forced by downwelling winds and evolve into an unstable coastal current. Under the influence of tide, it evolves into two dynamic regions: the bulge and a coastal current. In this situation, mixed baroclinic/barotropic instabilities are locally generated in both regions. Symmetric and vertical shear instabilities then develop near the mouth of the estuary. In this study, I showed that frontogenesis intensifies stratification and non-conservative fluxes erode the potential vorticity under downwelling winds.

In the second part, I was interested in the dynamics of a stratified and sheared plume under the influence of different physical parameters. They give rise to the instabilities of Kelvin-Helmholtz with a small spatial scale and a very short period. The turbulent mixing in this study is sensitive to Holmboe instabilities. Finally, the interaction of the plume in a turbulent coastal ocean was studied with realistic simulations. In the frontal region, the surface source of mixing is due to density/salinity gradients. The interaction of the front with the forcings induces injections/erosions of potential vorticity related to variable and intermittent wind dynamics, atmospheric fluxes and summer internal wave dynamics.